

NAVAL POSTGRADUATE SCHOOL

Monterey, California



THESIS

H 289 307

DESIGN AND CALIBRATION OF AN ELECTRODYNAMIC
DRIVER FOR THE SPACE THERMOACOUSTIC REFRIGERATOR

by

David Anthony Harris

June 1989

and

Richard Eugene Volkert

December 1989

Thesis Advisor:

Thomas J. Hofler

Co-Advisor:

Steven L. Garrett

Approved for public release; distribution is unlimited.

T244089

UNCLASSIFIED

Security Classification of this page

REPORT DOCUMENTATION PAGE

1a Report Security Classification UNCLASSIFIED			1b Restrictive Markings		
2a Security Classification Authority			3 Distribution Availability of Report		
2b Declassification/Downgrading Schedule			Approved for public release; distribution is unlimited.		
4 Performing Organization Report Number(s)			5 Monitoring Organization Report Number(s)		
5a Name of Performing Organization Naval Postgraduate School		6b Office Symbol (If Applicable) 61Gx	7a Name of Monitoring Organization Naval Postgraduate School		
6c Address (city, state, and ZIP code) Monterey, CA 93943-5000			7b Address (city, state, and ZIP code) Monterey, CA 93943-5000		
8a Name of Funding/Sponsoring Organization Naval Research Laboratory		8b Office Symbol Code (If Applicable) 8220	9 Procurement Instrument Identification Number		
8c Address (city, state, and ZIP code) 4555 Overlook Ave. Washington D.C. 20375-5000			10 Source of Funding Numbers		
			Program Element Number	Project No	Task No
			Work Unit Accession No		
1 Title (Include Security Classification) DESIGN AND CALIBRATION OF AN ELECTRODYNAMIC DRIVER FOR THE SPACE THERMOACOUSTIC REFRIGERATOR (UNCLASSIFIED)					
2 Personal Author(s) Harris, David A. and Volkert, Richard E.					
3a Type of Report Master's Thesis		13b Time Covered From To		14 Date of Report (year, month, day) 1989, June	
15 Page Count 220					
6 Supplementary Notation					
7 Cosati Codes			18 Subject Terms (continue on reverse if necessary and identify by block number)		
Field	Group	Subgroup	Electrodynamic Loudspeaker, Thermoacoustic Refrigerator		
9 Abstract (continue on reverse if necessary and identify by block number) The objective of the STAR project is to test and space qualify a continuous cycle cryogenic refrigeration system for the cooling of sensors and electronics based upon the thermoacoustic heat pumping effect. This thesis describes the design, assembly, and calibration of the electrodynamic driver and its associated performance monitoring and control instrumentation. The electroacoustic efficiency of the driver is measured under different operating conditions utilizing a prototype refrigerator resonator. These results are then compared to modelled efficiencies derived from a computer simulation program that uses the independently-measured individual component parameters to predict the driver performance. Good agreement between measured and predicted efficiencies is observed. Highest electroacoustic efficiencies are shown to occur when the resonance frequencies of the driver and resonator are most closely matched. A maximum electroacoustic efficiency of 50% is achieved under these conditions. More important however, is that the efficiency decreases by only 10% over a 30% bandwidth about resonance.					
20 Distribution/Availability of Abstract UNCLASSIFIED <input checked="" type="checkbox"/> unclassified/unlimited <input type="checkbox"/> same as report <input type="checkbox"/> DTIC users			21 Abstract Security Classification UNCLASSIFIED		
22a Name of Responsible Individual PROF. S. L. Garrett			22b Telephone (Include Area code) (408) 646-2540		22c Office Symbol 61Gx

DD FORM 1473, 84 MAR

83 APR edition may be used until exhausted

All other editions are obsolete

security classification of this page

UNCLASSIFIED

Approved for public release; distribution is unlimited

Design and Calibration of an Electrodynamic
Driver for the Space Thermoacoustic Refrigerator (STAR)

- by

David Anthony Harris
Captain, Canadian Air Force
B.S., Royal Roads Military College, 1981

June 1989
and

Richard Eugene Volkert
Lieutenant, United States Navy
B.A.E., Auburn University, 1982

December 1989

Submitted in partial fulfillment of the
requirements for the degree of

MASTER OF SCIENCE IN ENGINEERING ACOUSTICS

from the

NAVAL POSTGRADUATE SCHOOL
June 1989

ABSTRACT

The objective of the STAR project is to test and space qualify a continuous cycle cryogenic refrigeration system for the cooling of sensors and electronics based upon the thermoacoustic heat pumping effect. This thesis describes the design, assembly, and calibration of the electrodynamic driver and its associated performance monitoring and control instrumentation. The electroacoustic efficiency of the driver is measured under different operating conditions utilizing a prototype refrigerator resonator. These results are then compared to modelled efficiencies derived from a computer simulation program that uses the independently-measured individual component parameters to predict the driver performance. Good agreement between measured and predicted efficiencies is observed. Highest electroacoustic efficiencies are shown to occur when the resonance frequencies of the driver and resonator are most closely matched. A maximum electroacoustic efficiency of 50% is achieved under these conditions. More important however, is that the efficiency decreases by only 10% over a 30% bandwidth about resonance.

TABLE OF CONTENTS

I.	INTRODUCTION.....	1
A.	BACKGROUND.....	1
1.	History.....	1
2.	Refrigerator Efficiency.....	3
3.	Driver Optimization.....	7
B.	SPACE THERMOACOUSTIC REFRIGERATOR (STAR).....	9
1.	Motivation.....	9
2.	Get Away Special (GAS) Program.....	10
3.	Non-acoustical Subsystems.....	10
4.	Acoustical Subsystems.....	14
C.	SCOPE.....	18
II.	THE ELECTRODYNAMIC DRIVER.....	20
A.	ELECTRODYNAMIC DRIVER THEORY.....	20
1.	Introduction.....	20
2.	Lumped Parameter Modelling.....	25
B.	ELECTRODYNAMIC DRIVER PARAMETERS.....	26
1.	Driver Modifications.....	26
2.	Driver Measurements.....	28
a.	Transduction Coefficient.....	28
b.	Stiffness Determination.....	30
c.	Quality Factor and Mechanical Resistance.....	36
3.	Voice Coil Resistance.....	40

- 4. Accelerometer Calibration.....42
- C. STAR DRIVER HOUSING.....44
 - 1. Introduction.....44
 - 2. Design Considerations.....45
 - 3. Component Description.....50
 - 4. Microphone/FET Assembly.....60
 - 5. Housing Assembly.....64
 - 6. Vacuum Can Description.....67
- D. DRIVER/HOUSING MEASUREMENTS.....69
 - 1. Driver/Housing Parameters.....69
 - 2. Microphone Calibration.....74
 - 3. Volume Velocity Calibration.....76
- III. RESONATOR SUBSECTION.....81
 - A. OVERVIEW.....81
 - B. RESONATOR COMPONENTS.....82
 - C. HELIUM LEAK TESTING OF THE FRP NECK.....84
- IV. SYSTEM TEST.....89
 - A. EXPERIMENTAL APPARATUS AND PROCEDURE.....89
 - 1. Preliminary Requirements.....89
 - 2. Experimental Configuration.....92
 - 3. Experimental Procedure.....93
 - B. COMPUTER SIMULATION.....97
 - 1. Background.....97
 - 2. Modifications.....99
 - 3. Program Description.....99

C. EXPERIMENTAL RESULTS.....	103
1. Straight Tube.....	103
2. Refrigerator-type Resonator.....	109
3. Refrigerator-type Resonator with Stack.....	127
4. Power Measurements.....	138
V. CONCLUSIONS AND RECOMMENDATIONS.....	148
APPENDIX A - Capillary Flow Measurements.....	151
APPENDIX B - Computer Simulation Program.....	155
APPENDIX C - Selected Dimensional Drawings (Driver Housing).....	162
APPENDIX D - Description of the STAR Resonator.....	180
APPENDIX E - Manufacturer Specification Sheets.....	184
APPENDIX F - Gas Distribution System.....	201
REFERENCES.....	202
INITIAL DISTRIBUTION LIST.....	204

LIST OF TABLES

II-1	Mass Loading Transduction Coefficient.....	30
II-2	Measured Values for the Bellows and Driver Stiffness and Moving Mass.....	34
II-3	Stiffness and Moving Mass for Individual Components and Combined System.....	71
II-4	Driver Housing Parameters.....	74
IV-1	Measured Data from Straight Tube Experiment.....	104
IV-2	Summary of Measurements for Refrigerator-type Resonator.....	127
IV-3	Summary of Measurements for Refrigerator-type Resonator with Stack.....	137
IV-4	Summary of Power Measurements.....	147

LIST OF FIGURES

I-1	STAR Components.....	4
I-2	Electroacoustic Efficiency.....	6
I-3	Schematic Layout of the STAR within the GAS canister.....	12
I-4	Block Diagram of the STAR's Electronics.....	13
I-5	Hofler Prototype Thermoacoustic Refrigerator.....	15
I-6	Thermoacoustic Heat Transfer Process within a Resonator.....	17
II-1	Diagram of a Moving Coil Transducer.....	21
II-2	Mechanical Model for a Simple Harmonic Oscillator.....	24
II-3	Harmon-JBL 2450J Driver Indicating the Portions Removed for use on the STAR.....	27
II-4	Experimental Setup using the MTI Photonic Sensor to Measure Reducer Cone Displacement.....	31
II-5	Plot of the Square of the Period versus Added Mass for Determination of Driver Suspension Stiffness.....	33
II-6	Experimental Apparatus for Bellows Resonance Frequency Measurement.....	35
II-7	Sample Impedance Plot for the Driver as a Function of Frequency.....	37
II-8	Sample Free Decay used for Determination of the Quality Factor.....	39
II-9	Plot of the DC Resistance as a Function of Temperature for a 4" Voice Coil.....	41
II-10	Comparison of Experimental and Theoretical Techniques used in the Determination of the Accelerometer Sensitivity.....	43

II-11	Driver Housing Cross-sectional View.....	46
II-12	Driver Housing.....	47
II-13	Driver Housing Lid View.....	51
II-14	Section Y-Y' View of the Driver Housing.....	52
II-15	Schematic of the PX80 Pressure Sensor, Support Plate, and Strain Relief Fixture.....	56
II-16	The Electronic Feed-through Plug.....	58
II-17	Driver Housing Showing Electronic Feed-through Plug, DC Pressure Transducer Support Plate, and Strain Relief Fixture.....	59
II-18	Microphone/FET Assembly.....	65
II-19	Cross-sectional View of the Vacuum Can.....	68
II-20	Stiffness and Moving Mass Measurements of the Driver/Bellows System.....	71
II-21	Microphone Calibration.....	77
II-22	Volume Velocity Calibration.....	80
III-1	Diagram of the STAR Resonator.....	83
III-2	Fiber-Reinforced Test Pieces.....	86
III-3	Alcatel Helium Leak Tester and FRP Test Assembly.....	88
IV-1	Electrical Power Measuring Circuit.....	91
IV-2	Schematic Representation of the Experimental Apparatus.....	94
IV-3	Mathematical Derivation of Electroacoustic Efficiency in Terms of Measured Parameters.....	98
IV-4	Computer Simulation Strategy.....	101
IV-5	Predicted and Measured Electric Power for the Straight Tube at One Bar.....	106
IV-6	Predicted and Measured Acoustic Power for the Straight Tube at One Bar.....	107

IV-7	Predicted and Measured Electroacoustic Efficiency for the Straight Tube at One Bar.....	108
IV-8	Electroacoustic Efficiency as a Function of Tube Resonance for the Straight Tube.....	110
IV-9	Refrigerator-type Resonator.....	111
IV-10	Measured and Predicted Electric Power for the Refrigerator-like Resonator in 10 Bar Helium....	115
IV-11	Measured and Predicted Acoustic Power for the Refrigerator-like Resonator in 10 Bar Helium....	116
IV-12	Measured and Predicted Electroacoustic Efficiency for the Refrigerator-like Resonator in 10 Bar Helium.....	117
IV-13	Measured and Predicted Electroacoustic Efficiency for the Refrigerator-like Resonator ($f_0=511.6$ Hz).....	120
IV-14	Measured and Predicted Electroacoustic Efficiency for the Refrigerator-like Resonator ($f_0=436.5$ Hz).....	121
IV-15	Measured and Predicted Electroacoustic Efficiency for the Refrigerator-like Resonator ($f_0=415.4$ Hz).....	122
IV-16	Measured and Predicted Electroacoustic Efficiency for the Refrigerator-like Resonator ($f_0=393.1$ Hz).....	123
IV-17	Measured and Predicted Electroacoustic Efficiency for the Refrigerator-like Resonator ($f_0=377.1$ Hz).....	124
IV-18	Measured and Predicted Electroacoustic Efficiency for the Refrigerator-like Resonator in 10 Bar He-Ar (18.85% Ar).....	126
IV-19	Measured and Predicted Electroacoustic Efficiency for Resonator with Stack in 10 Bar He.....	129
IV-20	Measured and Predicted Electroacoustic Efficiency for the Resonator with Stack ($f_0=493.1$ Hz).....	131
IV-21	Measured and Predicted Electroacoustic Efficiency for the Resonator with Stack ($f_0=441.8$ Hz).....	132

IV-22	Measured and Predicted Electroacoustic Efficiency for the Resonator with Stack ($f_0=421.8$ Hz).....	133
IV-23	Measured and Predicted Electroacoustic Efficiency for the Resonator with Stack ($f_0=366.3$ Hz).....	134
IV-24	Measured and Predicted Electroacoustic Efficiency for the Resonator with Stack in 10 Bar He-Ar (18.85% Ar).....	135
IV-25	Electroacoustic Efficiency as a Function of the Tube Resonance Frequency.....	136
IV-26	Power Measurements without Stack at 540 Hz in 10 Bar Helium. a. power ratio. b. displacement/ current ratio.....	140
IV-27	Power Measurements without Stack at 560 Hz in 10 Bar Helium. a. power ratio. b. displacement/ current ratio.....	142
IV-28	Power Measurements without Stack at 570 Hz in 10 Bar Helium. a. power ratio. b. displacement/ current ratio.....	143
IV-29	Power Measurements with Stack at 520 Hz in 10 Bar Helium. a. power ratio. b. displacement/current ratio.....	144
IV-30	Power Measurements with Stack at 600 Hz in 10 Bar Helium. a. power ratio. b. displacement/current ratio.....	145
A-1	Possible Wire/Tubing Configurations a. Concentric b. Eccentric.....	154
C-1	Driver Housing - Lid (Top) View.....	162
C-2	Top View Detail of Figure C-1.....	163
C-3	Side View of the Driver Housing.....	164
C-4	Close-up Top View Detail of Figure C-1.....	165
C-5	Cross-sectional View of the Microphone/FET Housing.....	166
C-6	Top View of the Driver Housing.....	167
C-7	Bottom, or Resonator, View of the Driver Housing.....	168

C-8	Cross-sectional View of the Driver Housing (Vertical Dimensions).....	169
C-9	Cross-sectional View of the Driver Housing (Horizontal Dimensions).....	170
C-10	Close-up Cross-sectional View of the DC Pressure Transducer Port.....	171
C-11	Cross-sectional View along Y-Y' of Figure C-1...	172
C-12	Driver Housing Pressure Lid with Bolt Circle and O-ring Details.....	173
C-13	Plane and Section Views of the Pusher Plate with Taper Detail.....	174
C-14	The DC Pressure Transducer Support Plate in both Plane and Section Views.....	175
C-15	The Electronics Feed-through Plug without Connectors or Fittings in Plane and Section Views.....	176
C-16	Top View of the Vacuum Can Flange Section.....	177
C-17	Close-up Top View of the Vacuum Can Electronics Feed-through Port.....	178
C-18	Side View of the Vacuum Can Flange Section Showing Detail.....	179
D-1	Diagram of the STAR Resonator.....	181
E-1	Dimensions of the Valpey-Fisher Quartz Disk Showing Electrode Configuration.....	196
E-2	Schematic of Eltec Impedance Converter with Constant Current Source Circuitry.....	199
E-3	Eltec 304 Output Impedance and Current Supply Dropout Curves.....	200
F-1	Gas Distribution System.....	201

ACKNOWLEDGEMENT

The authors would like to thank the following people for their assistance and support in the building and testing of the STAR driver:

Mr. Fancher M. Murray, P.E., of JBL Incorporated for providing the Harmon-JBL™ neodymium-iron-boron electrodynamic driver used in the Space Thermoacoustic Refrigerator (STAR).

Dr. Greg W. Swift, of Los Alamos National Laboratories, for his assistance in the modification of voice coils for the STAR driver.

Mr. Glen Harrell, of the Naval Postgraduate School, for his knowledge, insights, and outstanding craftsmanship in the construction of the housing for the STAR driver.

Mr. Jay A. Adeff, of the Naval Postgraduate School, for his assistance in the construction of the fiber-reinforced-plastic test sections and of the system testing equipment.

In addition the authors would like to thank their thesis advisors for their insight, direction, and patience during the conduct of this research project.

I. INTRODUCTION

A. BACKGROUND

This thesis, in part, is a continuation of the work begun by Lt. M. Fitzpatrick¹ (1988) dealing with the Space Thermoacoustic Refrigerator (STAR) project. Much of her introductory material is applicable to this investigation and has therefore been reproduced where relevant. The theory pertaining to the thermodynamics and thermoacoustics involved in the design of the refrigerator is only briefly discussed. Fitzpatrick covered these topics in some detail and further reproduction of her work in these areas would be unnecessarily repetitious.

1. History

Thermoacoustics can be thought of as any process involving heat transport and sound propagation in which energy is converted from one form to the other. The study of thermoacoustic phenomena dates back many years. However it wasn't until only recently (late 1970's to early 1980's) that any major breakthroughs were made in the field. These were largely due to the work of Nikolaus Rott, who quantitatively described the thermoacoustic phenomena that his predecessors had observed. In a review article on thermoacoustics² Rott restricted his definition of the subject matter to the study of heat engines in which a net

heat transport in some gaseous medium is related to the acoustic properties of that medium. Rott discussed heat-driven oscillations in which a heat engine acts as a prime mover. In addition he explained the phenomenon he called "thermoacoustic streaming" in which a heat engine acts as a heat pump or a refrigerator.

Inspired by Rott's work, a group led by John Wheatley at the Los Alamos National Laboratory, began experimental research into the design of various thermoacoustic heat engines. The performance of these early prototypes was rather disappointing which resulted in the group devoting more time to the study of some simple thermoacoustic effects and comparing them to Rott's theory. In 1986, Tom Hofler, a student of Wheatley's, was able to numerically solve Rott's theoretical equations. Applying this knowledge, Hofler designed and built a working thermoacoustic refrigerator³ as part of his doctoral thesis.

Subsequent to Hofler's work, a proposal by Steve Garrett of the Naval Postgraduate School led to the conceptualization of a space-qualified version of Hofler's prototype refrigerator. Two of Garrett and Hofler's thesis students, Fitzpatrick and Susalla, commenced work on two different components of the refrigerator. This thesis is a continuation of their work into the design, fabrication and testing of a space-qualified thermoacoustic refrigerator.

2. Refrigerator Efficiency

In his doctoral dissertation, Hofler reported that the lowest ratio of cold temperature (T_c) to ambient temperature (T_h) attained with his prototype fridge was 0.66. Additionally he found that the highest coefficient of performance relative to Carnot was 12% at a temperature ratio of 0.82. In designing the space-qualified thermoacoustic refrigerator one of the principle objectives was to modify Hofler's prototype in an attempt to increase its overall efficiency. Achieving this goal requires a basic understanding of the refrigerator and the energy transformations that occur within it.

The actual design of the space thermoacoustic refrigerator (STAR) is depicted in Figure I-1. Basically an acoustic standing wave, produced by an electrodynamic driver, is excited within a closed resonator tube. A closely-spaced stack of plastic plates is critically-positioned near the pressure antinode within the resonator. The thermodynamic interaction between the acoustic wave and stack results in a net heat flow towards the pressure antinode. This assumes that minimal heat conduction occurs at the walls of the resonator in the vicinity of the stack. Though this description of the refrigeration process is over-simplified, it will suffice for now. For further discussion of this process, the reader is referred to Swift (1988).⁴ The main point concerning the present topic is

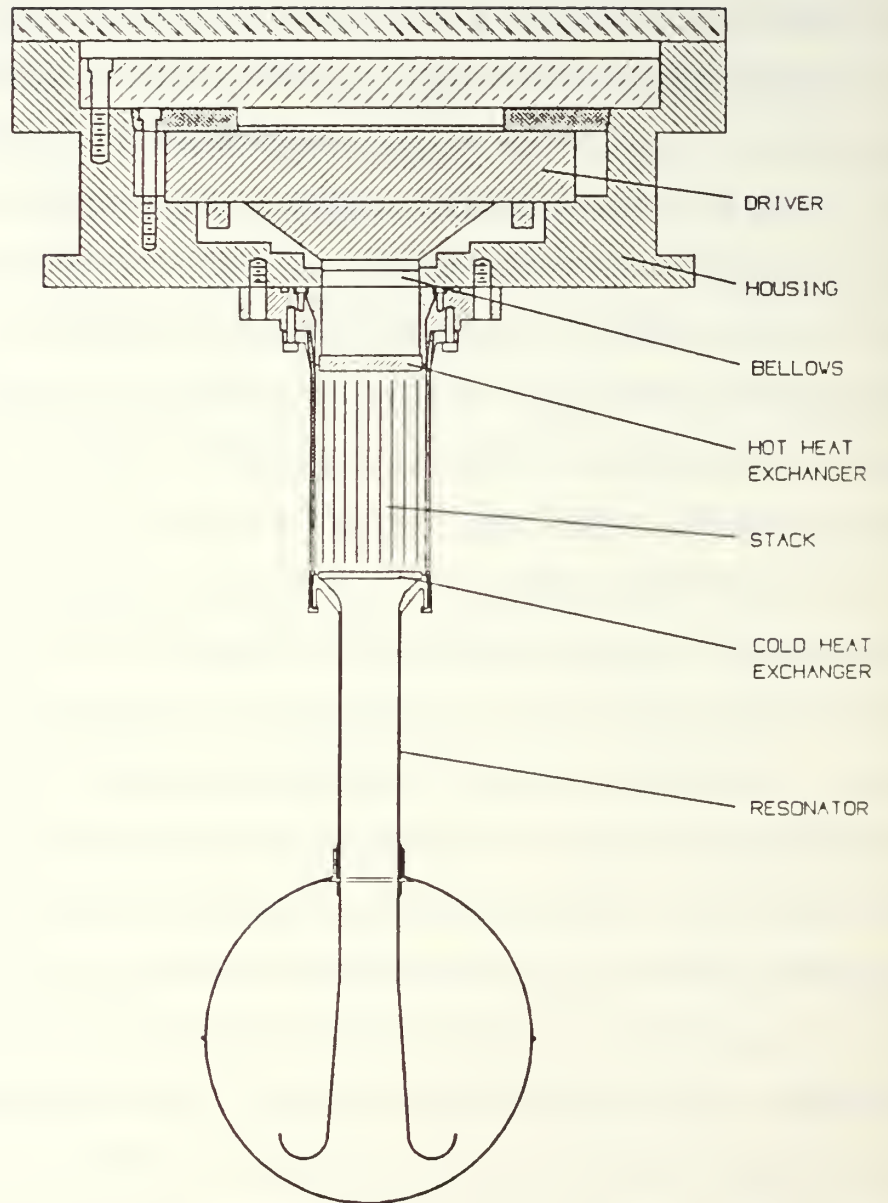


Figure I-1. STAR Components

that three forms of energy exist (electric, acoustic, and heat) and are interrelated in the definition of overall efficiency.

The first transformation to occur involves the electrodynamic driver, or transducer, which converts electrical energy into acoustical energy. The electrical power delivered to the driver (Π_{elec}) is proportional to the product of the input voltage (V), current (I), and the cosine of the phase angle (θ) between them. The acoustical power generated (Π_{ac}) is proportional to the product of the acoustic pressure (p), the volume velocity (U), and the cosine of the phase angle (ϕ) between them. Electroacoustic efficiency (η_{ea}) is then defined as the ratio of the output acoustic power to input electric power.

The second energy transformation involves the interaction between the acoustic pressure wave and the stack. For a given acoustic power, a net heat flow occurs resulting in the removal of heat (Q_c) from the "cold" end of the stack via a heat exchanger. In this case a common measure of performance, known as the coefficient of performance (COP), is equal to the ratio of heat removed to the acoustic power. (Figure I-2 summarizes the above discussion.)

Improvement of the overall performance of the Hofler prototype refrigerator required that the electroacoustic efficiency and coefficient of performance be maximized. The latter was dealt with by Susalla whose work in

$$\Pi_{\text{elec}} = I V \cos \theta$$

$$\Pi_{\text{ac}} = p U \cos \phi$$

$$\eta_{\text{ea}} = \frac{\Pi_{\text{ac}}}{\Pi_{\text{elec}}}$$

$$\text{COP} = \frac{Q_c}{\Pi_{\text{ac}}}$$

Figure I-2. Electroacoustic efficiency

designing and testing variations on the thermoacoustic stack in different inert gas mixtures resulted in significant improvements over previous designs. Using Hofler's refrigerator, Susalla was able to achieve a 93% improvement in the coefficient of performance relative to Carnot,⁵ (where the Carnot COP is defined to be the maximum attainable COP for a perfect refrigerator at a given temperature span).

3. Driver Optimization

Optimization of the electroacoustic efficiency was the topic of Fitzpatrick's research (1988). She discussed the need for a driver to have minimal moving mass (m_0) and minimal mechanical resistance (R_m) in order to reduce mechanical losses. She also explained the need for a driver to have as large a transduction coefficient (Bl) as possible in order to maximize acoustic power output. The driver Fitzpatrick initially selected for modification and testing was an Altec 260-16K electrodynamic transducer. This driver was selected because of its ability to produce the large pressure amplitudes and volume velocities required for space applications. The Altec driver was modified so that voice coil displacements could be directly translated to a flexible surface (the bellows) having approximately the same cross-sectional area as the resonator tube that would house the thermoacoustic stack. Fitzpatrick found that the electroacoustic efficiency of the driver (in air at 1 bar)

ranged from 75.9% to 84.2% for electric powers of 54.2 mW to 0.56mW respectively. Using a computer model developed by Susalla, Fitzpatrick was able to predict the electroacoustic efficiency of the Altec driver. She found that her measured efficiencies were about 15-20% higher than those predicted by computer simulation.

In addition to the Altec 290-16K, Fitzpatrick obtained a modified JBL model 2450J neodymium-iron-boron (NIB) compression driver. This driver employs the latest innovations in driver technology including a titanium suspension and aluminum voice coil in addition to the rare-earth magnetic structure. Imposed time limitations prevented modification of the NIB driver for refrigerator applications, however Fitzpatrick was able to determine the unmodified driver parameters. Using these as inputs for the computer program, and simulating different acoustic load impedances, Fitzpatrick was able to predict electroacoustic efficiencies of the NIB driver in 10 bar helium (He) and 10 bar helium-xenon (12.5% Xe) gas. Predicted efficiencies in helium were reported to be about 50% higher due to better impedance matching between the driver and acoustic load. Although this suggests that helium would be the preferred acoustic medium to be utilized by the fridge, Susalla observed that the coefficient of performance could be maximized by using a He-Xe gas mixture. For this thesis the electroacoustic efficiency of a modified NIB driver is

physically determined for various inert gas mixtures (at 10 bars) and compared with Fitzpatrick's predicted values.

B. SPACE THERMOACOUSTIC REFRIGERATOR (STAR)

1. Motivation

Numerous applications for spaced-based refrigeration systems presently exist in the form of cooling low noise and/or high speed electronics, high T_c superconductors, and infrared detectors. Presently, methods based on the evaporation of expendable cryogens (liquid helium, nitrogen, etc.) or on closed cycle processes (Stirling cycle, Vuilleumier cycle, etc.) are used. Both methods suffer from significant disadvantages. In evaporation based refrigerators, it is a limited supply of stored cryogens, for closed cycle systems, a high vibration level exists. Additionally the use of sliding seals in these refrigerators are a primary cause of system failure lowering their overall long term reliability.

The potential advantages of the STAR in increased reliability, reduced vibration, and simplicity over present space based refrigeration systems indicate that it could replace these systems in some applications. As a result of this it was determined that space-based testing of STAR was desirable. The absence of gravity would remove thermal convection as a heat transport mechanism and the vacuum of space would provide thermal insulation which would allow for

the most accurate determination of the systems overall efficiency.

On 3 February 1988 a Memorandum of Agreement between the Naval Postgraduate School (NPS) and the Air Force was signed that provided funding for the space based testing of STAR. The project was then assigned a National Aeronautics and Space Administration (NASA) payload number of G-337 and scheduled to fly onboard a future Space Shuttle mission as part of NASA's Get Away Special (GAS) program as a Quick Response Shuttle Payload.

2. Get Away Special (GAS) Program

NASA's GAS program is designed to allow small, self-contained payloads to be taken into earth orbit onboard the Space Shuttle in a standardized container at relatively low cost to the experimenter (Get Away Special Team, 1984).⁶ The standardized GAS container is designed to hold a payload of less than five cubic feet and 200 pounds. Each payload must be totally self-contained with its own electrical power, control, data acquisition, and storage subsystems, requiring only the operation of an ON/OFF switch by the Shuttle's astronauts at designated times during the mission.

3. Non-Acoustical Subsystems

Another group of NPS students and faculty led by Garrett (Boyd, et al., 1987)⁷ have taken advantage of the GAS program to measure the resonant acoustic modes of the shuttle payload bay and the ambient acoustic environment

produced as a result of main engine and booster operation during launch. This experiment is called "The Space Shuttle Cargo Bay Vibroacoustics Experiment" and is designated by NASA as payload G-313. Several subsystems that were developed for NASA G-313 will be used on NASA G-337 (STAR). A schematic of the STAR in its GAS can is shown in Figure I-3. One of the systems borrowed from NASA G-313 is the computer/controller system used to run that experiment and record the data. The recorder system consists of the INTEL model BPK 5V75 magnetic bubble memory module and an NSC 800 microprocessor-based controller. Two other NPS students, LT Charles B. Cameron, USN and CPT Ronald Byrnes, USA, will be designing the analog electronics and software to integrate these systems into the STAR experiment for their master's thesis.⁶ A block diagram of the electronics is shown in Figure I-4.

Another borrowed system is the power supply, which consists of Gates brand lead-acid battery cells (five Ampere-hour, two Volts each). These gelled electrolyte batteries are ideal for the STAR due to their high power density, low cost, and the absence of outgassing during discharge cycles. NASA G-313 used a one layer battery of 68 cells providing 680 watt-hours of energy and weighing about 80 pounds (including the cell's support structure). We will be using two battery layers with 42 cells each to provide a 28 Volt bus with a maximum of 840 watt-hours of available



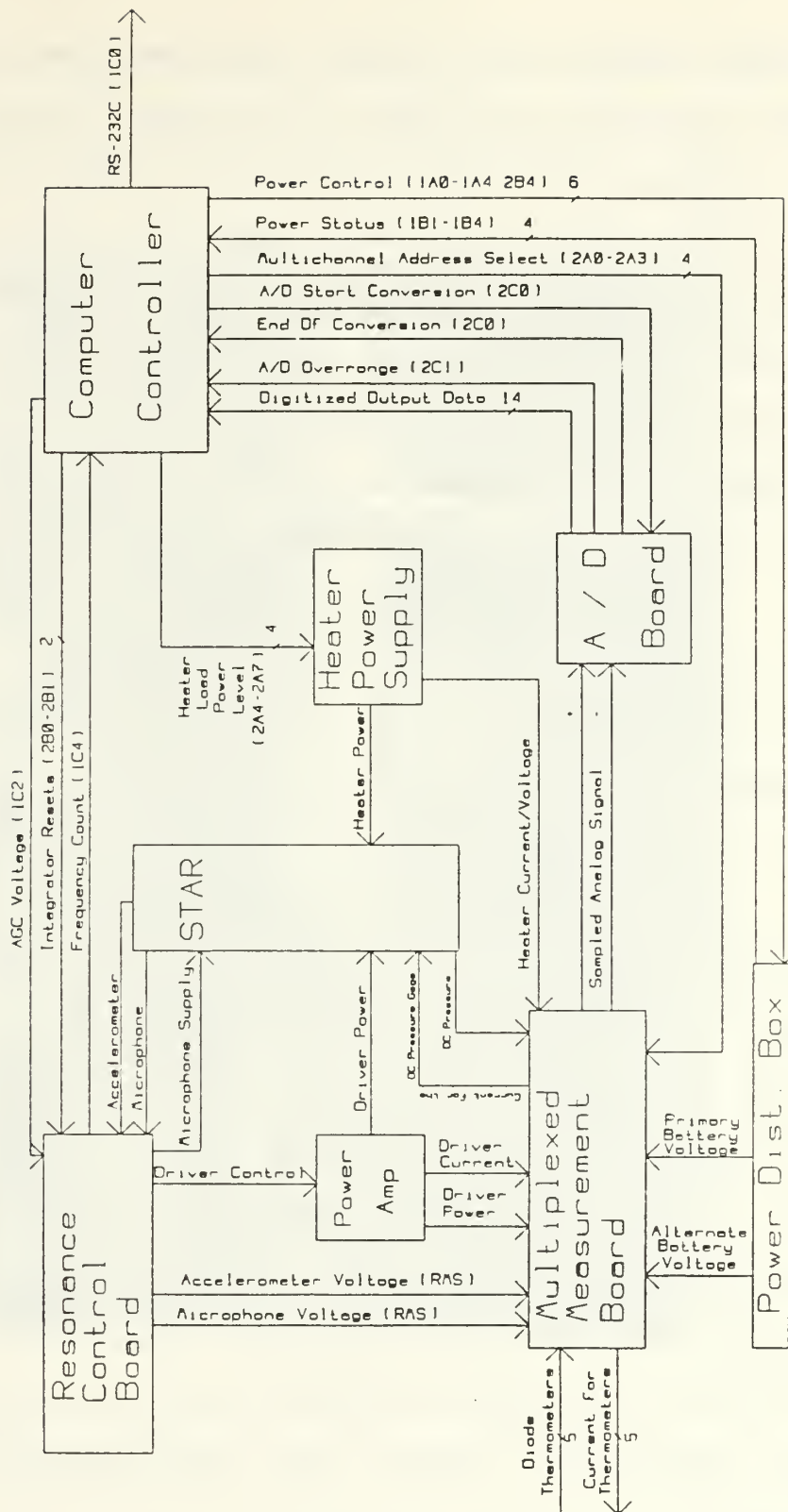


Figure I-4. Block Diagram of the STAR's Electronics

electrical energy and a battery weight between 118 and 130 pounds (including the weight of the sealed battery shelves).

The use of the GAS can imposes certain restrictions. Since we are using batteries to supply the power, the refrigerator has to be energy efficient. Also, the GAS can setup requires the STAR to be compact and lightweight. Figure I-5 shows a photograph of Hofler's prototype refrigerator. This setup is approximately six feet high (which includes vacuum pumps that are not required in space). In comparison, the maximum payload height for the GAS can is 28.25 inches, or less than 2.5 feet. These considerations played a major role in the choice of equipment for the STAR and its design.

4. Acoustical Subsystems

The acoustical subsystems of the STAR were designed to assist in the optimization of the thermoacoustic heat transfer process. Additionally they were designed to assist the STAR in meeting NASA safety requirements and the restrictions imposed by using the GAS container. The driver housing accomplished this by providing a pressure tight container that allowed the STAR to be operated in a ten atmosphere Helium-Xenon gas mixture. The driver housing also serves as a support mechanism for the electrodynamic driver subsystem and various test instrumentation and connectors.

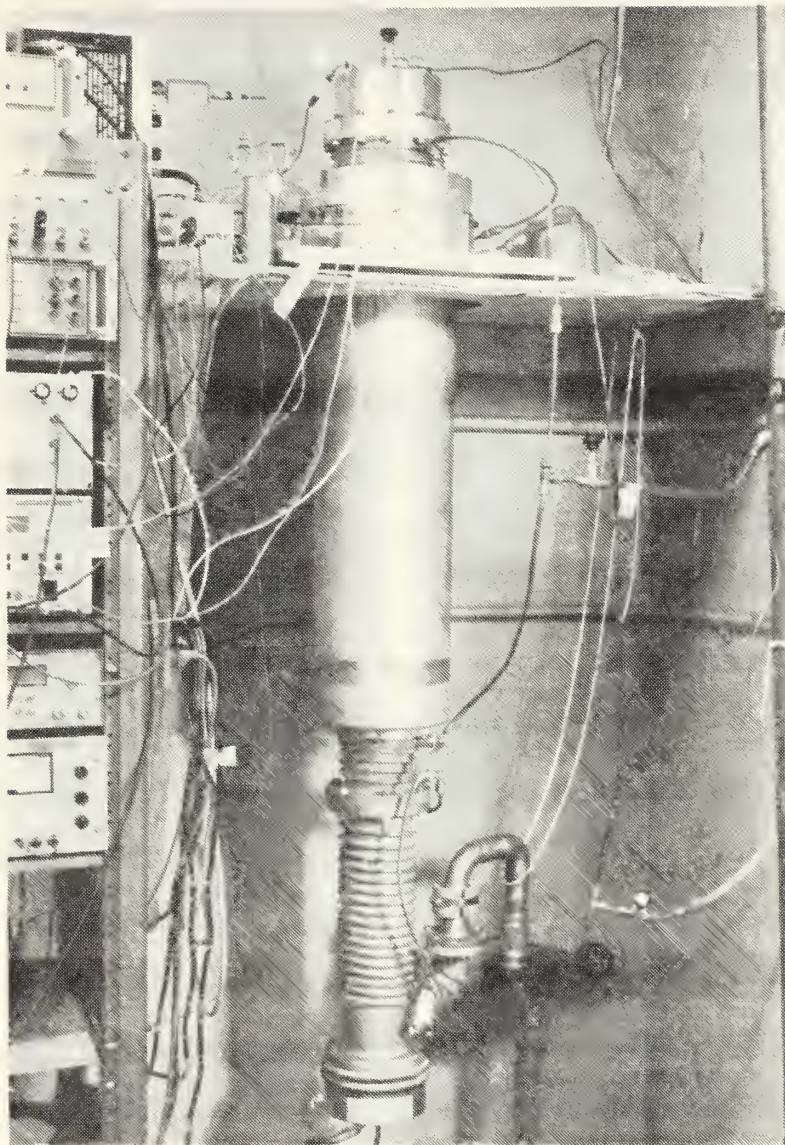


Figure I-5. Hofler Prototype Thermoacoustic Refrigerator

The driver subsystem is designed to efficiently convert the input electrical power from the power amplifier into acoustic power. In order to accomplish this a new type of driver which uses Neodymium-Iron-Boron (NIB) magnets was used in connection with a modified voice coil/reducer cone assembly. The electrodynamic driver assembly was then attached to a flexible bellows assembly designed to act as a pressure seal between the housing assembly and the resonator assembly.

Within the resonator assembly lies the core of the thermoacoustic refrigerator, a plastic stack, first developed by Hofler (1986), which allows for the transfer of heat when a standing wave is generated, as illustrated in Figure I-6. In this process acoustical energy can be converted into a thermal heat transfer. Primary considerations in the design of the resonator assembly were to reduce acoustic losses in the cold portion, reduce its overall length, and to reduce losses due to thermal conduction along the walls of the resonator tube in the vicinity of the plastic stack. The length and losses of the resonator were decreased by using an attached sphere to reduce the sealed resonator length from $1/2$ to $1/4$ of a wavelength and by varying the tube diameter. The losses due to heat transfer along the tube housing the stack were reduced by using a composite wall material with a low thermal conductivity.

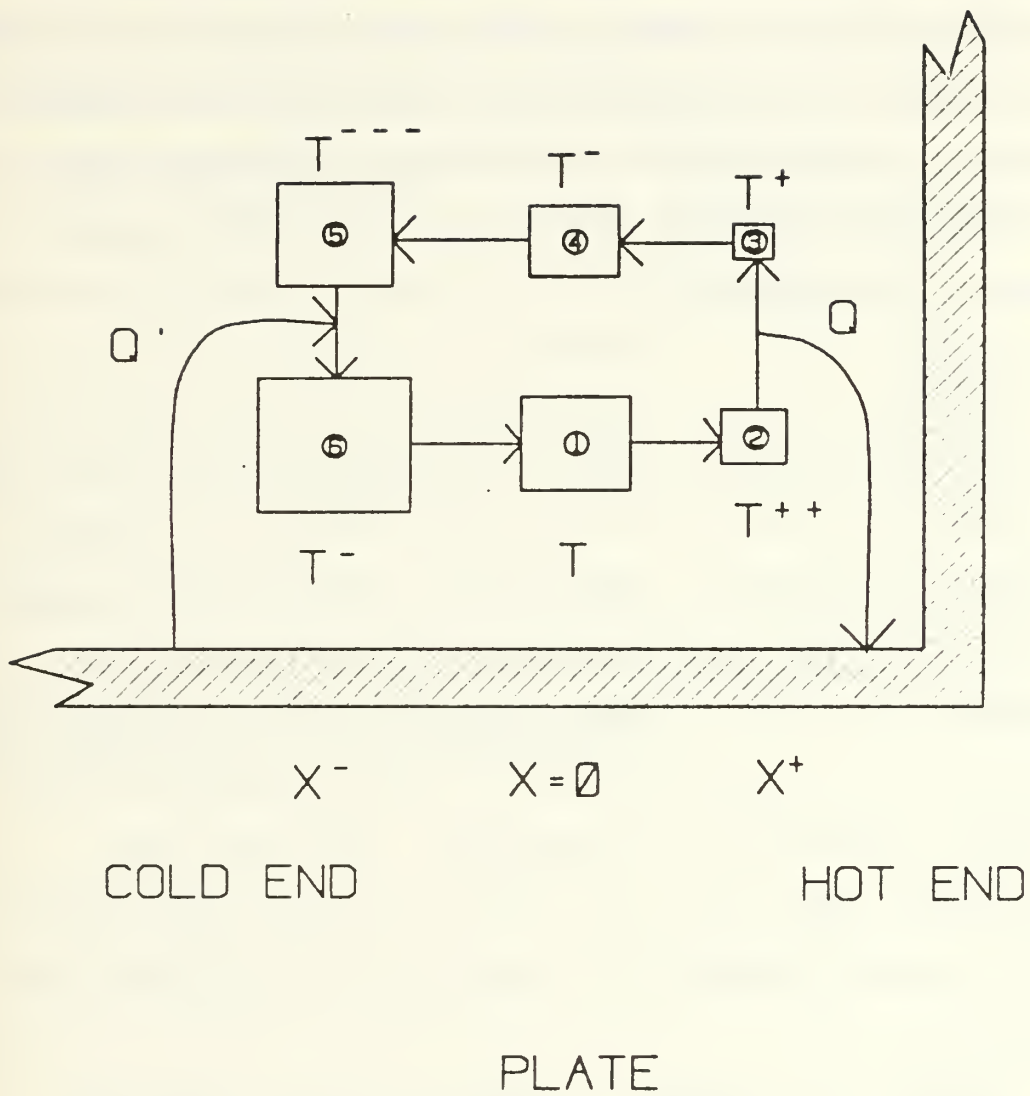


Figure I-6. Thermoacoustic Heat Transfer Process within a Resonator

The final component of the acoustical subsystem is the vacuum can which encloses the resonator assembly. Designed to reduce the heat leak by thermal conduction and radiation, the vacuum can and the superinsulation surrounding the resonator act as an insulator. In the STAR test project the vacuum can will also serve as a safety shield to prevent driver or resonator components from entering the remainder of the GAS can in the event of catastrophic failure.

C. SCOPE

Chapter II begins with a brief discussion of the theory involved in using an electrodynamic driver as a simple harmonic oscillator. Additionally, the ability to model a distributed system by lumped parameter modelling is reviewed. Next, an in-depth discussion of the modifications conducted to the STAR driver and the measurement of its component parameters is presented. Following this discussion, the design and testing of the driver housing and it's various components and subsystems is presented and analyzed.

Chapter III presents an overview on the important thermoacoustic components of the resonator being built for the STAR. A discussion of the limitations in using a helium based gas mixture with a fiber-reinforced plastic neck is presented. One method to overcome the stated liabilities is

discussed and experimental results shown to prove its validity.

Chapter IV presents an analysis of the electroacoustic efficiency of the STAR driver based upon measurements conducted using various gas mixtures and resonators. The experimental configuration and procedure used to meet the test requirements are discussed and schematically illustrated. Additionally a computer simulation program capable of providing a theoretical model of the electroacoustic efficiency is presented. Finally, a series of test measurements is presented for each test case and the results analyzed and compared to results from the simulation program.

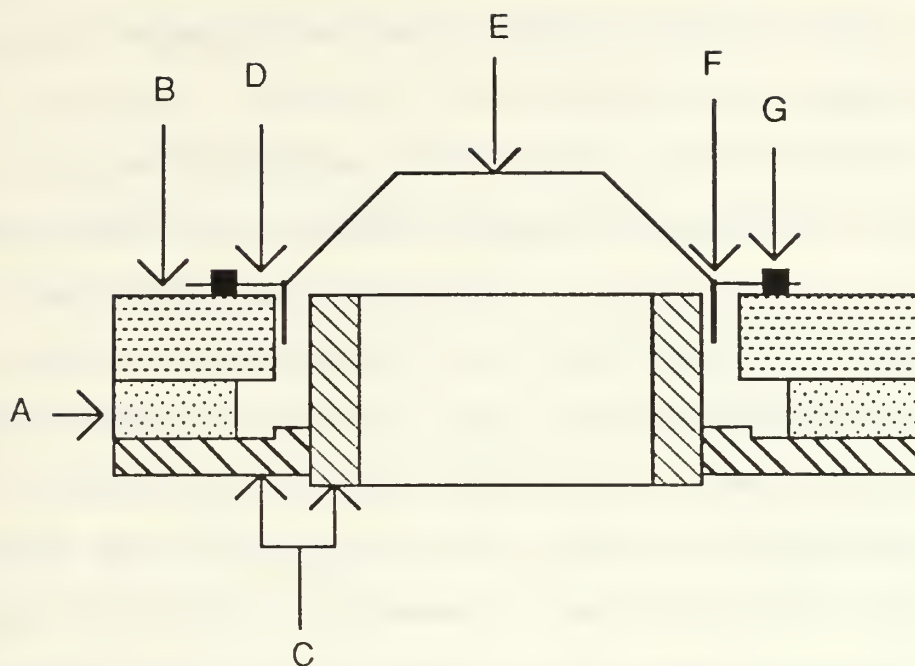
Chapter V provides conclusions from the development and testing of the STAR driver as well as recommendations for areas requiring further investigation.

II. THE ELECTRODYNAMIC DRIVER

A. ELECTRODYNAMIC DRIVER THEORY

1. Introduction

The electrodynamic driver exists for the purpose of converting alternating current (AC) electrical current into acoustic pressures (forces) within the resonator at high efficiencies. The driver subsystem is a modified Harmon-JBL model 2450J compression driver with a voice coil-reducer cone assembly and a bellows. The moving coil transducer consists of a permanent magnet structure energized with Nd-Fe-B magnetic material with an annular gap. Inserted into the gap is a wire wrapped cylindrical coil of known length (l), which is attached to a thin diaphragm as shown in Figure II-1. When an alternating current (I) is applied to the coil a force is generated on the coil. This force ($F=Bl \cdot I$) is a result of the interaction of the induced magnetic field of the coil on the permanent magnetic field (B). The frequency of the coils displacement is the same as the frequency of the alternating current used to drive the coil. An additional result of the coil's motion is the generation of a voltage within the coil which opposes the motion of the coil by Lenz's Law. This induced electromotive force is linearly related to the velocity (u) of the coil's motion and increases the driver's electrical



- | | |
|----------------------------------|------------------|
| (A) Magnet | (B) Back Plate |
| (C) Pole Piece | (D) Surround |
| (E) Reducer Cone | (F) Voice Coil |
| (G) Electrical Lead Connection | |

Figure II-1. Diagram of a Moving Coil Transducer

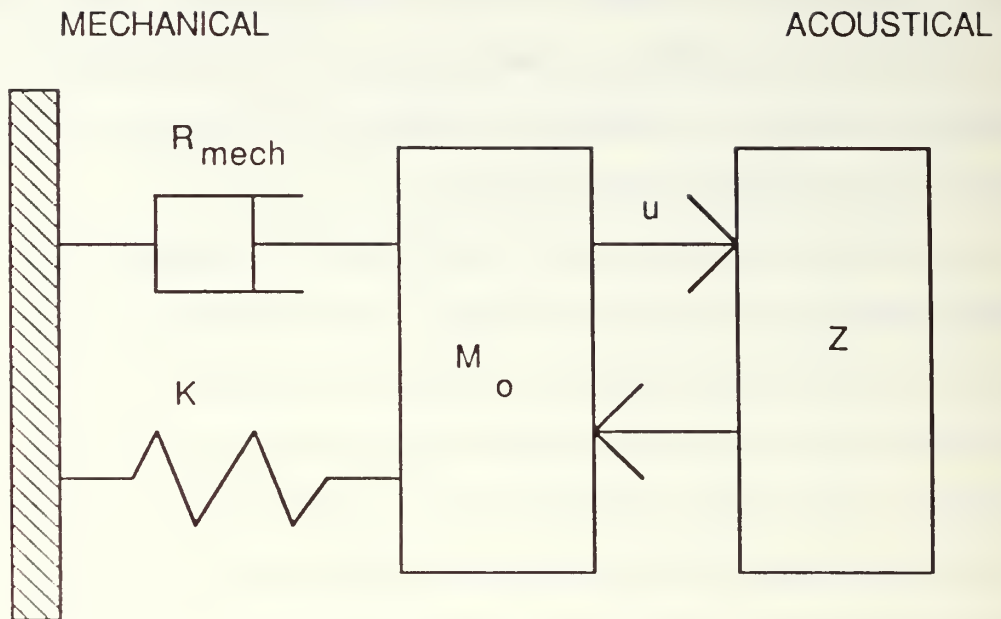
impedance. Measurement of the driver's impedance may therefore be used as an indication of the coil's motion and can be easily determined using a modern impedance analyzer (i.e; HP-4192, HP-4194).

To effectively transfer the mechanical motion of the voice coil into acoustic pressure waves within the resonator a reducer cone and dynamic bellows must be used. The purpose of the reducer cone is to transfer the linear motion from the 4" diameter voice coil to the 1.5" diameter dynamic bellows. To accomplish this, the reducer cone needs to move as one unit without flexure, while remaining light enough so that little energy is lost in overcoming the cone's inertia. This was accomplished for the STAR driver by machining the reducer cone from a single piece of 6061-T6 aluminum. The inertia of the cone was further reduced by drilling holes throughout its surface. In addition to reducing the mass of the cone, the holes allow for the free passage of gas within the driver housing thus reducing the gas induced stiffness of the driver.

The final element in the process of transferring the drivers mechanical motion into acoustical pressure waves is the bellows. This bellows is a custom built lightweight electroformed nickel bellows (see APPENDIX E). The purpose of the bellows is to produce a flexible gas tight seal between the driver housing and the resonator tube, while transferring the motion of the driver into pressure waves in

the gas filled resonator. Connection of the driver's voice coil to the reducer cone and of the reducer cone to the bellows was accomplished using STYCAST 2850FT epoxy. The 2850FT epoxy was selected for use based on its cure strength and relative temperature insensitivity in the temperature range of interest. APPENDIX E contains a listing of the specific properties of the epoxy.

Once assembled, the driver can be modelled as a simple harmonic oscillator (SHO).⁹ This modelling is illustrated schematically in Figure II-2 where the spring stiffness (k) is the sum of the voice coil suspension stiffness, the back stiffness due to trapped gas, and the stiffness of the dynamic bellows. The mass (m_0) shown in the figure is the sum of the moving masses of the voice coil-reducer cone assembly and of the bellows. Finally the mechanical resistance (R_m) of the system is the damping present due to viscous losses in the voice coil/gap and any other mechanical losses in the bellows or suspension. The driver's resonance frequency can then be determined by dividing the mass by the stiffness and taking the square root of the result. This mass is the sum of the moving masses plus any additional added mass. This yields the angular frequency (rad/s) of resonance (ω_0). Section II-B.2(b) describes the procedure used in more detail.



$$M_o = M_{\text{coil}} + M_{\text{bellows}} + M_{\text{driver}}$$

$$K = K_{\text{susp}} + K_{\text{bellows}} + K_{\text{gas vol.}}$$

$$F = B I^* i$$

Figure II-2. Mechanical Model for a Simple Harmonic Oscillator

2. Lumped Parameter Modelling

The ability to sum the individual masses of the system into one mass, illustrated in Figure II-2, is an example of lumped parameter modelling. In the previous section we indicated that we were able to accomplish this for not only the system's mass but also for its stiffness and mechanical resistance. Use of these values, along with knowledge of the driving force, provide all the parameters needed for modelling the mechanical side of the driver.

To analyze the effects of the acoustical portion of the system on the driver, it is necessary to model the distributed acoustical load as a mechanical impedance acting on the moving mass of the system. This method of modelling is described by Kinsler, et al¹⁰ and is practical as long as the largest diameter of the resonator is much smaller than the wavelength of the driving frequency. This mechanical impedance is useful in determining the acoustic pressure difference acting upon the mass. Once the resonator has been modelled, all the parameters are shown to act upon the moving mass of the system. Analysis about this point should then provide an indication of the coupled systems performance. A computer program for use in this analysis is discussed in Chapter IV.

B. ELECTRODYNAMIC DRIVER PARAMETERS

1. Driver modifications

The STAR driver must be capable of maximizing force while adhering to the limits imposed by the NASA GAS canister volume. The recent technological advance by Harmon-JBL in producing a Neodymium-Iron-Boron magnet based driver, the 2450J, resulted in a driver capable of meeting these imposed restrictions. A modified 2450J NIB driver was provided for use in the STAR project by Mr. F.M. Murray of Harmon-JBL. As shown in Figure II-3, the commercially available 2450J NIB driver was modified by cutting away unnecessary portions of the throat area. This resulted in a significant weight (4.4:1) and volume (2.2:1) reduction without a major loss in transduction coefficient (1:0.9) when compared to an earlier generation 2445J series driver.

Attached to the NIB driver is a voice coil-reducer cone assembly. This assembly consists of a standard 4" voice coil whose titanium diaphragm had been laser cut at the Los Alamos National Laboratory and removed at 0.25" above the surround. The aluminum reducer cone was then permanently bonded to the voice coil and the assembly treated as a single unit. Ideally a voice coil-reducer cone assembly should not be needed. A custom built driver would be capable of directly transferring the motion of its voice coil to the dynamic bellows, however such a project was beyond the resources of this experiment. Use of the voice

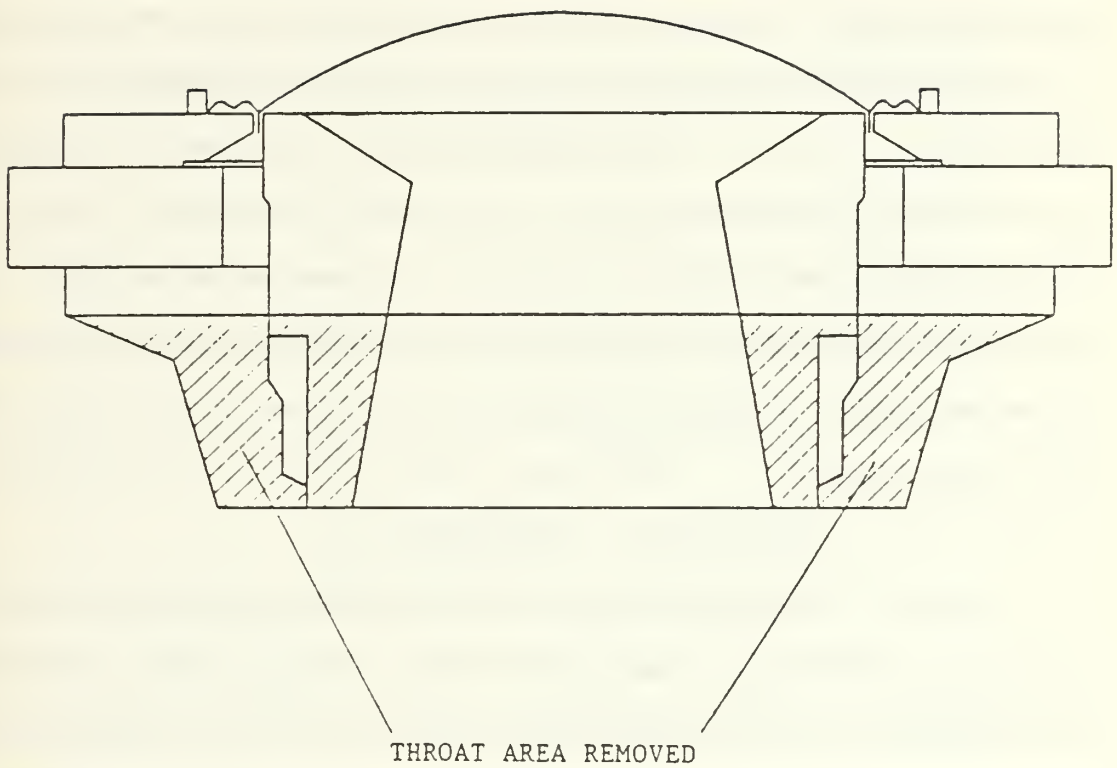


Figure II-3. Harmon-JBL 2450J Driver indicating the portions removed for use on the STAR

coil-reducer cone assembly therefore allows us to use a commercially available voice coil-suspension-magnet system for the STAR project. Finally the previously discussed bellows was bonded to the top of the reducer cone to form the completed driver.

2. Driver Measurements

The parameters needed to accurately model any electrodynamic driver include its moving mass, stiffness, transduction coefficient, and mechanical resistance. For this driver some of these measurements could be conducted on individual components prior to assembly and then summed, while others were determined on the assembled system. In most instances it was possible to obtain the parameters by both methods thereby providing a self-consistency check of the measurements.

a. Transduction Coefficient

The transduction coefficient was determined using two methods. The first method involved the direct measurement of the length of wire used in the assembly of the voice coil and of the strength of the driver's magnetic field. The length of the wire was determined by measuring the diameter (d) of the voice coil and counting the number of turns (N) of aluminum wire wrapped around it. From these two values the length of the wire was found to be 8.33 ± 0.04 meters. Measurement of the magnetic field strength was accomplished by using a Dowdy RFL Industries model 912

Gaussmeter (S/N 808) with a Hall Effect probe model 912015 (S/N 21122). The Dowdy Gaussmeter provides a time averaged measurement of the magnetic field of the NIB driver within the annular gap. Several readings were taken at different positions within the gap in order to average out any local differences due to variations in gap width. The average value over several positions was approximately 1.9 ± 0.3 Tesla. The transduction coefficient was then determined by taking the product of these two values and yielded a value of 15.8 ± 2.6 T-m for the NIB driver.

The above result can be checked by direct measurement of the force in a force balance experiment. Using the relationship between magnetic and gravitational force it can be shown that the transduction coefficient can be determined by the following equation;

$$Bl = mg/\Delta I \quad (II-1)$$

where g is the acceleration due to gravity, m is a known added mass, and ΔI is the additional current in the voice coil necessary to return the voice coil to its original (unloaded) position. Experimentally this value was determined by using a Mechanical Technology Incorporated's (MTI) 1000 series Fotonic Sensor (S/N 38010818) as a monitor of the reducer cone's displacement as shown in Figure II-4. Adding a known mass to the reducer cone produces a change in its net displacement. By applying DC current to the voice coil it was possible to force the reducer cone back to its

original position. As shown in TABLE II-1, a series of measurements were taken and the results averaged to yield a value of $Bl=15.3 \pm 0.7$ T-m. This value was found to agree within 3% of the previously measured value of the transduction coefficient well within experimental error.

TABLE II-1. MASS LOADING TRANSDUCTION COEFFICIENT

<u>ADDED MASS (gms)</u>	<u>CURRENT (mA_{DC})</u>	<u>Bl (Tm)</u>
0.0	0.03	-
265.5	-172.30	15.11
0.0	-0.48	-
265.5	-178.40	14.64
0.0	-0.82	-
265.5	-163.07	16.05

b. Stiffness Determination

The driver stiffness is composed of the stiffness of the voice coil surround, the bellows, and the back stiffness due to gases trapped behind the bellows. Due to the design of the voice coil-reducer cone assembly this latter effect was minimized. Measurement of the stiffness of the voice coil-reducer cone (the suspension stiffness) was accomplished using an added mass technique. The bellows stiffness was determined using a free decay measurement method. Both experimental methods were based on the relationship of the resonant frequency to the stiffness and mass of the system as described in section II.A.1.

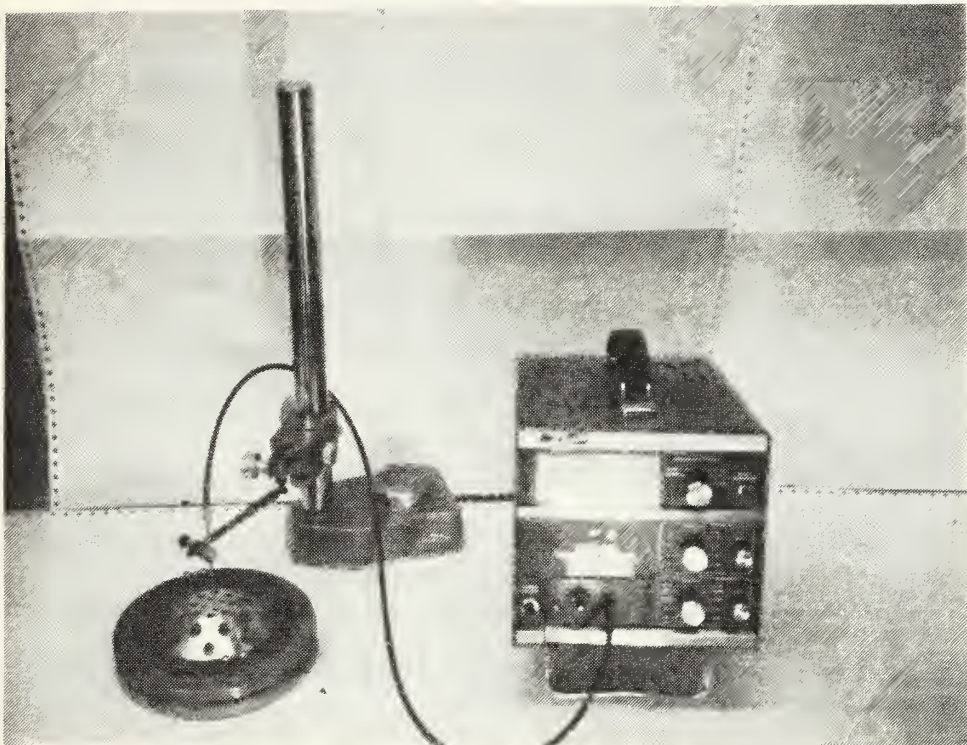


Figure II-4. Experimental Setup Using the MTI Fotonic Sensor to Measure Reducer Cone Displacement

The suspension stiffness was measured by mounting a series of known masses onto the reducer cone and observing the effect on the resonance frequency. Measurement of the resonance frequency was accomplished using a HP-4194 Impedance Analyzer in the impedance/phase mode. In this mode the resonance frequency for the system can be determined by locating the frequency of the maximum impedance. Measurement of the added masses was accomplished using a Sartorius model 2403 analytical balance. Using these measurement pairs, a plot of the square of the period versus its corresponding added mass was obtained as depicted in Figure II-5. The slope of a best-fit line drawn through these points will allow the determination of the suspension stiffness ($k_{\text{SUSP}} = 4\pi^2/\text{slope}$). The moving mass of the driver may also be determined from this figure by dividing the y axis intercept by the slope of the line. These measurements were conducted for the NIB driver in air and vacuum in order to determine the effect of mass loading due to atmospheric pressure and due to trapped gases within the driver. The results of a series of test runs are summarized in TABLE II-2. It is important to note that the difference in driver suspension stiffness in air and vacuum was found to be less than 2%, confirming the belief that the holes in the reducer cone would be effective in reducing back stiffness.

Measurement of the bellows stiffness was accomplished using a series of added masses and the MTI

DRIVER SUSPENSION STIFFNESS MEASUREMENTS

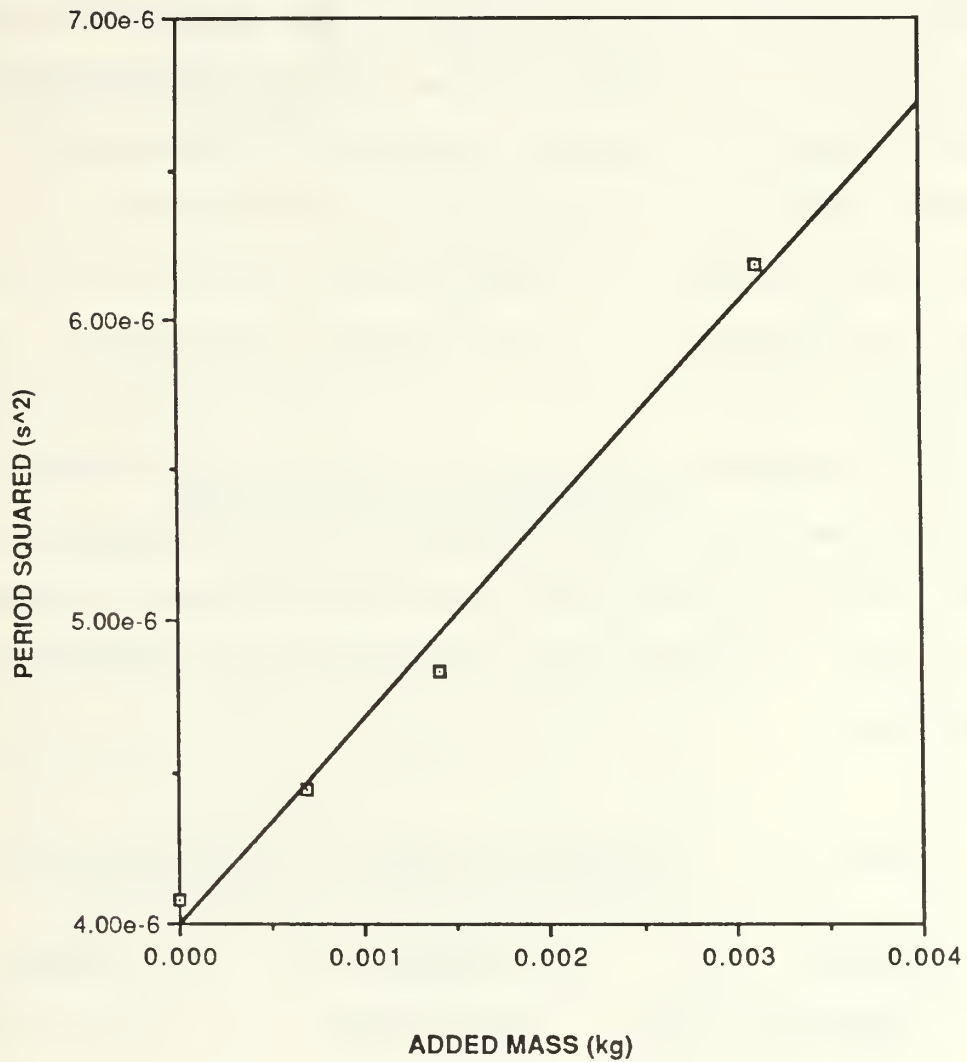


Figure II-5. Plot of the Square of the Period versus Added Mass for Determination of Driver Suspension Stiffness

Fotonic Sensor. The Fotonic was used to measure the displacement of the bellows surface after it had been disturbed (tapped) with a blunt instrument. The free decay of this oscillatory displacement was then displayed by a Nicolet model 310 digital storage oscilloscope and the resonant period of the bellows was thus determined. Figure II-6 provides a schematic of the experimental setup and the equations used in resonance frequency determinations. Several masses were attached to a plate mounted on top of the bellows in order to obtain a plot similar to the one used in determination of the suspension stiffness. The plate was mounted on top of the bellows in order to prevent the thin flexible surface of the bellows from deforming due to the added mass. Before determining the bellows moving mass, the mass of the plate and adhesive must be subtracted. The results of the bellows measurements are included in TABLE II-2.

TABLE II-2. MEASURED VALUES FOR THE BELLOWS AND DRIVER STIFFNESS AND MOVING MASS

<u>DRIVER</u>	<u>1 ATM AIR</u>	<u>VACUUM</u>
STIFFNESS (kN/m)	63.7 \pm 1.2	62.7 \pm 0.9
MOVING MASS (gm)	12.6 \pm 0.3	11.9 \pm 0.2
<u>BELLOWS</u>		
STIFFNESS (kN/m)	3.87 \pm .16	--
MOVING MASS (gm)	0.07 \pm .61	--

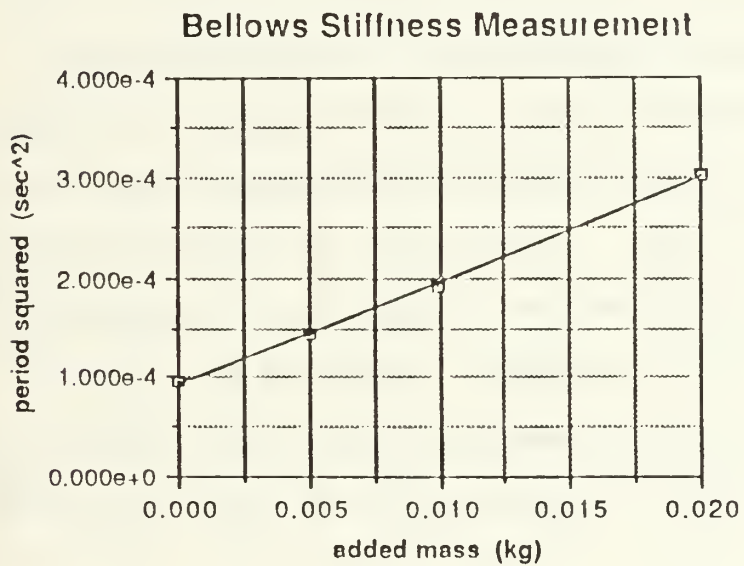
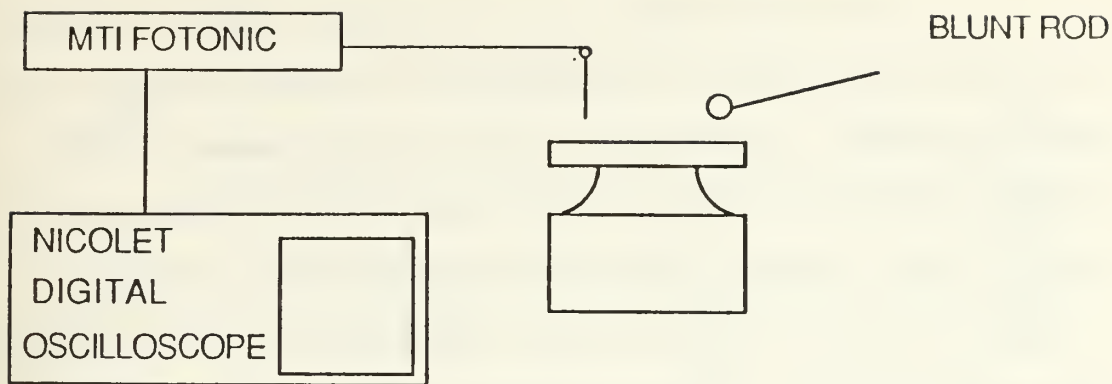


Figure II-6. Experimental Apparatus for Bellows Resonance Frequency Measurement

c. Quality Factor and Mechanical Resistance

The measurement of the driver's quality factor (Q) is an indication of the mechanical losses in the driver. Several methods are available for the measurement of the quality factor including a phase slope method discussed in section IV-B. Another method of measuring the quality factor consists of measuring the resonance frequency and the frequencies of the 3dB down points taken from a modified impedance plot (HP-4194 in impedance/phase mode). The quality factor can then be determined by dividing the resonance frequency by the difference between the 3dB frequencies. This measurement, when conducted using the Impedance Analyzer, must be corrected for the blocked electrical impedance present due to direct current resistance of the voice coil, test equipment, and test leads. This is easily accomplished by using the HP-4192 in the COMPENSATION MODE. Figure II-7 is representative of the impedance plots obtained as a function of frequency for the driver in air at 1 atmosphere. Analysis of the data indicates a resonance frequency of 364.25 Hz and half power frequencies of 353.75 Hz and 376.25 Hz yielding a Q of 16.2 ± 0.3 .

The driver's mechanical losses were also determined by measuring the free decay of an impulsive excitation. An Endevco model 22 Picomin accelerometer was calibrated (section II-A.4) and mounted on the underside of

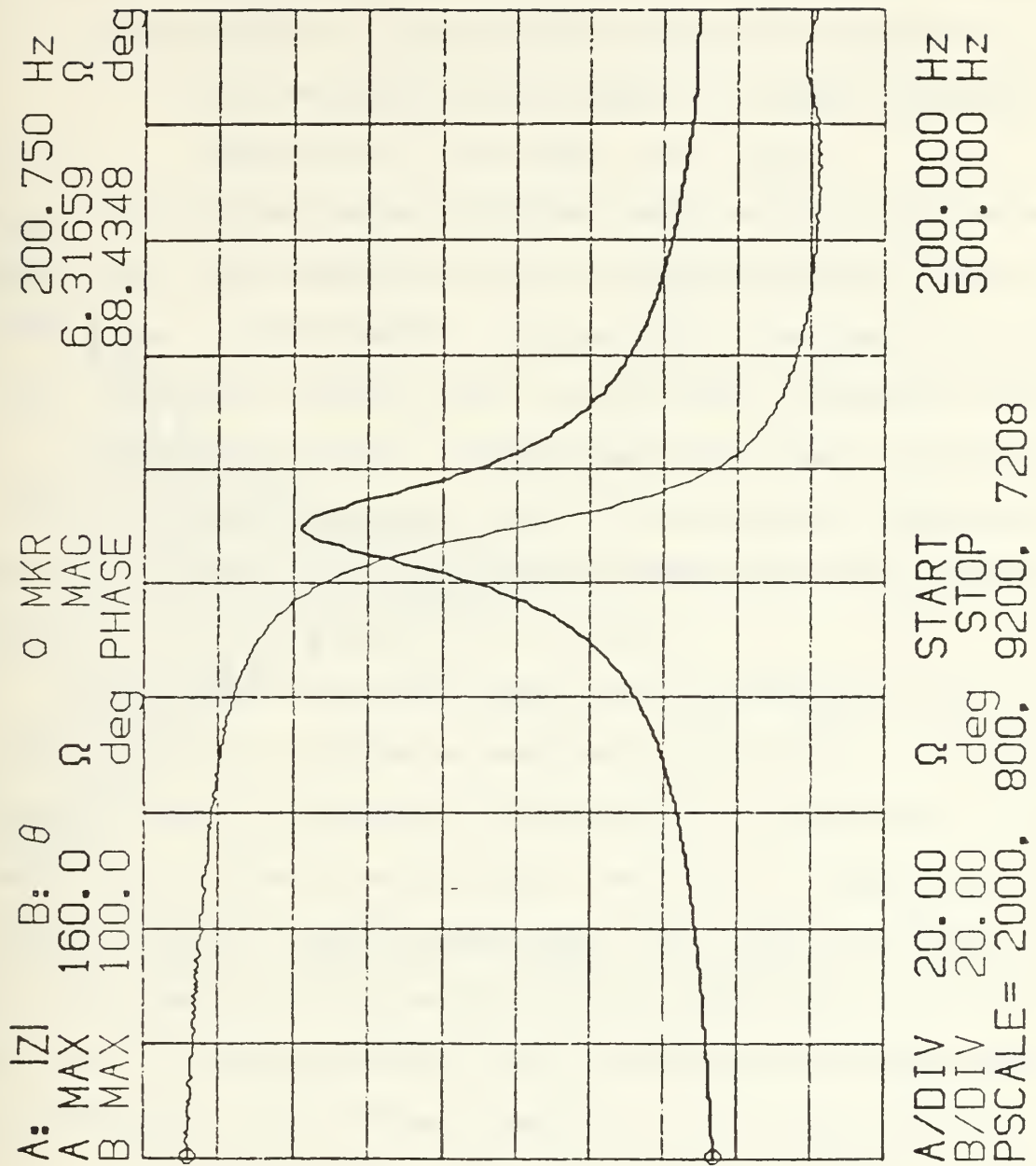


Figure II-7. Sample Impedance Plot for the driver as a function of frequency

the reducer cone. When triggered by the removal of the driving voltage, the signal from the accelerometer was sent to a Nicolet 310 digital oscilloscope. This decaying sinusoidal signal is described by equation II-2;

$$A(t) = A_0 * \exp(-nT/\tau) * \sin(\omega_0 t + \phi) \quad (\text{II-2})$$

where $A(t)$ is the signal amplitude as a function of time, A_0 is the initial amplitude, and nT represents the time elapsed during n periods of the signal. In addition, τ represents the exponential decay time, ω_0 the resonant angular frequency, and ϕ the phase angle. Taking the natural logarithm of equation II-2 then results in equation II-3, for the peak amplitudes of the signal as a function of time.

$$\ln A(n) = \ln A_0 - nT/\tau \quad (\text{II-3})$$

A plot of logrithm of the peak amplitude versus period number, n , can then be obtained as shown in Figure II-8. From this graph it is possible to determine Q by dividing π by the slope of the line. This follows from the definition of $Q = \omega_0 \tau / 2 = \pi \tau / T$. For experimental runs in air at one bar and in a vacuum, the quality factor of the driver system was determined to be between $Q_{\text{air}}=15.4$ and $Q_{\text{vacuum}}=17.2$. The value of the quality factor obtained from the two methods can be seen to agree to within 5% for the tests in air.

Once the quality factor has been measured the mechanical resistance can be easily determined ($R_m = \omega_0 m_0 / Q$). This was done for the two test cases in air and vacuum and yielded the values of $R_m(\text{air}) = 1.82 \text{ kg/s}$ and

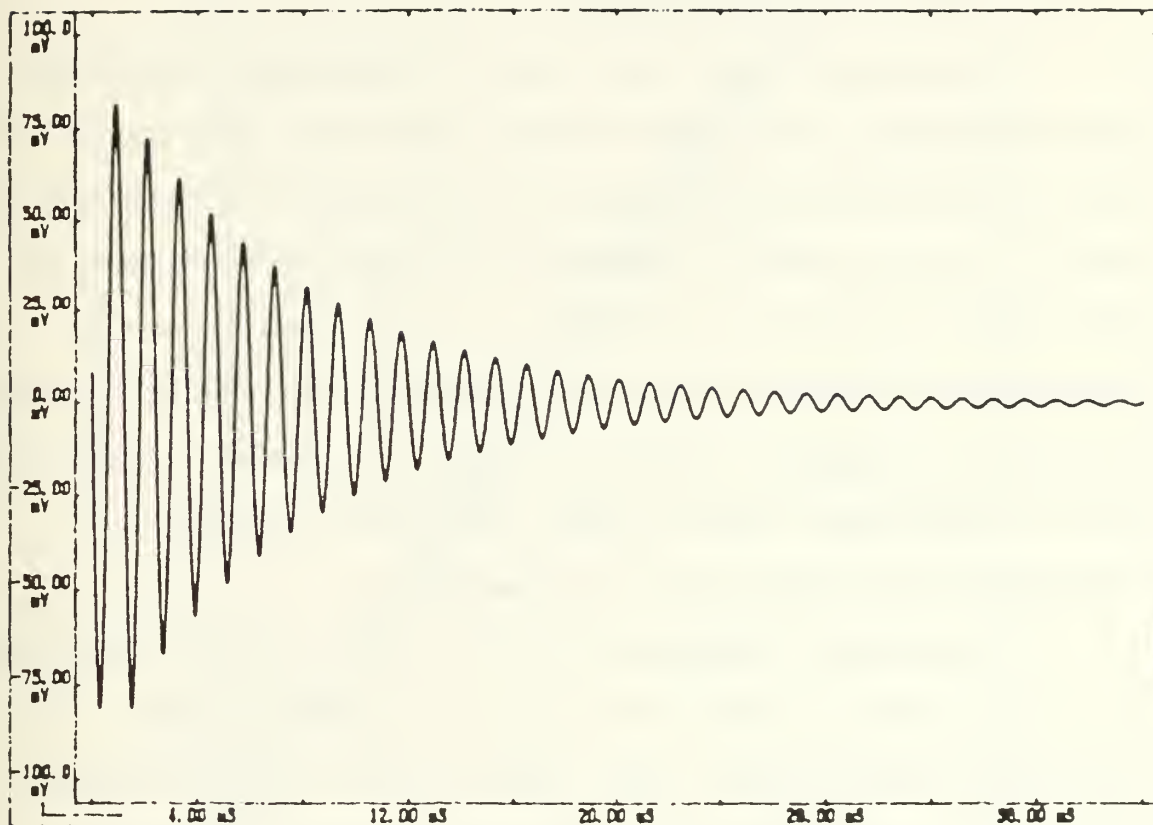


Figure II-8. Sample Free Decay used for determination of the quality factor

$R_m(\text{vacuum}) = 1.58 \text{ kg/s}$. Using this same formula for the quality factor from the impedance plot yielded a value of $R_m(\text{air}) = 1.78 \text{ kg/s}$. Once again it is possible to see a close agreement between the two independent measurement techniques.

3. Voice Coil Resistance

Heating of the voice coil as the driver operates cause changes in the value of the voice coil resistance. If the temperature coefficient of the voice coil resistance is known it can be used to provide an in situ measurement of the coil's temperature which can also be used as an indicator to predict voice coil failure. As long as no short circuits are present within the voice coil, the value of the coil's resistance should remain relatively constant, effected only by the coil's temperature.

Using the standard 4" voice coil modified similarly to the one used in the STAR driver, temperature and resistance measurements were taken as the coil was heated inside of a sealed oven. The direct current resistance measurements were taken using a four-wire measurement technique while a thermocouple was used for the temperature readings of the oven. These values were then plotted, as shown in Figure II-9, and indicate the relationship is linear (slope = $31 \text{ m}\Omega/\text{C}$) over a temperature range from 20.0°C to 50.0°C . For the actual STAR voice coil, an initial R_{DC} of

VOICE COIL TEMPERATURE SENSITIVITY

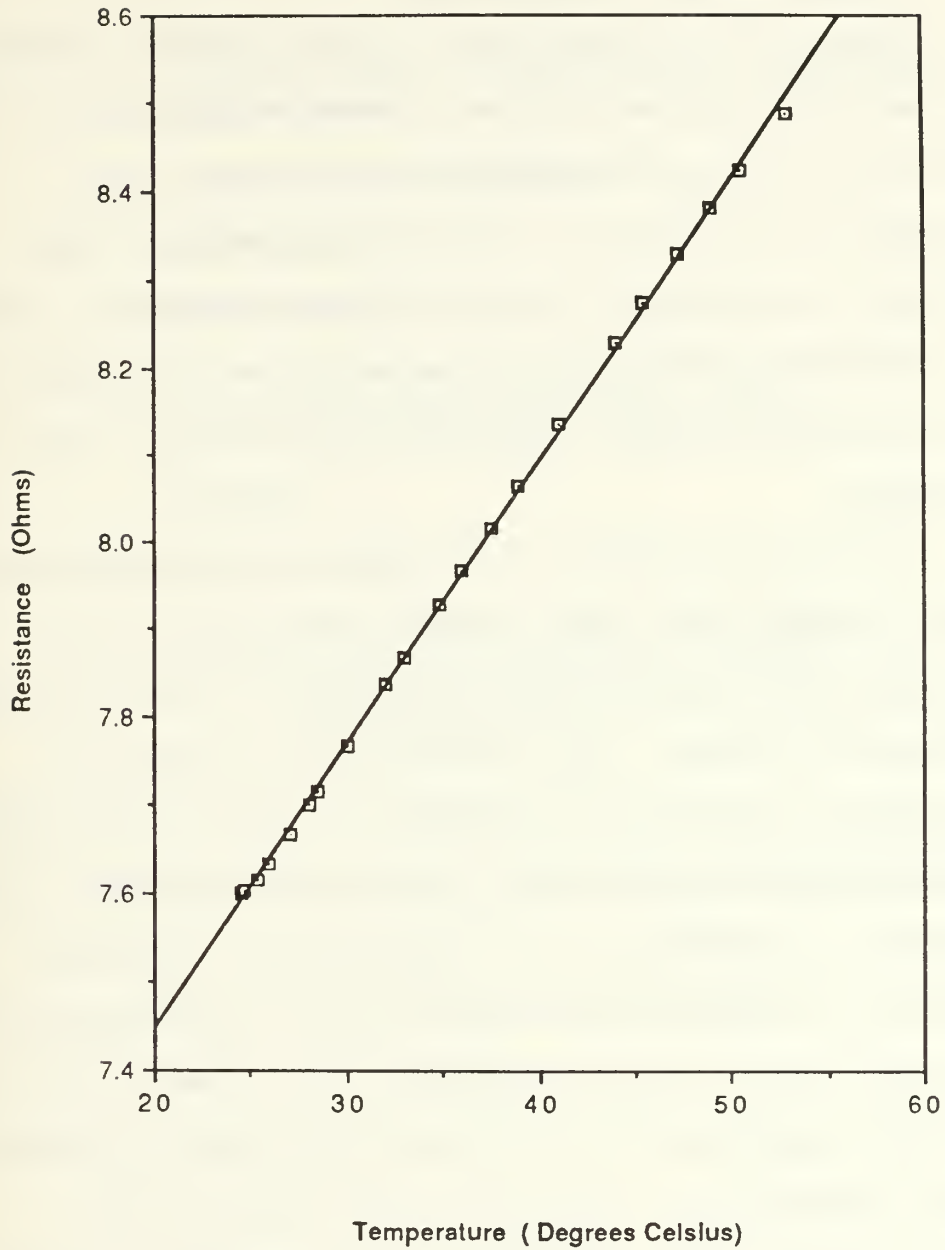


Figure II-9. Plot of DC Resistance as a Function of Temperature for a 4" Voice Coil

8.22 Ω was measured at T=20°C and minimal heating effects noted during extended test runs.

4. Accelerometer Calibration

Several test measurements of the driver required the use of an accelerometer mounted to the reducer cone. In addition to the driver parameter measurements, the monitoring of the driver's acceleration during actual operation is accomplished using this accelerometer. Given these two requirements, knowledge of the accelerometer's sensitivity is extremely important in analysis of the STAR's performance.

For an accelerometer of known charge sensitivity, the open circuit (voltage) sensitivity (M_{acc}) can be determined as a function of acceleration if the total system capacitance is known. This sensitivity can also be experimentally determined by measuring the voltage output of the accelerometer for a known driving acceleration. Since the system's capacitance will vary up until the final version of the STAR is connected to its flight electronics, it is important to verify that the value based on the charge sensitivity specification accurately reflects the actual measured sensitivity. Figure II-10 illustrates the equations used in the theoretical and experimental methods as well as the results of two test runs with different system capacitances. From these two test cases, in which a B&K model 4294 Calibration Exciter was used to supply a

A PICOMIN MODEL 22 MICROMINIATURE, PIEZOELECTRIC
ACCELEROMETER

CALIBRATION

THEORETICAL

$$M_{acc} = (\alpha/g)/\Sigma C$$

α = accelerometers charge sensitivity (pC/g)

g = gravitational acceleration (m/s²)

ΣC = sum of the system's capacitance (pF)

MEASURED

$$M_{acc} = (V_{out}/G)/a$$

V_{out} = accelerometer output voltage (mV)

G = gain factor (operator selected)

a = 10 m/s² at 158.75 Hz from a B&K 4294
calibration exciter

RESULTS

C_{TOTAL} (pF)	THEORY(V-s ² /m)	MEASURED(V-s ² /m)	%DIFFERENCE
604.6	83.45 *10 ⁻⁶	79.43 *10 ⁻⁶	4.8
288.5	174.37 *10 ⁻⁶	175.40 *10 ⁻⁶	0.6
620.1	81.07 *10 ⁻⁶	----	---

Figure II-10. Comparision of Experimental and Theoretical
Techniques Used in the Determination of the
Accelerometer Sensitivity

constant 10 m/s^2 acceleration at 159 Hz, agreement between the two methods was shown to be between 0.6% and 4.8%. For the test system used throughout the rest of the component and system testing a theoretical value of $M_{\text{acc}} = 81.1 \text{ Vs}^2/\text{m}$ was determined based on a measured capacitance of 620.1 pF. This measured capacitance included the capacitance of the accelerometer (283.5 pF), its cabling (116.5 pF), and the amplifier input capacitance (20.0 pF). From the agreement between the two test measurements we believe this value to be accurate to within at least 5%.

C. STAR DRIVER HOUSING

1. Introduction

The design of the STAR driver housing is based upon the mechanical drawings provided by Fitzpatrick in her thesis¹ and the continuing work done by Hofler in the field of thermoacoustics. Adapting lessons learned from Hofler's prototype refrigerator,¹¹ and incorporating new materials and innovations has led to the current driver housing design.

The purpose of the housing is to rigidly support the modified JBL driver, to serve as a pressure vessel for the working medium (a 10 bar He-Xe gas mixture), and to accommodate the required electronics which will monitor and control system parameters and acoustical performance.

In developing a design for the STAR driver housing there were a number of system requirements that had to be satisfied. Though some of these were stipulated by NASA, many resulted from the innovative technology devised by Hofler and Garrett. The following sections will discuss the design considerations in detail, the individual components and subsystems contained within the housing, and the assembly of those components into an integrated system.

2. Design Considerations

The first and foremost design considerations pertained to the limited space available in the Get-Away Special (GAS) canister and the weight limitations imposed by NASA. The GAS canister is approximately 28.25 inches high having an inside diameter of about 19.75 inches and is limited to a maximum payload of 200 pounds. Ensuring that the driver housing is as light and compact as possible provides more space for other system components, including additional battery cells to prolong the STAR lifetime while in orbit. Furthermore, the housing had to be designed to attach to the lid of the GAS canister via twelve #10-32 bolts on a 9.5 inch diameter bolt circle. Since the modified JBL driver is approximately 6.3 inches in diameter and 1.9 inches high, the imposed size limitations provided no unmanageable restrictions. The result was the driver housing depicted in Figures II-11 and II-12, having a height

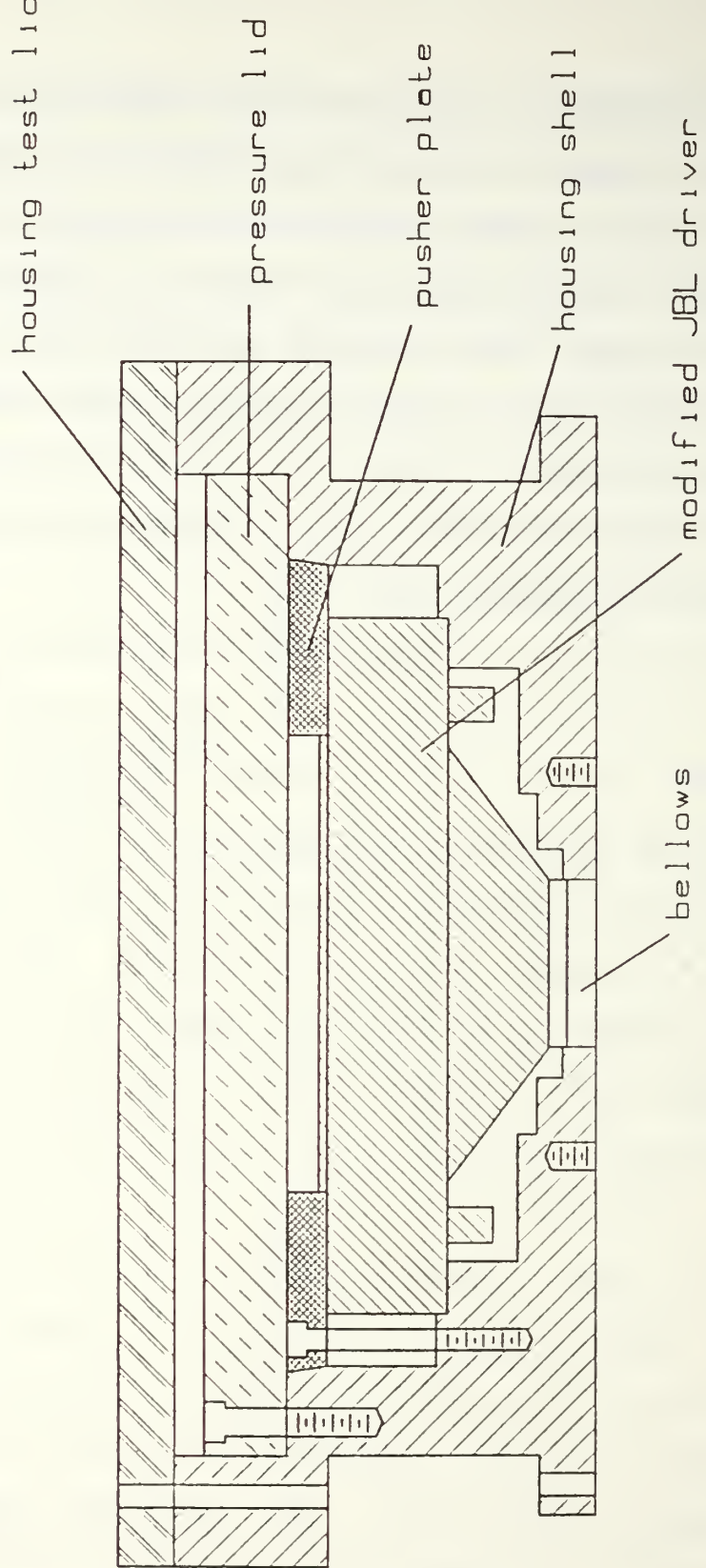


Figure II-11. Driver Housing Cross-Sectional View

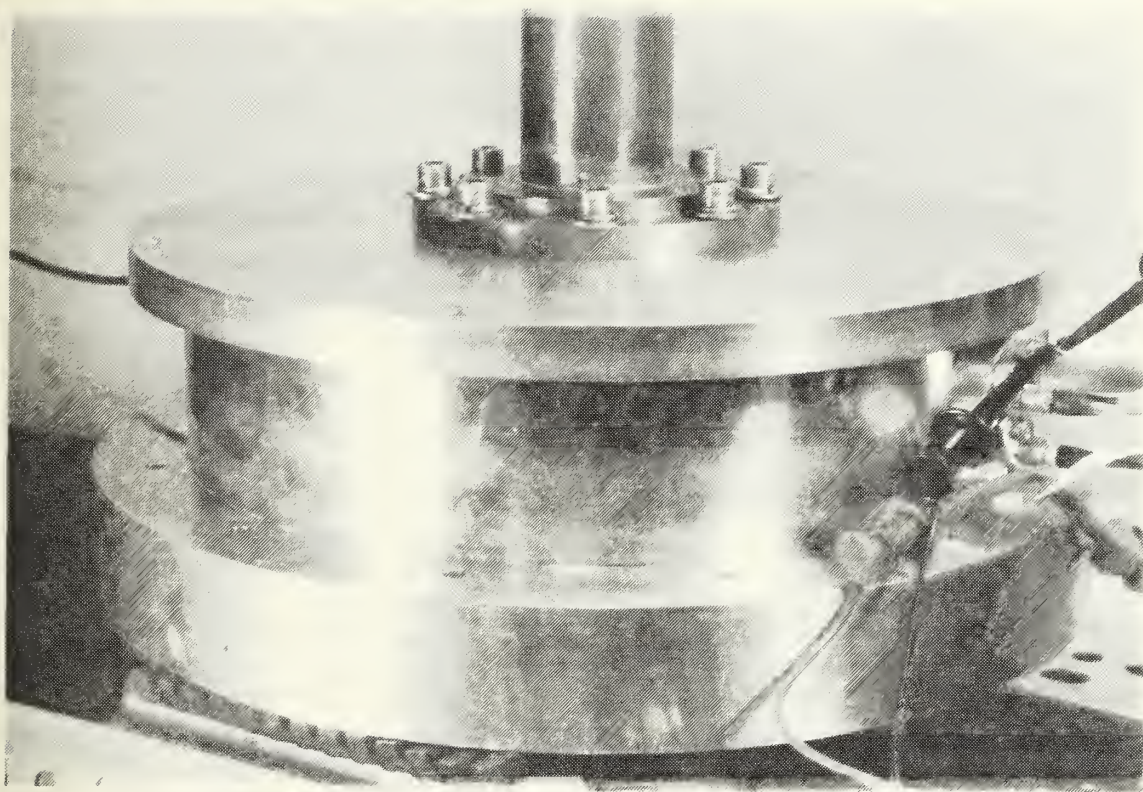


Figure II-12. Driver Housing

of approximately 3.75 inches and a maximum diameter of 10.80 inches, machined from 6061-T6 aluminum.

Aside from the NASA requirements, it was desirable to ensure that the housing be capable of interfacing with the resonator subsystem developed by Hofler for his prototype refrigerator. By doing so, the integrity and performance of the driver housing could be verified prior to completion of the STAR resonator by testing with components from the earlier designs. This had a direct impact on the placement of the microphone/FET electronics package that would be mounted within the housing to help monitor and control system acoustical performance.

The size and placement of the electronic feed-through port, DC pressure transducer port, and gas fill port were another consideration. The placement of the electronic feed-through port was based on the location of the microphone/FET package. The DC pressure transducer port was placed as close as possible to the electronic feed-through port so that all housing electronics could be easily accessed by the external signal processing package. The size of the transducer port was dependent on the dimensions of the commercially-available Omega[®] PX-80 pressure sensor. The gas fill port was situated such that its placement was in the vicinity of the STAR's gas reservoir. The size of the fill port was determined by the choice of gas fitting (1/8 inch Swagelok[™]).

Two critical considerations resulted from the design requirements that the working fluid in the refrigeration system be a He-Xe gas mixture pressurized to 10 atmospheres. First of all, the housing (once closed) would have to be capable of withstanding the forces produced by the 150 lb/in² gas mixture within it. Obviously internal regions of the housing having the largest surface areas would be subjected to the greatest forces. In particular the lid(s) used to close the housing and isolate the internal workings from the surrounding environment would have to be strong and rigid. The bolts used to rigidly mount these lid(s) in place would have to be numerous enough and have sufficient tensile strength to handle the distributed load. This led to the design of a single pressure lid that is fixed to the housing by 12 equally-spaced #1/4-20 machine bolts.

The second consideration arose due to the ability of helium to penetrate through all known insulators at ordinary temperatures. This was a concern not only for system performance but also because of a NASA requirement that the venting of the inert gas mixture be kept to a leak rate that was less than 10^{-4} standard cm³/s. As a result it was decided to use lead O-rings to seal all lids and fixtures in place.

A final consideration was based on the amount of vibration the housing and its components would experience upon launch and landing of the Space Shuttle. In particular

the driver/bellows configuration would have to retain its integrity. To ensure that this occurred a pusher plate was devised which clamps down on the underside of the driver rendering it immobile. At the same time this plate is responsible for conduction of heat from the electrodynamic driver to the GAS lid for removal via radiation into space.

3. Component Description

The housing has a number of components and subsystems associated with it. The components include the housing shell, a test lid, a pressure lid, a pusher plate, a DC pressure transducer support plate with strain relief fixture, and an electronic feed-through plug. All of these were milled from 6061-T6 aluminum. The associated subsystems include the driver/bellows assembly (with Endevco model #22 accelerometer), an Omega PX-80 high pressure sensor and a microphone/FET package.

The inside of the housing shell is tiered to allow precise placement of the driver assembly, pusher plate, and pressure lid (see Figures II-13 and II-14 for a top and cross sectional view of the housing shell). The 1.5 inch diameter hole in the bottom of the shell is where the Servometer single convolution 0.003 inch thick electroformed nickel bellows is epoxied into place. The 1/32 inch diameter hole that runs through the bottom of the housing is for a 0.8 inch length of copper-nickel capillary tubing (inner diameter of 0.010 inches). This capillary serves to

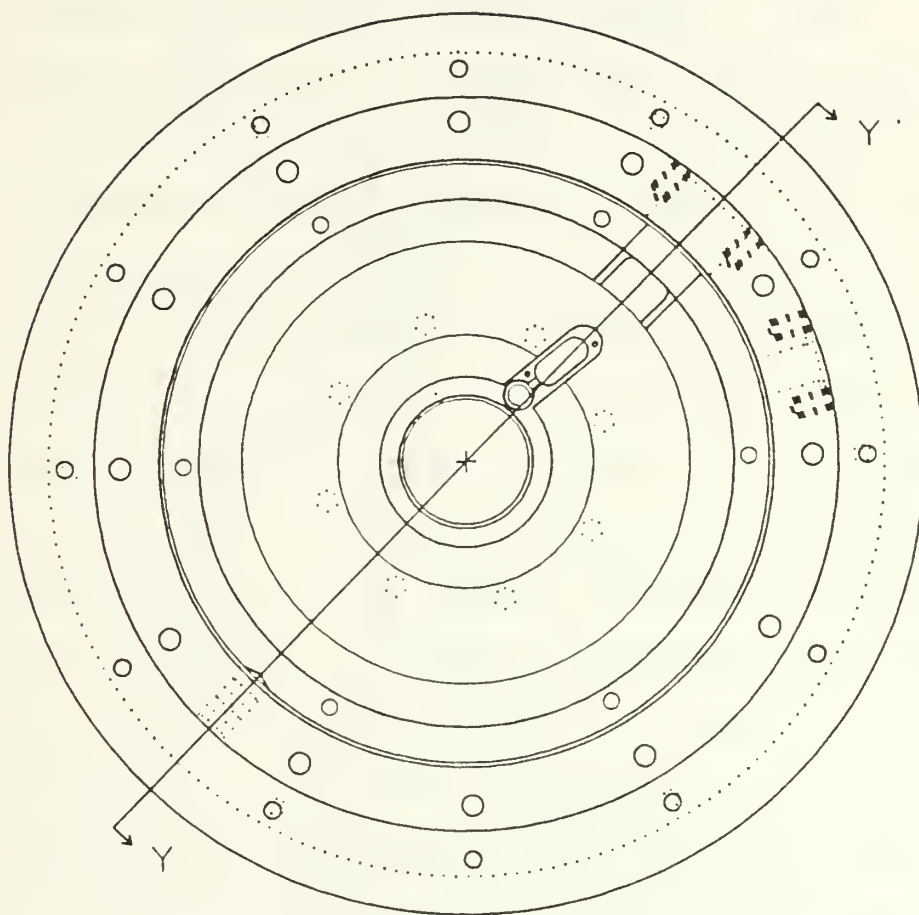


Figure II-13. Driver Housing Lid View

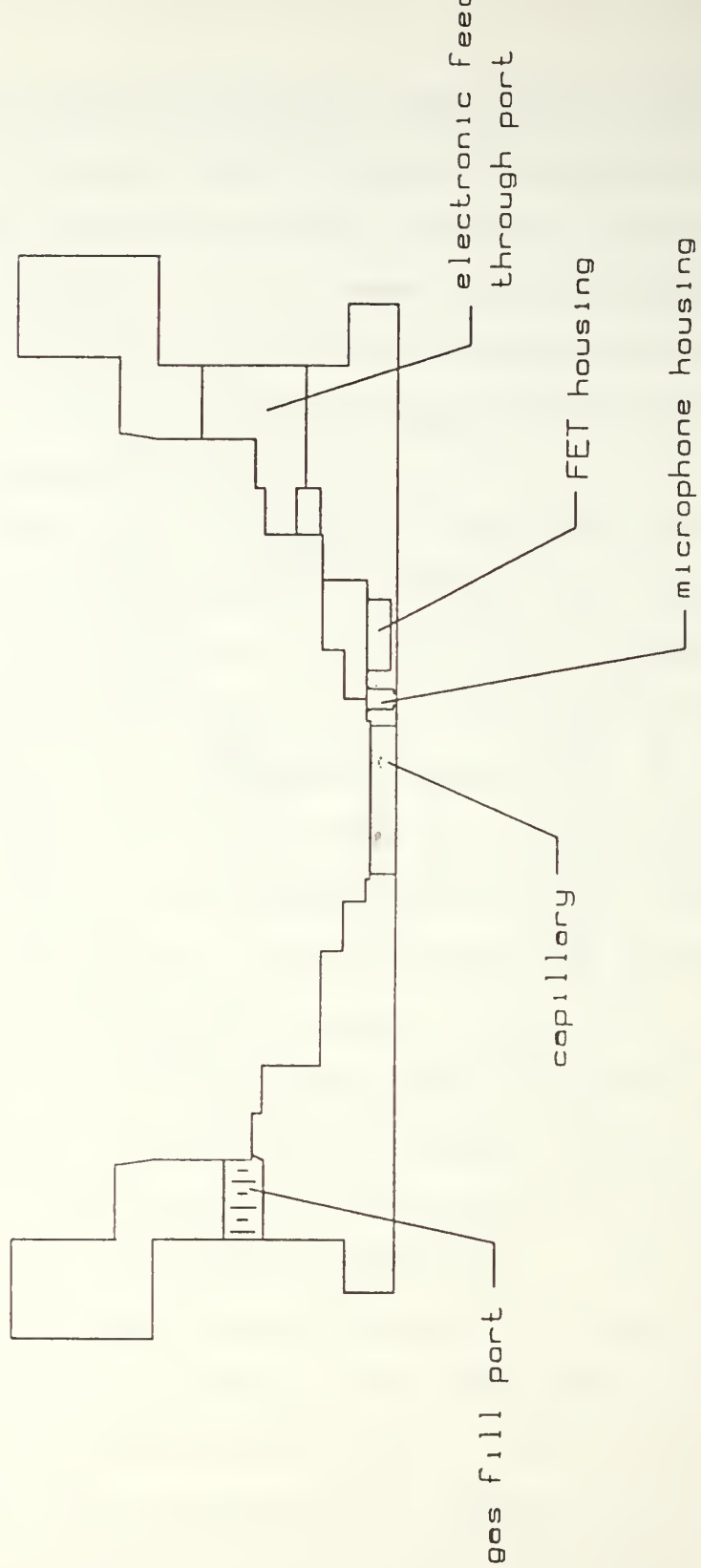


Figure II-14. Section Y-Y' View of the Driver Housing

equalize static pressure between the housing and resonator. At the same time its diameter (and hence flow conductance) has been kept small enough that at the operating frequency of the STAR system it maintains a dynamic pressure seal. Additionally, in the bottom of the shell, there are two small cavities connected by a narrow channel. The cylindrical cavity houses a Valpey-Fisher quartz plate which acts as a microphone while the other accomodates an Eltec model 304 P-channel MOSFET impedance converter. The #0-80 tapped holes located in the vicinity of these cavities are used to mount a brass plate which shields the electronics.

Externally, the housing shell has two flanges. The upper mounts directly to the GAS canister lid via 12 equally spaced #10-32 bolts on a 9.5 inch diameter bolt circle. The lower flange has a 9.3 inch diameter bolt hole circle that permits the mounting of a vacuum can which provides thermal insulation for the resonator and acts as a protective shield should the resonator rupture. At the location of the electronic feed-through and pressure transducer ports, the housing shell has been appropriately machined to provide a flat surface to mount the respective components. The 1/8" NPT pipe thread tap situated in the side of the housing shell directly opposite the electronic feed-through port is for a Swagelok pipe fixture which serves as the gas fill port.

The housing test lid performs the same function as the GAS canister lid. It has a groove for a rubber O-ring

so that when mounted to the housing it will provide a sufficiently leak-tight seal for ground testing purposes. It also has a centrally-located single tiered orifice which is where a small length of 1-1/8 inch diameter aluminum tubing is welded into place. In this configuration the test lid (and housing) can be mounted onto an Alcatel ASM 110 Turbo CL helium leak detector and checked for leaks.

The pressure lid provides a leak-tight seal capable of withstanding the forces developed from the 10 atmosphere He-Xe gas mixture within the housing. It is approximately 3/4 inch thick for rigidity and strength and is secured to the housing shell with 12 equally-spaced #1/4-20 high strength carbon steel machine bolts. Applying a little physics and assuming equal distribution of the load on the bolts one can readily determine that each bolt must be capable of withstanding a force of approximately 660 pounds. Actual tensile strength tests performed on the carbon steel bolts (using an Instron Model 6027) indicated that their average yield was in the order of 5400 pounds force. Regular stainless steel bolts were also tested and found to be approximately half as strong as their carbon steel counterparts.

There are two O-ring grooves cut into the pressure lid. The outer is for a 1/32 inch diameter wire lead O-ring to prevent helium leakage. The inner groove is for a rubber O-ring which serves as a backup for the lead. Since the

STAR system will be assembled and filled with He-Xe gas as much as several months prior to it's Shuttle launch date, the lead O-ring is critical to ensure that the system remain charged and not leak an appreciable amount of helium. Should the lead O-ring fail during launch due to excessive vibrations, the rubber O-ring should be sufficient to minimize helium leakage during a six day mission.

The role of the pusher plate is to secure the driver/bellows assembly in place and provide a heat conduction path from the driver (voice coil) to the housing. The plate edge has a 10° taper that mates perfectly with the taper inside the housing shell (seen in Figure II-14). The motivation for this design was to maximize the effectiveness of the plate as a heat conduction path. A narrow channel and notch were cut into the plate to serve as a passageway for the accelerometer lead coming from the underside of the driver's reducer cone.

The DC pressure transducer support plate is required to rigidly hold the Omega PX-80 piezoresistive pressure sensor in place as depicted in Figure II-15. A 0.45 inch diameter hole located in the center of the plate provides a passageway for electronic leads to and from the transducer. Encircling this opening is a shallow 0.6 inch diameter lip in which the sensor is seated. The plate does not require an O-ring groove since a leak-tight seal is achieved by placing a lead O-ring between the transducer and housing.

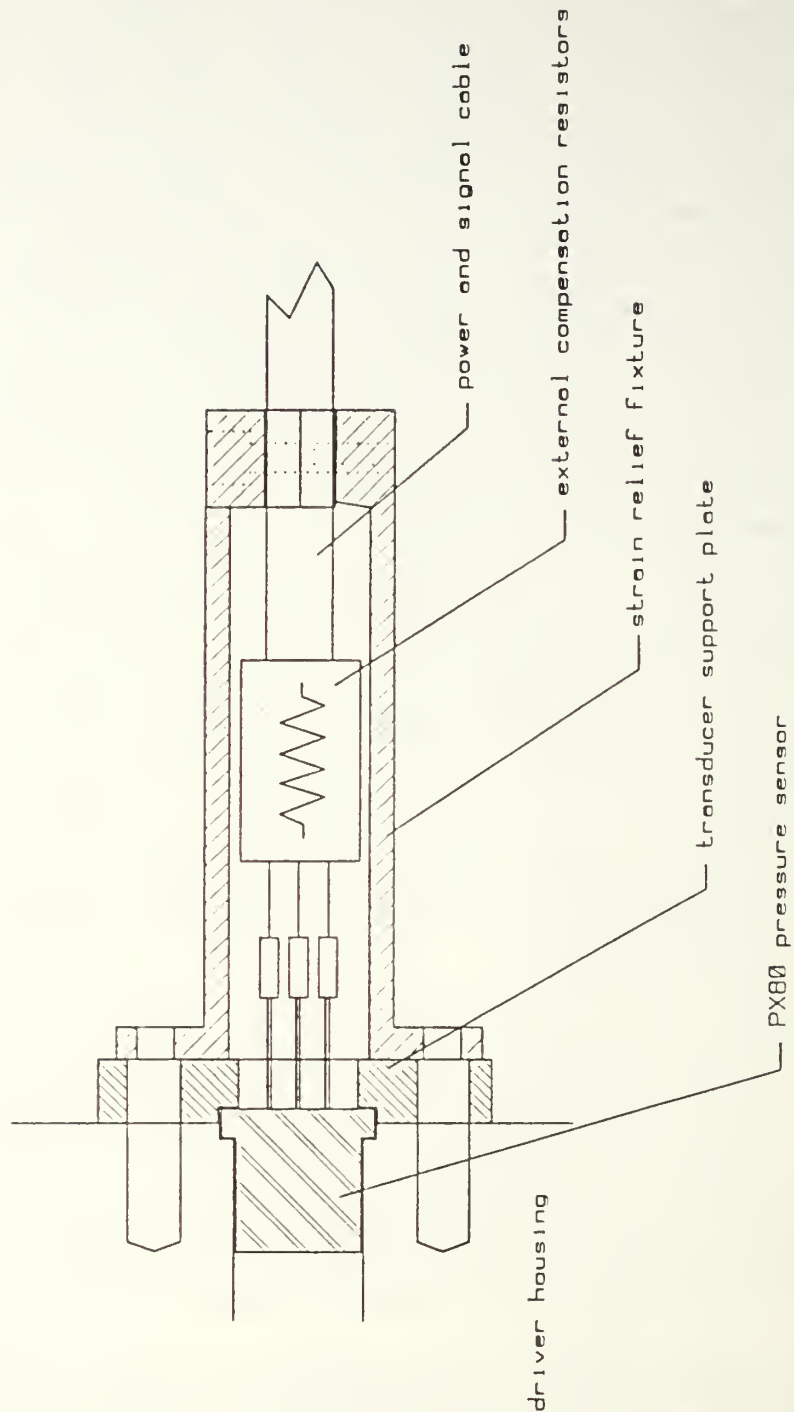


Figure II-15. Schematic of the PX80 Pressure Sensor, Support Plate, and Strain Relief Fixture

Attached to the support plate via two #6-32 machine bolts is a strain relief fixture. This component serves a dual purpose in that it houses the external compensation resistors for the PX-80 transducer and provides strain relief for the leads connecting the sensor to a $1.5 \text{ mA}_{\text{DC}}$ current supply and to the signal processing electronics. (The DC current supply is used to energize the piezoresistive strain gage bridge within the sensor).

The most complicated component in the housing is the electronic feed-through plug shown in Figures II-16 and II-17. It has feed-throughs for six leads; two for the driver, one for the accelerometer, two for the microphone, and a spare. The main concern in the design of this component was to minimize the potentially devastating helium leak rate that would exist where the electrical leads were fed through the housing shell. To accomplish this each feed-through has a 0.3 inch long section that is only 0.040 inches in diameter. Additionally, glass particle-filled epoxy was used to insulate the bare copper electrical leads and seal the six narrow conduits. The selected epoxy was Emerson and Cumming's STYCAST 2850FT and was proven effective by Fitzpatrick in her thesis.

Each feed-through also has a #10-32 tapped hole on either side of the narrow channel. Microdot coaxial connectors and flat-top #8-32 brass bolts (each having a length of bare copper wire soldered to them) were

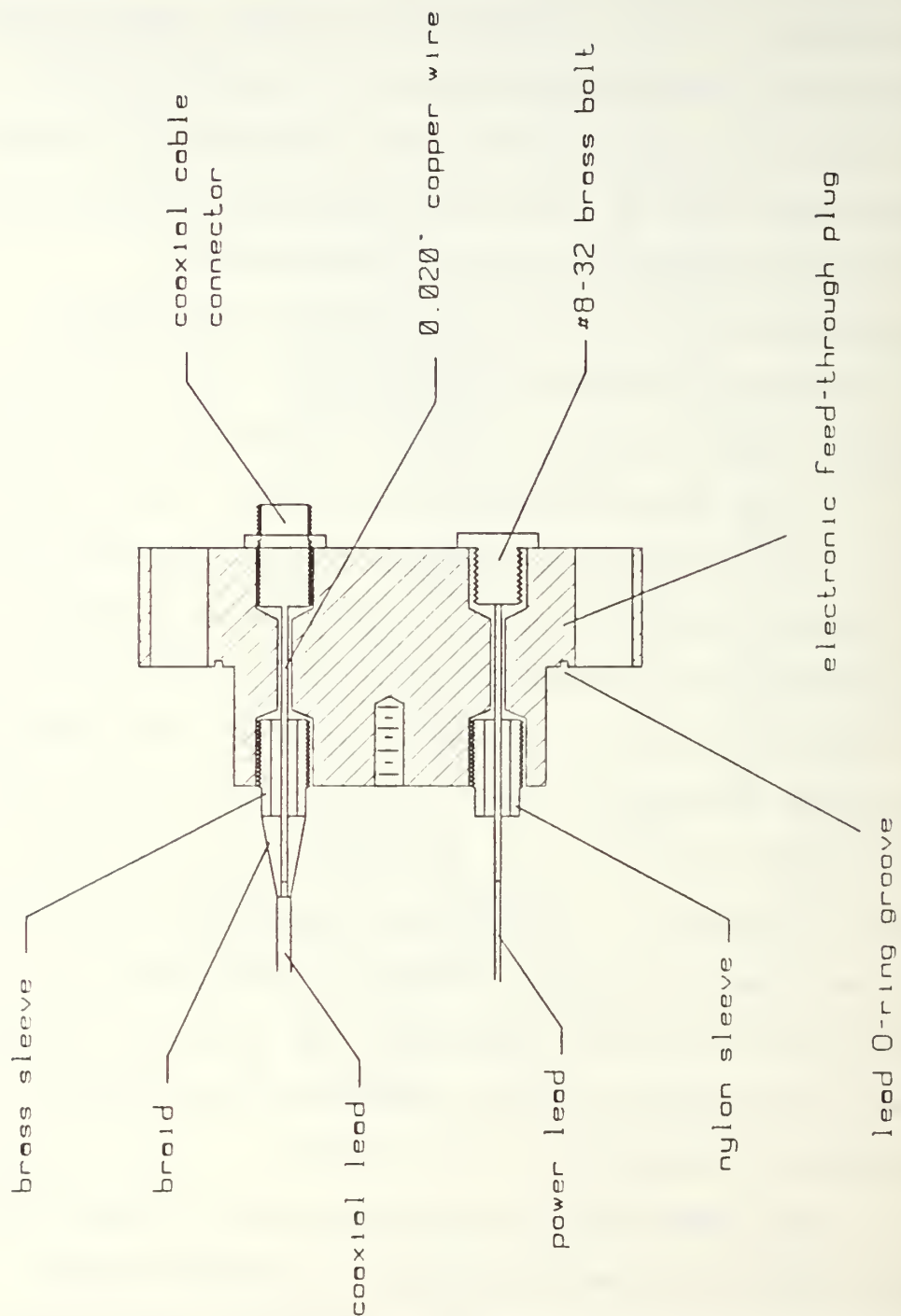


Figure II-16. The Electronic Feed-Through Plug

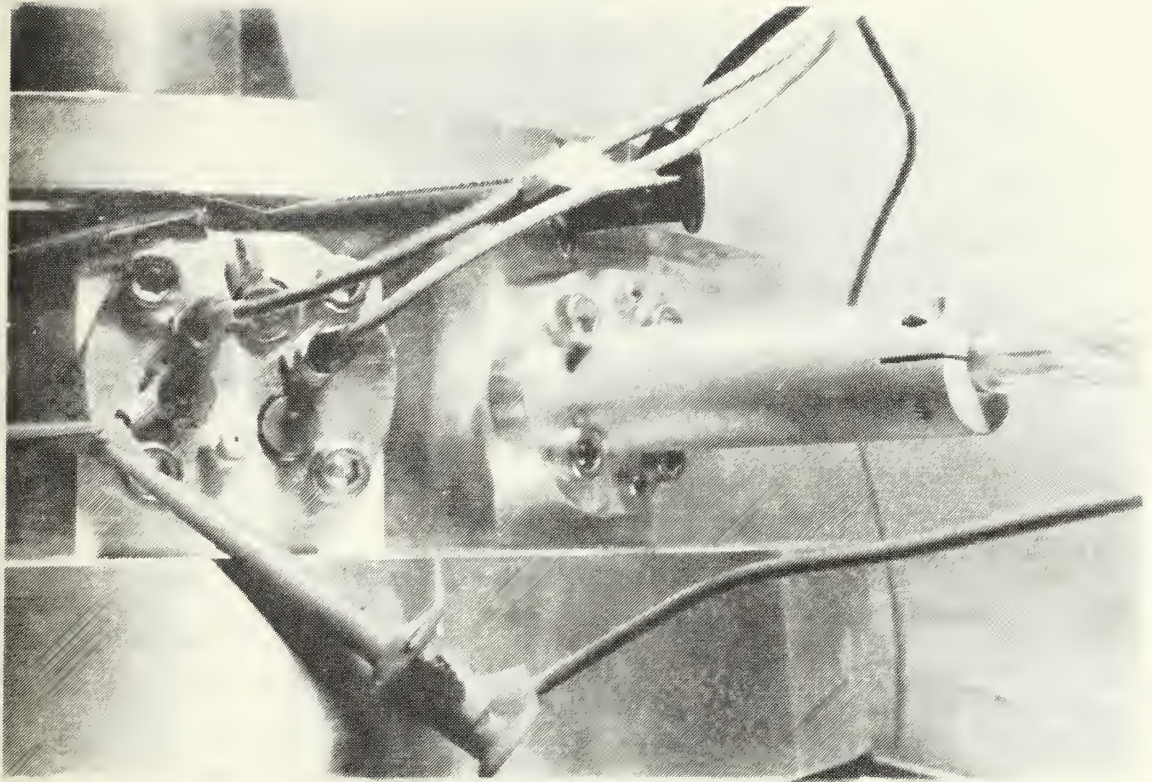


Figure II-17. Driver Housing Showing Electronic Feed-through Plug, DC Pressure Transducer Support Plate, and Strain Relief Fixture

alternately mounted into the tapped holes on the external face of the plug using the STYCAST epoxy. Enough epoxy was used to ensure that the copper leads were properly insulated as they passed through the narrow ducts. On the internal face of the plug threaded brass and nylon sleeves were alternately epoxied into place (opposite the coaxial connectors and brass bolts respectively). Each brass sleeve had a 3/4 inch section of shielding braid soldered to it. This braid was used to strengthen the connection between the bare copper wires that would be joined to coaxial leads coming from the microphone, MOSFET and accelerometer. Additionally the braid provides electrical shielding to those connections. Each of the three other copper wires (passing through the nylon sleeves) had a length of teflon-coated wire soldered to them. The resulting joints were then insulated using a teflon heat-shrinkable tubing. Ring connectors were attached to two of these leads that would eventually be connected to the driver.

A lead O-ring groove was cut into the plug to provide a leak-tight seal between it and the housing. A final feature of the feed-through plug is a #4-40 tapped hole on the internal face which was included as a possible accessory mount.

4. Microphone/FET Assembly

Critical to the operation of the STAR are the Valpey-Fisher quartz microphone and Eltec MOSFET impedance

converter. The microphone detects pressure changes at the driver end of the resonator while the MOSFET converts high impedance microphone signals into easily measureable low impedance signals with approximately unity gain. Once calibrated, the output from this assembly permits accurate measurement of operating frequency and pressure amplitude thus providing the means of monitoring the system for feedback control resonance tracking.⁸

The Eltec impedance converter (a MOSFET source follower) was additionally connected to a constant current source circuit consisting of a 6.8 k Ω resistor and 2N5457 JFET transistor (see APPENDIX E). The purpose of this configuration was primarily to stabilize it's gain. The impedance converter network was experimentally shown to have an output impedance of 3.03 k Ω and a gain of 0.97. It was also shown that for signals ranging in frequency from 200 Hz to 500 Hz (the operating region for the STAR) the phase shift of the output signal introduced by this amplifier was less than 0.14° (a highly desirable characteristic in that the phase is used to control the resonance frequency).

Once the impedance converter network was certified as being fully operational it was potted (using STYCAST 1266 epoxy) into a small oblong cavity having the same dimensions as the one in the bottom of the housing. Care was taken to ensure that leads were left exposed and fully accessible. Once dry, the assembly was removed from it's mold and

epoxied (again using STYCAST 1266) into the oblong cavity in the bottom of the driver housing.

The microphone consists of a y-cut quartz disk (see APPENDIX E) epoxied to a quartz ring using STYCAST 1266 epoxy. Leads were attached to electrode tabs on the disk using a silver paint. A fine bead of Dow Corning 732 Multi-purpose Sealant was put on the bottom of the ring and the assembly was gently lowered onto the lower lip of the small cylindrical cavity in the bottom of the housing.

A small insert for the channel connecting the microphone and impedance converter was manufactured using STYCAST 1266 epoxy. A narrow groove was cut into the piece allowing for the placement of a lead connecting the microphone output to the pre-amp input. The insert was then epoxied into place and the connection between the microphone output and MOSFET input was completed.

The microphone back volume of approximately 0.4 cm^3 was sealed with a circular brass plate having a small capillary leak. The leak allows the static pressure between the microphone back volume and housing to equalize while the system is being pressurized. At the same time, the leak is small enough that a dynamic pressure seal exists ensuring that no undesirable acoustic pressure is introduced into the microphone back volume. The leak was created by inserting 3 mil copper wire into a one centimeter long piece of 4 mil bore copper-nickel tubing. Based upon the theory of flow

between concentric cylinders¹² and the requirement that phase errors be kept to less than 0.5° , it was theoretically determined that a minimum acceptable value for flow resistance would be approximately 5×10^6 gm/cm⁴-s. The above tubing configuration was experimentally shown to have a flow resistance per unit length of about 6×10^6 gm/cm⁵-s and so the use of a one centimeter length of tubing was sufficient to prevent the unwanted phase errors. The theoretical and experimental derivations of flow resistance within the capillary are explained in APPENDIX A.

The tubing was inserted into a hole in the brass plate and soldered in place. The second lead from the microphone was grounded by attaching it to the underside of the brass plate with silver paint. The brass plate was then placed on the upper lip of the microphone cavity and carefully epoxied into place. A more viscous, fast drying epoxy (TRA-BOND BA-2106) was then used to seal the small gap that existed where the channel insert met the brass plate.

The final microphone/FET assembly requirement was to install a brass plate to shield the electronics. The plate had three holes drilled into it; one for the MOSFET ground, and two for coaxial cable connection. The braids of the cables (Microdot type 250-3866-0000 low noise coaxial cable) were soldered to the top surface of the brass plate while the center conductors were permitted to pass through the plate for connection to the MOSFET. The MOSFET ground was

also soldered to the plate. With all appropriate connections made the brass plate was then mounted to the housing with two #0-80 screws and the microphone/FET was finally ready for testing. Figure II-18 shows the completed microphone/FET assembly.

5. Housing Assembly

With the microphone/FET electronics installed the assembly of the housing was ready to commence. The threads of an 1/8 inch Swagelok gas fitting were wrapped with teflon tape and the fixture was then installed in the gas fill port. The electronic feed-through plug (complete with connectors and fittings) and DC pressure transducer were then mounted ensuring that their respective lead O-rings were crushed to provide leak-tight seals. The two coaxial leads coming from the microphone/FET package were coupled with coaxial cables from the feed-through plug using Malco microdot coaxial connectors (part numbers 031-0034-0001 (female) and 032-0023-0001 (male)). The two teflon-coated power leads from the feed-through plug with the ring connectors attached were then connected to the driver. The driver was then carefully placed in position ensuring that it's leads did not touch the reducer cone and that the microphone cables were not disturbed or damaged. With these connections made, any excessive lengths of electrical leads were neatly placed in the available space between the driver and inner wall of the housing. The underside of the

leads to electronic
feed-through plug

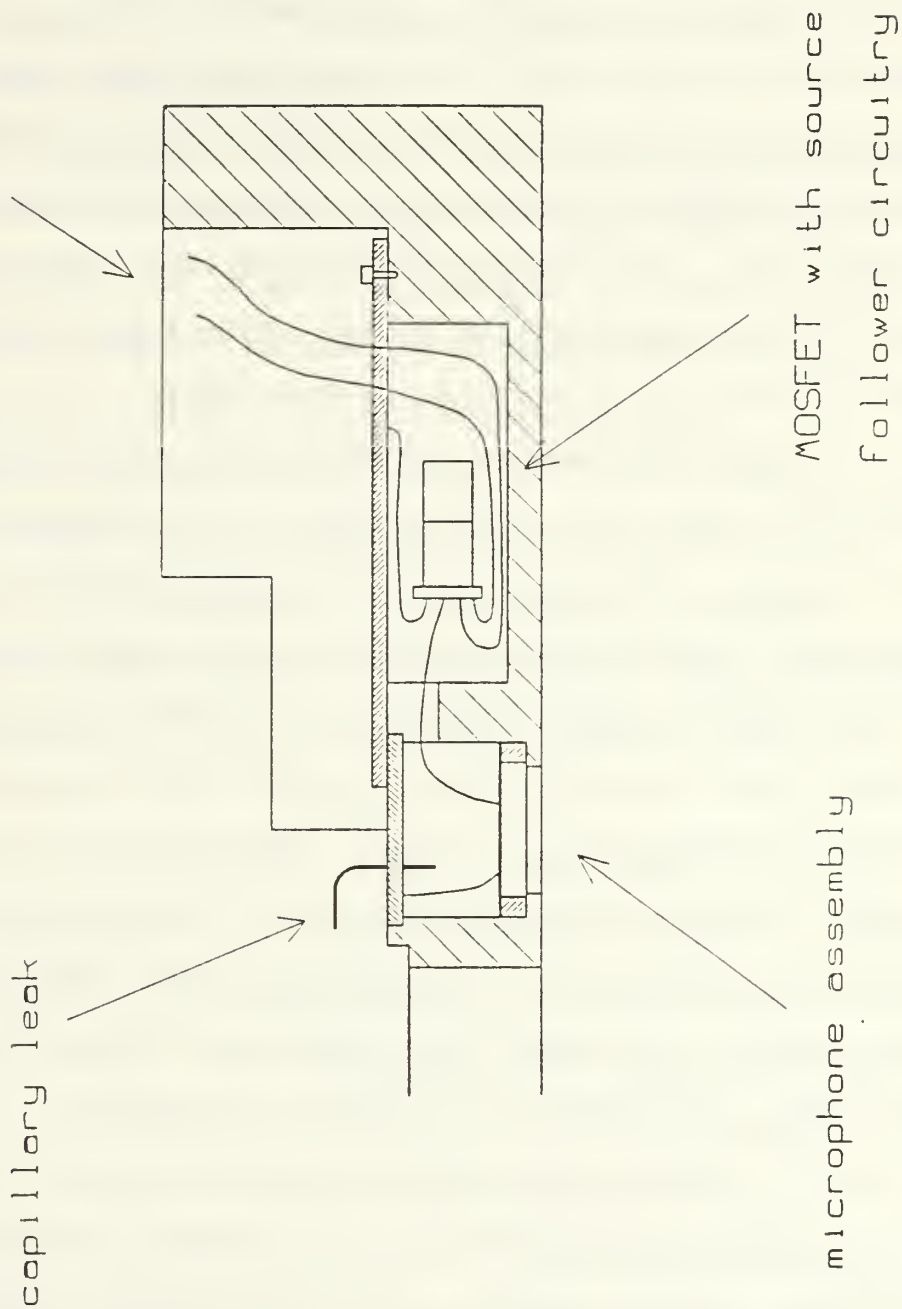


Figure II-18. Microphone/FET Assembly

driver's magnetic structure that would make contact with the pusher plate was then coated with heat sink grease (EG&G Wakefield Engineering Inc. Type 120 Thermal Joint Compound) to improve the heat conduction path from the driver to surrounding environment. The pusher plate was then installed ensuring that the driver was firmly held in place. The coaxial lead coming from the cone-mounted accelerometer was then connected to the third coaxial cable from the feed-through plug. Any excessive accelerometer lead was tucked into the same gap occupied by the other leads through the small cutaway section in the pusher plate.

The driver housing structure was then inverted (resonator side up) in preparation for the bellows installation. The flat section of the reducer cone that would make contact with the bellows was lightly coated with STYCAST 2850FT epoxy. The 1.5 inch diameter opening in the housing which would also make contact with the bellows was coated with STYCAST 1266 epoxy. The bellows was then gently lowered into position ensuring that it made good contact with the reducer cone. Additional STYCAST 1266 epoxy was then allowed to be drawn (via capillary action) into the very small gap between the bellows and housing. After allowing a suitable time for the epoxies to cure (24 hours) the pressure lid was installed to complete the assembly of the driver housing system. The strain relief fixture was attached once the housing was ready for connection to all

external electrical leads. At this point the components were ready for preliminary testing to determine system parameters (such as moving mass, stiffness, etc.) and to calibrate the microphone and accelerometer sensitivities. These procedures will be presented in section II.D.

6. Vacuum Can Description

The vacuum can requires a brief description here as it is a critical accessory to ensure proper functioning of the refrigerator. It's main function is to insulate the resonator from the surrounding environment and thus allow the refrigeration process to be measured without uncontrolled, extraneous heat loads. It is 15 inches long in order to completely encase the resonator and it's insulation, and is composed of three sections that are welded together (depicted in Figure II-19). Like all other system components, it too is constructed out of 6061-T6 aluminum.

It has a 9.86 inch diameter flange section which mates with the smaller of the two housing flanges. A groove has been cut into the upper face of the flange for a Parker 2-174 rubber O-ring. Two ports have been milled into this section. One is an electronic feed-through port for a commercially available six pin plug (Hermetic Seal Corporation SS7201-10B-6P-1 mod 1). The electronics plug is for connection to thermocouple leads (that monitor hot and cold heat exchanger temperatures) and for connection to a

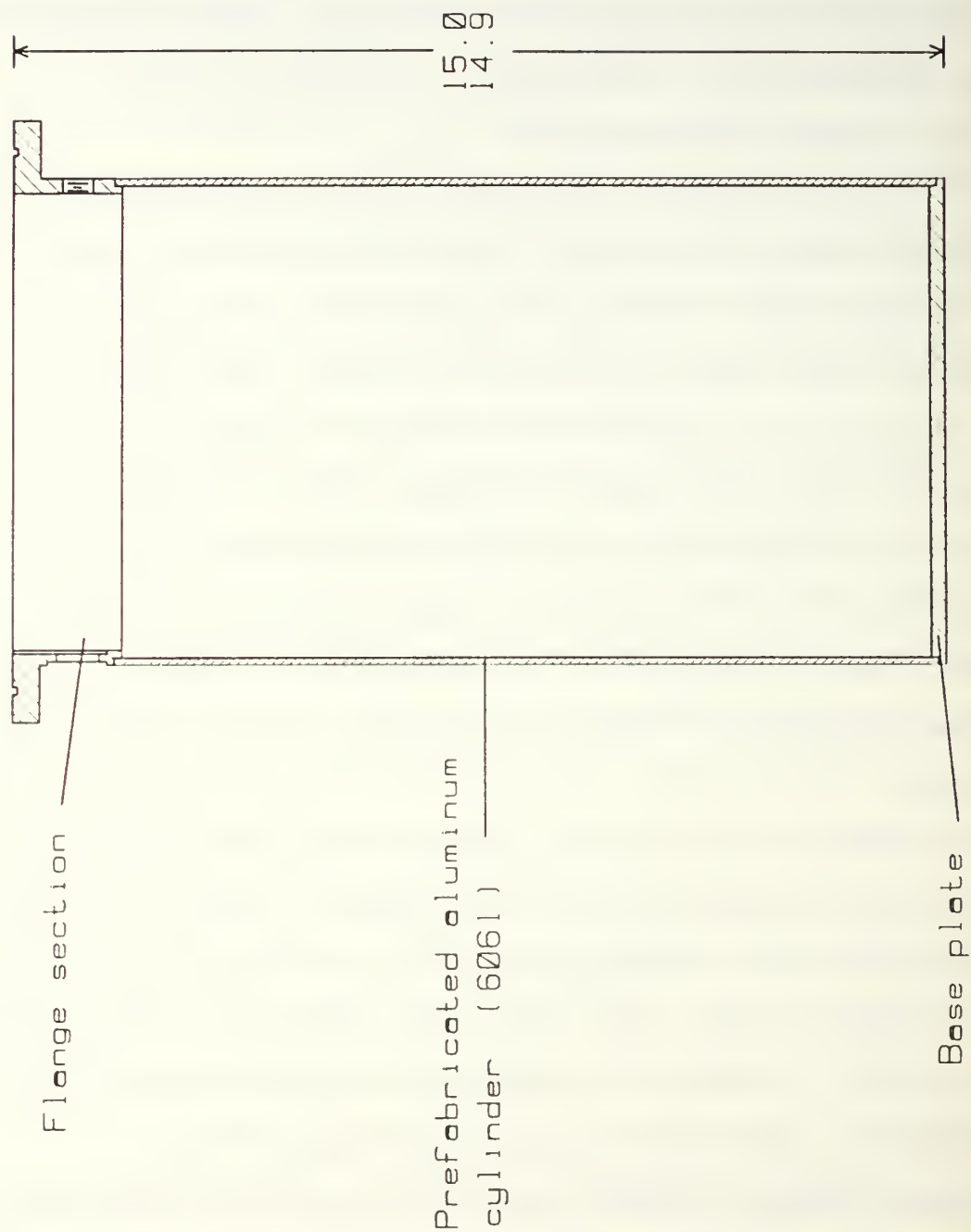


Figure II-19. Cross-Sectional View of the Vacuum Can

heater used during the actual refrigerator tests. The other port is a vent hole into which a 1/4 inch Swagelok pipe fitting will be installed that permits evacuation of the can.

The wall thickness of the flange section has been limited to 1/4 inch to reduce overall weight but still maintain rigidity. At the electronic feed-through port the flange section has been machined on both the inner and outer walls to provide flat surfaces for ease of mounting the feed-through plug and for the feed-through O-ring seal. An 1/8 inch lip cut into the bottom of the flange section around its entire diameter is for placement of length of 1/8 inch thick prefabricated aluminum tubing having an outer diameter of eight inches.

One final vacuum can component is a 1/4 inch thick base plate. An 1/8 inch lip has been milled around its outer diameter in order that it be able to fit securely onto the end of the aluminum tube prior to being welded in place.

D. DRIVER/HOUSING MEASUREMENTS

1. Driver/Housing Parameters

With the driver assembly completed, the first measurements to be made established driver parameters including the moving mass (m_o), stiffness (k), mechanical resistance (R_m), quality factor (Q), and resonance frequency (f_o) of the system. Several other parameters were also

determined that will be discussed at the end of this section.

The resonance frequency was easily found by connecting the driver (via the electronic feed-through plug) to an HP-4194 Impedance Analyzer. Resonance was observed to occur at approximately 350 Hz in air.

The moving mass and stiffness of the driver/bellows system were determined using the previously discussed dynamic mass loading procedure. Measurement of the resonance frequency for a given added mass yields the desired parameters if a graph of period squared versus added mass is constructed (see Figure II-20). The slope of the resulting straight line permits the calculation of stiffness while the ratio of the slope to y-intercept determines the moving mass of the system. Again the only instrumentation required was an HP-4194 to measure resonance frequency. The experimental results yielded a stiffness of 6.83×10^4 N/m ($\pm 1.0\%$) and a moving mass of 1.43×10^{-2} kg ($\pm 1.1\%$) when done in air. Since both stiffness and moving mass are additive when dealing with this multi-component system, it is worthwhile comparing the above results to those parameters determined for the driver and bellows prior to system assembly (refer to TABLE II-3). Summation of the individual driver and bellows stiffnesses yields a value of 6.75×10^4 N/m (about 1% lower than the value above) which is reasonable within experimental error. Summation of the

TABLE II-3. STIFFNESS AND MOVING MASS FOR INDIVIDUAL COMPONENTS AND COMBINED SYSTEM

	DRIVER	BELLOWS	COMBINED	DRIVER/BELLOWS
stiffness (kg/s)	6.37×10^4 $\pm 1.21 \times 10^3$	3.87×10^3 $\pm 1.16 \times 10^2$	6.76×10^4 $\pm 1.33 \times 10^3$	6.83×10^4 $\pm 6.83 \times 10^2$
moving mass (gm)	12.60 ± 0.29	0.07 ± 0.61	12.67 ± 0.90	14.26 ± 0.16

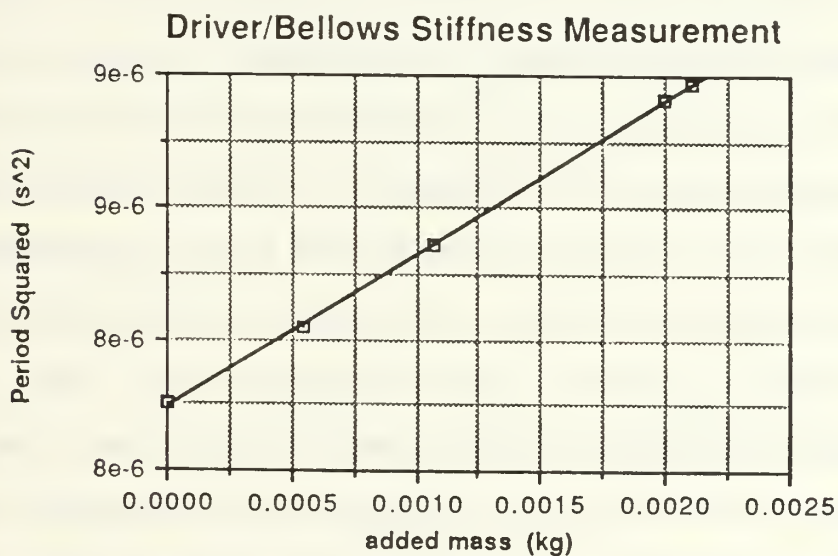


Figure II-20. Stiffness and Moving Mass Measurements of the Driver/Bellows System

moving masses yields a value of 1.27×10^{-2} kg (about 11% lower than above). The contribution of the bellows to this total is only 0.07 grams which seems rather low considering that the mass of the bellows is 1.86 grams. It is therefore believed that the large difference between the summation of moving masses and that of the driver/bellows system is due to experimental error.

The quality factor and mechanical resistance of the system were determined using the free-decay method in 10 bar helium. To maintain a leak-tight system a small test volume (12.7 cm^3) was mounted onto the resonator side of the housing. By momentarily exciting the driver (by means of a D-cell battery) and observing the output of the driver-mounted accelerometer on a digital oscilloscope, both Q and R_m were readily ascertained. Measurement of peak voltages over several cycles of the exponentially-decaying signal provided the necessary information to graph the natural logarithm of the voltage peaks versus their respective peak numbers (starting at zero). The slope of the resulting curve yielded a quality factor of 20.4 ± 1.8 . The mechanical resistance was then determined to be 1.96 ± 0.18 kg/s based on the relationship that $R_m = \omega m_0 / Q$ (where ω was the angular resonance frequency with the test volume in place).

Additional parameters that were determined included the driver back volume (V_d), the stiffness of the back

volume (k_d), the internal volume of the bellows (V_b), and the effective piston area of the bellows (A_{eff}). The internal volume of the bellows was required for use in determining the volume acceleration sensitivity to be discussed in section II.D.3. The volume of the bellows was determined to be 10.8 cm^3 by filling it with a measurable quantity of water. Despite the non-scientific approach the accuracy of this measurement was better than 2%. The effective piston area of the bellows was calculated to be $6.87 \times 10^{-4} \text{ m}^2$ which was about 8% lower than the value of 7.46×10^{-4} given in the bellows specification sheet. Its derivation is also discussed in section II.D.3.

The driver back volume was estimated using the known dimensions of the the driver and housing, and assuming that the volume between the driver's magnetic structure and inner wall of the driver housing could be ignored since it is blocked acoustically by the pusher plate. Knowledge of the driver back volume and effective piston area were required in order to determine the stiffness of the back volume and to show that it was negligibly small in comparison to the stiffness of the rest of the system. The relationship between quantities is given by,

$$k_d = (\gamma P_o A_{eff}^2) / V_d \quad (\text{II-4})$$

where γ is the ratio of specific heats and P_o is the ambient gas pressure within the housing. The values that resulted were a back volume of $4.12 \times 10^{-4} \text{ m}^3$ having a stiffness of

2.27×10^2 N/m. As expected the back volume stiffness was less than 0.5% of the overall system stiffness. A summary of all the driver parameters listed above is provided in TABLE II-4.

2. Microphone Calibration

The microphone located in the resonator end of the housing has a critical role in monitoring the system performance and therefore requires an accurate calibration. It is the microphone output that is used in conjunction with the accelerometer signal to determine the acoustic power delivered by the driver to the resonator. If the electric power to the driver is known then the overall electroacoustic efficiency of the system can be determined

TABLE II-4. Driver Housing Parameters

resonance frequency	f_o	350	[Hz]
moving mass	m_o	1.43×10^{-2}	[kg]
driver/bellows stiffness	k	6.83×10^4	[N/m]
quality factor	Q	20.4	
mechanical resistance	R_m	1.96	[kg/s]
driver back volume	V_d	4.12×10^{-4}	[m ³]
back volume stiffness	k_d	2.27×10^2	[N/m]
bellows volume	V_b	10.8×10^{-6}	[m ³]
effective piston area	A_{eff}	6.87×10^{-4}	[m ²]

from the ratio of the two powers. By feeding the microphone signal to the STAR signal processing package, the electronic control systems ensure that peak efficiency is maintained.⁸

The first test conducted on the microphone was carried out prior to installing the driver and was to ensure that there were no sizeable leaks in the microphone back volume. A test microphone installed in a flanged fixture was mounted to the resonator side of the housing. A loudspeaker was placed above the housing and allowed to radiate into the open cavity. The signals from the two microphones were compared using an oscilloscope (as a visual reference) and an HP-4194 Gain/Phase Analyzer. Since both microphones were essentially co-located it was verified that there was zero phase difference between the signals. Any unreasonable phase difference over the operating frequency range would have been an indicator that a leak was present. Upon verification that the microphone back volume was leak-tight, the driver was installed and the housing was closed up.

A calibrated microphone, with known sensitivity of $15.7 \mu\text{V}/\text{Pa}$ ($\pm 2\%$), mounted in a test assembly was bolted to the resonator side of the driver. The housing and test assembly were then pressurized with 10 bar helium and the driver was provided with a low power signal from the HP-4192. By measuring the ratio of output voltages from both microphones a simple comparison calibration was

conducted to determine the sensitivity of the housing microphone. This calibration was conducted for a number of different frequencies over a range from 100Hz to 1kHz to determine if the microphone sensitivity was reasonably flat (frequency independent) in the operating region of the STAR. Calculated sensitivities ranged from 25.6 $\mu\text{V}/\text{Pa}$ at 100 Hz to 26.1 $\mu\text{V}/\text{Pa}$ at 1kHz (a change of only 2% over the entire range) with a mean of 25.8 $\mu\text{V}/\text{Pa}$. The housing and test fixture were then evacuated and repressurized with a 10 bar He-Ar gas mixture (18.85% Ar). The comparison calibration was carried out once again to ensure that changing gas mixtures would have little affect on microphone sensitivity. The resulting sensitivities ranged from 25.7 $\mu\text{V}/\text{Pa}$ at 100 Hz to 26.1 $\mu\text{V}/\text{Pa}$ at 1kHz with a mean of 26.0 $\mu\text{V}/\text{Pa}$ (agreement to within one percent of the mean value in pure helium). The results of the comparison calibrations are summarized in Figure II-22.

3. Volume Velocity Calibration

Acoustic power can be expressed as the product of acoustic pressure, volume velocity, and the cosine of the phase between them. Acoustic pressure is readily determined by taking the ratio of the microphone output voltage to microphone sensitivity. Volume velocity can be determined from the accelerometer output but requires that a volume velocity sensitivity be known. The following section is based on the procedures outlined by Hofler in his thesis (as

Comparison Calibration :
$$M_{mic} = \frac{V_{mic} M_{cal}}{V_{cal}}$$

Microphone Calibration at 10 Bars

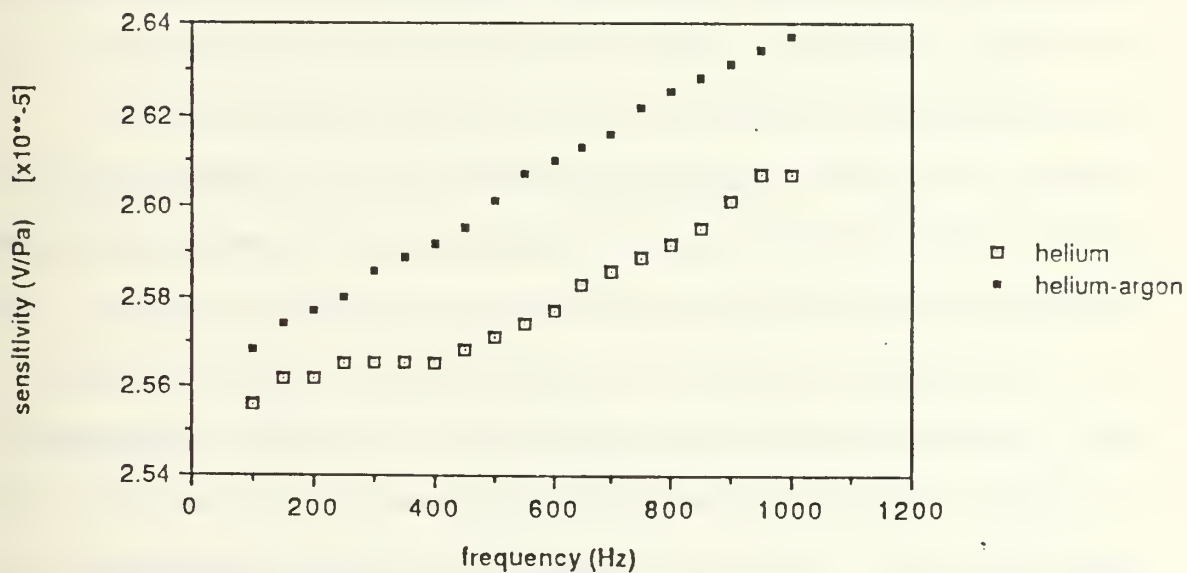


Figure II-21. Microphone Calibration

well as a related JASA article¹³⁾ for determining this sensitivity.

A small cylindrical calibration volume having a known acoustic impedance (easily determined by summing its volume with the internal volume of the bellows) was mounted to the resonator side of the housing. The housing and test volume were evacuated and then pressurized to 10 bar with helium. Since volume velocity is equal to the ratio of acoustic pressure to acoustic impedance, knowledge of a given load impedance and measurement of the pressure amplitude at a given frequency completely determines the desired parameter. It has already been shown how acoustic pressure can be determined from the microphone sensitivity and output voltage. Similarly volume velocity can be determined from a sensitivity and measureable velocity signal. In Hofler's thesis he electrically integrates the accelerometer output signal to produce a velocity signal and uses this to define a volume velocity sensitivity (M_u). In the following procedure the accelerometer output voltage (V_{acc}) is used directly but is divided by angular frequency to yield a volume acceleration sensitivity (M_u^*) having units of $V\text{-s}^2/\text{m}^3$. Volume velocity (U) is then given by $U = V_{acc} / \omega M_u^*$. Since volume velocity is also equal to the product of particle velocity (u) and effective piston area (A_{eff}), then the later parameter can be easily determined by

$A_{\text{eff}} = M_{\text{acc}} / M_u^*$ if we define $u = V_{\text{acc}} / \omega M_{\text{acc}}$ where M_{acc} is the accelerometer sensitivity.

By measuring the ratio of output voltages of the accelerometer and microphone, a value for the volume acceleration sensitivity was readily determined for a given frequency. Sensitivities were calculated over a range of frequencies from 100 Hz to 1 kHz and varied from 0.120 $\text{V-s}^2/\text{m}^3$ to 0.116 $\text{V-s}^2/\text{m}^3$ with a mean of 0.118 $\text{V-s}^2/\text{m}^3$. The calibration was repeated in a 10 bar He-Ar gas mixture (18.85% Ar) with similar results. The mean value of the sensitivity in He-Ar was again 0.118 $\text{V-s}^2/\text{m}^3$. Using this value an effective piston area of $6.78 \times 10^{-4} \text{ m}^2$ was determined as reported in TABLE II-4. The theory and results of the above procedure are summarized in Figure II-23.

One additional piece of data obtained from the volume acceleration sensitivity calibration was the phase difference between the accelerometer and microphone signals. This varied between -2.4 to -2.8 degrees in the operating region of the STAR and is believed to be due to phase differences existing in the electronics used to measure the data. It is noted here as a required correction to the phase between pressure and volume velocity. An additional phase correction of $+90^\circ$ is also required when calculating acoustic power using the accelerometer output directly since pressure and velocity (not acceleration) are required to determine acoustic power.

Impedance of a small :
$$Z_{cav} = \frac{i \gamma p_m}{\omega V_o}$$

cylindrical volume

where

γ = ratio of specific heats

p_m = internal ambient gas pressure [N/m²]

ω = angular frequency [rad/sec]

V_o = volume of cavity [m³]

$i = (-1)^{0.5}$

Volume acceleration :
$$M_u^* = \frac{V_{acc} M_{mic} |Z_{cav}|}{\omega V_{mic}}$$

sensitivity

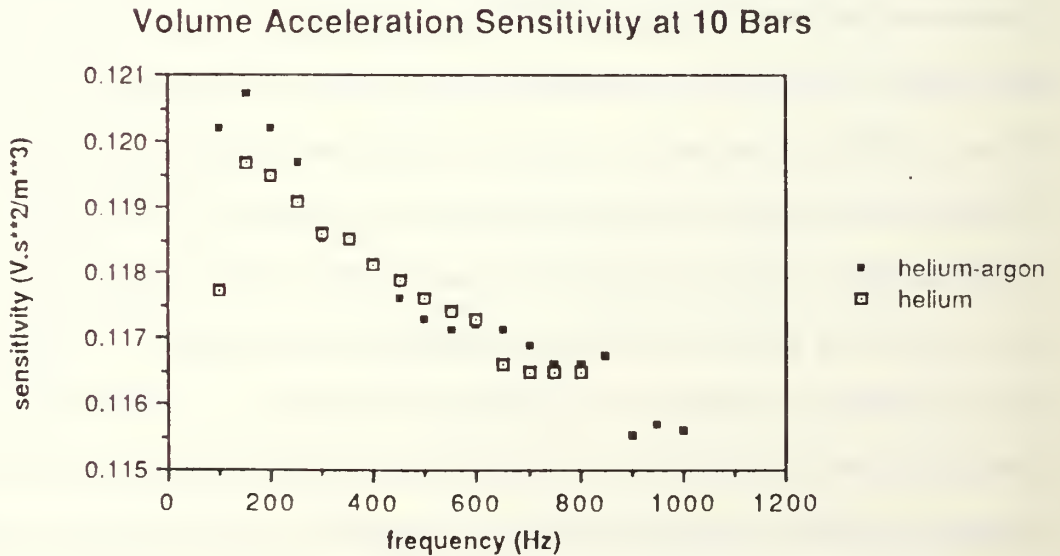


Figure II-22. Volume Velocity Calibration

III. RESONATOR SUBSECTION

A. OVERVIEW

The resonator is designed to support an acoustic standing wave and to serve as a housing for the pressurized gas and thermoacoustic elements, including the stack and heat exchangers. The interaction of the standing wave and the stack transports heat. The geometry and the construction of the resonator is constrained by the desire to minimize extraneous heat loads due to unwanted thermal conduction between the hot and cold portions of the stack. In addition it is desirable to reduce acoustic losses due to thermoviscous attenuation within the resonator and to meet the size restrictions imposed by using the GAS canister. In his doctoral dissertation, Hofler (1986) discussed the loss mechanisms in detail along with resonator design considerations. For use in the STAR project a custom resonator was designed by Hofler, as illustrated in APPENDIX D. Due to time limitations, the construction of this resonator was not completed in time for use in the experimental measurements discussed in Chapter IV. These measurements were conducted with a resonator that is acoustically similar to the one the STAR resonator, but that has not been optimized for thermoacoustic transfer. The

resonator used in the space-qualified system will be described in the forthcoming thesis by Jay Adeff.

B. RESONATOR COMPONENTS

As shown in Figure III-1, the STAR resonator is a complex mechanical fixture composed of several components joined together. The base assembly (1) is machined from oxygen free, high conductivity (OFHC) copper (CRA 110) and is designed to form a helium leak tight interface between the driver housing and the fiber-reinforced plastic (FRP) neck. The FRP neck (2) consists of a hollow composite fiberglass and epoxy tube bonded to a .001" stainless steel sleeve. Connected at the opposite end of the FRP neck is a small diameter copper tube (3) which flares out as it enters an attached stainless steel sphere (4). The spherical volume is used to simulate an open-end termination, while allowing the system to be closed. This results in the resonator behaving as a $1/4$ wavelength tube.

Within the FRP neck is the heart of the thermal heat pumping process. This section is composed of a plastic stack (5) which allows the thermoacoustic transport of heat energy to occur along its length, and two heat exchangers (6,7). The heat exchangers are multiple layers of parallel thin copper strips bonded together and aligned perpendicularly to the resonator's longitudinal axis. The purpose of the heat exchangers is to provide a good thermal

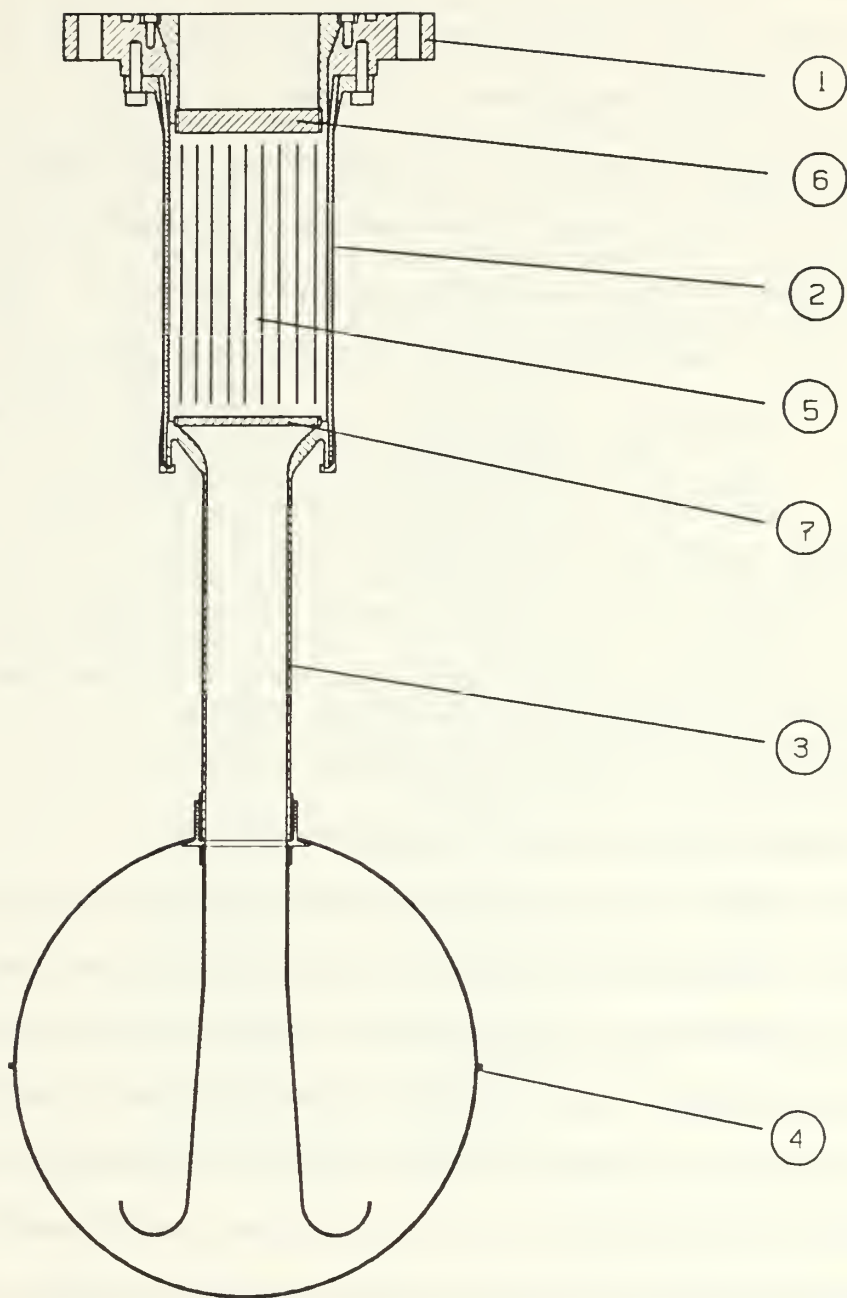


Figure III-1. Diagram of the STAR resonator

transfer at the two ends of the stack in order to prevent unnecessary losses, and to serve as a contact point between the stack, the high temperature reservoir, and the cryogenic load. In this experiment the load is simply an electrical heater (MINCO thermofoil heater model HK5232R45.8112a1-7). Details of the stack construction and thermodynamics were discussed by Susalla in his masters thesis.⁵ Basically, the stack is a long sheet of 0.003" thick plastic film with a series of parallel sections of monofilament strings attached to it. This film is then spiral wound around a small diameter plastic rod to form a stack with a 38.1 mm diameter and a length of 78.5 mm. One of these stacks, built at Los Alamos National Laboratory, was used for the test measurements conducted in Chapter IV.

C. HELIUM LEAK TESTING OF THE FRP NECK

In order to prevent unwanted thermal losses due to thermal conduction, the wall material of the FRP neck must have low thermal conductivity. The decision was made to use fiberglass and epoxy (Dexter HYSOL EA9396) for the FRP neck based upon its availability, ease of fabrication, high mechanical strength, and low thermal conductivity. The choice of helium as the major component of the working gas creates certain problems. Helium is known to diffuse through all known insulators at room temperature. One method of overcoming this problem is to insert a metal vapor

barrier between the FRP and the area exposed to the helium based gas. A one mil thick piece of stainless steel (Precision Brand™ 698158) was chosen from the metals available based upon its high tensile strength and its low thermal conductivity. When soldered to the two copper tube sections, this will provide a solid metal barrier to helium diffusion, but until overlaid with the fiberglass epoxy will lack strength and rigidity.

In order to verify that the leak rate would be insignificant with the stainless steel liner and that a leak-tight seal could be obtained, two test pieces (Figure III-2) were manufactured. These pieces were scaled to represent the actual driver resonator and consisted of two copper pipe sections with a connecting piece of stainless steel overlaid with fiberglass epoxy. In the construction of one of the test pieces, leak paths were left along the seam of the stainless steel liner. These leak paths were designed to allow us to determine the effect of minor holes in the stainless steel sleeve. The relative thinness of the stainless steel required that a mandrel be inserted inside the sleeve. Once the epoxy and fiberglass composite was bonded to the stainless and copper parts, giving strength to the test piece, the mandrel was removed. Prior to applying the fiberglass it was verified that the completely sealed test piece was leaktight in air at 1 atmosphere using an

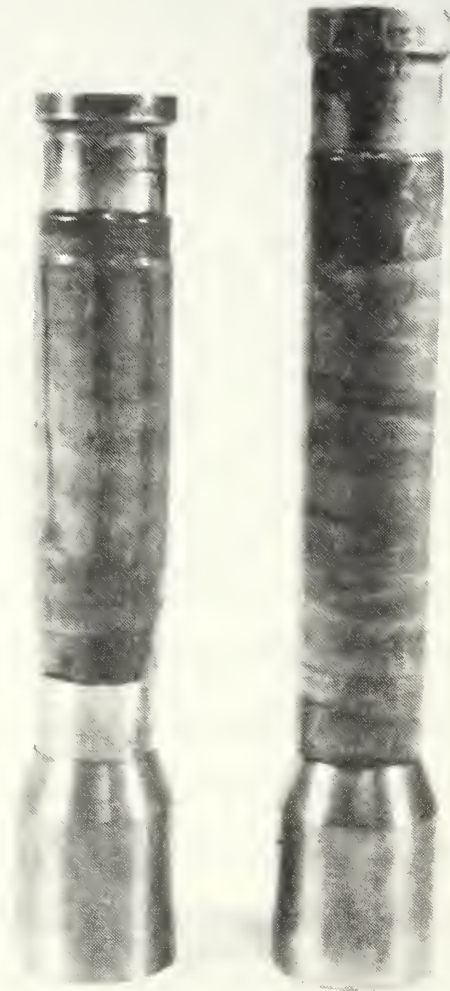


Figure III-2. Fiber-Reinforced Test Pieces

Alcatel helium leak detector. The Alcatel He leak detector was used for all such leak-testing procedures.

Once the two test pieces were covered with epoxy, it was important to determine the leak rate for each piece. Using a custom built testing stand shown in Figure III-3, the interior of the test pieces were pressurized with 3 atmospheres of helium to saturate the FRP material exposed to the helium by any leaks. A vacuum was then applied to the exterior of the test piece, such as it will experience during actual use, and sampling for helium conducted. The first piece to be tested was the leak tight stainless section after having been left pressurized with helium for 24 hours. After a sampling run of several hours no helium diffusion above 10^{-10} standard cm^3/s , the Alcatel's lowest detection range, was detected and the test piece was assumed to be helium leak tight. For the test piece with leak paths in the stainless, but leak tight to air after having been wrapped in fiberglass, helium was immediately detected diffusing through the FRP neck. With this test piece it was impossible to obtain a helium leak rate of less than 10^{-6} standard cm^3/s , the Alcatel's upper limit. As a result of these two tests it was verified that controlling the helium leak rate through the composite by using a thin metallic vapor barrier was necessary and possible.

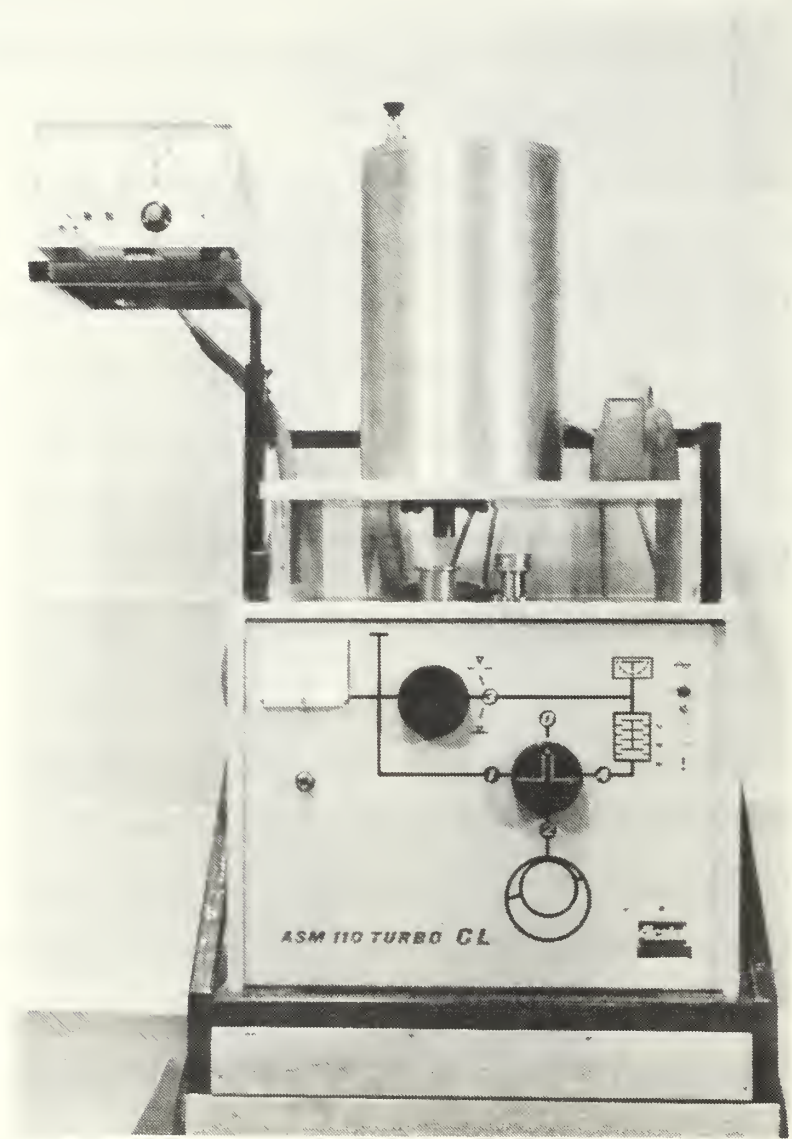


Figure III-3. Alcatel Helium Leak Tester and FRP Test Assembly

IV. SYSTEM TEST

A. EXPERIMENTAL APPARATUS AND PROCEDURE

1. Preliminary Requirements

In order to determine the electroacoustic efficiency of the STAR driver a procedure was required whereby electric and acoustic power could be easily ascertained either directly or indirectly. If the microphone and volume velocity transducer sensitivities are known, then acoustic power can be determined from measurement of the microphone output voltage at the bellows location, the bellows-mounted accelerometer output voltage, and the phase difference between these signals. Therefore the first of three preliminary requirements was to ensure that the microphone and bellows accelerometer were accurately calibrated as discussed in the sections II.D.2 and II.D.3.

The second requirement, prior to making any measurements, was to devise a reliable (and hopefully convenient) means of determining the electric power supplied to the driver. This could have been determined by measuring the input current and voltage to the driver and noting the phase difference between them. Instead, a more automatic approach was used whereby an electric power measuring circuit was designed that provided the desired parameter directly in the form of a DC voltage proportional to the

electrical power delivered to the driver. This circuit is depicted in Figure IV-1. Basically a $0.10\ \Omega$ current sensing resistor was placed in series with the driver. The voltage across both the driver and resistor then provided the necessary inputs to the power measuring circuit. The voltage across the resistor was used to ascertain the rms current to the driver and as an input to the power measurement. The power was determined by feeding the two input voltages through a four-quadrant multiplier chip (Analog Devices AD534) and then low-pass filtering the output with a 1.6 second time constant to remove the AC component. The average power was then directly available by measuring the remaining DC voltage on a multimeter. The measured value of power was 0.1 Watt/Volt. The rms current was determined by feeding the $0.10\ \Omega$ resistor voltage through an rms-to-DC converter (Analog Devices AD536) and then measuring the output directly. The DC output voltage was 1.0 Volt/Amp(rms) due to the voltage gain of ten provided by the INA110 instrumentation amplifier.

The final necessity was to design and build a gas handling system that was capable of both evacuating the refrigeration system and pressurizing it up to 150 psia (10^6 Pa). The system (see APPENDIX F) consists of a wall-mounted control panel having a differential pressure guage, inputs for two sources of pressurized gas, a vacuum port, a venting port and two pressure measuring devices (a Heise

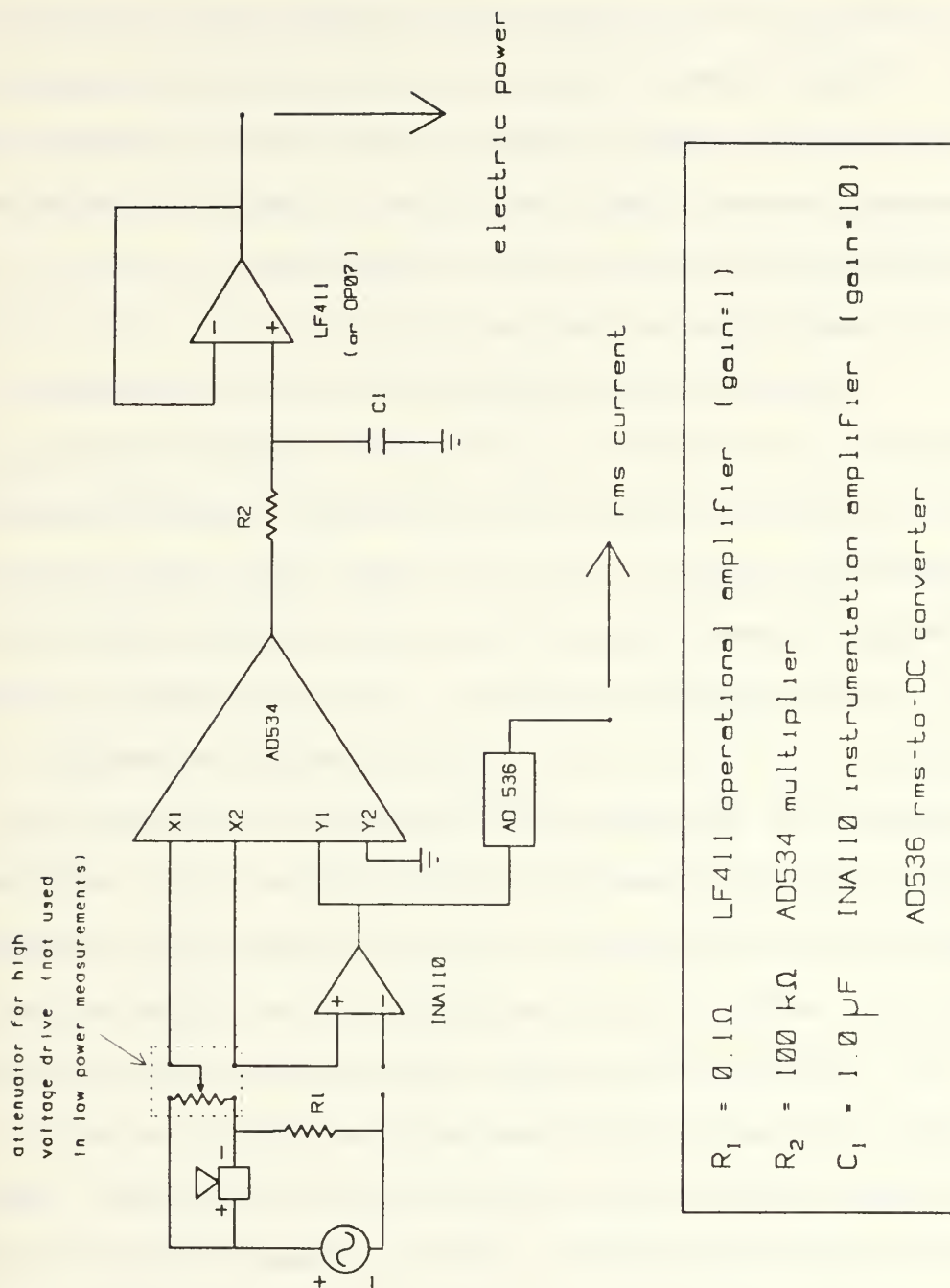


Figure IV-1. Electrical Power Measuring Circuit

guage and an Omega PX304 pressure sensor). The role of the differential pressure guage is to ensure that the STAR system does not pressurize (or depressurize) at too fast a rate. Rapid pressure changes could result in damage to either the microphone or bellows since both components are dependent on small capillary leaks to equalize pressure between their inner and outer boundaries.

2. Experimental Configuration

The driver was configured with two different resonators, neither of which was the actual flight-ready STAR resonator. The first, a straight, rigidly-terminated tube having constant cross-sectional area, was used to perfect measurement techniques with a system that could be easily analyzed theoretically. The second resonator was originally built by Hofler for the purpose of making acoustic loss measurements. Though its design was not optimal for refrigeration, it was an acceptable substitute, capable of housing a stack and having basically the same shape and acoustic characteristics as the STAR resonator.

An HP-4192 Impedance Analyzer was used as both a signal source and gain/phase measurement device and therefore played a central role in the experiment. The signal output from the HP-4192 was passed through a $50.0\ \Omega$ load prior to the power amplifier to ensure that a constant voltage was maintained for all frequencies of operation.

The signal was then fed to both the driver and power measuring circuit.

The microphone/FET was powered by a +15 V_{DC} supply. Its output, and that of the accelerometer, were passed through separate Ithaco 1201 pre-amplifiers in order to filter out unwanted noise and provide the necessary signal gain. The amplified microphone and accelerometer signals were then fed to the HP4192 for gain/phase measurements and to an oscilloscope for visual monitoring purposes.

Other instrumentation such as constant DC voltage and current supplies and multimeters were present for peripherals such as the power measuring circuit and Omega PX80 and PX304 pressure sensors. The experimental apparatus is shown schematically in its entirety in Figure IV-2.

3. Experimental Procedure

Although helium-xenon is the preferred gas mixture for the STAR, it is expensive and difficult to obtain. For this reason various gas mixtures of helium and helium-argon were used in all phases of these experiments. The primary purpose for using different gas mixtures was to alter the tube resonance frequency so that it ranged from above, to below the driver resonance frequency. By doing so, the performance of the system could be studied under different operating conditions.

Once the driver/resonator was pressurized with a particular gas mixture, the first information to be recorded

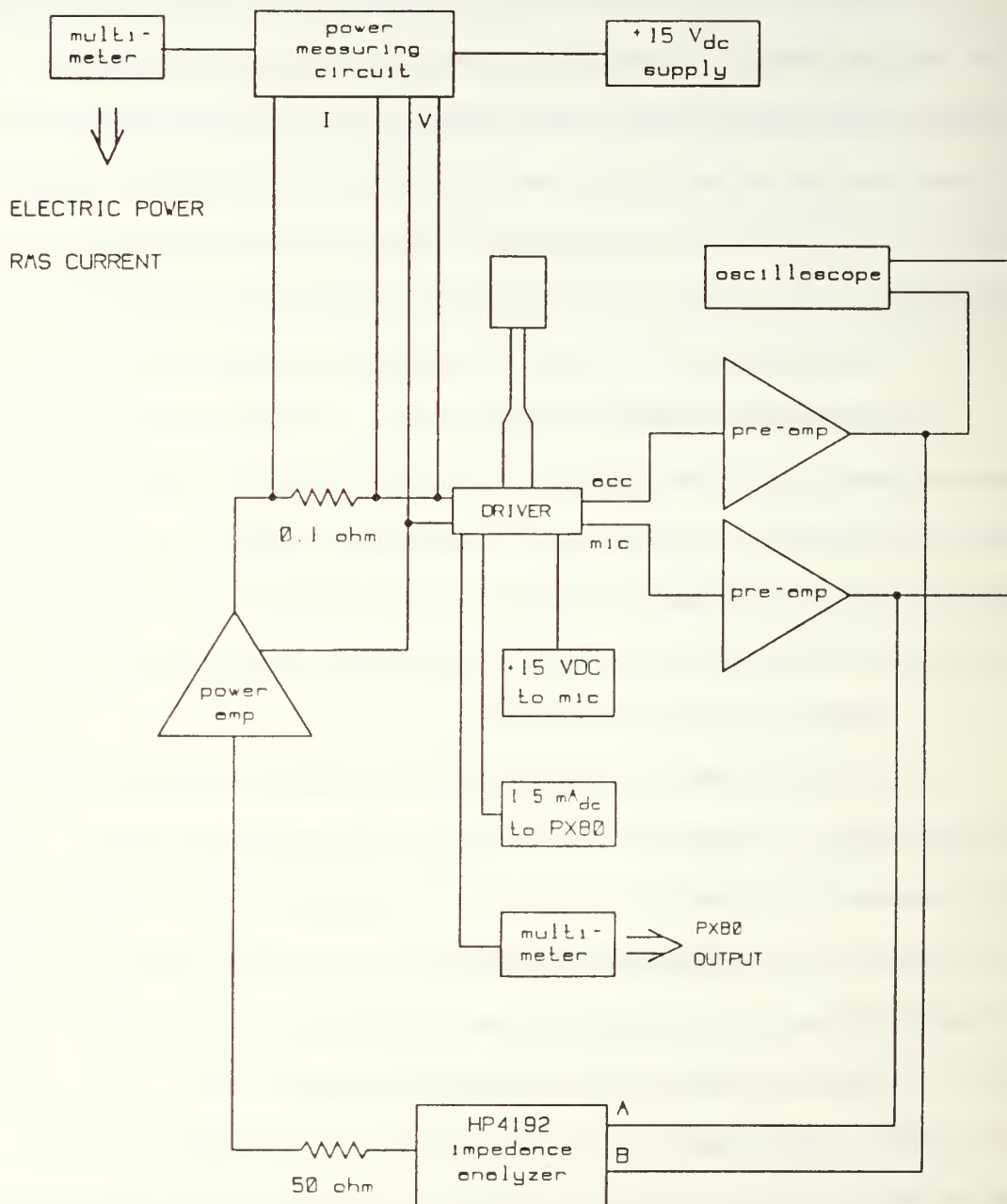


Figure IV-2. Schematic Representation of the Experimental Apparatus

was the ambient room temperature and pressure gauge readings. These were important in determining the speed of sound (c) and density (ρ) of the working medium. The resonance frequency and quality factor of the resonator were determined next. These two values provided some insight into the behaviour of the combined driver/resonator system. A knowledge of how closely matched the tube's resonance frequency is to that of the driver is an indicator of system efficiency. The quality factor defines the "sharpness of resonance"¹⁴ and is an indicator of how sensitive the system will be to frequency changes. The higher the quality factor the more sensitive the system is to change particularly as the two resonances approach one another.

With the preliminary information recorded, the system was run through a range of frequencies ensuring that the tube resonance frequency was sufficiently bracketed. For each run the frequency (f_o), microphone voltage (V_{mic}), accelerometer voltage (V_{acc}), phase difference (ϕ), electric power (Π_{elec}), power offset (Π_{off}) and rms current (I_{rms}) were recorded. The last three were obtained from a multimeter that was connected to the power measuring circuit outputs. The first four quantities were recorded directly from the HP-4192. Once it was determined that enough data had been taken for a given operating condition, the gas mixture in the system was changed and the procedure was repeated. A sample data set is provided in section IV.C.1 (TABLE IV-1).

The actual electric power delivered to the driver was determined by making a correction to the measured value by subtracting off the measured DC offset as well as a constant scaling factor. The constant scaling factor was determined by replacing the driver with a known resistance and measuring the voltage drop across that resistor. The power delivered to the resistor was easily calculated and could be compared with the value determined by the electronic circuit. For low power measurements (below 0.25 W) the scaling factor was determined to be 95 percent of the difference between the measured electric power and electric power offset.

The acoustic power provided by the driver to the resonator was determined by first calculating acoustic pressure (p) and volume velocity (U) from the microphone and accelerometer voltage levels. The phase difference between the two signals was then corrected by $+92.6^\circ$ for reasons previously discussed (electric phase shifts and acceleration-to-velocity conversion). Finally acoustic power was determined by taking the product of pressure, volume velocity, and the cosine of the corrected phase angle.

The electroacoustic efficiency was then readily determined from the ratio of the acoustic to corrected electric power ($\Pi_{\text{elec}}\{\text{corr}\}$) at each frequency measured in a particular gas mixture. A plot of efficiency versus

frequency provided a quick indication of how well the resonance frequencies of the driver and tube were matched. A mathematical derivation of the electroacoustic efficiency based on the measured parameters is provided in Figure IV-3.

To lessen the amount of time required for the necessary computations, a program written by Susalla and used by Fitzpatrick was modified to calculate and plot acoustic power, electric power, and efficiency as a function of frequency based on the measured data. These in turn could be compared with theoretical values generated by the program. The next sub-section discusses this program and it's modifications in detail.

B. COMPUTER SIMULATION

1. Background

The purpose of the original program written by Susalla was to determine the various performance characteristics of a generic driver/resonator system by treating it as an equivalent electric circuit driven by a constant current source. Input to the program consisted of sixteen operator-modifiable parameters that fully described each sub-system. Basic principles in acoustic and transduction theory were applied¹⁵ to the given data set to yield values for voltage, piston velocity, acoustic power, and electroacoustic efficiency as functions of frequency.

$$\Pi_{ac} = p U \cos (\phi + \phi_{corr})$$

$$\Pi_{ac} = \frac{V_{mic}}{M_{mic}} \frac{V_{acc}}{\omega M_u^*} \cos (\phi + \phi_{corr})$$

$$\Pi_{elec}(corr) = 0.95 (\Pi_{elec_m} - \Pi_{off})$$

$$\eta_{ea} = \frac{\Pi_{ac}}{\Pi_{elec}}$$

Figure IV-3. Mathematical Derivation of Electroacoustic Efficiency in terms of Measured Parameters

These results were then graphically depicted using a standard plotting routine.

2. Modifications

The Susalla program suffered from a number of deficiencies in its application to the experiment at hand. To correct this, a number of modifications were made to the program. To begin with, the program was altered so that it's only outputs were frequency, electric power, acoustic power, and electroacoustic efficiency. Secondly, provisions were made to allow the operator to input measured data so that actual experimentally determined values of electric power, acoustic power, and electroacoustic efficiency could be computed and compared graphically with theory. Finally, the program was modified to deal with a constant voltage source rather than constant current source since this is the mode of excitation used in the experiments discussed in this thesis and in the actual flight system. A copy of the modified Susalla program is located in the APPENDIX B.

3. Program Description

Before running the program, the user must modify a series of data statements located within the program which define the electromechanical properties of the driver and geometrical properties of the resonator. The parameters defined in these statements include the mechanical resistance (RM), moving mass (M), stiffness (SSUP), and transduction coefficient (BL) of the driver. Additionally,

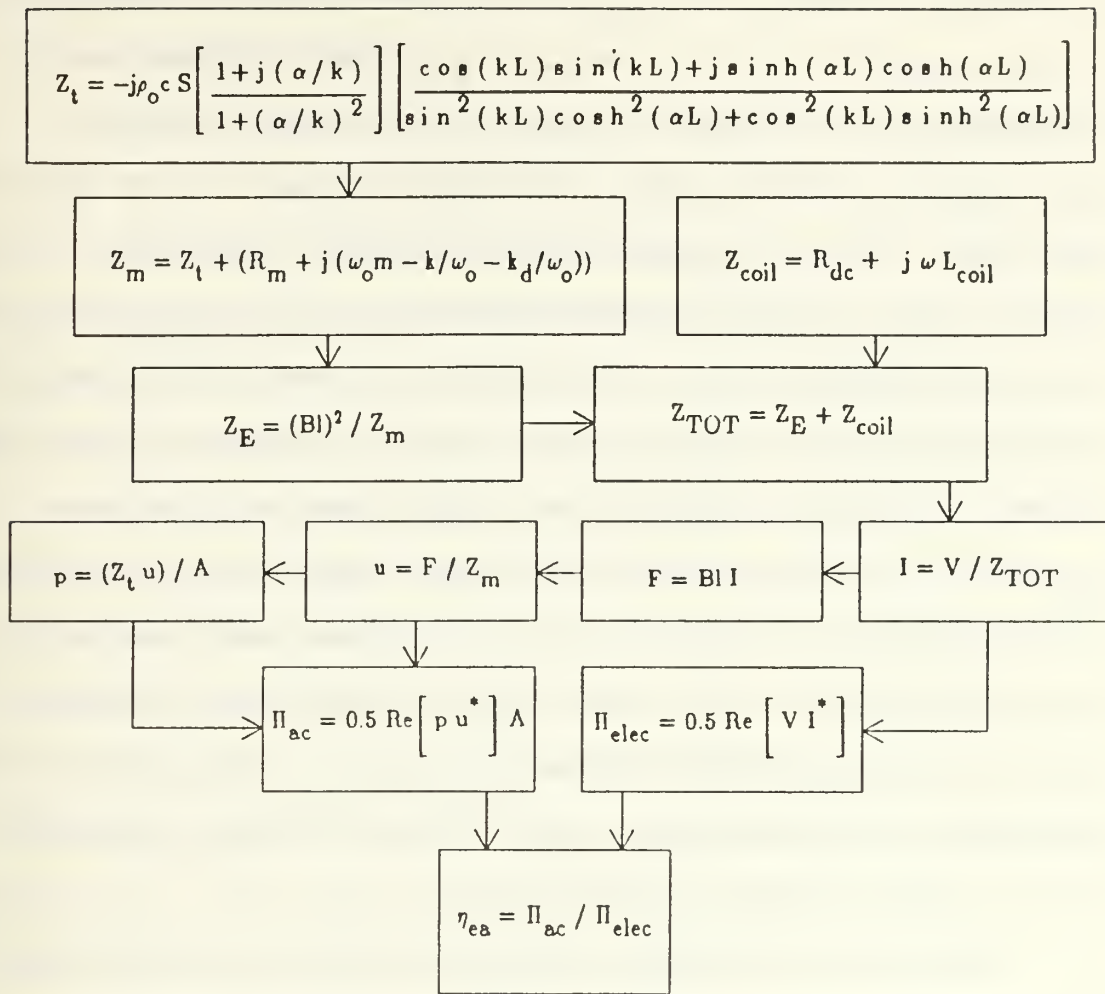
the driver back volume (VOL), voice coil inductance (LE), coil resistance (RE) and driver piston area (A) are defined. The parameters defining resonator shape include cross-sectional area (S) and effective length (L) of the tube (corresponding to one-half wavelength).

When the program is run it requests information pertaining to the particular operating conditions of the driver/resonator system. The user must then input gas density (RHO), sound speed (C), quality factor of the tube (Q), resonance frequency of the tube (FO), and the driving voltage (V). With this information the desired quantities are computed over a frequency range from one quarter to three halves of the tube resonance and stored in a data file. The quality factor is used to compute the absorption coefficient (α) for the medium within the resonator based upon the relationship that

$$\alpha = \omega_o / (2Qc) \quad (IV-1)$$

as discussed by Kinsler, Frey, et al.¹⁶ A description of the remaining computations is provided in Figure IV-4. Additional details pertaining to these computations are available in APPENDIX B.

The user is then given the option of inputting measured data for analysis and display. If this is desired, the program then requests a value for amplifier gain (which



where

Z_t is the mechanical impedance of the tube

Z_m is the mechanical impedance of the system

Z_{coil} is the voice coil electrical impedance

Z_E is the transformed electrical impedance of the mechanical system

Z_{tot} is the total electrical impedance of the system

Figure IV-4. Computer Simulation Strategy

is assumed constant for all measurements taken). The user is then prompted for six measured quantities corresponding to frequency, microphone voltage, accelerometer voltage, phase angle, electric power, and power offset. With this input, the program computes acoustic power, corrected electric power, and electroacoustic efficiency for a given frequency and stores it in a data file. The user is then given the option to input another set of measured data. The program continues asking for data and then storing the outputs until the user indicates that there are no more data to be analyzed. At this point the program ends leaving a message to the user that two data files have been created containing measured and theoretical data. Instructions are also provided enabling the user to obtain graphs comparing the two sets of data in those files.

It should be noted that the "program" as described above actually consists of two parts, both of which are written in Fortran-77 code. The numerical analysis part (FRIDGE FORTRAN A1) produces the two data files. The second part is the plotting routine (GRAFRI FORTRAN A1) which is invoked by simply typing "DISSPLA GRAFRI" once the data files have been created. GRAFRI FORTRAN has been programmed to output three plots to the IBM mainframe laser printer (SHERPA). To actually receive hard copies of these plots the user must type "SHERPA STAR SHGRAPH A1" after typing "DISSPLA GRAFRI".

C. EXPERIMENTAL RESULTS

1. Straight Tube

As previously mentioned, the straight tube is useful in that it can be easily modelled using basic acoustic theory. The first experiment conducted with this resonator was to determine the acoustic impedance of the tube in air and compare the results with theory. This served as a validation of the two sensitivities previously determined. By measuring microphone and accelerometer outputs at tube resonance and converting them to acoustic pressure and volume velocity respectively, the acoustic impedance could be readily ascertained based on the ratio of the two quantities. The value obtained experimentally was $1.59 \times 10^7 \text{ N-s/m}^5$. By applying the expression for Z_t shown in Figure IV-4, the acoustic impedance of the tube was calculated to be $1.74 \times 10^7 \text{ N-s/m}^5$ (a difference of about 8.5%) at resonance. This was acceptable agreement within experimental error.

The next procedure was to validate the modified Susalla program by comparing measured data with theoretical values. The tube was pressurized with helium to approximately three atmospheres (45 lb/in²) and measurements were taken over a range of frequencies that spanned the tube resonance (475.5 Hz). The measured data is provided in TABLE IV-1. The quality factor of the tube was determined to be 63.5 based on the frequency dependence of phase

TABLE IV-1. MEASURED DATA FROM STRAIGHT TUBE EXPERIMENT

$$f_o = 475.6 \text{ Hz}$$

$$T = 20.5 \text{ }^{\circ}\text{C} = 293.5 \text{ K}$$

$$Q = 63.5$$

$$V_{\text{rms}} = 0.26 \text{ V} = 0.37 \text{ V}_{\text{peak}}$$

$$c = 1009 \text{ m/s}$$

$$\rho = 0.50 \text{ kg/m}^3$$

freq (Hz)	V _{mic} (dBV)	V _{acc} (dBV)	phase (deg)	Π_{elec} (mW)	Π_{off} (mW)	I _{rms} (mA)
375.0	-35.28	-10.51	-178.0	1.6	1.0	3.2
400.0	-32.05	-10.04	-177.4	2.1	1.2	7.6
420.0	-29.68	-9.82	-175.5	2.5	1.1	11.0
440.0	-25.32	-9.73	-175.0	3.2	1.2	14.1
450.0	-22.62	-9.76	-172.7	3.2	1.1	15.6
460.0	-18.73	-9.93	-167.7	3.8	1.0	17.2
465.0	-15.93	-10.17	-161.8	4.1	1.2	18.2
470.0	-12.14	-10.79	-147.6	4.5	1.0	18.9
472.0	-10.36	-11.27	-135.4	4.8	1.0	18.8
474.0	-8.74	-11.78	-114.6	4.9	1.1	17.8
475.6	-8.00	-11.78	-91.31	4.6	1.0	16.1
478.0	-8.57	-10.80	-58.04	3.7	1.0	13.5
480.0	-10.18	-10.06	-40.94	3.5	1.0	15.6
485.0	-14.54	-9.41	-22.39	3.3	0.9	15.2
495.0	-20.49	-9.33	-11.73	3.6	0.9	17.8
515.0	-27.06	-9.42	-6.35	4.4	0.9	20.3
530.0	-30.33	-9.50	-5.00	4.8	0.9	21.6
550.0	-33.71	-9.56	-3.91	5.3	0.9	22.7

between pressure and volume velocity in the vicinity of tube resonance. The relationship (as given by Hofler) is

$$Q = (f_o/2) (d\phi/df) |_{f_o} \quad (IV-2)$$

where ϕ is in radians.

Using a constant source voltage of 0.26 V_{rms}, the average electric power input to the driver never exceeded 5 mW during the entire experiment in order to prevent damage to the voice coil and titanium surround of the driver. The maximum measured electroacoustic efficiency was about 38% and occurred when the system was driven at 478 Hz. In the vicinity of the driver resonance (350 Hz) the efficiency was only about one percent, indicative of a large acoustic impedance mismatch between the driver and resonator under those operating conditions (as expected). In comparison the maximum efficiency determined by the model was about 51% and occurred at 480 Hz. Graphical comparison of measured electric power, acoustic power, and electroacoustic efficiency to the theoretical values showed that the model was a reasonable approximation to reality. Measured values appeared to follow the theoretical curves quite well, but tended to have smaller magnitudes. The results are graphically depicted in Figures IV-5 to IV-7.

The final experiment conducted with the straight tube was to measure the electroacoustic efficiency at tube resonance for a number of different gas mixtures at one bar.

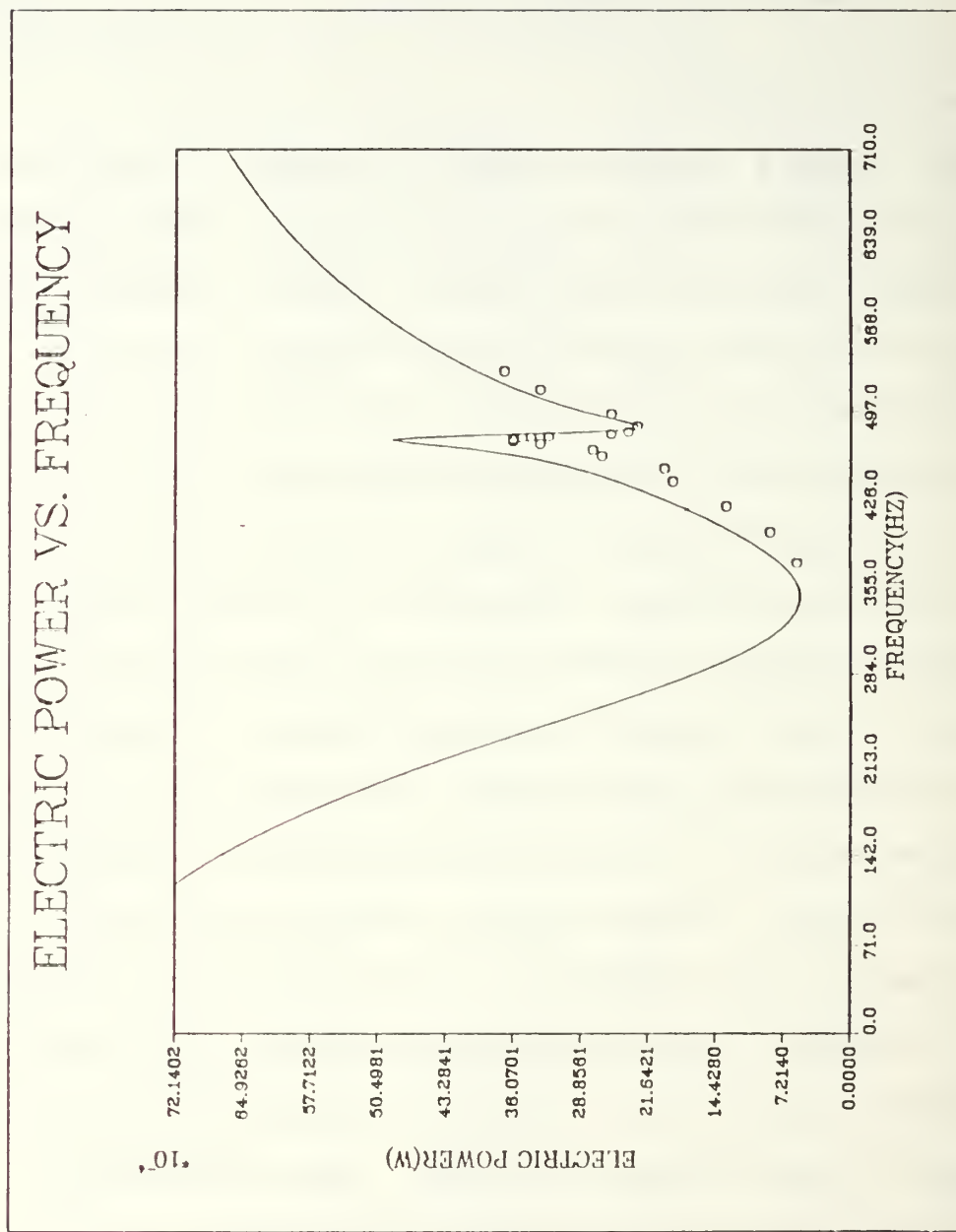


Figure IV-5. Predicted and Measured Electric Power for the Straight Tube at One Bar

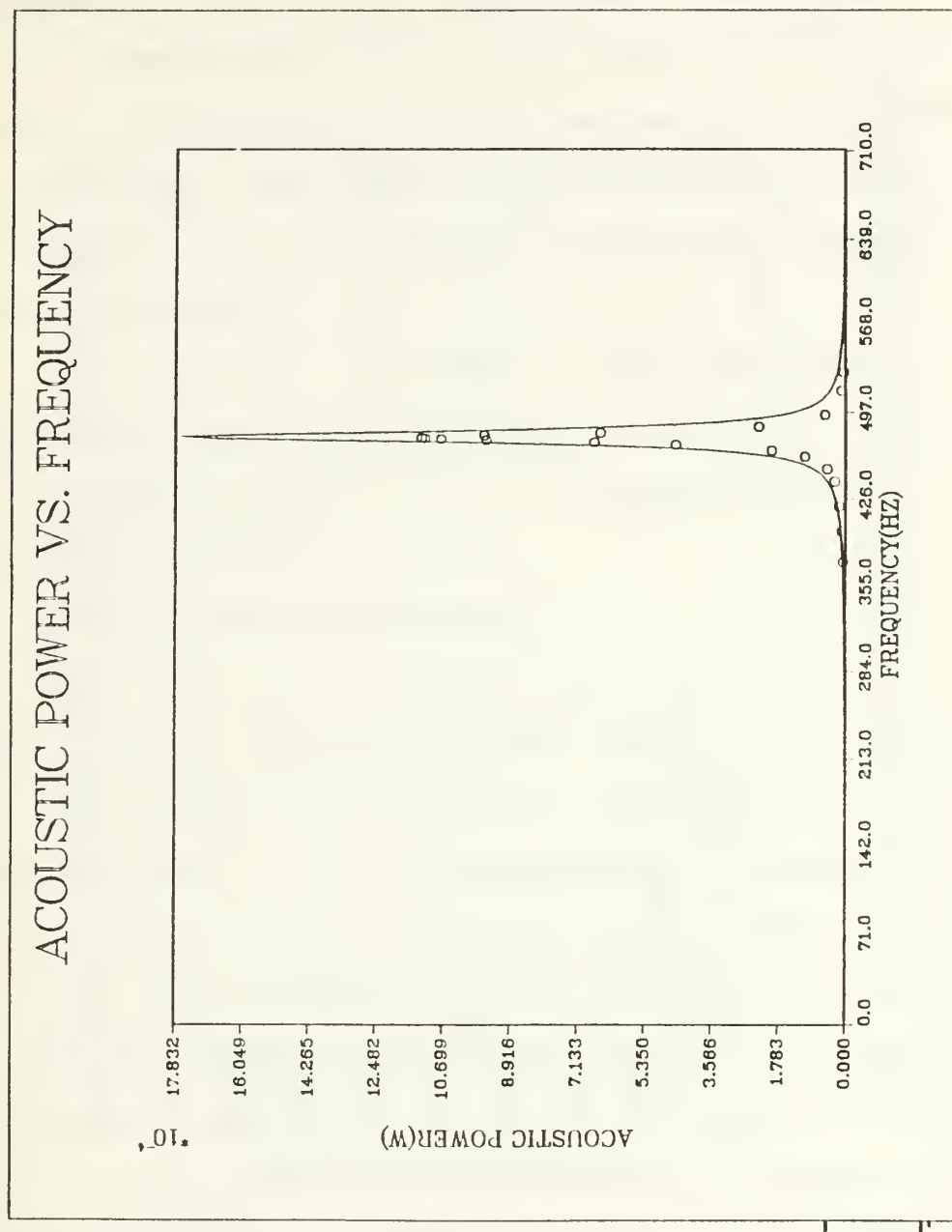


Figure IV-6. Predicted and Measured Acoustic Power for the Straight Tube at One Bar

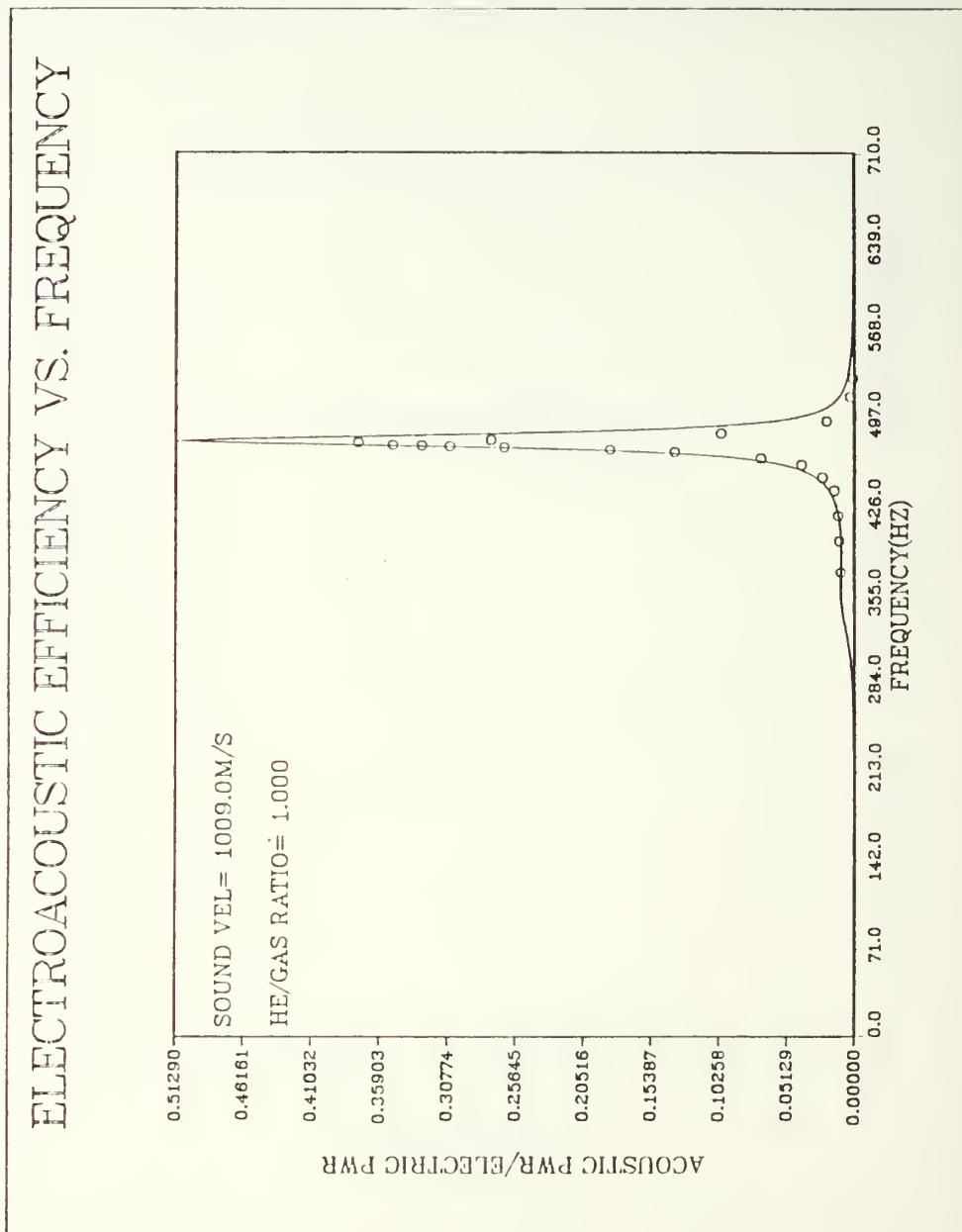


Figure IV-7. Predicted and Measured Electroacoustic Efficiency for the Straight Tube at One Bar

Ideally, the maximum efficiency would occur when the resonance frequencies of the driver and tube were the same. The results are presented in Figure IV-8. The highest efficiency measured was 50.8% at 359.4 Hz (3% off driver resonance) and was achieved using a helium-argon gas mixture (with <18.85% Ar). The lowest efficiency occurred when pure helium was used since this created the greatest mismatch of resonance frequencies.

With reasonable confidence in both measurement techniques and theory, the next phase of testing for the STAR driver involved the use of a refrigerator-type resonator pressurized to 10 bars.

2. Refrigerator-Type Resonator

This resonator consisted of two tubes having different diameters that were joined together with a tapered section that smoothed the transition from larger to smaller diameter (see Figure IV-9). The resonator was attached to the driver via a flanged section that was integral to the larger tube. A cylindrical section was attached to the end of the smaller diameter tube thereby making the resonator a closed system. Additionally a cold heat exchanger was fixed within the resonator at the end of the larger diameter section (just before the tapered section). Since the aim of the experiment was to estimate driver performance under simulated operating conditions, this refrigerator-type resonator is a good facsimile of the actual STAR resonator.

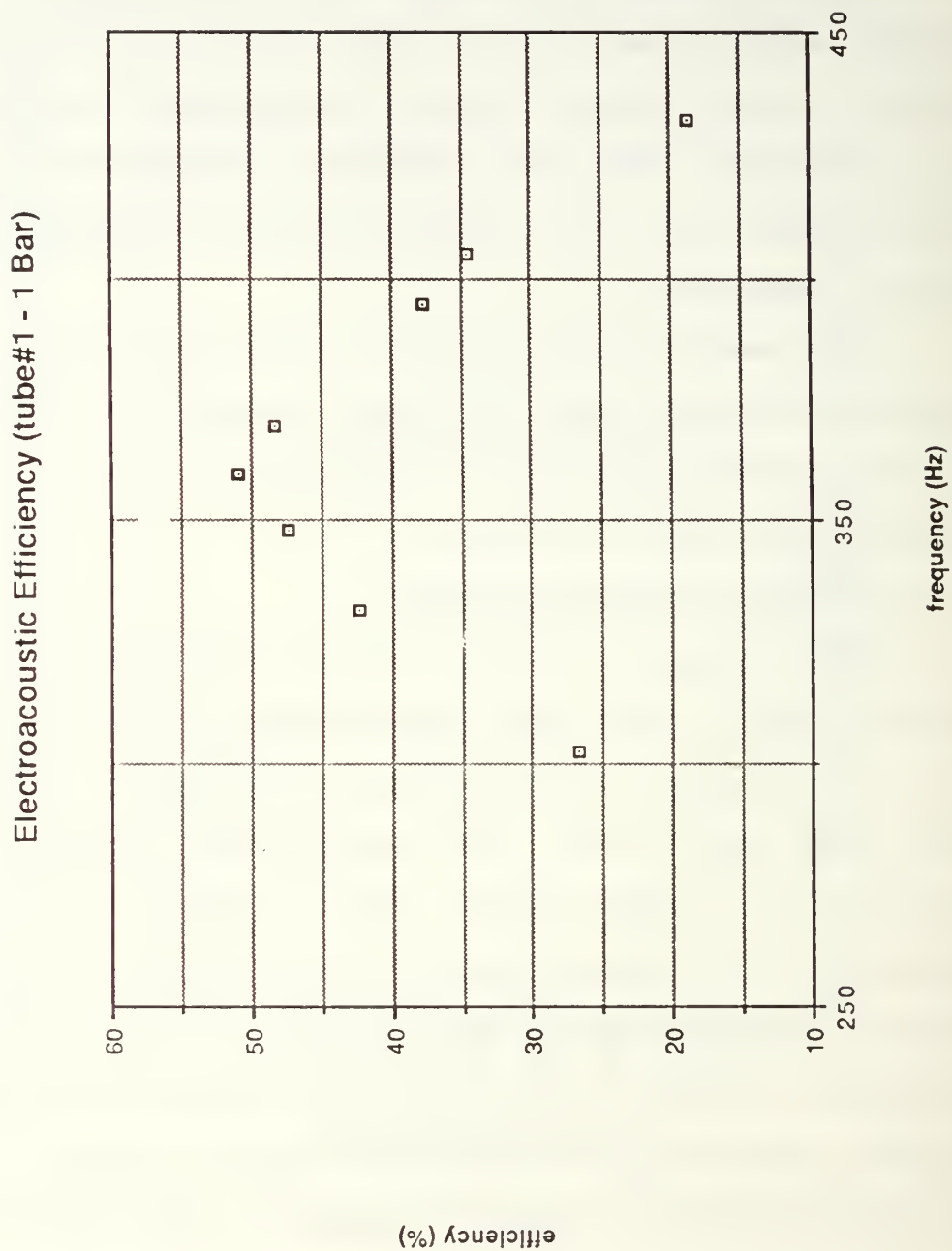


Figure IV-8. Electroacoustic Efficiency as a Function of Tube Resonance for the Straight Tube

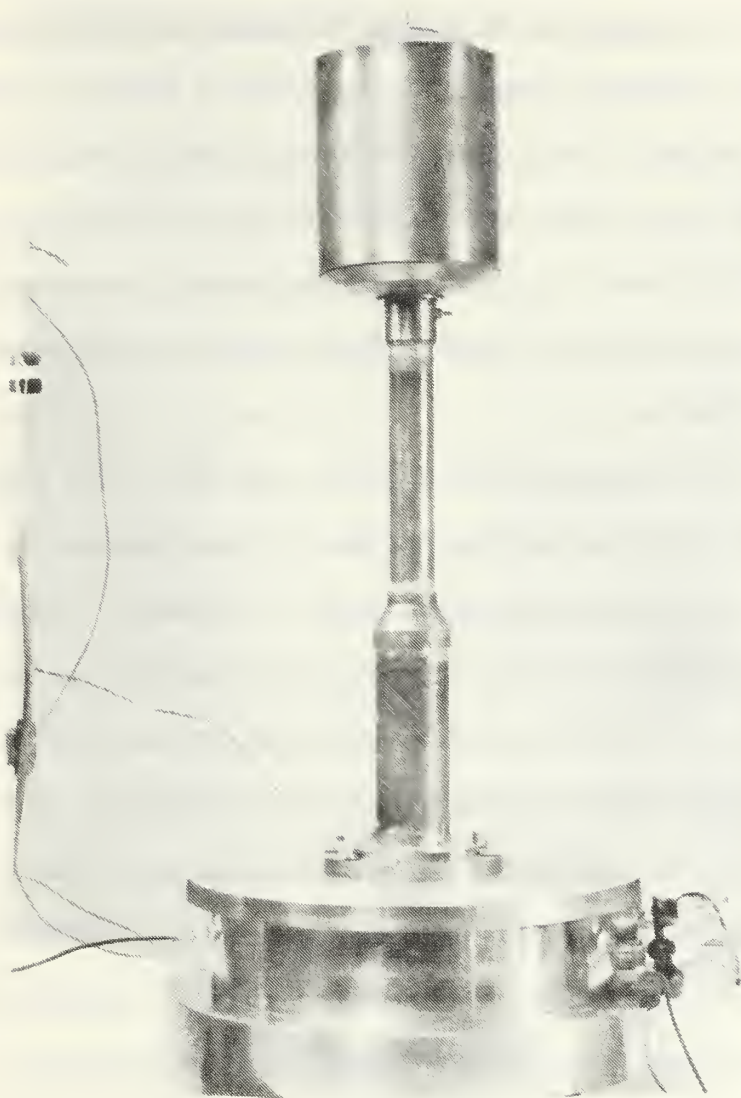


Figure IV-9. Refrigerator-type Resonator

The only difficulty in using this resonator was in determining an expression for its input mechanical impedance (accounting for absorptive processes). This was considered unnecessary and beyond the scope of this thesis and therefore it was assumed that the expression for tube impedance given at the top of Figure IV-4 would suffice for modelling purposes. In using this expression the resonator cross-sectional area (S) was taken to be $1.14 \times 10^{-3} \text{ m}^2$ corresponding to that of the larger diameter resonator section. The absorption coefficient was the same as previously defined.

With the resonator mounted in place, the system was pressurized to 10 bars with helium. Under these conditions the maximum possible tube resonance frequency could be achieved. The primary reason for beginning with pure helium was that gas characteristics like sound speed and density were readily available.¹⁷ Knowledge of these values for a given ambient temperature permits easy calculation of sound speeds and densities for unknown gas mixtures (assuming constant temperature and constant ratio of heat capacities) from the following relationship,

$$\rho_{\text{gas}} = (C_{\text{He}}/C_{\text{gas}})^2 \rho_{\text{He}} \quad (\text{IV-3})$$

Additionally, measurement of the tube resonance frequency in pure helium allows one to readily determine the effective

length of the resonator. Numerically this is given as

$$L_{\text{eff}} = c / (2f_o) \quad (\text{IV-4})$$

where the effective length is equal to one half of the wavelength. Since the computer model requires accurate values for gas density, sound speed, and effective resonator length in order to predict driver performance, it follows that taking a set of measurements in a known (pure) medium first is imperative if the simulation is to have any value.

In pure helium at 10 bars (with an ambient temperature of 21°C), the resonance frequency and quality factor of the tube were determined to be 553.6 Hz and 74 respectively. Based on this information it was expected that system efficiency would be minimal due to the difference between driver and tube resonance. Furthermore, it was anticipated that small changes in frequency would constitute large changes in efficiency due to the large quality factor. These system characteristics were verified upon examination of the measured data. With the electric power to the driver kept below 40 mW (constant drive voltage of 0.25 V_{rms}), the maximum measured electroacoustic efficiency was about 34% at 570 Hz. Of interest is that when the system was driven at tube resonance (only 16 Hz below 570 Hz) the efficiency was down by a factor of two indicative of the effects of a resonator having a large

quality factor. At driver resonance (350 Hz) the system efficiency was only about 2%. The measured and modelled performance characteristics of the system are depicted in Figures IV-10 to IV-12. The "HE/GAS RATIO" of 1.0 in Figure IV-12 represents a ratio of the density of helium at 10 bars to the density of the gas mixture used in the experiment. Though this is trivial for this first experiment it is a convenient means of comparison when various helium-argon gas mixtures are used later.

In all three plots the agreement with theory is quite satisfactory especially when considering the low power levels at which the system was driven. Note in Figure IV-10 that there are two dips and a peak in the electric power over the given frequency range. The first dip occurs at a frequency where the system mechanical impedance is at a relative minimum permitting a maximum displacement of the bellows and voice coil. The motion of the voice coil in the permanent magnetic field of the driver results in the generation of a large back emf. The net result is that the electrical impedance becomes a relative maximum thus reducing the input electric power. The small peak occurs in the vicinity of the tube resonance. At this frequency the mechanical impedance of the system is at a relative maximum effectively blocking the motion of the bellows/coil. As a result the back emf produced is at a relative minimum

ELECTRIC POWER VS. FREQUENCY

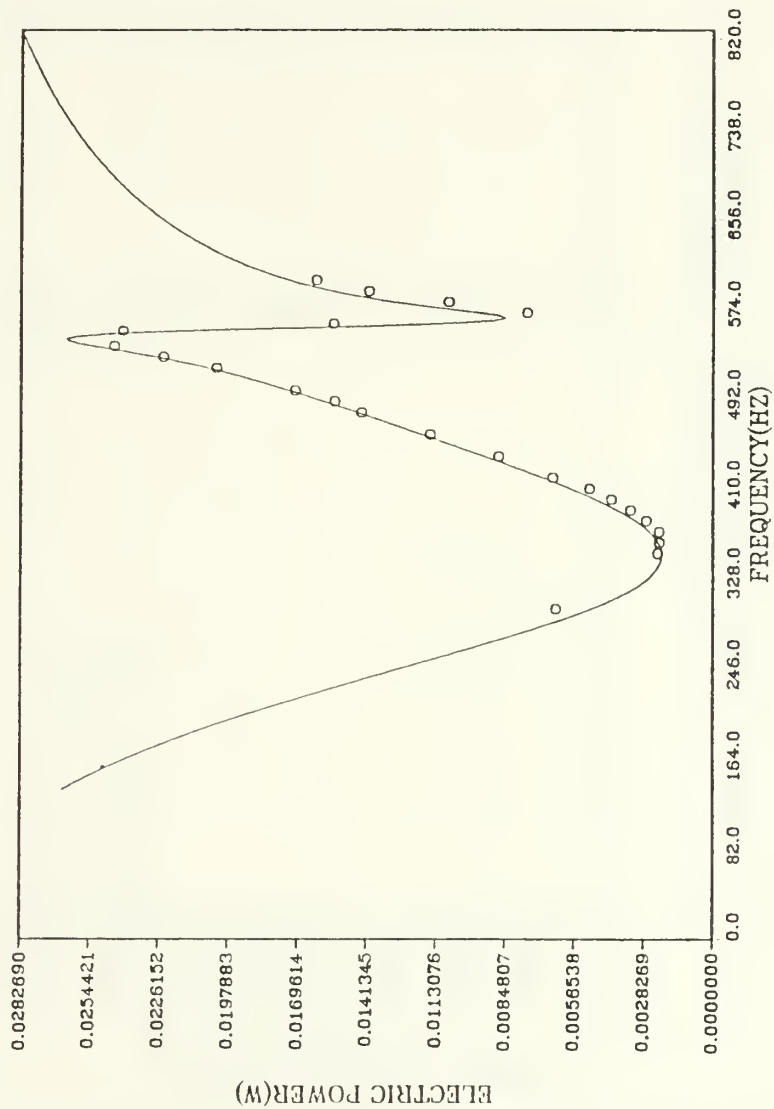


Figure IV-10. Measured and Predicted Electric Power for the Refrigerator-like Resonator in 10 Bar Helium

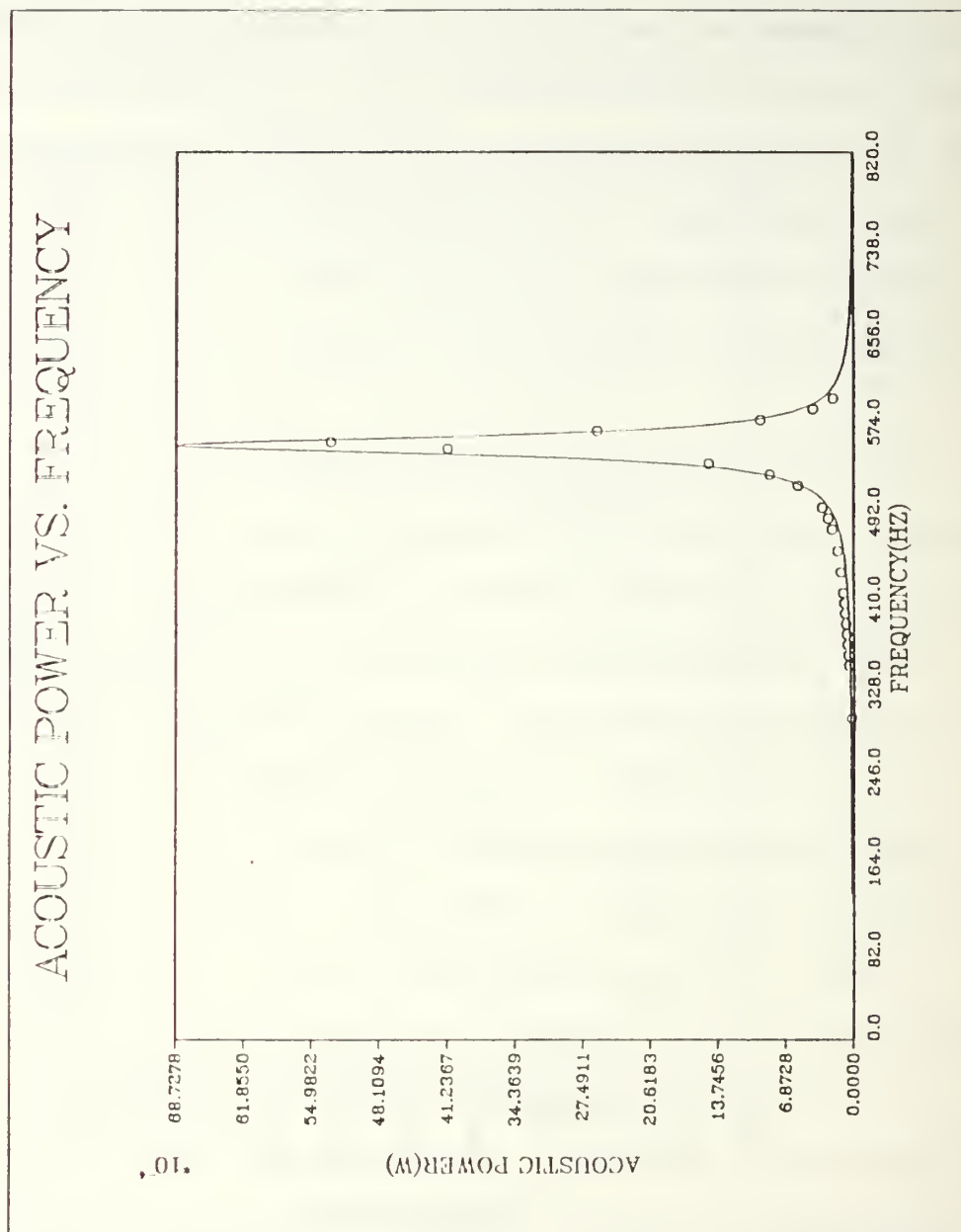


Figure IV-11. Measured and Predicted Acoustic Power for the Refrigerator-like Resonator in 10 Bar Helium

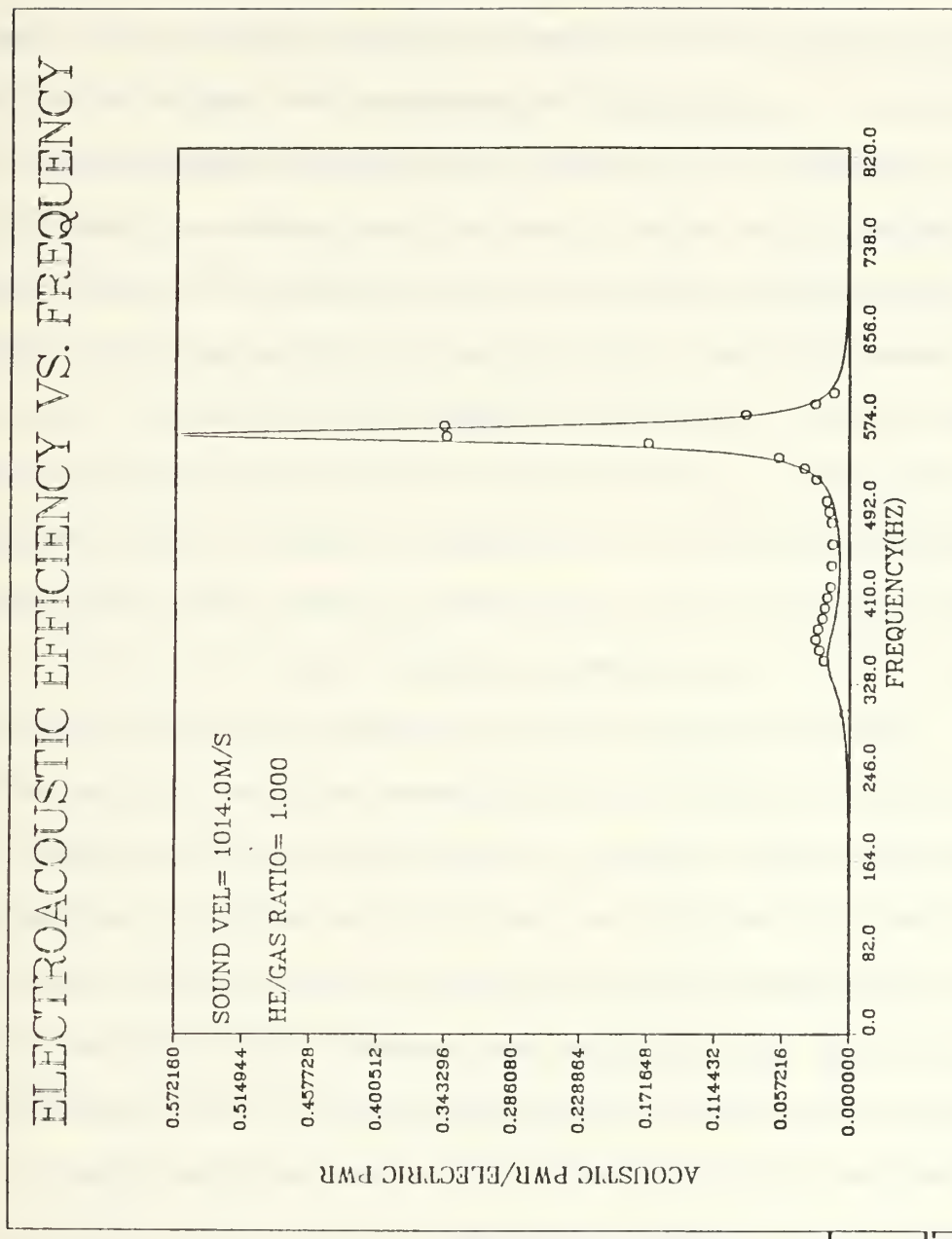


Figure IV-12. Measured and Predicted Electroacoustic Efficiency for the Refrigerator-like Resonator in 10 Bar Helium

meaning that more current can flow to the driver thus increasing the input electric power.

Turning one's attention to Figure IV-11 it is apparent that maximum acoustic power occurs at the tube resonance frequency and decreases as the system is driven off resonance. This makes sense since maximum dissipation of energy in the tube occurs at its resonance frequency. By combining the results shown in Figures IV-10 and IV-11 the electroacoustic efficiency is nothing more than the ratio of the two individual power measurements. Note in Figure IV-12 that the ratio of acoustic to electric powers yields not one but two efficiency peaks over the frequency range. One is due to a minimum electric power while the other is due to a maximum acoustic power.

For the next set of measurements, the system was partially vented and then repressurized to 10 bars with a helium-argon gas mixture. The effect of this "doping" was to decrease the speed of sound in the acoustic medium in order to decrease the resonance frequency of the tube. This was done in an attempt to better match the tube and driver resonances in order to improve overall system performance and because this simulates the actual refrigerator operation. The doping resulted in a new tube resonance frequency of 511.6 Hz and quality factor of 77. At resonance the electroacoustic efficiency was about 16%, less than half the 36% measured at 520 Hz. Again the effects of

the large quality factor are observed. Figure IV-13 compares the measured efficiency with that modelled and again there is good agreement between the two. Notice how the smaller efficiency peak has increased somewhat in magnitude under the new operating conditions.

The system was doped with the helium-argon gas mixture four more times and resulted in the measured values shown in Figures IV-14 to IV-17. The modelled efficiencies become more and more dissimilar to those measured as the driver and tube resonances approach each other. At the same time the overall system efficiency decreases. As the two efficiency peaks change in magnitude it appears that what one loses the other gains. Driver and tube resonances are nearly matched when the peaks are roughly equal in magnitude. The only redeeming quality of this feature is that instead of having a sharp peak, the efficiency is almost flat over a broader frequency range. This is highly desirable for the STAR so that frequency fluctuations due to temperature changes will not impose any major limitations. Ideally with the STAR however, one would expect efficiencies in this flat region to be significantly better than the 10 to 15 percent measured under the above operating conditions.

A final set of measurements was taken after purging the system and refilling it to 10 bars with the helium-argon gas used previously to dope the system. This particular gas mixture consisted of 18.85% argon and resulted in the lowest

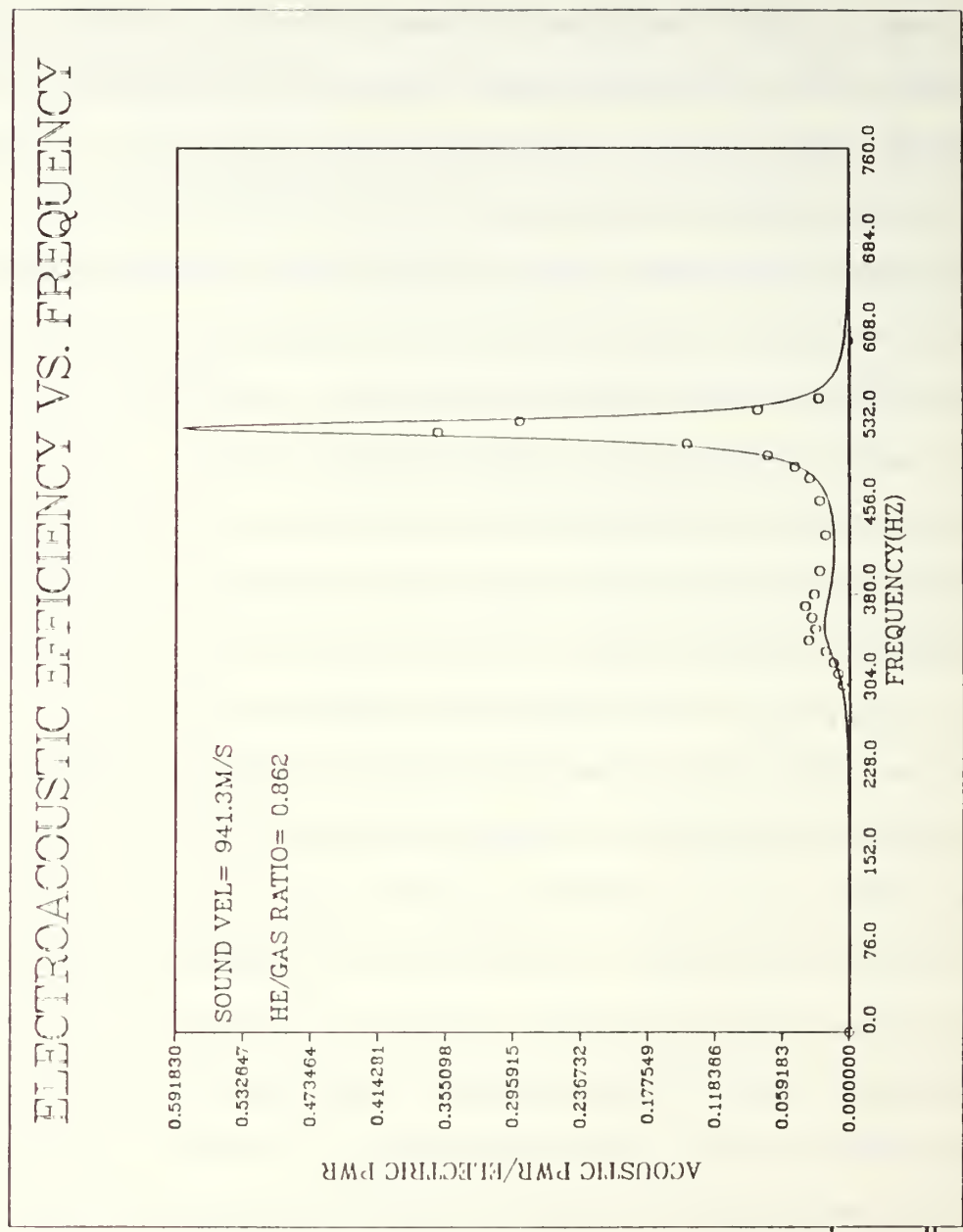


Figure IV-13. Measured and Predicted Electroacoustic Efficiency for the Refrigerator-like Resonator ($f_0=511.6$ Hz)

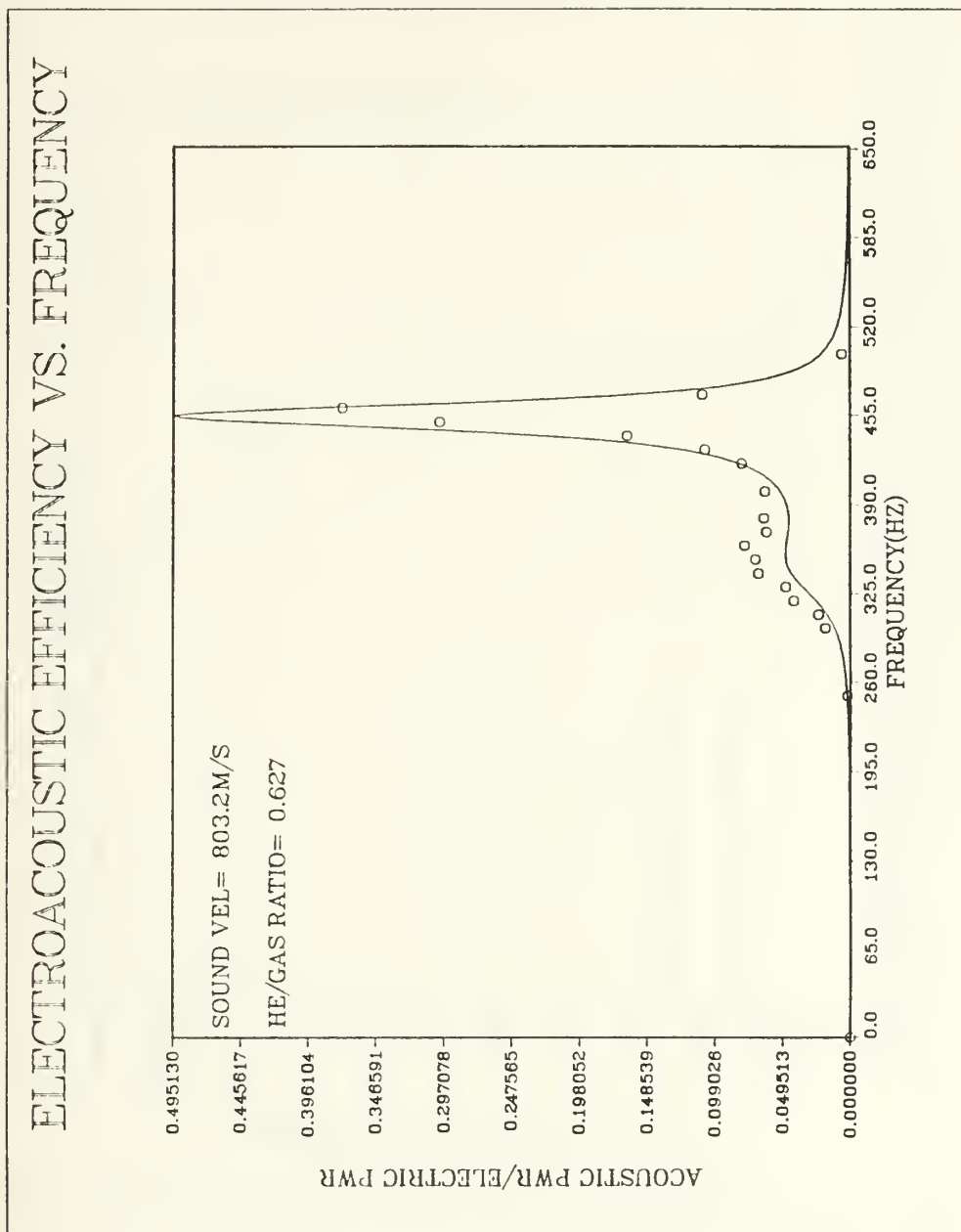


Figure IV-14. Measured and Predicted Electroacoustic Efficiency for the Refrigerator-like Resonator ($f_0=436.5$ Hz)

ELECTROACOUSTIC EFFICIENCY VS. FREQUENCY

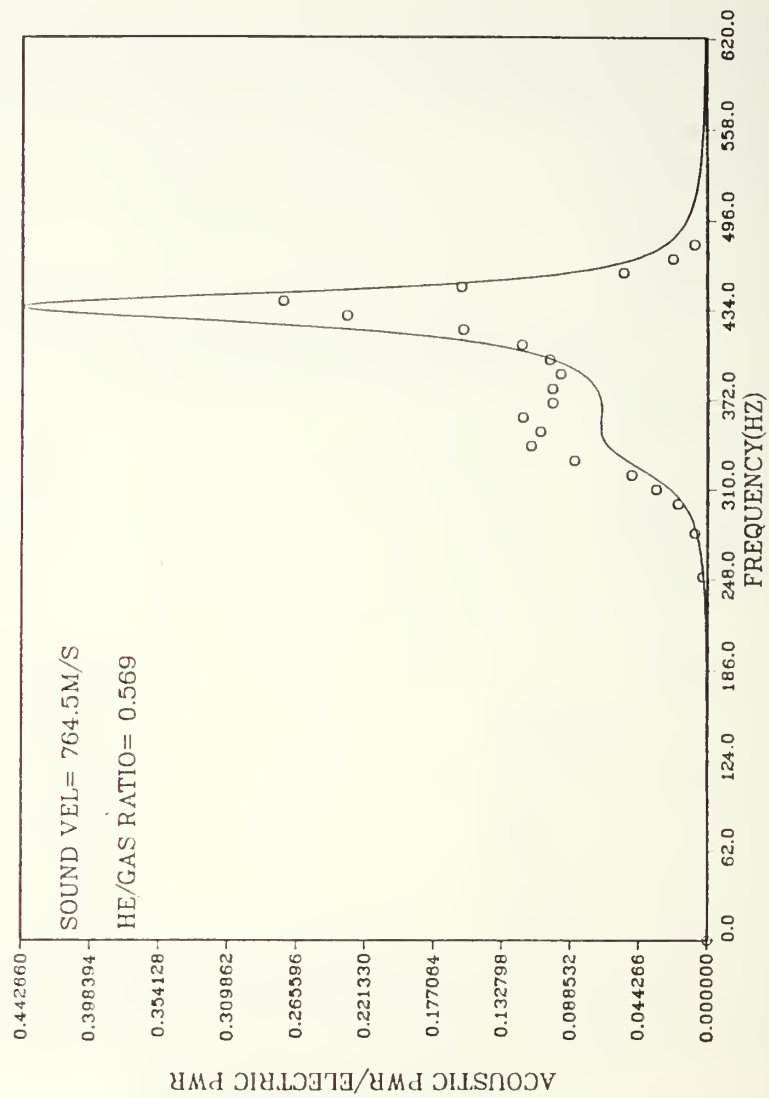


Figure IV-15. Measured and Predicted Electroacoustic Efficiency for the Refrigerator-like Resonator ($f_0=415.4$ Hz)

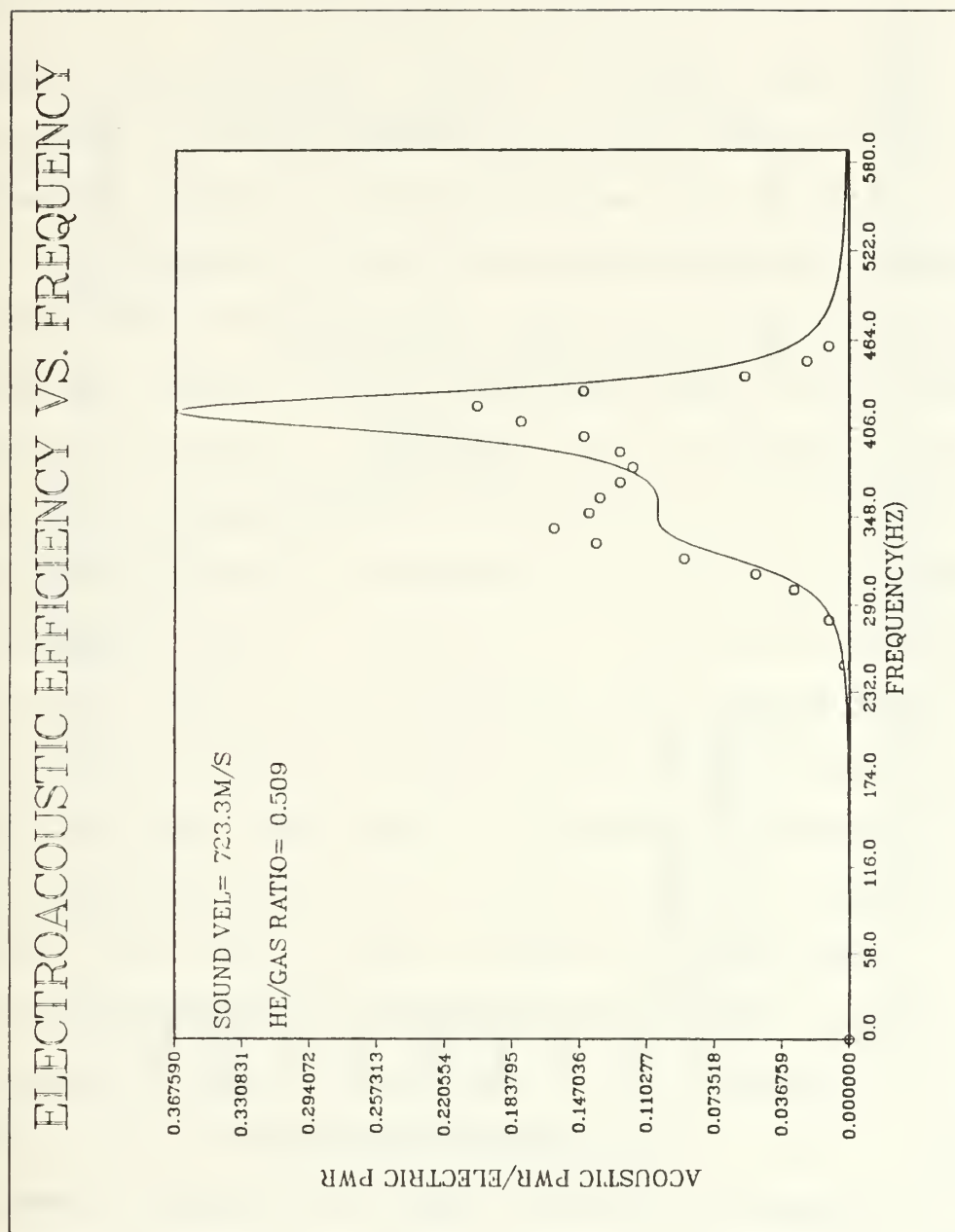


Figure IV-16. Measured and Predicted Electroacoustic Efficiency for the Refrigerator-like Resonator ($f_0=393.1$ Hz)

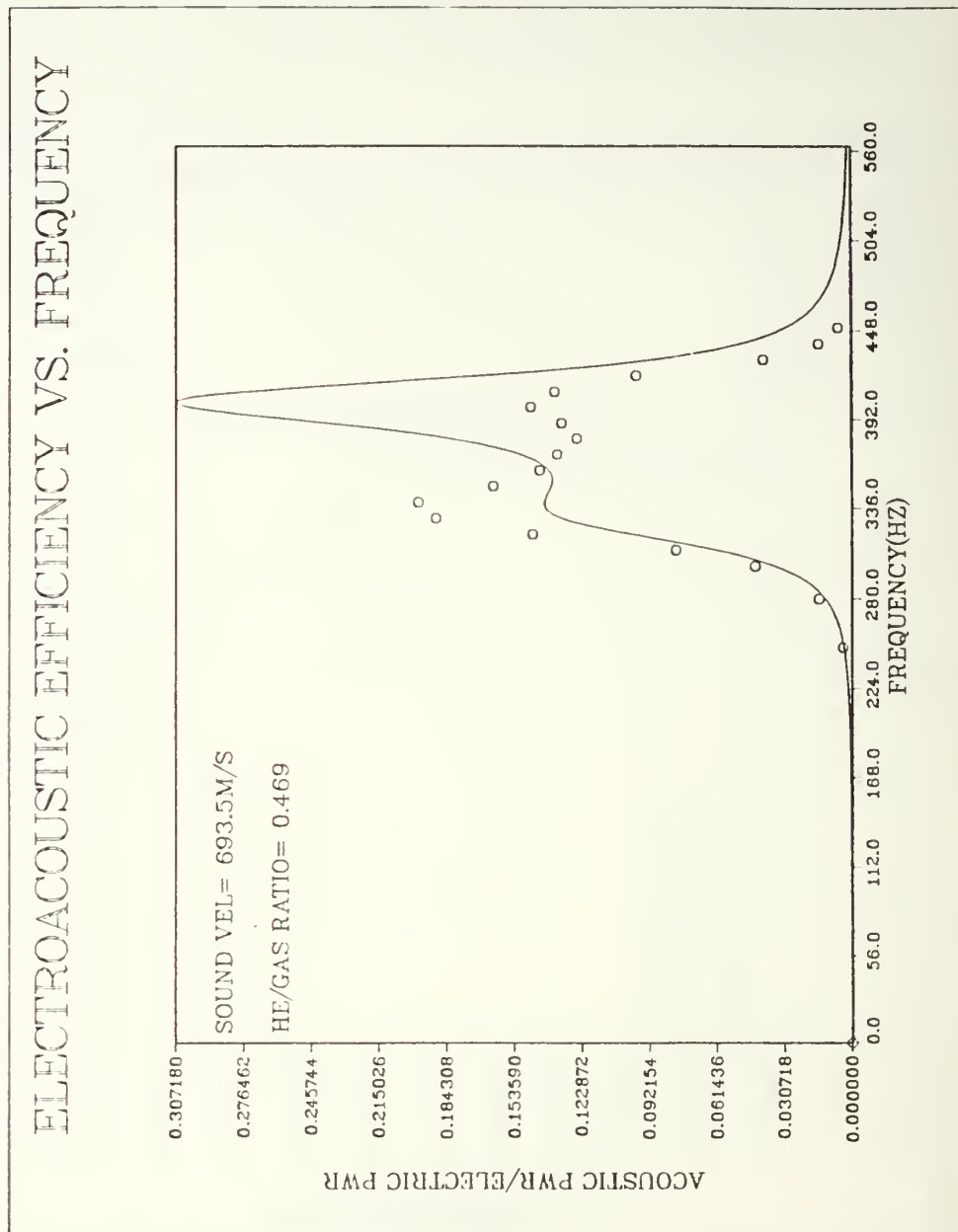


Figure IV-17. Measured and Predicted Electroacoustic Efficiency for the Refrigerator-like Resonator ($f_0=377.1$ Hz)

measured tube resonance (335.3 Hz). The resulting measured and predicted electroacoustic efficiencies are depicted in Figure IV-18. Again there are discrepancies between measured and theoretical values. A maximum measured efficiency of 30% was measured at 310 Hz however this dropped off rapidly to 11% at the tube resonance.

The results of the above measurements are summarized in TABLE IV-2. In particular, the tube resonance frequency and quality factors are recorded along with the electroacoustic efficiency at resonance. Also included in the table are the peak efficiencies (eff peak₁ and eff peak₂) and the corresponding frequencies at which they occurred (f_1 and f_2 respectively). Inspection of these data shows that, unlike the results of the straight tube, maximum efficiency did not occur when the driver and tube resonances were most closely matched. The results of the above experiment were rather disappointing in that maximum measured efficiencies were not very high and that a number of unexplained discrepancies between measurements and theory existed. It is unclear at this time why many of the predicted efficiencies differed from those measured in the vicinity of the peaks. Possibly the model is severely degraded by high Q resonators or perhaps the assumption pertaining to the modelled resonator impedance is invalid.

Whatever the case, the next experiment to be conducted was to install a prototype stack and a crude hot

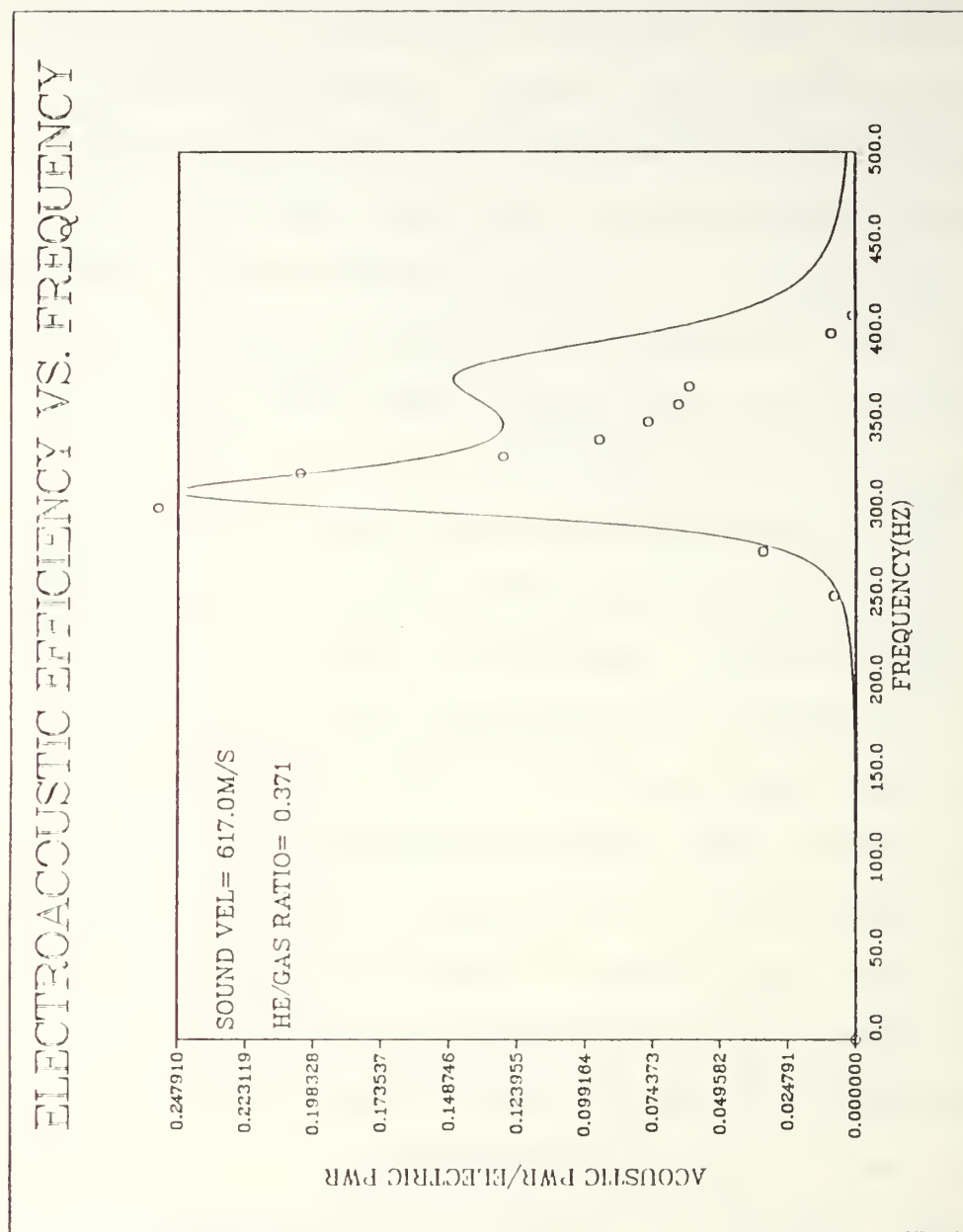


Figure IV-18. Measured and Predicted Electroacoustic Efficiency for the Refrigerator-like Resonator in 10 Bar He-Ar (18.85% Ar)

TABLE IV-2. SUMMARY OF MEASUREMENTS FOR
REFRIGERATOR-TYPE RESONATOR

gas ratio	Q_t	f_0 (Hz)	eff (%)	f_1 (Hz)	eff peak ₁	f_2 (Hz)	eff peak ₂
1.000	74.4	553.6	17.1	370	2.9	570	34.4
0.862	77.6	511.6	16.3	370	3.9	520	36.2
0.627	79.4	436.5	13.6	360	7.7	460	37.1
0.569	75.9	415.4	13.8	360	11.9	440	27.4
0.509	74.9	393.1	12.9	340	16.1	420	20.3
0.469	74.6	377.1	12.4	340	19.7	400	14.6
0.371	83.3	335.3	11.0	310	30.0	---	----

heat exchanger into the refrigerator-type resonator. It was felt that this particular configuration would best represent the actual STAR resonator and would therefore serve to provide the most realistic driver performance data.

3. Refrigerator-Type Resonator with Stack

There was a keen interest to see what effects would occur if an actual thermoacoustic stack was installed into the resonator of the previous section, since this would actually simulate the refrigerator. It was expected that when configured in this manner, the quality factor of the resonator would be much lower due to greater losses and thus the acoustic load impedance would be much lower. The

electroacoustic efficiency is expected to depend on the magnitude of the acoustic load impedance. By lowering the quality factor the system performance would be less sensitive to variations in frequency, especially when driver and tube resonances coincide.

The experimental procedures of the previous section were repeated beginning with a set of measurements in pure helium at 10 bars. The input electric power was again kept below 5mW for the same reasons as previously described. The quality factor of the resonator was reduced to 11 by adding the stack and heat exchanger. Figure IV-19 shows the measured and theoretical values of the electroacoustic efficiency over a frequency range spanning the tube resonance of 557.6 Hz. It is interesting to note the difference between these pure helium measurements and those of the last section (Figure IV-12). In Figure IV-19 there are clearly two distinct efficiency peaks neither of which is as sharp as the the one shown in Figure IV-12. Additionally the relative difference between peak efficiencies is much less with the low Q resonator. Although the maximum measured efficiency was higher when the resonator was not configured with a stack, analysis of system performance measured over the given frequency range shows that higher efficiencies exist off resonance. Finally, as in Figure IV-11, the predicted efficiencies show reasonably good agreement with those measured.

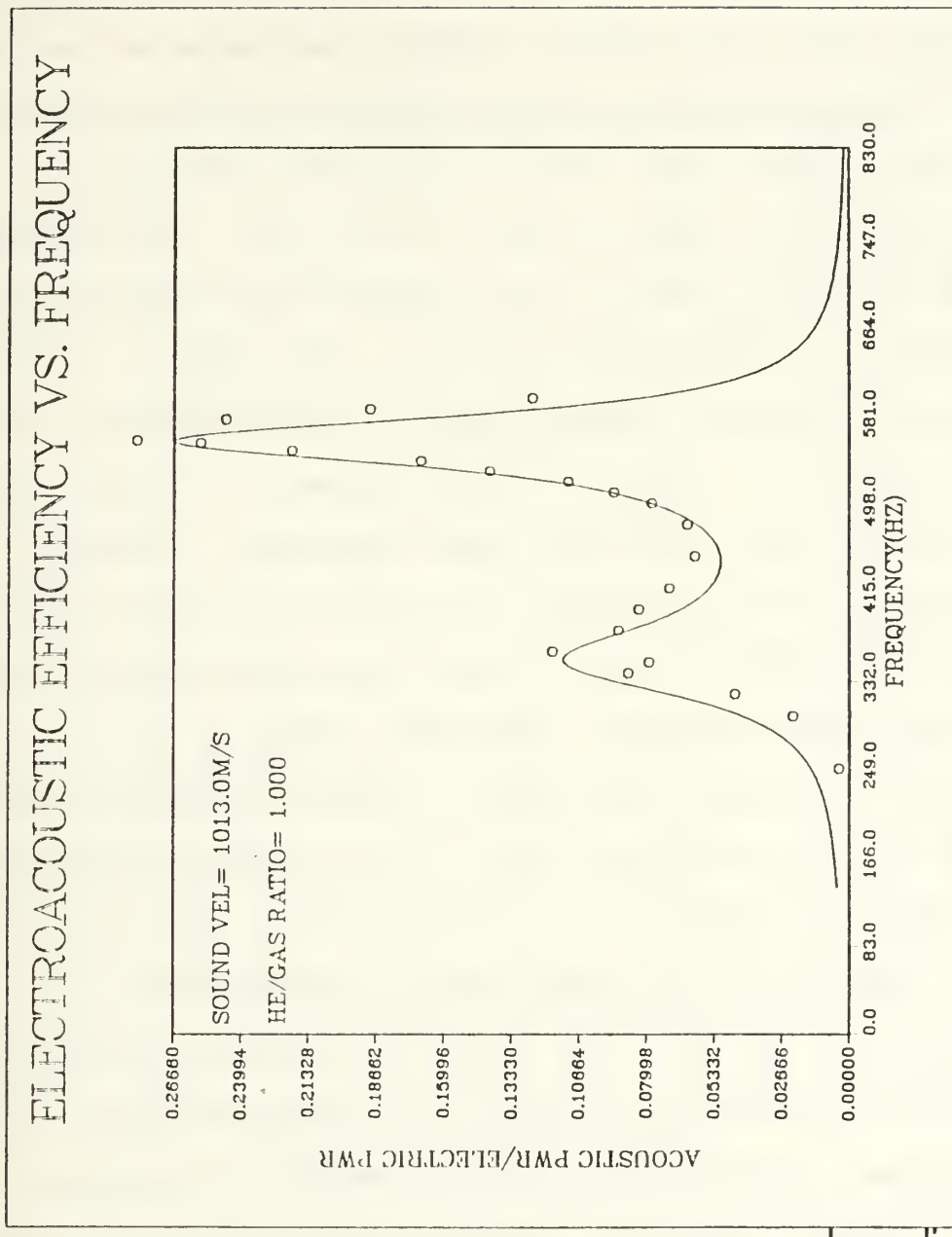


Figure IV-19. Measured and Predicted Electroacoustic Efficiency for the Resonator with Stack in 10 Bar Helium

The system was doped with a helium-argon gas mixture (18.85% Ar) lowering the tube resonance frequency to 493.1 Hz. After taking a set of measurements this procedure was repeated three more times. Finally the system was purged and re-pressurized to 10 bars with the 18.85% Ar gas mixture for one last data set. At this point the resonance frequency of the tube was down to 341.5 Hz. The performance of the system for each of the different gas mixtures is depicted in Figures IV-20 to IV-24. The effect of adding the stack, thereby lowering the Q, is very apparent. The first noticeable feature in every figure is how well the predicted values agree with those measured. Another noticeable feature is that as the tube and driver resonances approach each other the two efficiency peaks slowly combine to form a broad plateau. The best example of this is depicted in Figure IV-23 where a minimum electroacoustic efficiency of 40% occurs over a 100 Hz band of frequencies. The resonance frequency in this particular case was 366.3 Hz (less than 5% off the experimentally-determined driver frequency of 350 Hz). The effect of matching resonances is graphically-depicted in Figure IV-25 where efficiency is plotted as a function of the tube resonance frequency. A broad region of moderately high efficiencies is observed to occur in the vicinity where the driver and tube resonances are close. These results are most satisfactory and are

ELECTROACOUSTIC EFFICIENCY VS. FREQUENCY

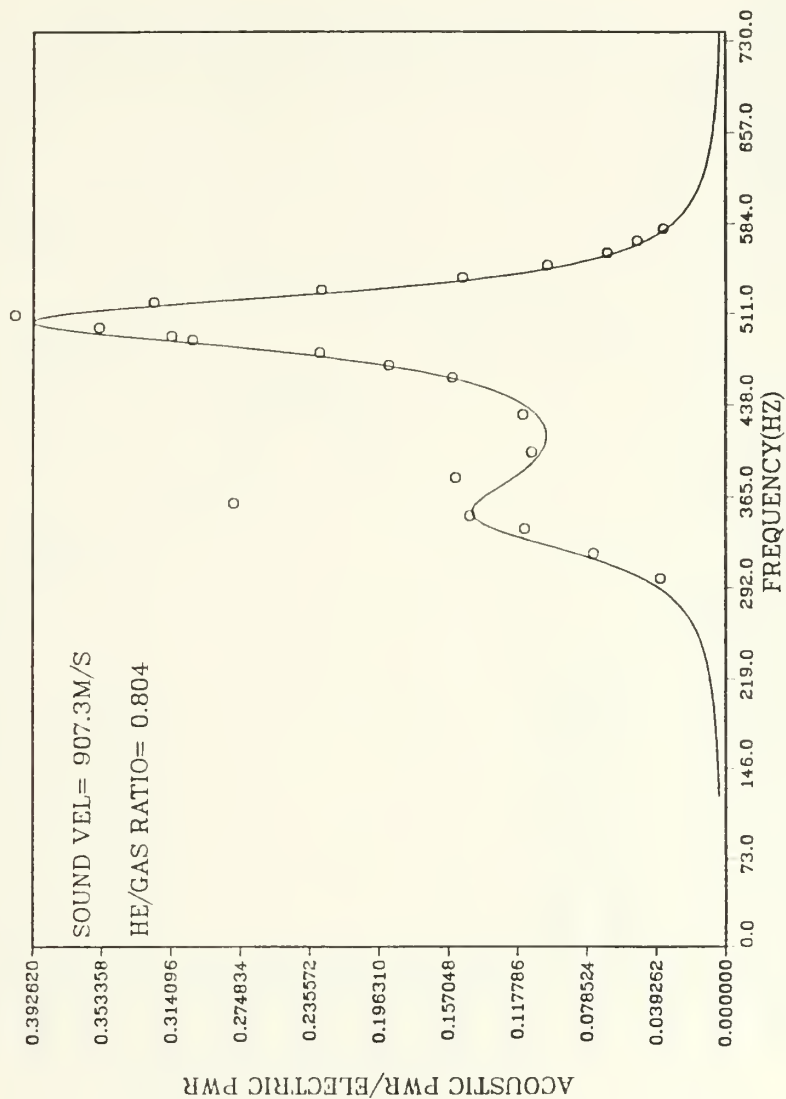


Figure IV-20. Measured and Predicted Electroacoustic Efficiency for the Resonator with Stack ($f_o = 493.1$ Hz)

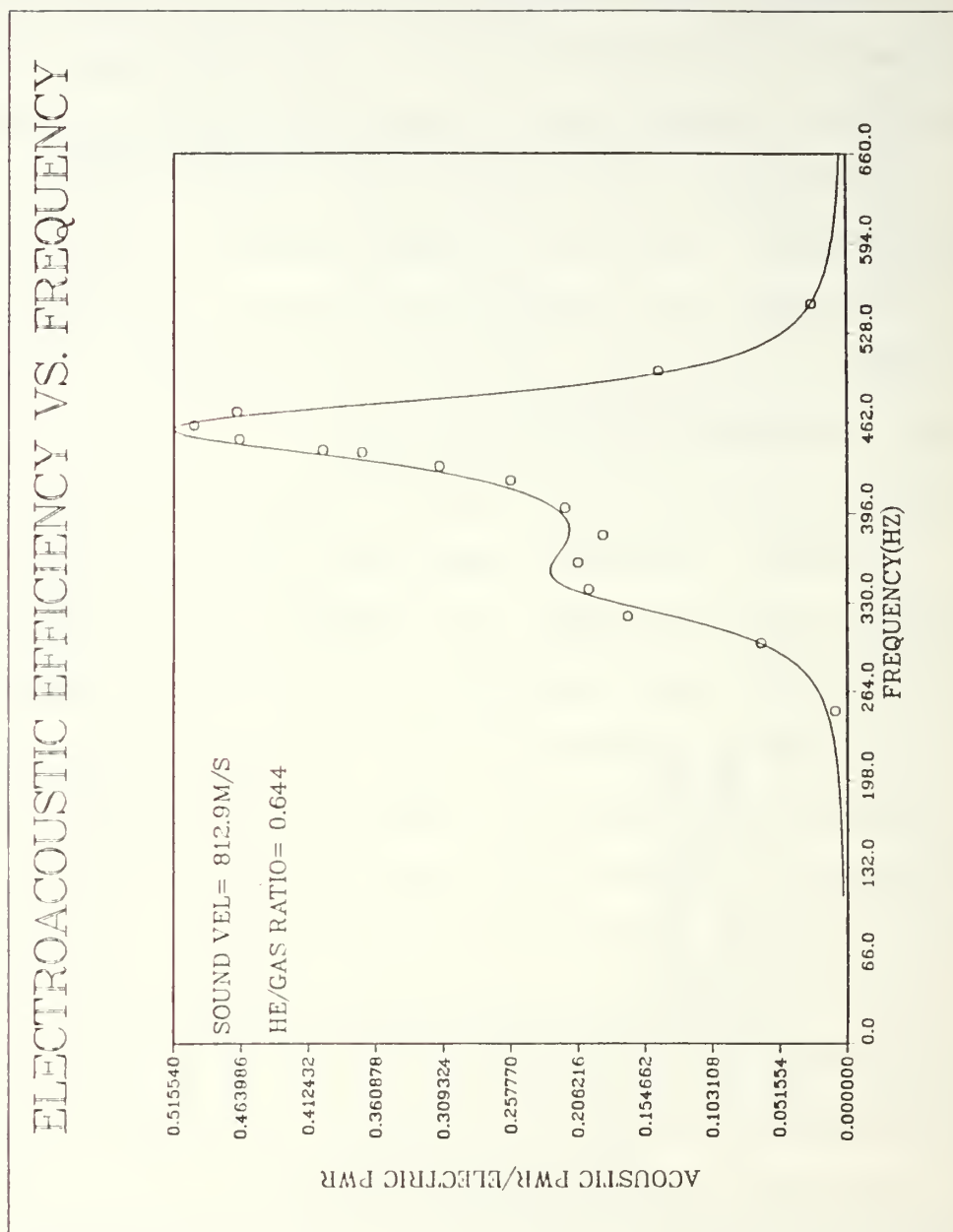


Figure IV-21. Measured and Predicted Electroacoustic Efficiency for the Resonator with Stack ($f_o = 441.8$ Hz)

ELECTROACOUSTIC EFFICIENCY VS. FREQUENCY

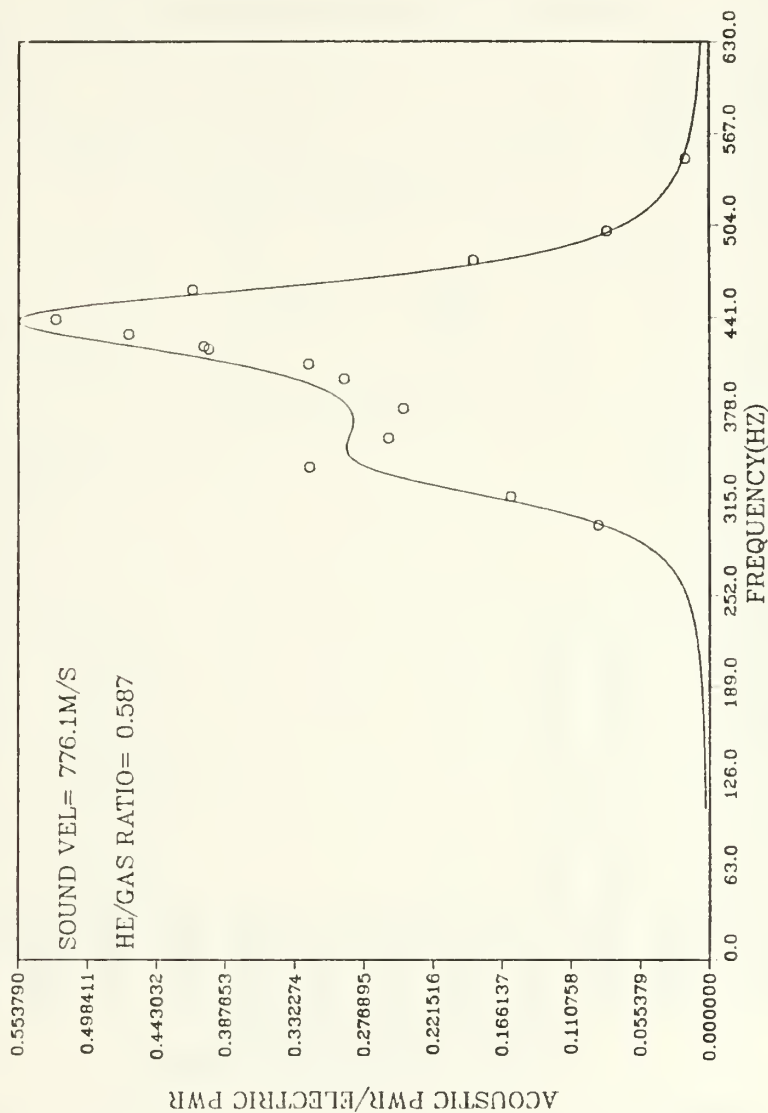


Figure IV-22. Measured and Predicted Electroacoustic Efficiency for the Resonator with Stack ($f_o = 421.8$ Hz)

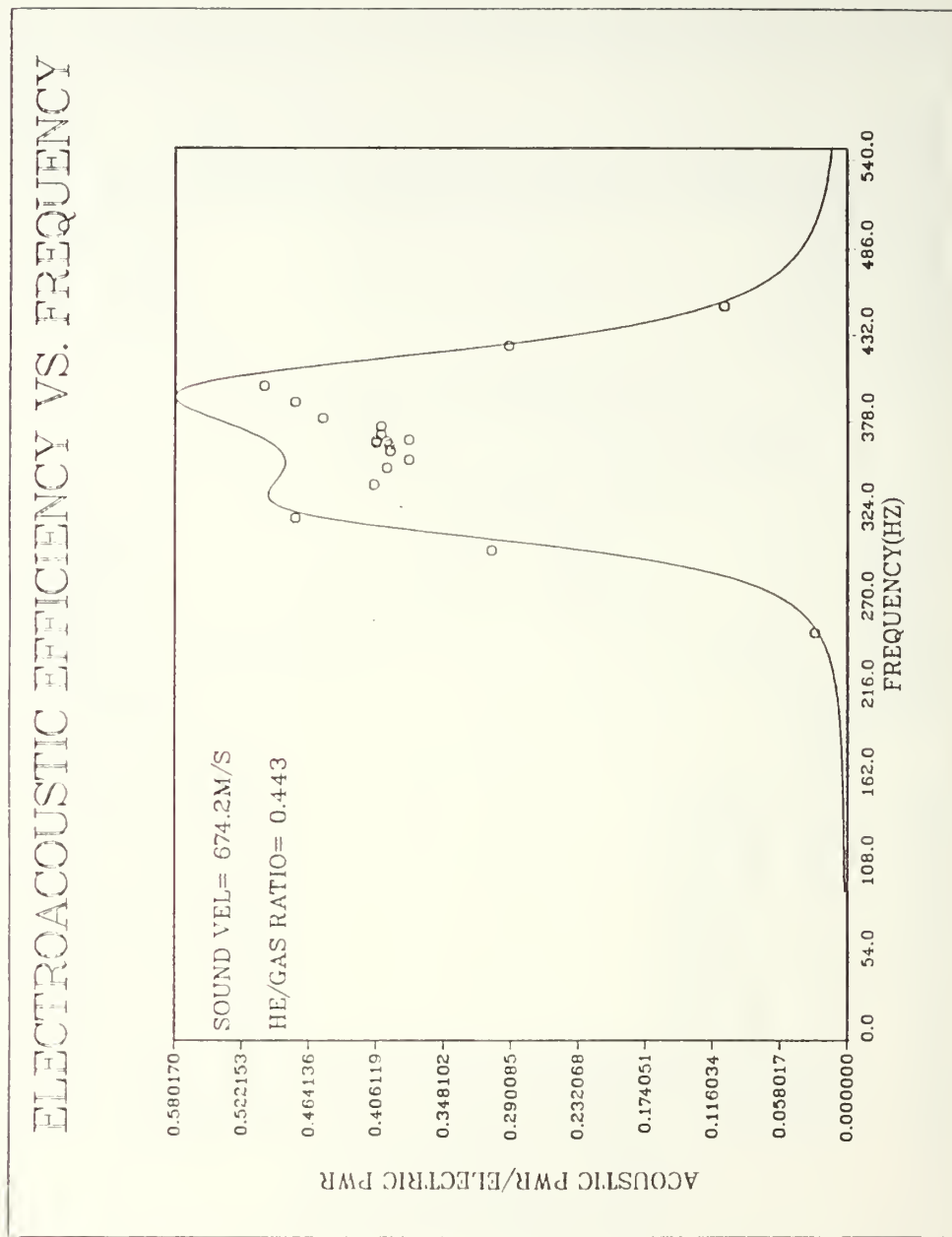


Figure IV-23. Measured and Predicted Electroacoustic Efficiency for the Resonator with Stack ($f_0 = 366.3$ Hz)

ELECTROACOUSTIC EFFICIENCY VS. FREQUENCY

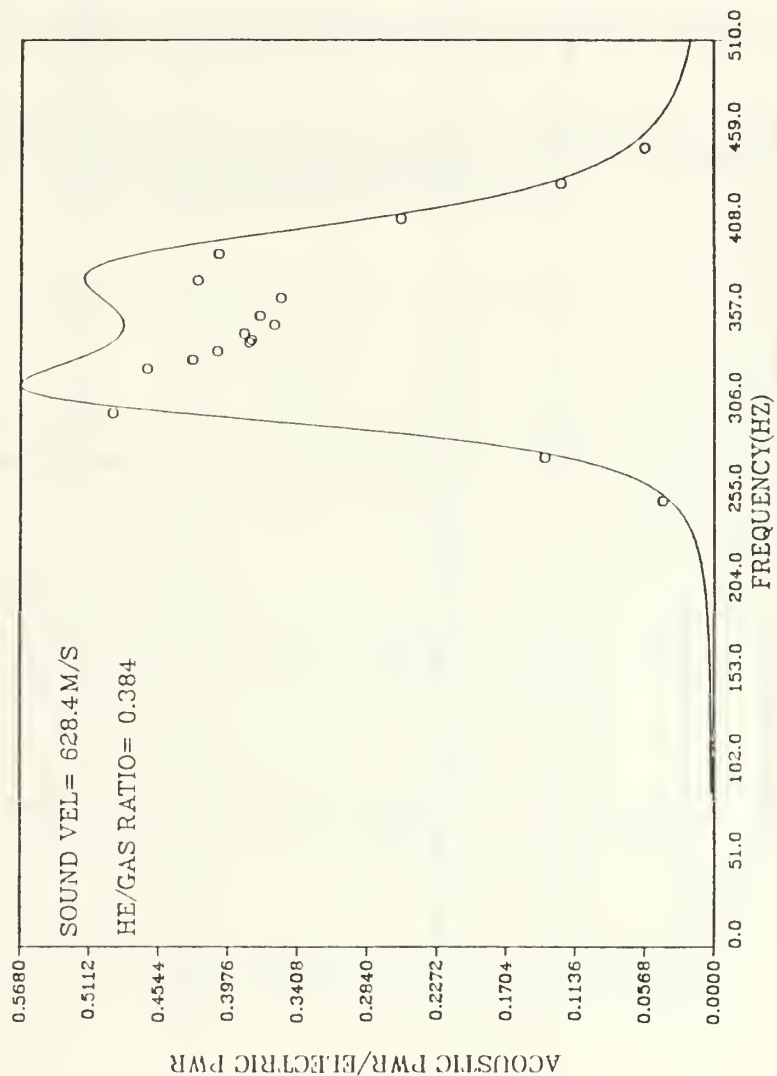


Figure IV-24. Measured and Predicted Electroacoustic Efficiency for the Resonator with Stack in 10 Bar He-Ar (18.85% Ar)

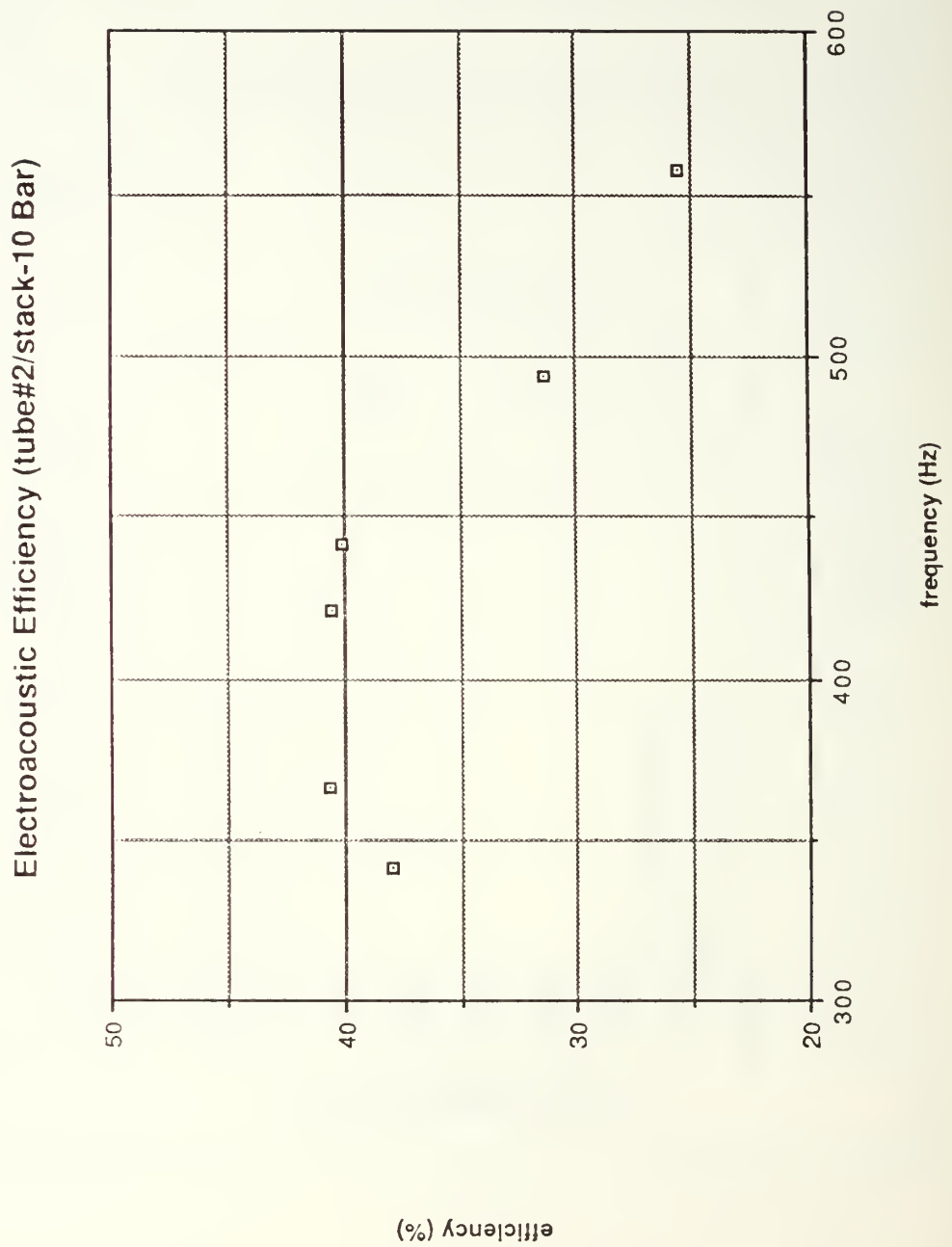


Figure IV-25. Electroacoustic Efficiency as a Function of the Tube Resonance Frequency

representative of the desired electroacoustic characteristics of the STAR.

Compared to the system without a stack, the results of this section are most reassuring and have been summarized in TABLE IV-3. Modelled efficiencies were surprisingly good

TABLE IV-3. SUMMARY OF MEASUREMENTS FOR REFRIGERATOR-TYPE RESONATOR WITH STACK

gas ratio	Q_t	f_0 (Hz)	eff (%)	f_1 (Hz)	eff peak ₁	f_2 (Hz)	eff peak ₂
1.000	11.0	557.6	25.6	360	11.7	570	29.8
0.804	11.5	493.1	31.4	360	27.9	510	40.3
0.644	11.4	441.8	40.1	360	20.6	460	50.0
0.587	11.0	421.3	40.5	340	32.0	440	52.4
0.443	11.4	366.3	40.6	320	47.6	400	50.3
0.384	11.5	341.5	37.9	300	49.2	375	42.3

especially considering the low power levels used to drive the system. It would appear that the poor results of the last section were due to the effects of the high Q resonator as speculated.

4. Power Measurements

The use of low power levels to drive the system was sufficient for the electroacoustic measurements above. However, in order to achieve the desired pressure levels within the resonator for refrigeration, the system has to be driven at higher powers. The amount of power used to drive the system is limited by the performance characteristics of the voice coil/reducer cone/bellows assembly. The voice coil can only handle a limited amount of current (1-2 A_{rms}) before becoming permanently damaged by self-heating. Additionally, the total displacement of the assembly has a limit before the titanium component breaks up. Although this limit is unknown, it is desired that the bellows peak displacement be at least 0.010 inches in order to produce the required pressure amplitudes within the resonator. Determination of the peak bellows displacement (Δx) is achieved by measuring the accelerometer output and applying the following relationship,

$$\Delta x = (\sqrt{2} V_{acc}) / (\omega^2 M_{acc}) \quad (IV-5)$$

where M_{acc} is the accelerometer sensitivity in volts-s²/m and V_{acc} is the rms accelerometer output voltage. To better characterize the performance of the driver under actual operating conditions, a series of experiments were conducted using progressively higher input power. The experimental

setup was the same as before except that for the present set of measurements the frequency was held constant as electric power was increased. Additionally, a multimeter was used to monitor the voice coil resistance to ensure that it was not overheating. In all cases, driving current was kept below $1.0 A_{rms}$.

For the first experiment, the refrigerator-type resonator (without stack) was mounted to the driver/housing and the system was pressurized to 10 bars with helium. The system was then driven at a 540 Hz (below tube resonance) with less than 10 mW and measurements were taken to yield values for driving current, electric power, acoustic power, and peak bellows displacement. The input power was increased and another set of measurements was taken. The procedure continued as long as the driving current remained below $1.0 A_{rms}$ and there was no noticeable distortion in the accelerometer output signal. For this first experiment a maximum bellows displacement of 3.2 mil (peak) was achieved when an average input power of 6.8 W was supplied to the driver. Attempting to drive the system at higher powers resulted in a distorted accelerometer signal. It is believed that this distortion was due to the amplifier and not the driver. Plots of acoustic versus electric power and bellows displacement versus driving current were generated with these data and are shown in Figure IV-26. The slope of the first graph represents the electroacoustic efficiency

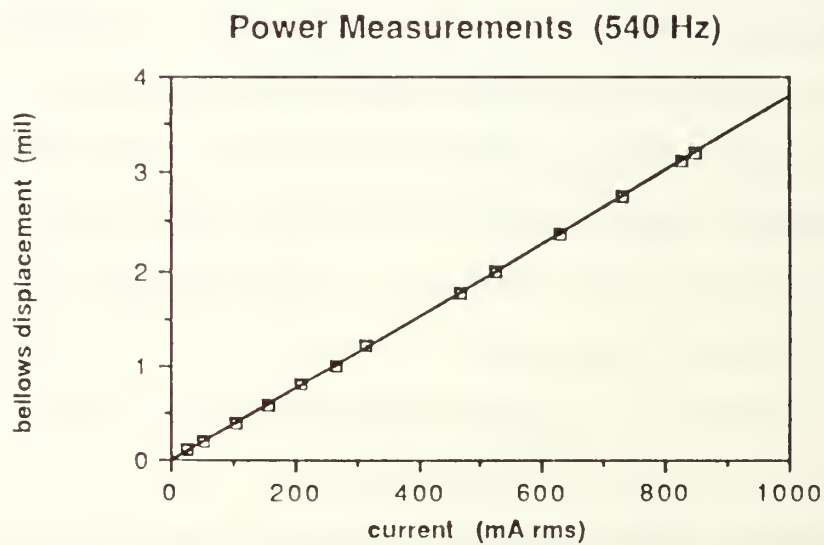
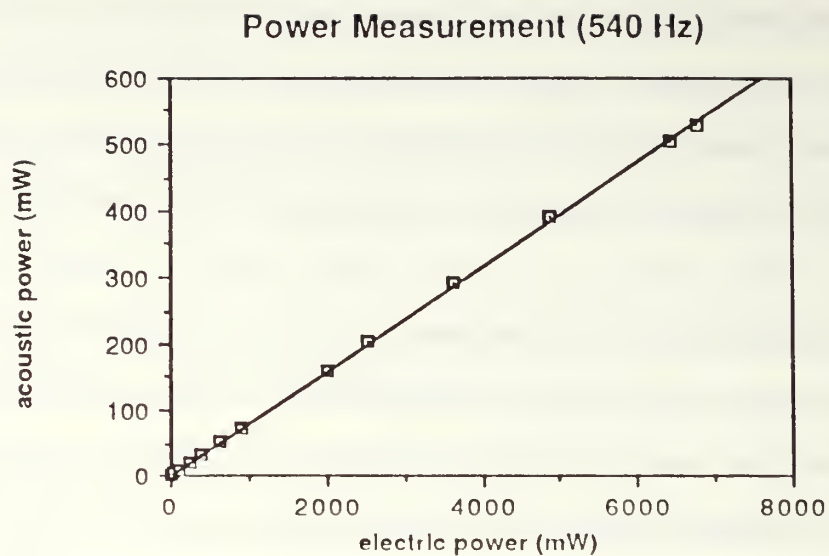


Figure IV-26. Power measurements without stack at 540 Hz in 10 bar Helium
a. power ratio
b. displacement/current ratio

and is equal to 7.8%. The linearity of the curve indicates that the efficiency is independent of the input power. The slope of the second graph is also constant indicating that a linear relationship exists between the bellows displacement and driving current.

The above procedure was repeated again at 570 Hz (above resonance) and at 560 Hz (in the vicinity of tube resonance). The results are graphically depicted in Figures IV-27 and IV-28. With the exception of the displacement versus current plot at 560 Hz, all the curves are linear over the power range observed. It is interesting to note that although a best fit can be made to the 560 Hz displacement/current data, it appears that the curve tends to decrease in slope with increasing current. At 560 Hz the maximum bellows displacement was 6.0 mil (peak) resulting from an input electric power of 4.8W to the driver. By comparison a 7.5 mil (peak) displacement was measured at 570 Hz with only 3.5 W input to the driver.

For the next set of measurements the resonator was configured with a stack and heat exchanger. Once again the system was pressurized with helium to 10 bars. The first data set was taken below tube resonance at 520 Hz followed by a second set at 600 Hz (above resonance). The maximum bellows displacement measured in both cases was about 5 mil achieved by driving the system with approximately 5 W. The results are shown in Figures IV-29 and IV-30 and again

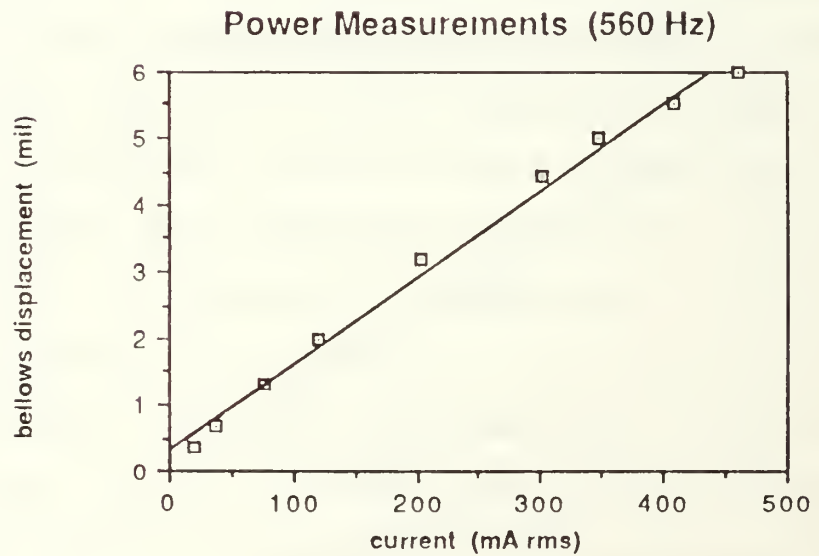
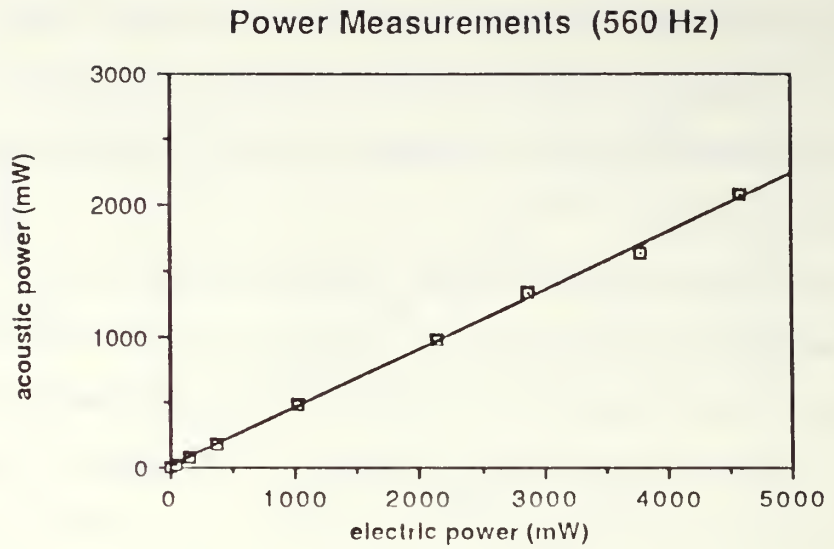
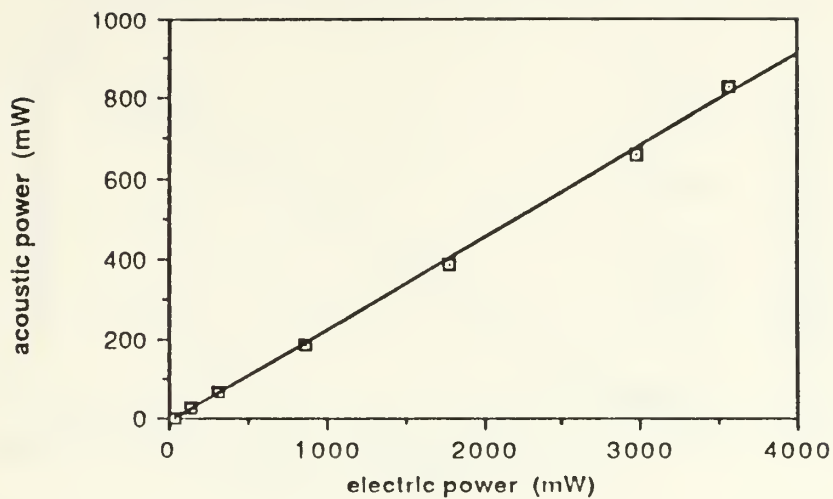


Figure IV-27. Power measurements without stack
at 560 Hz in 10 bar Helium
a. power ratio
b. displacement/current ratio

Power Measurements (570 Hz)



Power Measurements (570 Hz)

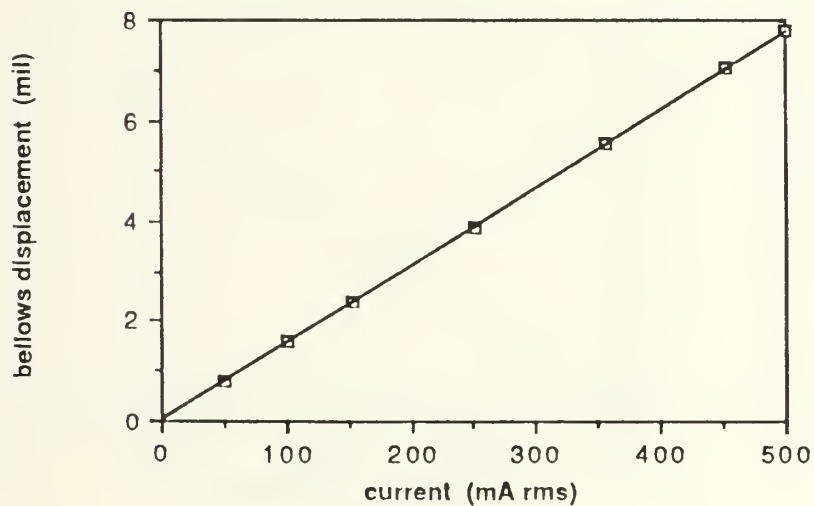


Figure IV-28. Power measurements without stack
at 570 Hz in 10 bar Helium
a. power ratio
b. displacement/current ratio

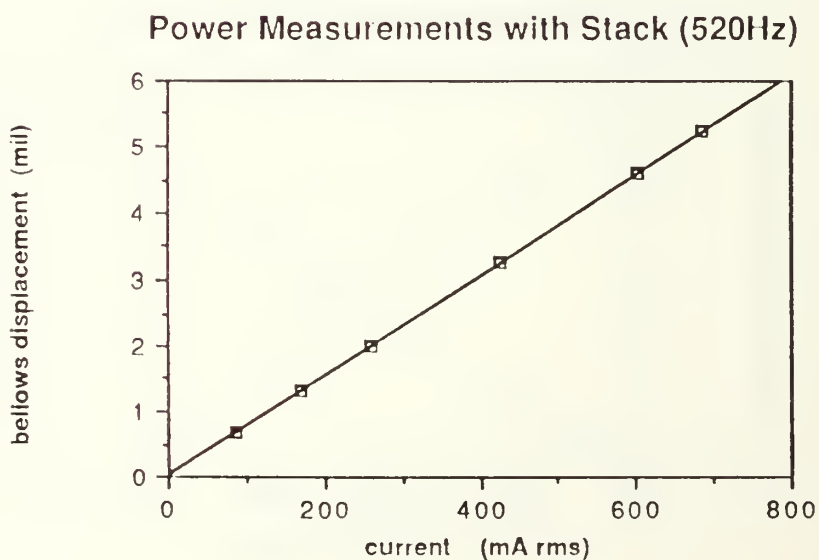
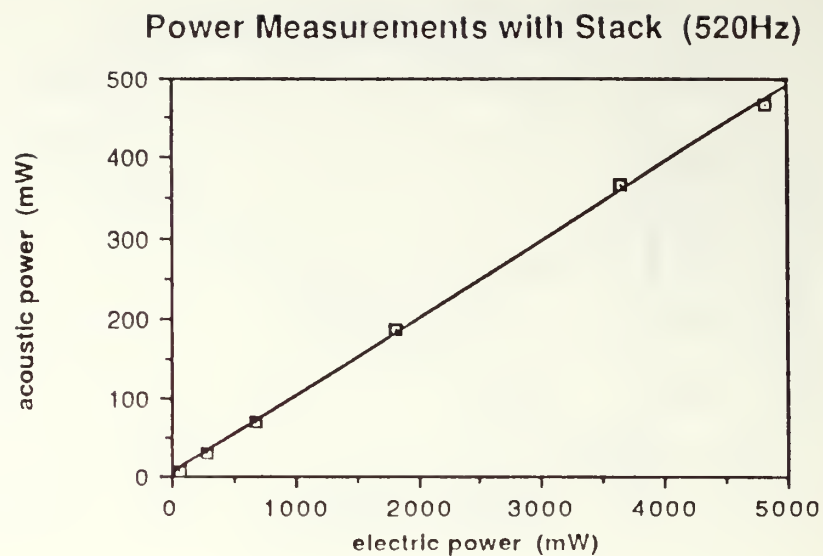


Figure IV-29. Power measurements with stack at 520 Hz in 10 bar Helium
a. power ratio
b. displacement/current ratio

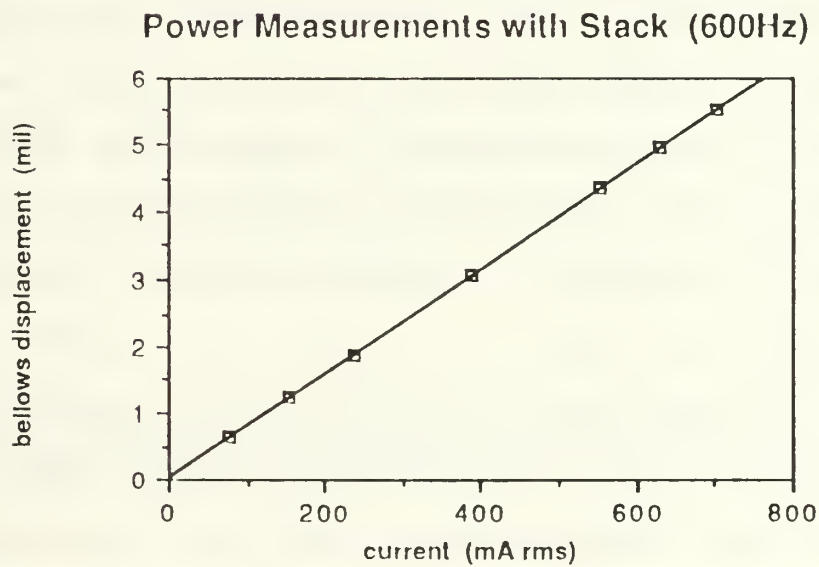
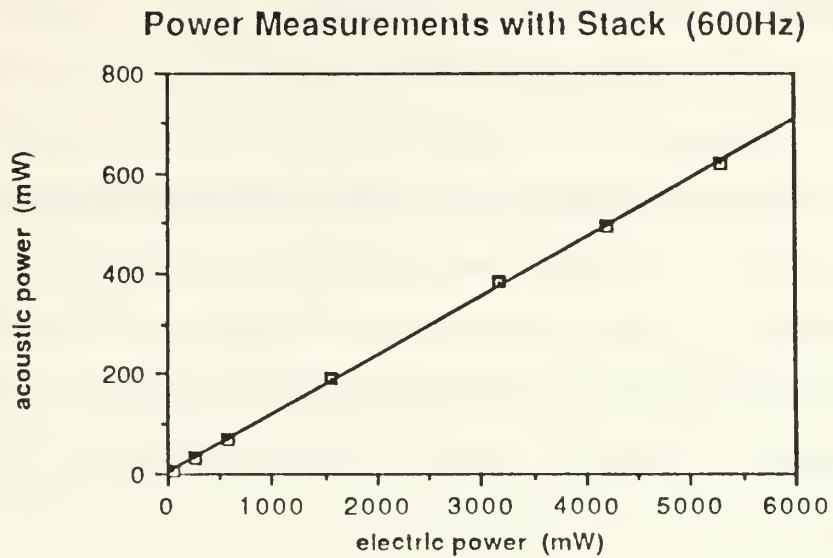


Figure IV-30. Power measurements with stack
at 600 Hz in 10 bar Helium
a. power ratio
b. displacement/current ratio

demonstrate the desired characteristic of linearity between the respective measured quantities.

All the power measurement results (with and without stack) are summarized in TABLE IV-4. In this format a number of observations can be made regarding the system performance under high power operating conditions. First and foremost is that the driver is capable of handling the input electric power to produce the required bellows displacement. Finally, there is good consistency in the measured data over a broad frequency range for the resonator with stack configuration. Unfortunately, power measurements were not taken near resonance for the stack configuration. In an attempt at estimating the maximum electric power that could be delivered to the driver under the above operating conditions, one must make the following assumptions: that there is a linear relationship between bellows displacement and input current, and that the maximum electric power delivered to the driver is limited by either a peak bellows displacement of 10 mils or a maximum input current of $1.5 A_{rms}$. Extrapolation of the data used to generate Figure IV-19 (resonator with stack in 10 Bar helium) indicates that the system will be displacement limited at 10 mil peak, to a maximum input electric power of about 26 Watts producing an output acoustic power of approximately 7 Watts (where $f_o=557.6$ Hz, $V_{mic}=5.39mV_{rms}$, $V_{acc}=2.37$ mV_{rms}, $I=19.1$ mA_{rms}, $M_{mic}=81.1 \times 10^{-6}$ V/Pa, $\Pi_{ac}=1.19$ mW, and $\Pi_{elec}=4.65$ mW). At this

acoustic power level the corresponding acoustic pressure would be about 0.07 bar peak.

TABLE IV-4. SUMMARY OF POWER MEASUREMENTS

system configuration	freq (Hz)	P_{elec} (W)	Δx (mil)	eff (%)	slope _o (%)	slope _b (mil/mA)
10 BAR HE WITHOUT STACK	540	6.8	3.2	7.8	7.8	0.0038
	560	4.8	6.0	48.0	44.7	0.0130
	570	3.5	7.5	23.0	23.0	0.0154
10 BAR HE WITH STACK	520	4.8	5.2	9.7	9.7	0.0076
	600	5.3	5.5	11.7	11.7	0.0078

* Note that the actual value for $B1/k$ based on the measured data is approximately $0.0088''/A_{rms}$

V. CONCLUSIONS AND RECOMMENDATIONS

The objective of the STAR project is to test and space qualify a continuous cycle cryogenic refrigeration system for the cooling of sensors and electronics based upon the thermoacoustic heat pumping effect. This thesis deals with the design, assembly, and calibration of the electrodynamic driver subsystem and its associated performance monitoring and control instrumentation. Accurate measurement of all driver parameters (stiffness, moving mass, transduction coefficient, and mechanical resistance) were obtained for use in a computer simulation of the driver's performance. Attachment of a test resonator to the driver allowed measurement of the electroacoustical efficiencies under different operating conditions. Comparison of measured and predicted efficiencies was graphically obtained and shown to be in good agreement, with the highest efficiencies occurring when the resonance frequencies of the driver and resonator were closely matched. For a Helium-Argon doped resonator, using a Los Alamos National Laboratory stack, a maximum electroacoustic efficiency of 50% was obtained. More important however, was that only a 10% decrease in efficiency was seen when the resonator and driver resonance frequencies were mismatched by as much as $\pm 14\%$.

A flight resonator has been designed for use in the STAR and construction techniques were tested. Due to the nature of the working gas of the system it was found that a layer of metal was necessary in the FRP neck to prevent diffusion of the helium through the epoxy. The task for the next group of students will be to construct and test the actual flight resonator and to repeat the series of measurements conducted in this thesis for the flight system. Their measurements will also allow for the first determination of the STAR's overall thermoelectric efficiency.

As discussed in Chapter II, the best design of the STAR driver would incorporate a custom built driver capable of transferring the motion of the voice coil to the bellows with a smaller, less massive, more rigid reducer cone. Theoretically, this should increase the system's overall efficiency and reliability, investigation into this area is recommended as a follow-on project. Another area to be investigated is the relationship between the modelled resonator impedance used in the computer simulation and the actual test resonator. The simulation program models the resonator as a $1/2$ wavelength tube of constant diameter and thus ignores losses due to the changes in the actual resonator's configuration. Based on the correlation between experimental and measured values of electroacoustic efficiency it is believed that this factor is minor. However

a better modelling of the resonator to include these changes in cross-sectional area might help to bring the two sets of values into even closer agreement.

APPENDIX A. CAPILLARY FLOW MEASUREMENTS

A critical requirement to ensure that the housing microphone does not get damaged due to excessive pressure changes within the housing, is to provide a capillary leak through the microphone back plate. This is achieved by inserting a length of 3 mil diameter copper wire into a slightly shorter piece of 4 mil bore copper-nickel tubing. The actual length of tubing to be used is dependent on the flow resistance of gas through the tiny capillary and the requirement that induced phase errors are kept to a minimum.

Flow between concentric cylinders¹² is given by,

$$U_{cyl} = \frac{\pi}{8 \eta l} \left[b^4 - a^4 - \frac{(b^2 - a^2)^2}{\ln(b/a)} \right] \quad (A-1)$$

where η is the shear viscosity of the working medium, ΔP is the pressure difference between the ends which are separated by a distance, l , a is the outer diameter of the wire, b is the inner diameter of the tube, and U_{cyl} is the volumetric velocity (m^3/s) of the flow. When the ratio of b to a approaches unity, the flow between concentric cylinders can be approximated with a similar expression describing flow between plates. This is given as,

$$U_{plate} = \frac{h^3 w \Delta P}{12 \eta l} \quad (A-2)$$

where $h=(b-a)$ and $w=\pi(a+b)$. This in turn leads to the following expression for flow resistance,

$$R = \frac{\Delta P}{U} = \frac{12\eta l}{wh^3} \quad (A-3)$$

The capillary and microphone back volume act as a low pass filter having a related time constant which can be derived from the adiabatic gas law as follows,

$$\frac{\delta P}{P_o} = -\frac{\gamma \delta V}{V_o} \rightarrow \frac{1}{P_o} \frac{\delta P}{\delta t} = -\frac{\gamma}{V_o} \frac{\delta V}{\delta t} = -\frac{\gamma}{V_o} U \quad (A-4)$$

where δP is the pressure variation inside the microphone back volume. Using equation A-3, and the assumption of harmonic time dependance ($\delta/\delta t \approx j\omega$) one obtains,

$$j\omega \delta P = -\frac{\gamma P_o}{RV_o} \Delta P \quad (A-5)$$

At the -3 dB point for this acoustic filter there exists an angular frequency ($\omega=\omega_o$) where $\delta P=\Delta P$. In this instance equation A-5 becomes,

$$\omega_o = \frac{\gamma P_o}{RV_o} \quad (A-6)$$

where V_o is the volume of the microphone cavity, γ is ratio of specific heat, P_o is the pressure within the cavity, and the exponential relaxation time, τ , is defined to be $1/\omega_o$.

If the operating frequency is $\omega = 2\pi(300 \text{ Hz})$ then $\omega\tau > 100$ in order that unwanted phase errors be kept below 0.5° . Setting $\omega\tau = 200$ yields a time constant of 0.11 seconds. The required flow resistance is then found to be 4.6×10^6 gm/cm⁴-sec (for helium at 10 atmospheres) by substituting into equation A-6 as follows,

$$R = \frac{\gamma P_o \tau}{V_o} = \frac{(5/3)(1.0 \times 10^7 \text{ dynes/cm}^2)}{(0.4 \text{ cm}^3)} (0.11 \text{ sec}) \quad (\text{A-7})$$

By substituting appropriate values into equation A-1 a maximum resistance per length (R/l) of 41×10^6 gm/cm⁵-sec is determined if the wire is concentric to the tube axis (as shown in Figure 1a). Based on the value of R derived in equation A-7, the capillary is required to have a minimum length of 1.2 mm.

The actual flow resistance per length for the capillary was experimentally determined by measuring the time taken for a given volume of helium ($\eta = 196 \times 10^{-6}$ poise at 20°C) at a certain constant pressure to flow through the capillary. The experiment was conducted a number of times using different lengths of copper-nickel tubing/copper wire. The net result was an average value for R/l of 6.3×10^6 gm/cm⁵-sec. Since this is smaller than the maximum value stated above, a one centimeter length of tubing was used to achieve a desirable leak rate. There are two possible causes for the discrepancy between the experimental and theoretical

values for R/l . The first is due to the fact that the actual dimensions of the wire and tubing are only known to within about 10%. A second source of error could be due to the positioning of the copper wire within the tubing. Rather than having the perfectly centered concentric cylinder case, the inner wire was most likely pressed against the inner wall of the tubing (as depicted in Figure A-1b). In this case the flow resistance is approximated by equation A-3 with $h=2(b-a)$ and $w=\pi b$. For these conditions (which are closer to reality, but less precise theoretically) R/l is approximately equal to $9 \times 10^6 \text{ gm/cm}^5\text{-s}$.

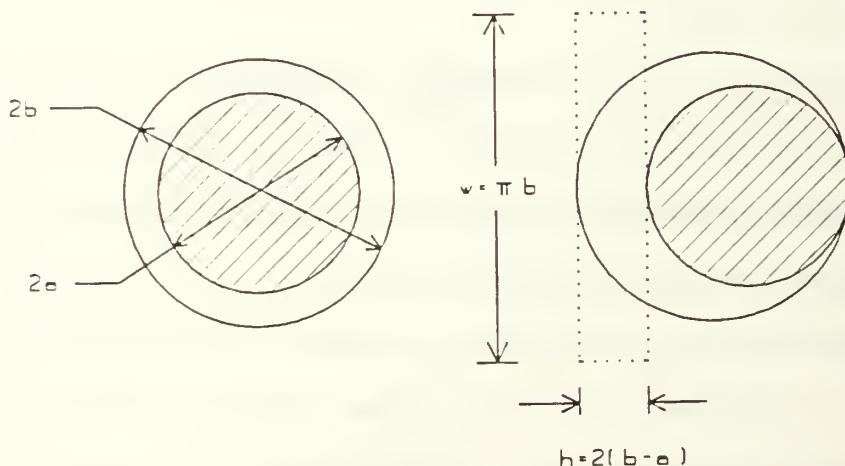


Figure A-1. Possible Wire/Tubing Configurations
a. Concentric b. Eccentric

APPENDIX B. COMPUTER SIMULATION PROGRAM

C *****

C

C

PROGRAM: FRIDGE FORTRAN

C

MODIFIED BY CAPT. D. HARRIS (CF) 11 JUNE 1989

C

C THIS IS A MODIFIED VERSION OF A PROGRAM WRITTEN BY LT. MICHAEL
C SUSALLA THAT WAS USED BY LT. MICHELE FITZPATRICK IN HER THESIS.
C THE PURPOSE OF THE PROGRAM IS TO DETERMINE VARIOUS PERFORMANCE
C CHARACTERISTICS OF A GENERIC DRIVER/RESONATOR SYSTEM BY TREATING
C IT AS AN EQUIVALENT ELECTRIC CIRCUIT DRIVEN BY A CONSTANT VOLTAGE
C SOURCE.

C

C BEFORE RUNNING THE PROGRAM, THE USER MUST MODIFY A SERIES OF DATA
C STATEMENTS WITHIN THE PROGRAM WHICH DEFINE THE ELECTROMECHANICAL
C PROPERTIES OF THE DRIVER AND THE GEOMETRIC PROPERTIES OF THE
C RESONATOR. ONCE THE PROGRAM IS INITIATED, THE USER IS REQUESTED
C TO DEFINE SOME ADDITIONAL PARAMETERS WHICH DESCRIBE THE OPERATING
C CONDITIONS FOR A GIVEN EXPERIMENT.

C

C THE PROGRAM THEN COMPUTES VALUES FOR ELECTRIC POWER
C DELIVERED TO THE SYSTEM, ACOUSTIC POWER PRODUCED, AND THE ELECTRO-
C ACOUSTIC EFFICIENCY OF THE DRIVER, ALL AS FUNCTIONS OF FREQUENCY
C (RANGING FROM 1/4 TO 3/2 THE RESONANCE FREQUENCY OF THE RESONATOR).
C THESE VALUES ARE THEN OUTPUT TO A DATA FILE ("FRIDGE OUTPUT") FOR
C LATER USE BY THE PLOTTING PROGRAM "GRAFRI FORTRAN".

C

C THE USER IS THEN GIVEN THE OPTION OF INPUTTING MEASURED DATA
C FOR ANALYSIS AND COMPARISON TO THEORY. VALUES FOR ELECTRIC
C POWER, ACOUSTIC POWER, AND ELECTROACOUSTIC EFFICIENCY ARE DETERMINED
C AND OUTPUT TO A DATA FILE CALLED "EFF OUTPUT". THIS DATA CAN THEN
C BE RETRIEVED BY "GRAFRI FORTRAN" AND PLOTTED WITH THE THEORETICAL
C VALUES DETERMINED ABOVE AS A MEANS OF VISUAL COMPARISON.

C

C THE FOLLOWING IS A LIST OF ALL VARIABLES USED IN THIS PROGRAM:

C

C RM - MECHANICAL RESISTANCE OF THE DRIVER'S MOVING MASS (KG/S)

C M - DRIVER MOVING MASS (KG)

C SSUP - MECHANICAL STIFFNESS OF THE DRIVER (N/M)

C S - CROSS-SECTIONAL AREA OF THE RESONATOR (M**2)

C BL - DRIVER TRANSDUCTION COEFFICIENT (T.M)

C A - EFFECTIVE PISTON AREA OF THE DRIVER (BELLOWS) (M**2)

C VOL - DRIVER BACK VOLUME (M**3)

C LE - VOICE COIL INDUCTANCE (HENRY)

C RE - VOICE COIL RESISTANCE (OHM)

C RHOHE - DENSITY OF HELIUM AT A GIVEN TEMP. AND PRESS. (KG/M**3)

```

C      L - EFFECTIVE RESONATOR LENGTH (HALF WAVELENGTH) (M)
C      RHO - DENSITY OF MEDIUM USED IN EXPERIMENT (KG/M**3)
C      C - SPEED OF SOUND IN MEDIUM (M/S)
C      Q - QUALITY FACTOR OF RESONATOR
C      FO - RESONANCE FREQUENCY OF RESONATOR (HZ)
C      V - INPUT DRIVING VOLTAGE (VPEAK)
C      SVOL - STIFFNESS OF GAS IN DRIVER BACK VOLUME
C      WO - ANGULAR RESONANCE FREQUENCY
C      ALPHA - ABSORPTION COEFFICIENT FOR MEDIUM WITHIN THE RESONATOR
C      RD - RATIO OF DENSITIES (PURE HELIUM TO GAS MIXTURE USED)
C      F - FREQUENCY
C      W - ANGULAR FREQUENCY
C      K - WAVE NUMBER
C      LCOIL - VOICE COIL ELECTRICAL IMPEDANCE DUE TO COIL INDUCTANCE
C      REZM - REAL PART OF THE MECHANICAL IMPEDANCE OF THE SYSTEM
C      IMZM - IMAGINARY PART OF THE MECHANICAL IMPEDANCE OF THE SYSTEM
C      ZM - COMPLEX MECHANICAL IMPEDANCE OF THE SYSTEM
C      ZE - TRANSFORMED ELECTRICAL IMPEDANCE OF THE MECHANICAL SYSTEM
C      ZCOIL - COMPLEX ELECTRICAL IMPEDANCE OF THE VOICE COIL
C      ZTOT - TOTAL COMPLEX ELECTRICAL IMPEDANCE OF THE SYSTEM
C      I - CURRENT DRIVING THE SYSTEM (AT A GIVEN FREQUENCY)
C      FORCE - FORCE ON DRIVER MOVING MASS DUE TO VOICE COIL MOTION
C      U - PISTON VELOCITY
C      REZT - REAL PART OF THE RESONATOR'S MECHANICAL IMPEDANCE
C      IMZT - IMAGINARY PART OF THE RESONATOR'S MECHANICAL IMPEDANCE
C      ZTUBE - COMPLEX MECHANICAL IMPEDANCE OF RESONATOR
C      P - COMPLEX PRESSURE PRODUCED AT BELLOWS/RESONATOR INTERFACE
C      PU - ACOUSTIC POWER GENERATED
C      PWR - ELECTRIC POWER DELIVERED TO DRIVER
C      PUPWR - ELECTROACOUSTIC EFFICIENCY OF DRIVER
C      GA - AMPLIFIER GAIN USED FOR MEASURED DATA
C      FR - FREQUENCY (HZ)
C      VM - VOLTAGE OUTPUT FROM MICROPHONE (DBV RE 1V)
C      VA - VOLTAGE OUTPUT FROM ACCELEROMETER (DBV RE 1V)
C      TH - PHASE ANGLE BETWEEN VM AND VA (DEG)
C      PO - ELECTRIC POWER MEASURED (MW)
C      O - POWER OFFSET (MW)
C      PE - ELECTRIC POWER (CORRECTED FOR O AND CONST. SCALING FACTOR)
C      PA - ACOUSTIC POWER MEASURED
C      EFF - ELECTROACOUSTIC EFFICIENCY MEASURED
C      II,IJ,J,JJ,Y, - DUMMY VARIABLES
C
C *****
      REAL LCOIL,K,IMZM,IMZT,M,L,LE,V,MAGV
      COMPLEX ZM,ZE,ZCOIL,ZTOT,I,U,ZTUBE,P,FORCE
      PI=3.141592654
C
C USER-MODIFIABLE DATA STATEMENTS
C
      DATA RM,M,SSUP,S,BL/1.96,0.01426,68266,1.14E-3,15.3/
      DATA A,VOL,LE,RE/6.348E-4,4.12E-4,2.3E-4,8.22/
      DATA Y,RHOHE,L/0.0,0.524,1.037/

```



```

C
C REQUEST FOR DATA DESCRIBING OPERATING CONDITIONS
C
  WRITE(*,*)'INPUT A VALUE FOR GAS DENSITY (KG/M**3)'
  READ(*,*)RHO
  WRITE(*,*)'INPUT SOUND SPEED OF MEDIUM (M/S)'
  READ(*,*)C
  WRITE(*,*)'INPUT QUALITY FACTOR OF RESONATOR'
  READ(*,*)Q
  WRITE(*,*)'INPUT RESONANCE FREQUENCY OF TUBE (HZ)'
  READ(*,*)FO
  WRITE(*,*)'INPUT DRIVING VOLTAGE (VPEAK)'
  READ(*,*)V

C
C CALCULATION SECTION FOR THEORETICAL VALUES OF ELECTRIC POWER,
C ACOUSTIC POWER, AND ELECTROACOUSTIC EFFICIENCY
C

```

```

  SVOL=(A*A*RHO*C*C)/VOL
  WO=2*PI*FO
  ALPHA=WO/(2*Q*C)
  RD=RHOHE/RHO
  OPEN(UNIT=69,FILE='FRIDGE OUTPUT A1',Iostat=IOS)
  OPEN(UNIT=22,FILE='EFF OUTPUT A1',Iostat=IOS)
  WRITE(69,*)' SOUND VEL      HE/GAS RATIO'
  WRITE(69,1)C,RD
  WRITE(69,*)'      FREQUENCY      POWER(AC)      EFFICIENCY      POWER(EL)'
1  FORMAT(F6.1,10X,F5.3)
  DO 10 J=1,300
    F=(FO/4)+((J-1)*(FO/240))
    W=2*PI*F
    K=W/C
    LCOIL=W*LE
    T=S
    REZM=RM+(((RHO*C*T*ALPHA*COS(K*L)*SIN(K*L))+(K*RHO*C*T*SINH(ALH
*HA*L)*COSH(ALPHA*L)))/(K*(1+(ALPHA/K)**2)*(((SIN(K*L))**2)*((COSH
*(ALPHA*L))**2))+(((COS(K*L))**2)*((SINH(ALPHA*L))**2))))
    IMZM=(W*M)-(SSUP/W)-(SVOL/W)+(((RHO*C*T*ALPHA*SINH(ALPHA*L)*COS
*H(ALPHA*L))-(K*RHO*C*T*COS(K*L)*SIN(K*L)))/(K*(1+(ALPHA/K)**2)*(((
*(SIN(K*L))**2)*((COSH(ALPHA*L))**2))+(((COS(K*L))**2)*((SINH(ALPHA
**L))**2))))
    ZM=CMPLX(REZM,IMZM)
    ZE=(BL**2)/ZM
    ZCOIL=CMPLX(RE,LCOIL)
    ZTOT=ZCOIL+ZE
    I=V/ZTOT
    FORCE=BL*I
    U=FORCE/ZM
    REZT=REZM-RM
    IMZT=IMZM-(W*M)+(SSUP/W)+(SVOL/W)
    ZTUBE=CMPLX(REZT,IMZT)
    P=(ZTUBE*U)/A

```

```

      PU=0.5*(REAL(P*CONJG(U))*A)
      PWR=0.5*(REAL(V*CONJG(I)))
      PUPWR=PU/PWR
C
C SAVE DESIRED VALUES TO "FRIDGE OUTPUT" FILE
C
      WRITE(69,100)F,PU,PUPWR,PWR
100  FORMAT(E13.5,E13.5,E13.5,E13.5)
      10 CONTINUE
      CLOSE(69)
C
C INPUT MEASURED DATA FOR COMPARISON TO THEORY
C
      WRITE(*,*)'CALCULATE AND PLOT MEASURED DATA? (Y=1,N=0)'
      READ(*,*)II
      IF(II.EQ.0)GOTO125
      WRITE(*,*)'INPUT VALUE OF GAIN USED FOR MEASURED VOLTAGES'
      READ(*,*)GA
      CALL EXCMS('CLRSCRN')
110  WRITE(*,*)'INPUT MEASURED VALUES (FR,VM,VA,TH,PO,O)'
      READ(*,*)FR,VM,VA,TH,PO,O
      WRITE(*,*)'CHECK YOUR INPUT-IF OKAY TYPE "1" IF NOT TYPE "0"'
      READ(*,*)JJ
      IF(JJ.EQ.0)GOTO110
C
C CALCULATION OF MEASURED ELECTRIC POWER, ACOUSTIC POWER, AND
C ELECTROACOUSTIC EFFICIENCY
C
      PE=PO-O-((PO-O)*.05)
      PA=((((10**((VM/20))/GA)*((10**((VA/20))/GA)))/(1.9277E-5*FR))*COS((
      *TH+92.6)*.01745))*1000
      EFF=(PA/PE)*100
C
C SAVE DESIRED VALUES TO "EFF OUTPUT" FILE
C
      WRITE(*,115)PE,PA,EFF
115  FORMAT(F5.2,5X,F6.3,5X,F5.1)
      WRITE(22,120)FR,EFF,PE,PA
120  FORMAT(F5.1,1X,F5.1,1X,F5.2,1X,F6.3)
      WRITE(*,*)'DO YOU WISH TO CONTINUE? Y=1,N=0'
      READ(*,*)IJ
      IF(IJ.EQ.1)GOTO110
      WRITE(22,15)Y
      15  FORMAT(F5.1)
125  CALL EXCMS('CLRSCRN')
C
C EXPLANATION OF OUTPUT FILES AND HOW TO GENERATE PLOTS OF THE DATA
C
      WRITE(*,*)'THIS PORTION OF THE PROGRAM IS COMPLETE'
      WRITE(*,*)'YOU NOW HAVE TWO OUTPUT FILES ON YOUR DISK'
      WRITE(*,*)'THE "EFF OUTPUT A1" FILE PROVIDES MEASURED EFFICIENCY'

```



```

WRITE(*,*)'THE "FRIDGE OUTPUT A1" FILE CONTAINS THEORETICAL DATA'
WRITE(*,*)'TO GENERATE PLOTS TYPE "DISSPLA GRAFRI" WHEN READY'
WRITE(*,*)'THE FOLLOWING THREE PLOTS WILL BE GENERATED:'
WRITE(*,*)'          1.  ELECTRIC POWER VS FREQUENCY'
WRITE(*,*)'          2.  ACOUSTIC POWER VS FREQUENCY'
WRITE(*,*)'          3.  ELECTROACOUSTIC EFFICIENCY VS FREQUENCY'
WRITE(*,*)'FOR HARDCOPY TYPE "SHERPA STAR SHGRAPH A" ONCE DISSPLA
* GRAFRI EXECUTED'
STOP
END

```

C *****

C

C

PROGRAM: GRAFRI FORTRAN

C

MODIFIED BY CAPT D. HARRIS (CF) 11 JUNE 1989

C

C THIS IS A MODIFIED VERSION OF A PLOTTING PROGRAM WRITTEN BY
C LT. MICHAEL SUSALLA THAT IS USED IN CONJUNCTION WITH THE FRIDGE
C FORTRAN PROGRAM. THE PROGRAM RETRIEVES THE "FRIDGE OUTPUT" AND "EFF
C OUTPUT" FILES AND GENERATES THREE DIFFERENT PLOTS WHICH INCLUDES:

C

C

1. ELECTRIC POWER VERSUS FREQUENCY

C

2. ACOUSTIC POWER VERSUS FREQUENCY

C

3. ELECTROACOUSTIC EFFICIENCY VERSUS FREQUENCY

C

C FOR THE FREQUENCY RANGE DEFINED BY THE "FRIDGE FORTRAN" PROGRAM.

C

C THIS PROGRAM MUST BE COMPILED IN FORTVS PRIOR TO GENERATING ANY
C PLOTS SINCE VARIOUS DISSPLA SUBROUTINES ARE REQUIRED TO GRAPH THE
C DATA.

C

C *****

DIMENSION D(300),H(300),O(300),T(300),F(50),E(50),EL(50),AC(50)

CHARACTER*80 NEW1\$,DUMMY\$

REAL D,H,O,T,M

DATA XMAX,YMAX2,YMAX3,YMAX4/0.,0.,0.,0./

NEW1\$='RENAME '///' FRIDGE OUTPUT A1'///' FILE XYZ1 A1'

CALL EXCMS(NEW1\$)

CALL EXCMS('FILEDEF 22 DISK EFF OUTPUT A1')

C

C RETRIEVE THEORETICAL DATA FROM "FRIDGE OUTPUT" FILE

C

OPEN (69,FILE='XYZ1')

READ (69,'(A80)')DUMMY\$

READ (69,1)C,RD

READ (69,'(A80)')DUMMY\$

1 FORMAT (F6.1,10X,F5.3)

DO 20 J=1,300

READ (69,15,END=21)D(J),H(J),O(J),T(J)

15 FORMAT (E13.5,E13.5,E13.5,E13.5)

C

C DETERMINE MAXIMUM VALUES FOR AXES OF GRAPHS

```

C
    IF(D(J).GT.XMAX)THEN
    XMAX=D(J)
    ENDIF
    IF(H(J).GT.YMAX2)THEN
    YMAX2=H(J)
    ENDIF
    IF(O(J).GT.YMAX3)THEN
    YMAX3=O(J)
    ENDIF
    IF(T(J).GT.YMAX4)THEN
    YMAX4=T(J)
    ENDIF
20 CONTINUE
21 CLOSE(69)
    I=1
C
C RETRIEVE MEASURED DATA FROM "EFF OUTPUT" FILE
C
24 READ(22,25)F(I),E(I),EL(I),AC(I)
25 FORMAT(F5.1,1X,F5.1,1X,F5.2,1X,F6.3)
    IF(F(I).EQ.0.0)GOTO26
    E(I)=E(I)/100
    EL(I)=EL(I)/1000
    AC(I)=AC(I)/1000
    I=I+1
    GOTO 24
26 I=I-1
C
C DETERMINE INCREMENTAL STEPS FOR EACH AXIS OF THE VARIOUS PLOTS
C
    INC=INT(XMAX/10.)
    YINC2=YMAX2/10.
    YINC3=YMAX3/10.
    YINC4=YMAX4/10.
    MAX=INT(XMAX)
    NEW1$='RENAME '///' FILE XYZ1 A1'///' FRIDGE OUTPUT A1'
    CALL EXCMS(NEW1$)
C
    CALL TEK618
    CALL SHERPA('STAR      ','A',3)
    CALL BLOWUP(1.5)
    CALL YAXANG(0)
C
C PLOT MEASURED AND THEORETICAL ELECTRIC POWER VERSUS FREQUENCY
C
    CALL PAGE(11,8.5)
    CALL AREA2D(8.,6.)
    CALL SCMPLEX
    CALL XNAME('FREQUENCY(HZ)$',100)
    CALL YNAME('ELECTRIC POWER(W)$',100)
    CALL HEADIN('ELECTRIC POWER VS. FREQUENCY$',100,2.,1)
    CALL THKFRM(.02)

```

```

CALL FRAME
CALL GRAF(0.0, INC, MAX, 0.0, YINC4, YMAX4)
CALL CURVE(D, T, 300, 0)
CALL CURVE(F, EL, I, -1)
CALL ENDPL(0)

C
C PLOT MEASURED AND THEORETICAL ACOUSTIC POWER VERSUS FREQUENCY
C
CALL AREA2D(8., 6.)
CALL XNAME('FREQUENCY(HZ)$', 100)
CALL YNAME('ACOUSTIC POWER(W)$', 100)
CALL HEADIN('ACOUSTIC POWER VS. FREQUENCY$', 100, 2., 1)
CALL THKFRM(.02)
CALL FRAME
CALL GRAF(0.0, INC, MAX, 0.0, YINC2, YMAX2)
CALL CURVE(D, H, 300, 0)
CALL CURVE(F, AC, I, -1)
CALL ENDPL(0)

C
C PLOT MEASURED AND THEORETICAL ELECTROACOUSTIC EFFICIENCY VERSUS
C FREQUENCY
C
CALL AREA2D(8., 6.)
CALL MESSAG('SOUND VEL=$', 100, 0.1, 5.5)
CALL REALNO(C, 1, 'ABUT', 'ABUT')
CALL MESSAG('M/S$', 100, 'ABUT', 'ABUT')
CALL MESSAG('HE/GAS RATIO=$', 100, 0.1, 5.)
CALL REALNO(RD, 3, 'ABUT', 'ABUT')
CALL XNAME('FREQUENCY(HZ)$', 100)
CALL YNAME('ACOUSTIC PWR/ELECTRIC PWR$', 100)
CALL HEADIN('ELECTROACOUSTIC EFFICIENCY VS. FREQUENCY$', 100, 2., 1)
CALL THKFRM(.02)
CALL FRAME
CALL GRAF(0.0, INC, MAX, 0.0, YINC3, YMAX3)
CALL CURVE(D, O, 300, 0)
CALL CURVE(F, E, I, -1)
CALL ENDPL(0)
CALL DONEPL
STOP
END

```

APPENDIX C. SELECTED DIMENSIONAL DRAWINGS (DRIVER HOUSING)

(dimensions in inches)

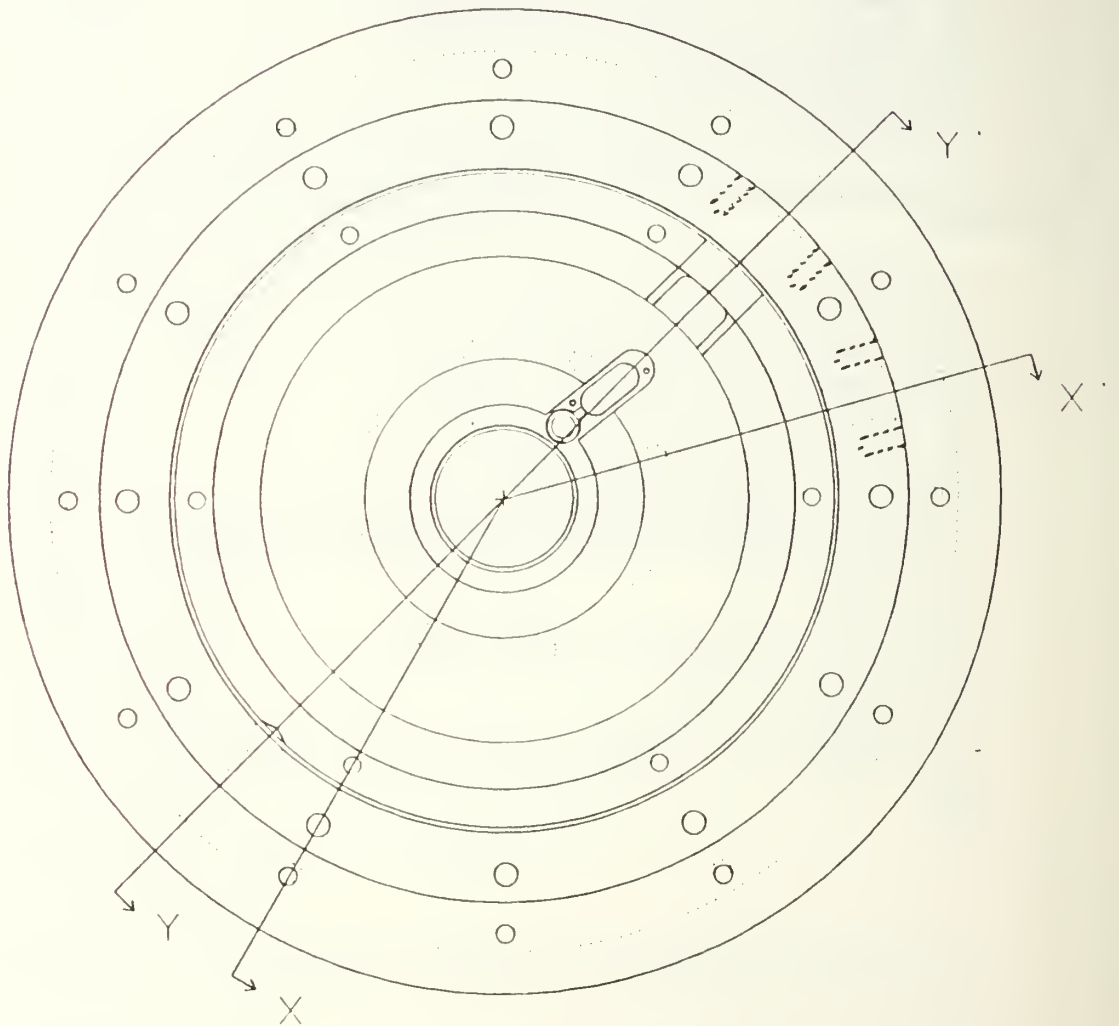


Figure C-1. Driver Housing - Lid (Top) View

LID VIEW - PORTHOLES FOR ELECTRONICS PLUG AND PRESSURE TRANSDUCER (all dimensions in inches)

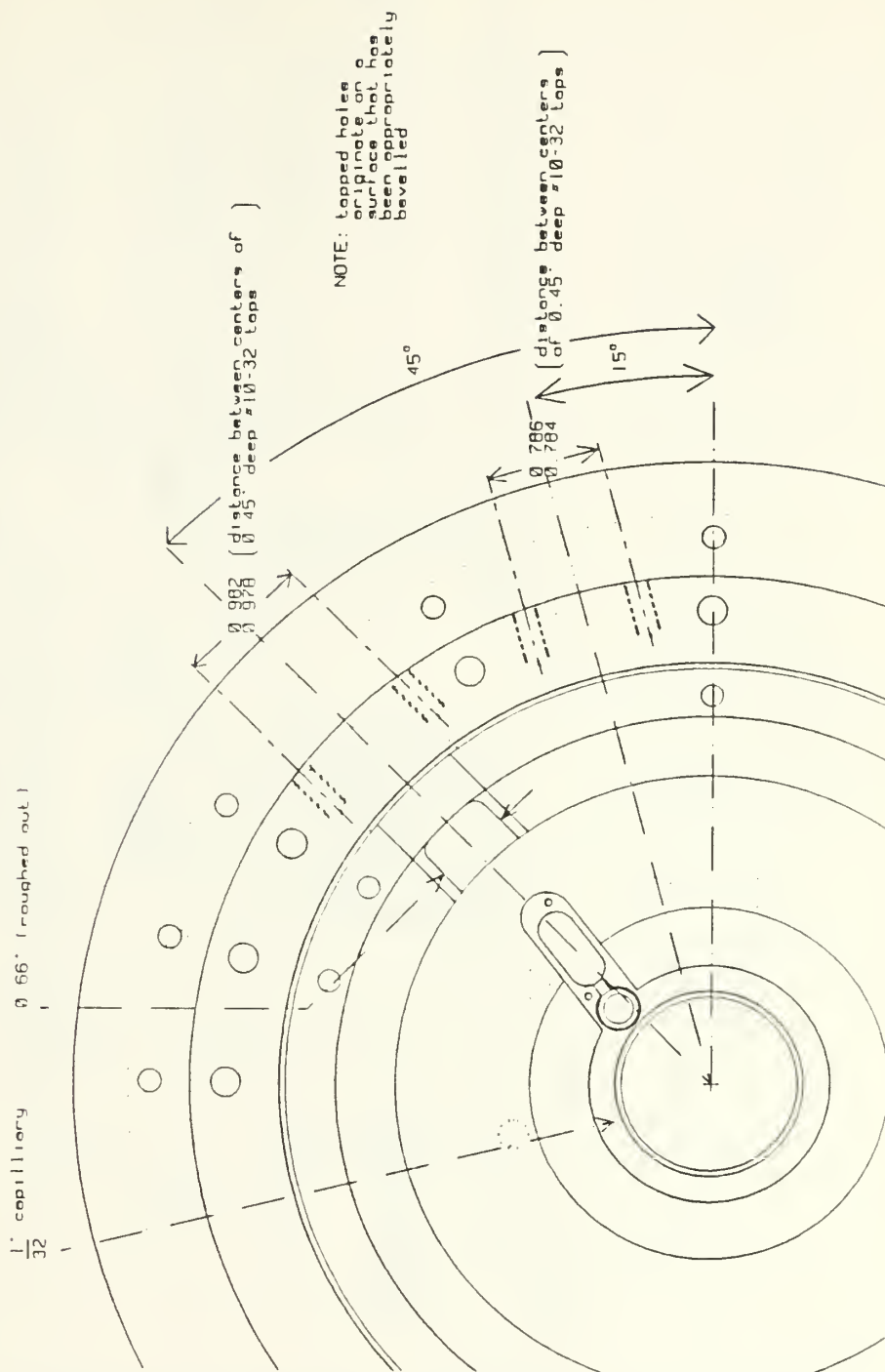
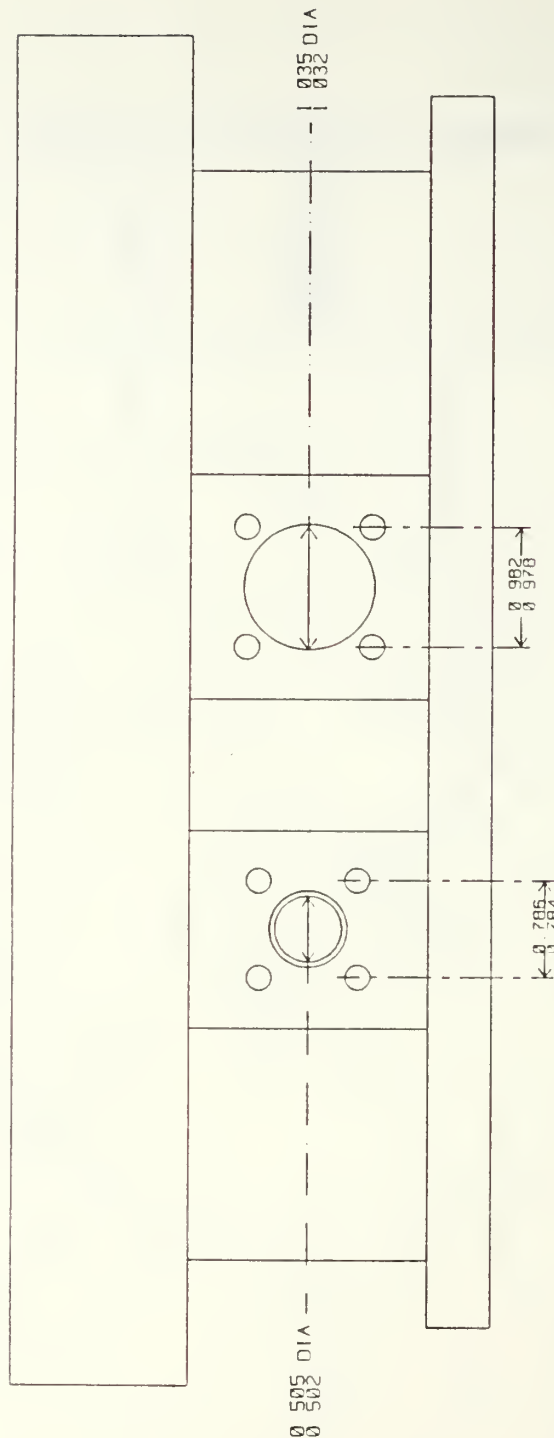


Figure C-2. Top View Detail of Figure C-1 Showing the Ports for the Electronics Feed-through Plug and DC Pressure Transducer



DRIVER HOUSING - SIDE VIEW SHOWING PORTHOLES

(dimensions in inches)
(all hidden lines omitted)

Figure C-3. Side View of the Driver Housing Showing the Bevelled Surfaces to which the Electronics Feed-through Plug and DC Pressure Transducer Support Plate are Mounted

MIC AND FET HOUSING

(all dimensions in inches)

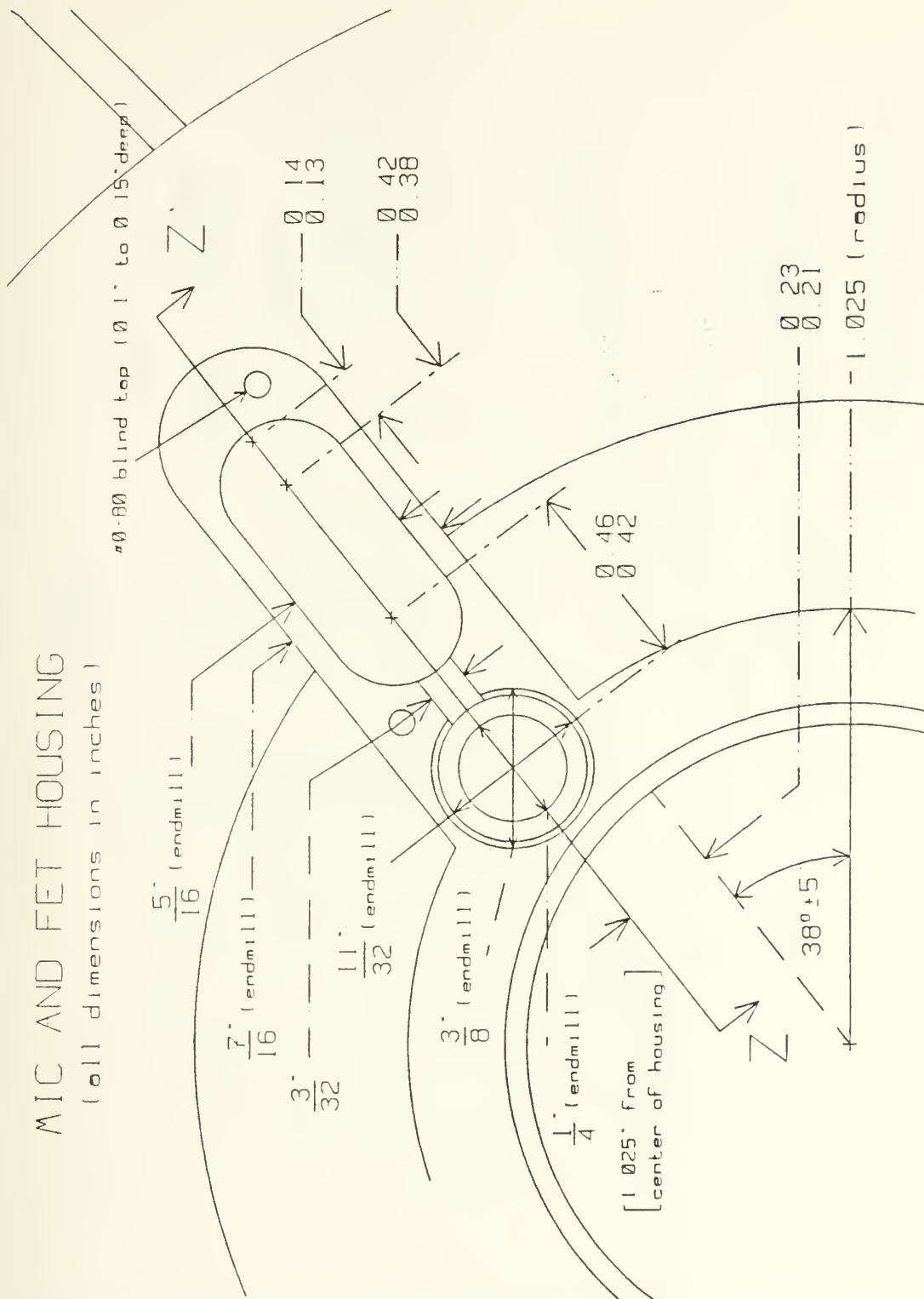


Figure C-4. Close-up Top View Detail of Figure C-1 Showing the Microphone/FET Housing

MICROPHONE and FET HOUSING
VIEW ZZ
(dimensions in inches)

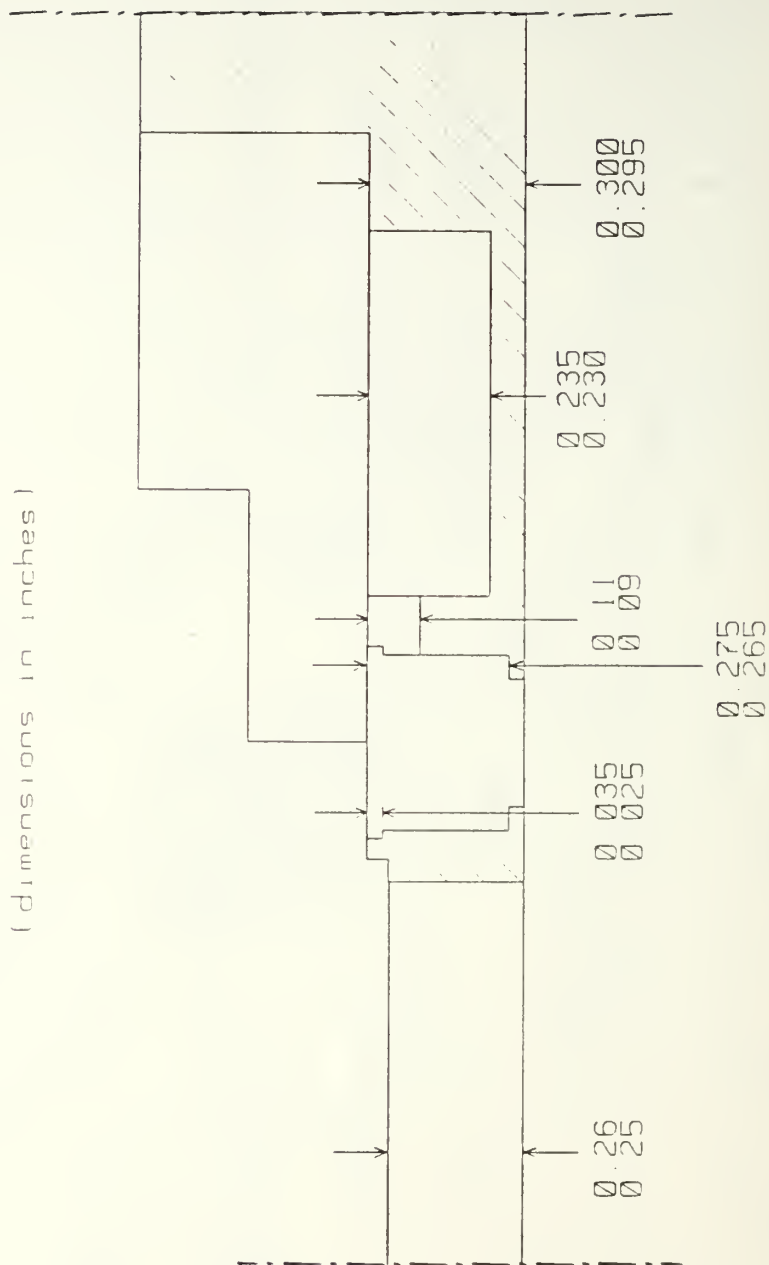


Figure C-5. Cross-sectional View of the Microphone/FET Housing along Z-Z' of Figure C-4

(all dimensions in inches)

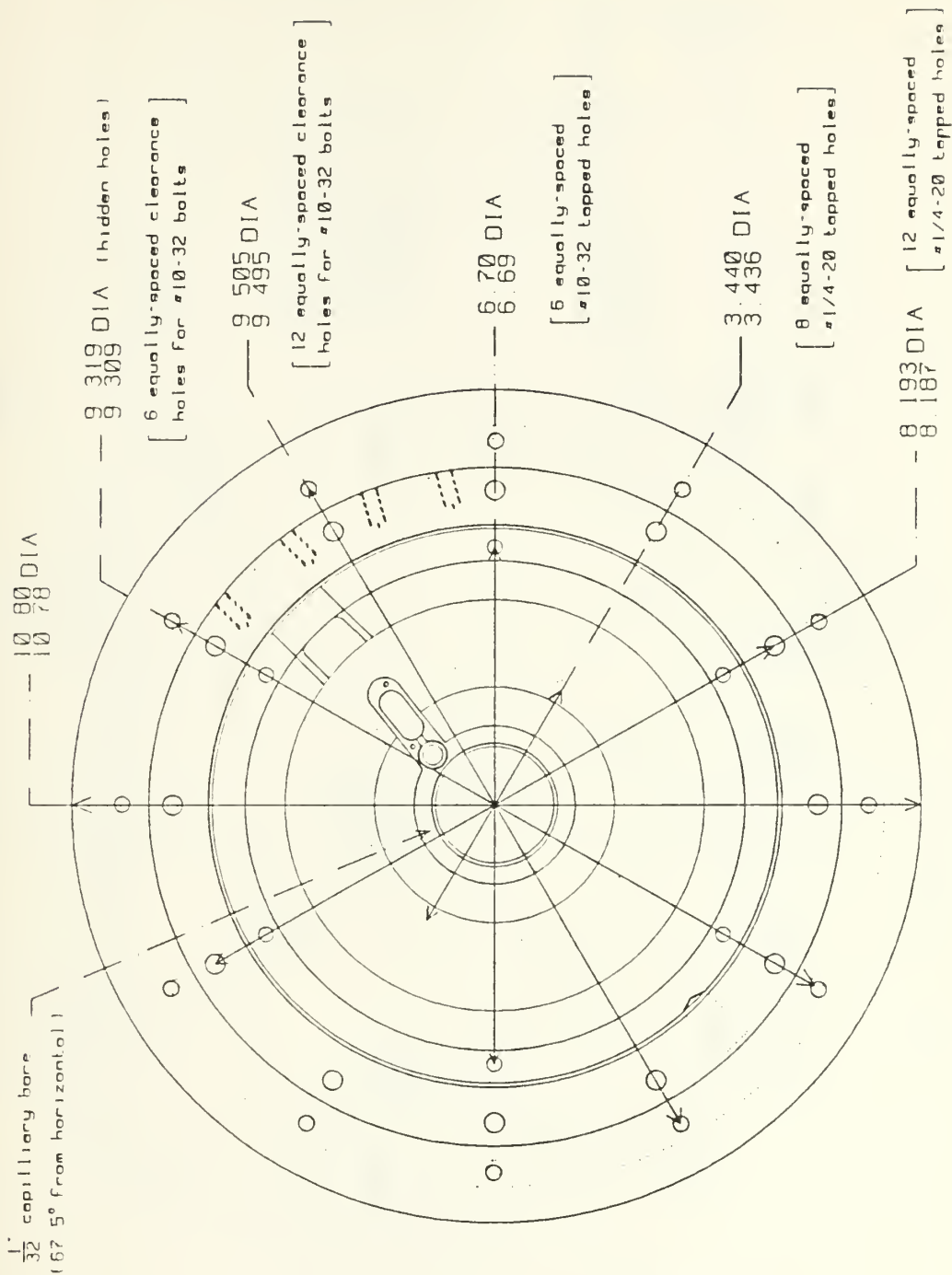


Figure C-6. Top View of the Driver Housing Showing the Bolt Circle Dimensions

(all dimensions in inches)

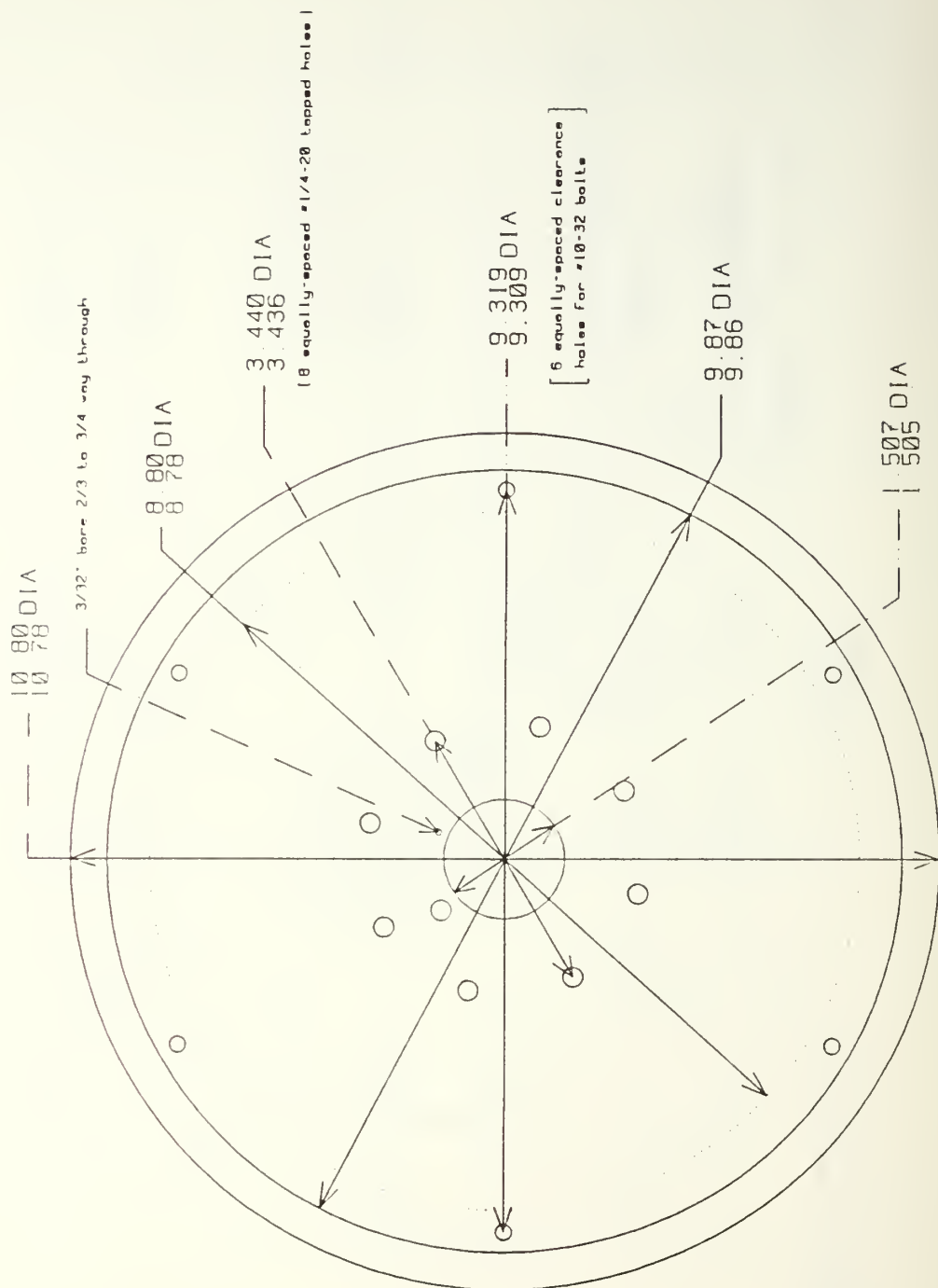


Figure C-7. Bottom, or Resonator View of the Driver Housing

DRIVER HOUSING - VIEW XX (dimensions in inches)

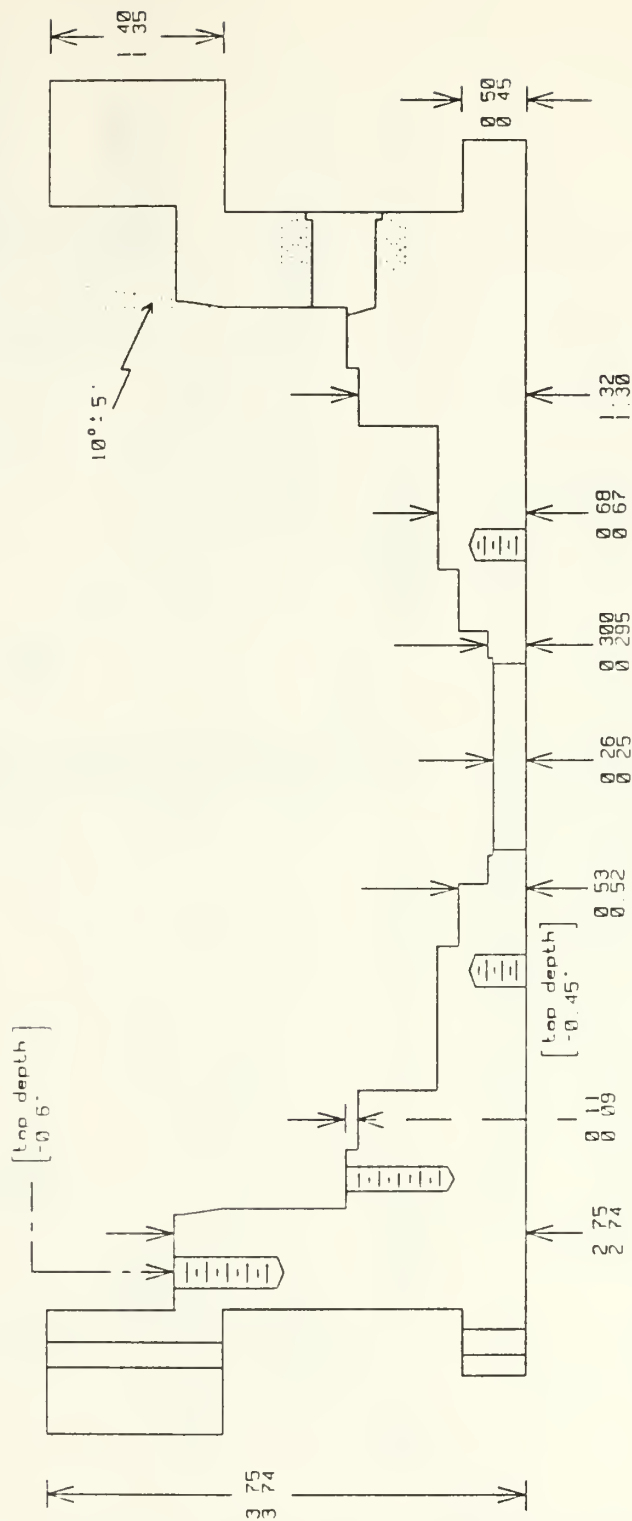


Figure C-8. Cross-sectional View of the Driver Housing Showing Vertical Dimensions along X-X' in Figure C-1

DRIVER HOUSING - VIEW XX

(dimensions in inches)

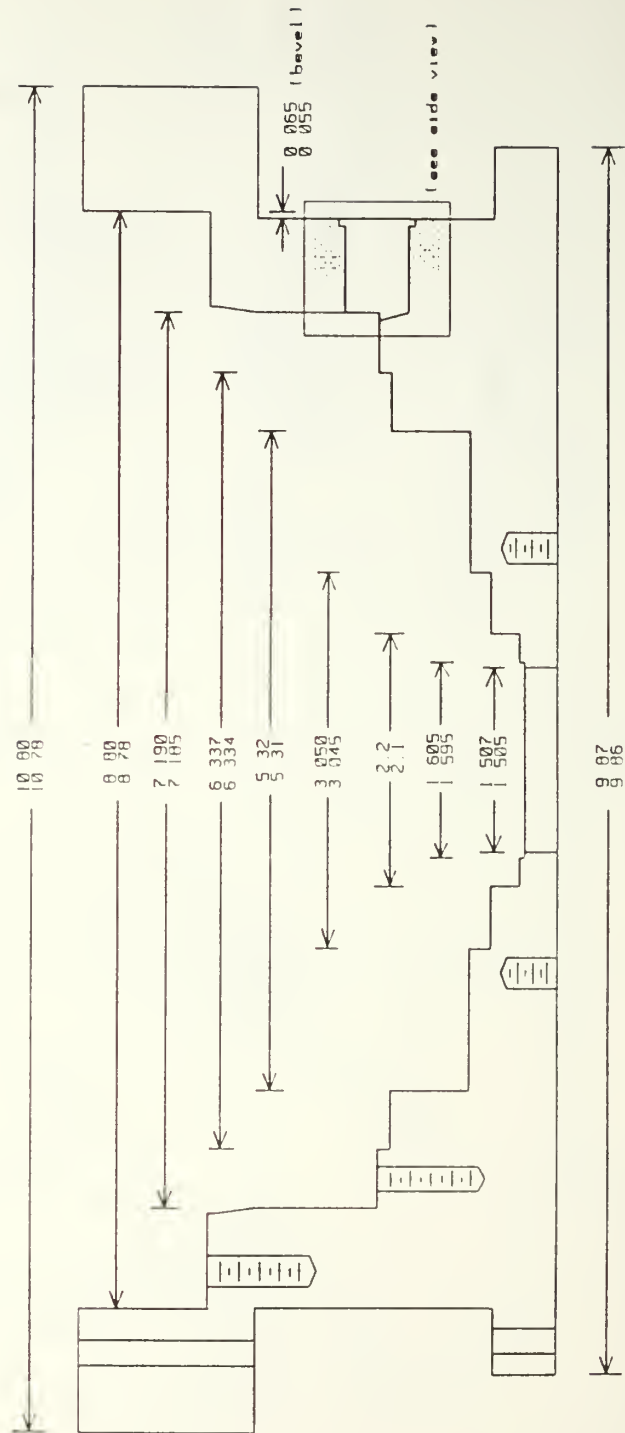


Figure C-9. Cross-sectional View of the Driver Housing Showing Horizontal Dimensions along X-X' in Figure C-1

(all dimensions in inches)

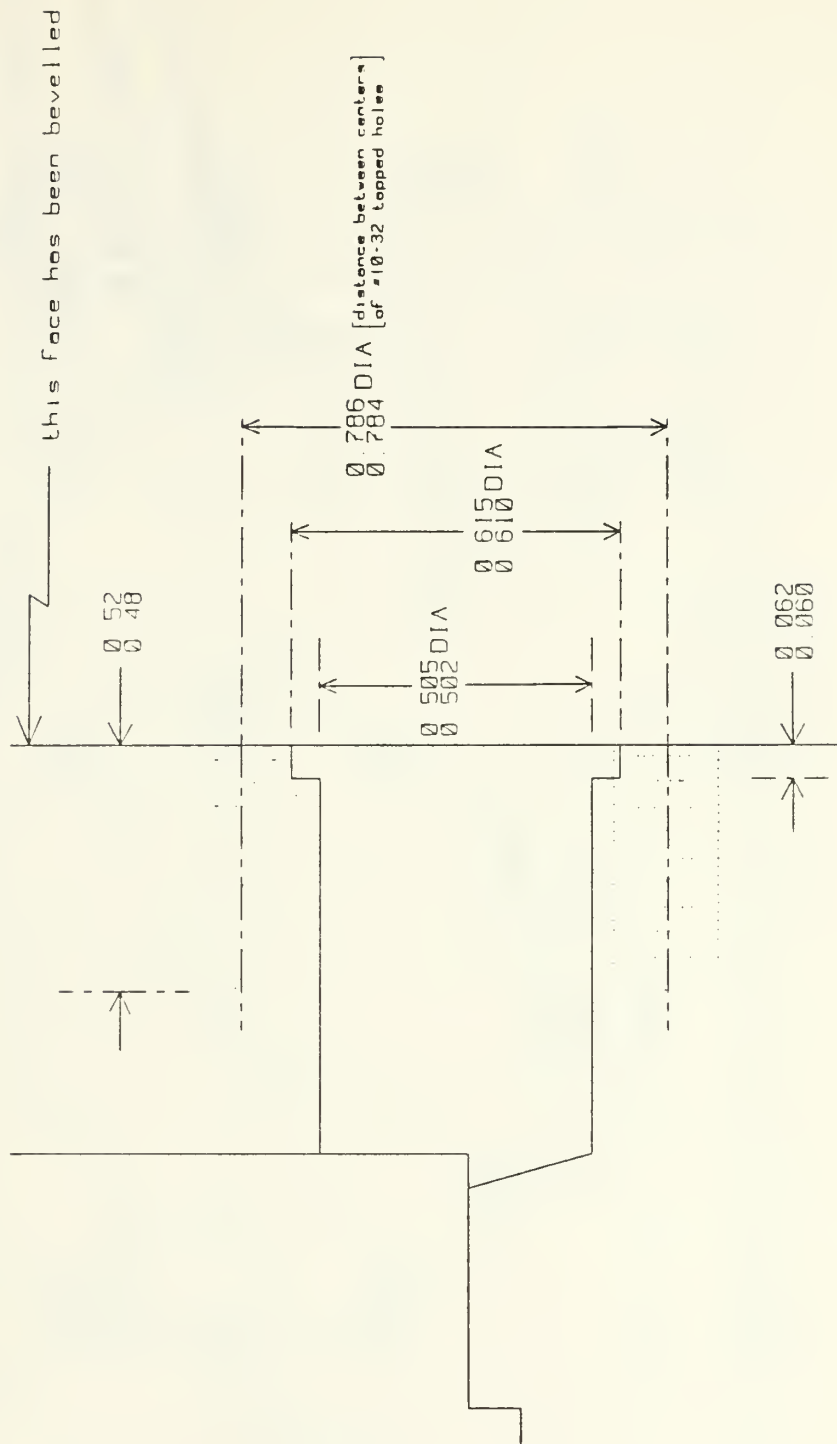


Figure C-10. Close-up Cross-sectional View of the DC Pressure Transducer Port

DRIVER HOUSING - VIEW YY' (dimensions in inches)

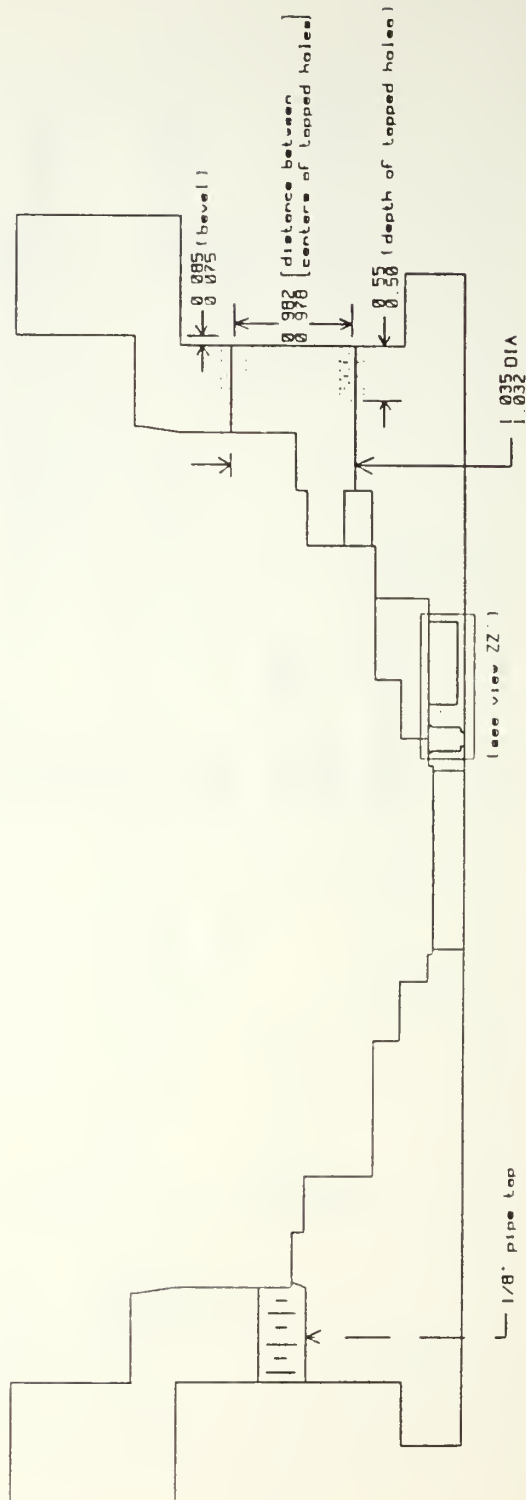


Figure C-11. Cross-sectional View along Y-Y' of Figure C-1 Showing the Electronics Feed-through Port and Gas Fill Port

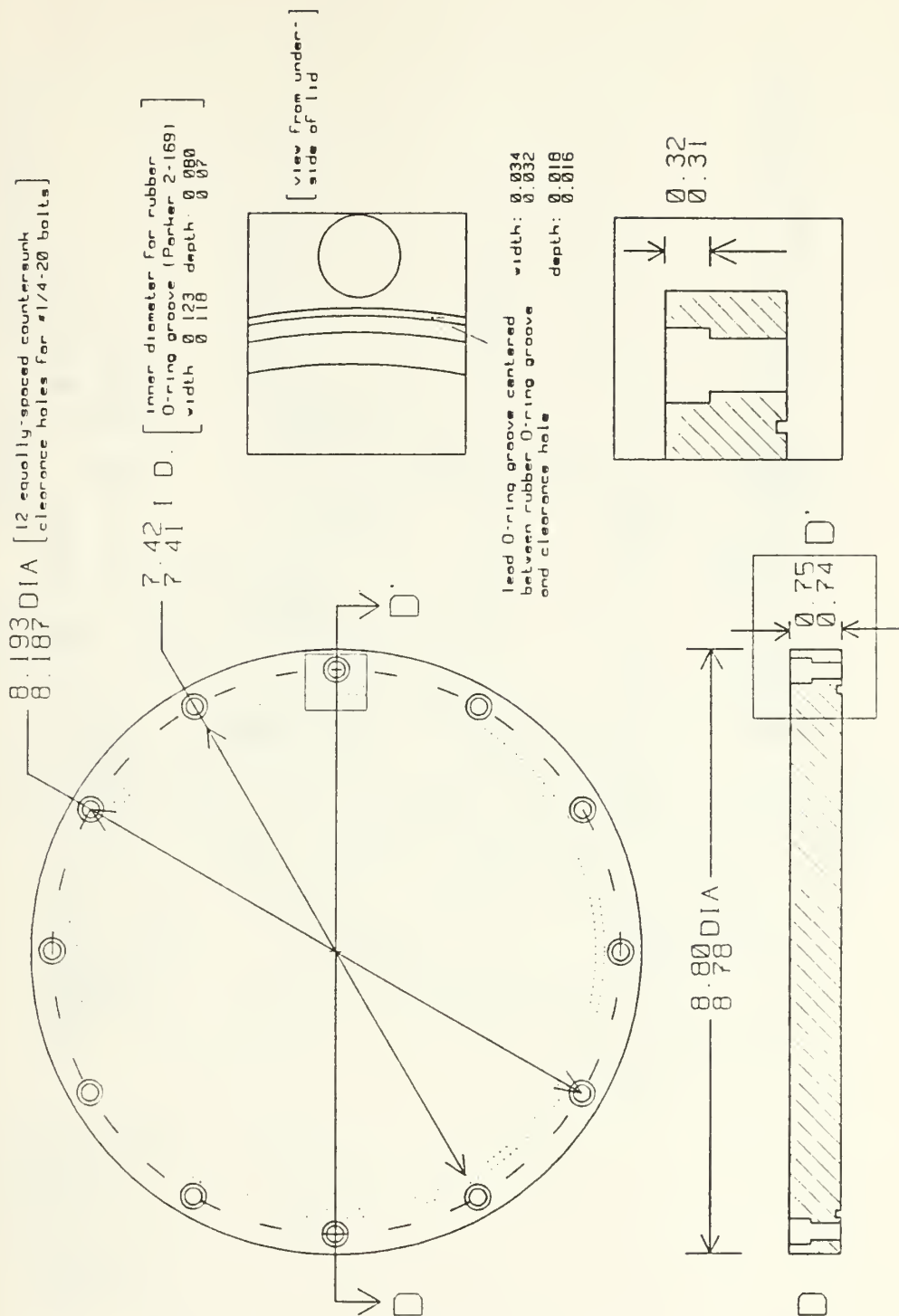


Figure C-12. Driver Housing Pressure Lid with Bolt Circle and O-ring Details

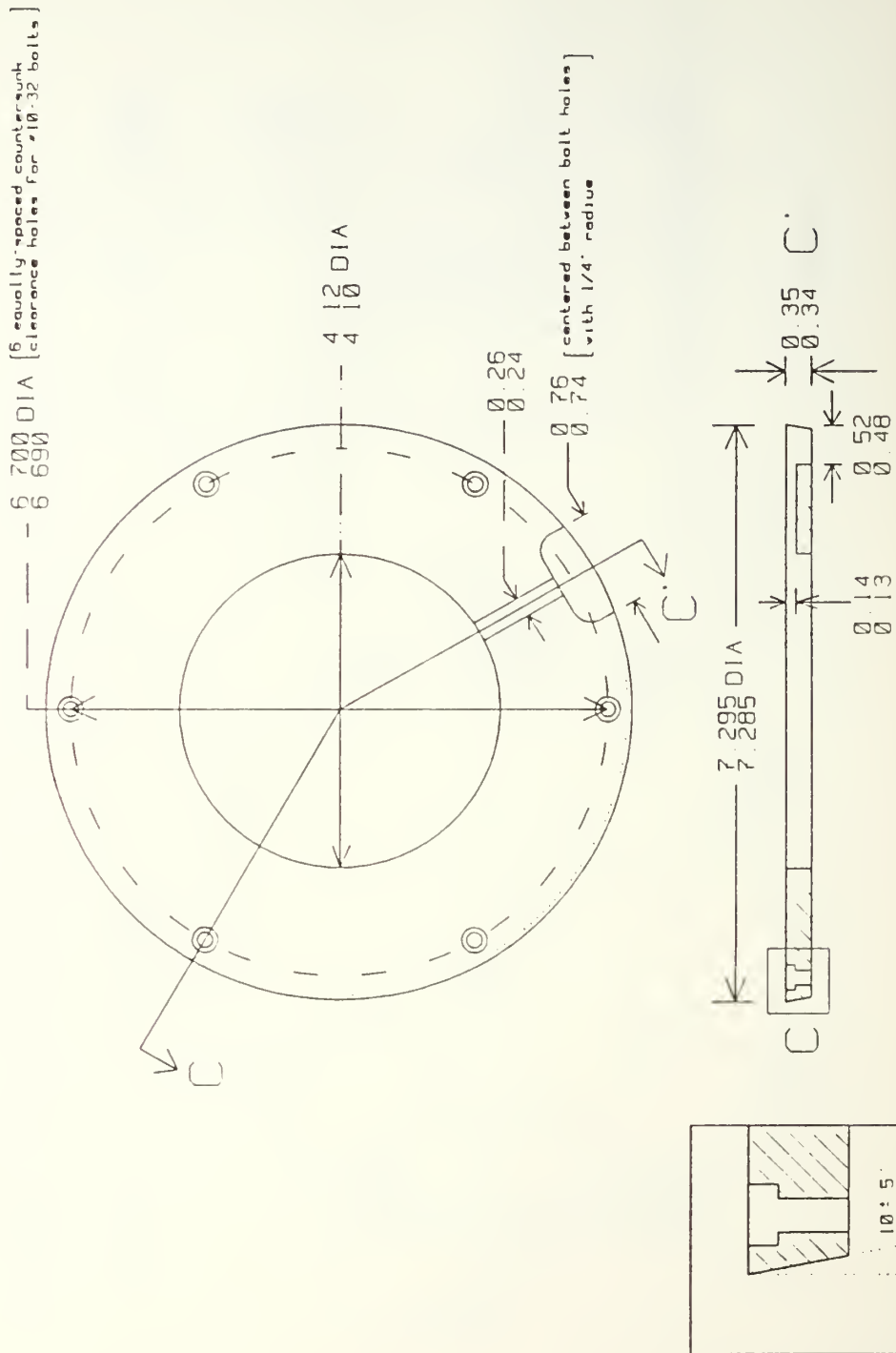


Figure C-13. Plane and Section Views of the Pusher Plate with Taper Detail

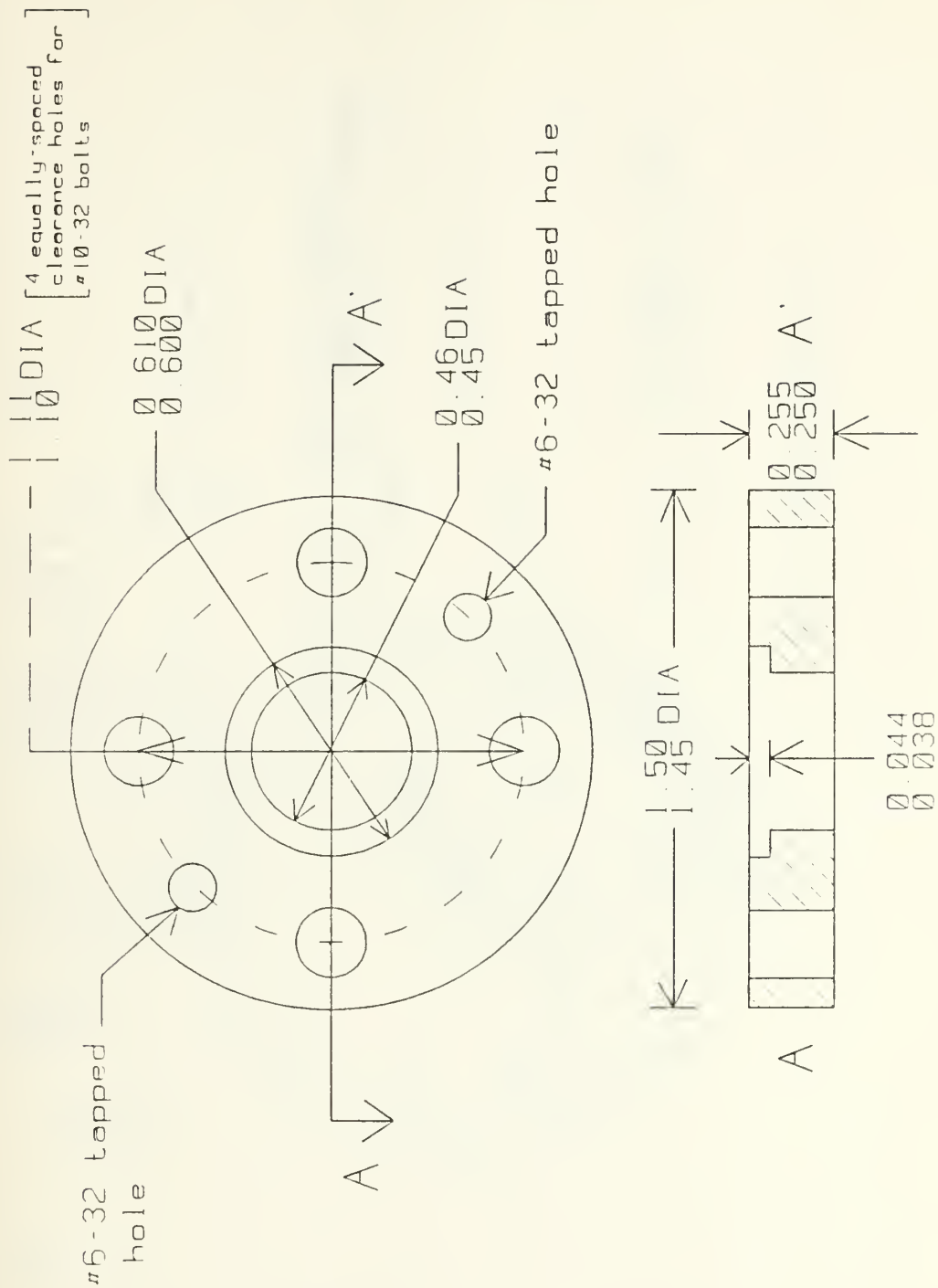


Figure C-14. The DC Pressure Transducer Support Plate in Both Plane and Section Views

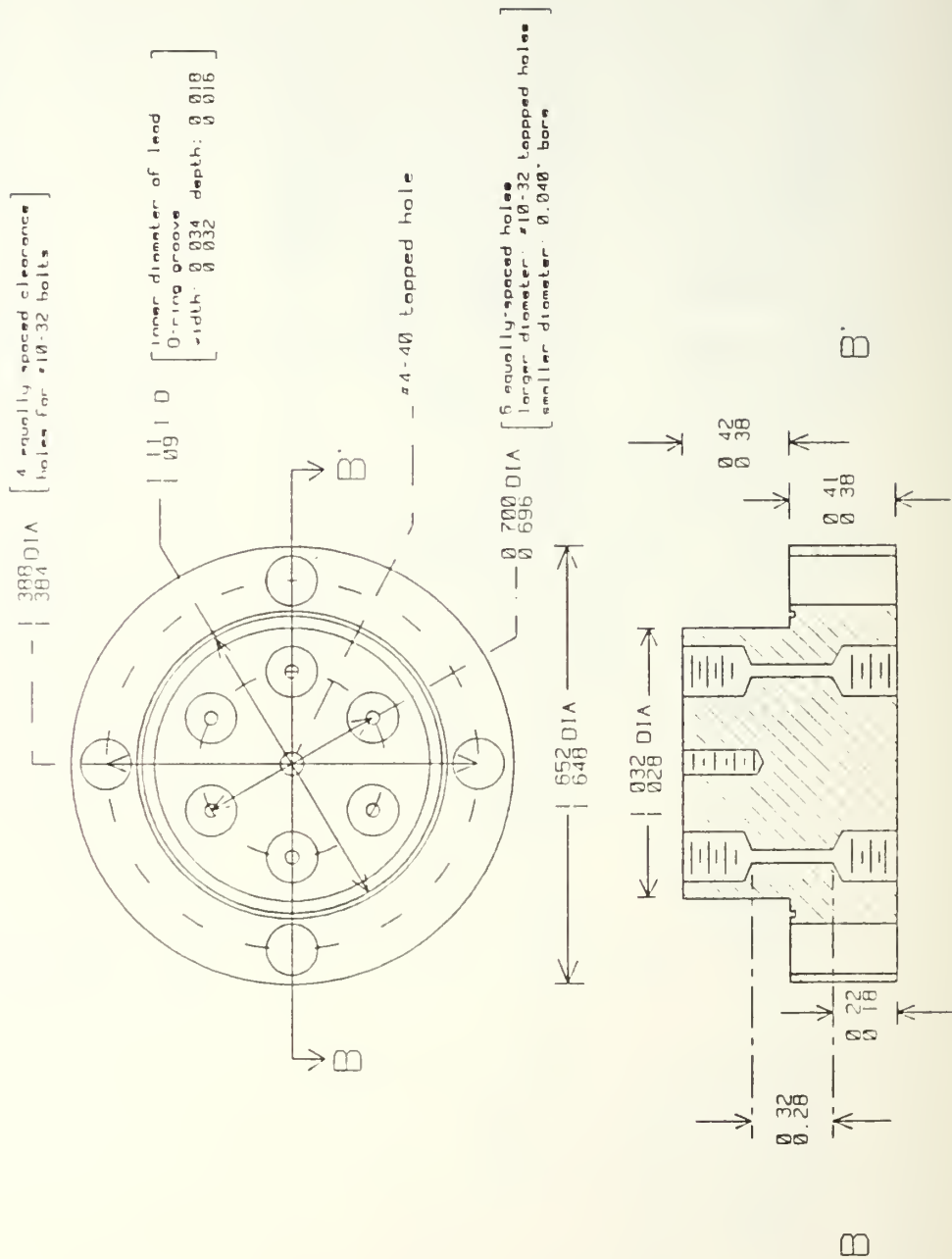


Figure C-15. The Electronics Feed-through Plug without Connectors or Fittings in Plane and Section Views

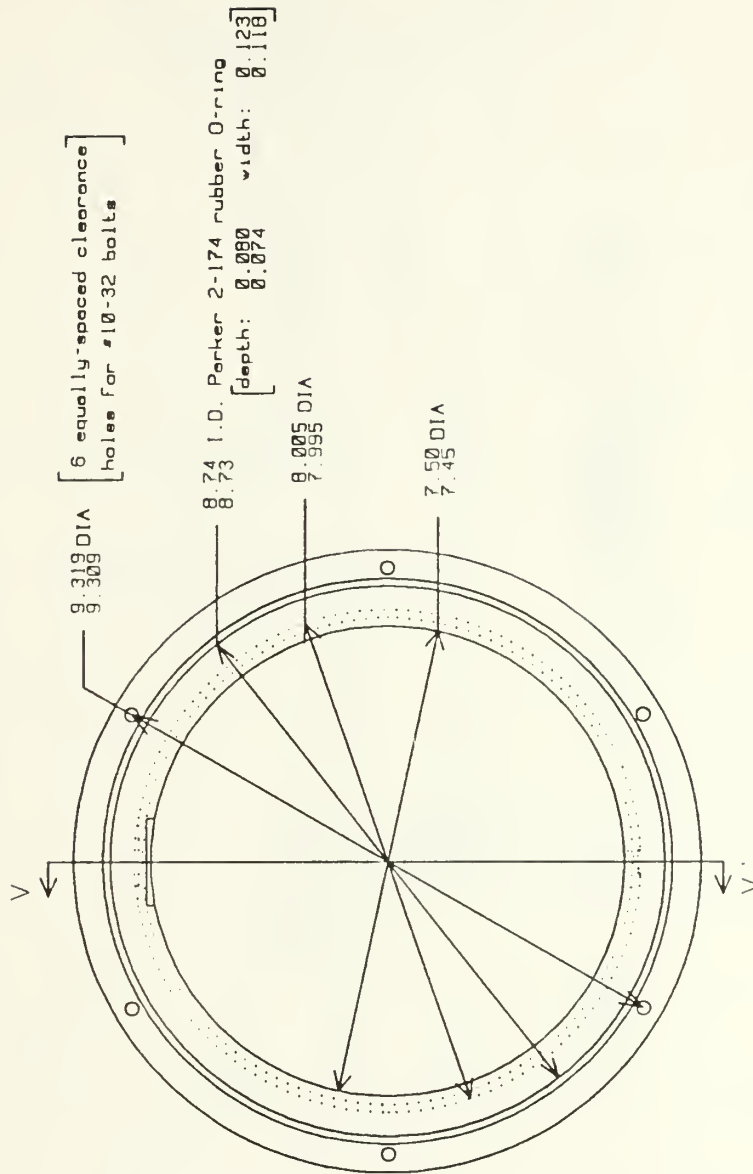


Figure C-16. Top View of the Vacuum Can Flange Section

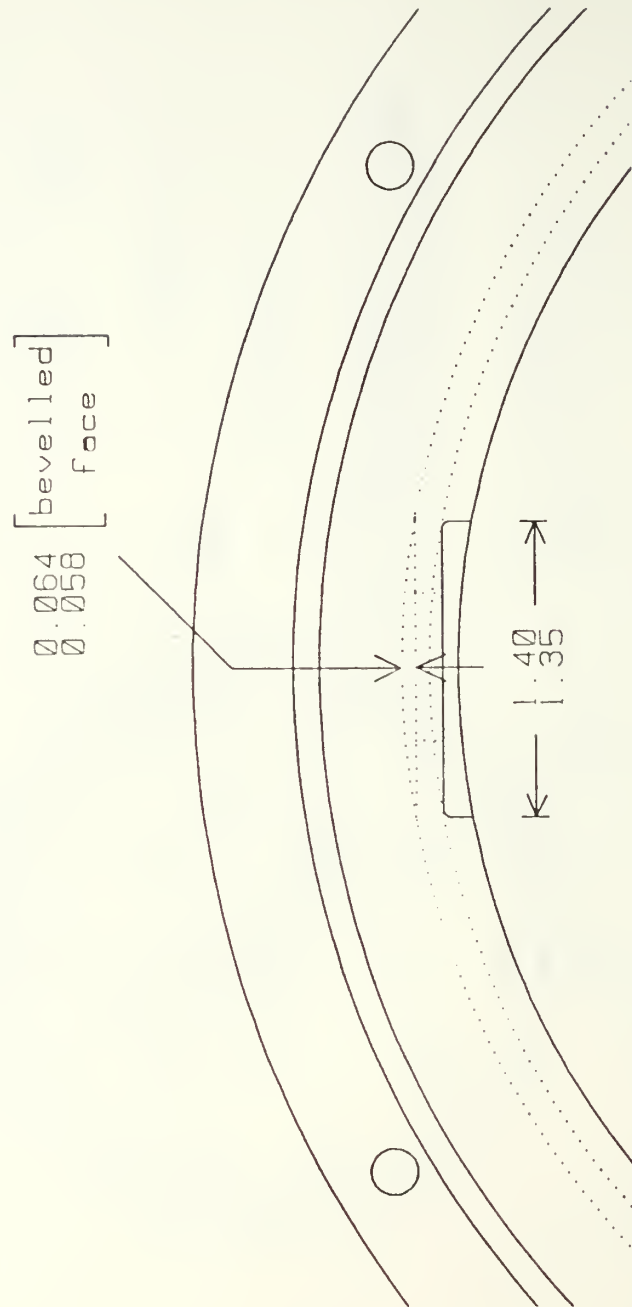
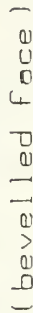


Figure C-17. Close-up Top View of the Vacuum Can Electronics Feed-through Port



179

APPENDIX D. DESCRIPTION OF THE STAR RESONATOR

This appendix is used to further describe the preliminary design of the STAR resonator mentioned in Chapter III. Design requirements for the resonator included the fact that the resonator must be able to effectively contain ten atmospheres of pressure, have low thermal conductivity across the FRP neck, and acoustically simulate an open ended tube. Figure D-1, is a scale drawing illustrating the initial resonator design that is presently being constructed.

All copper parts of the resonator were constructed from oxygen free, high conductivity copper which was chosen for high thermal conductivity. The component parts of the resonator include a copper flange (1) with eight #1/4"-20 bolt holes designed to allow the resonator to mate firmly to the driver housing. The groove on the bottom of the flange is designed for a lead O-ring, used to seal the resonator to the driver housing. A copper heat exchanger insert (2) is designed to fit within the flange, reducing the inside diameter of the flange to a 1.5" diameter. The primary function of the insert is to restrain the hot heat exchanger element (4) next to the thermoacoustic stack and provide a high thermal conductivity path from the heat exchanger to the driver. Connected to the flange is a 1.84" O.D. FRP

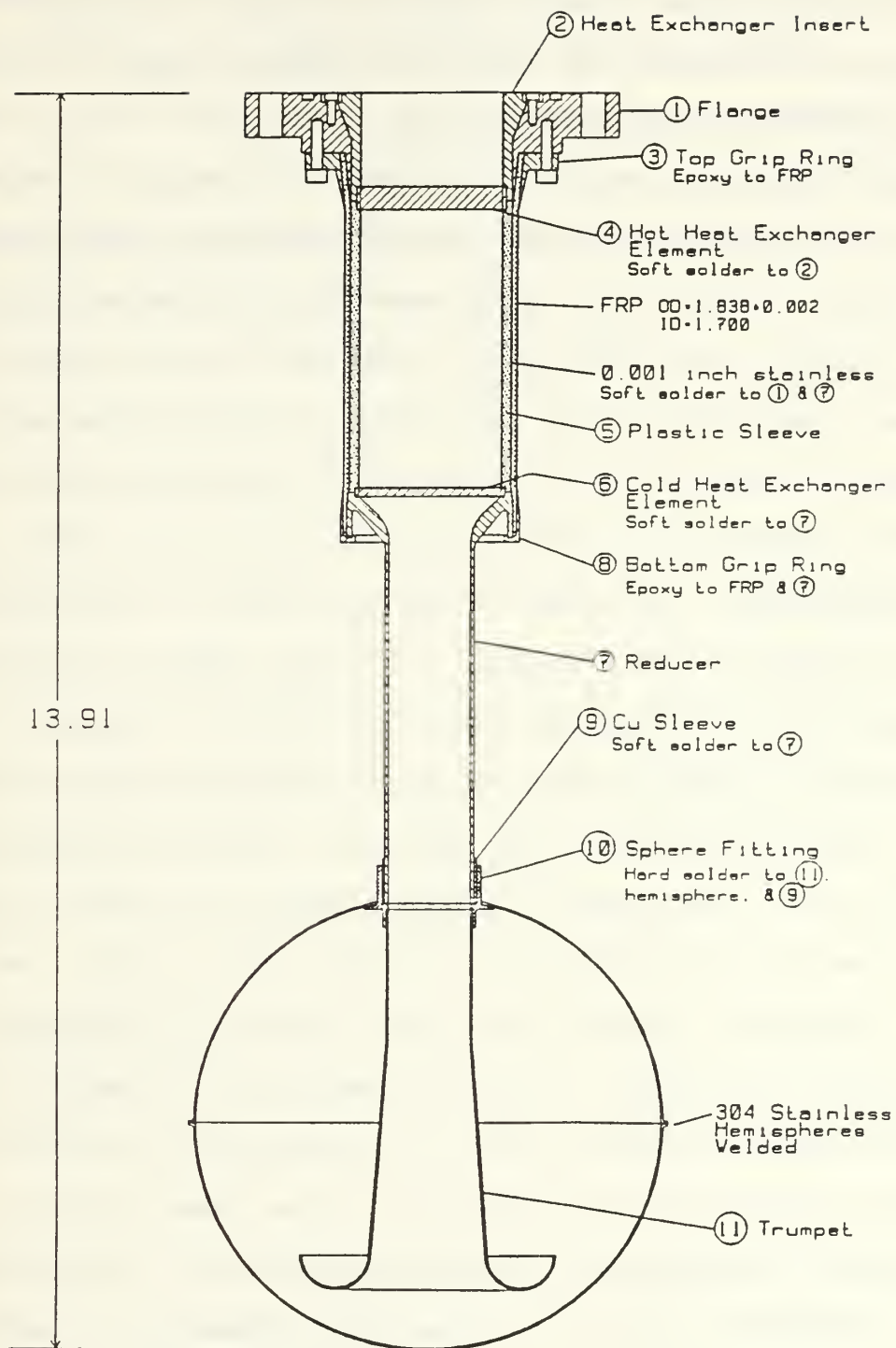


Figure D-1. Diagram of the STAR resonator

neck constructed as described in Chapter III. The FRP neck with its stainless steel liner is attached to the mating flange at its lower end and to the reducer tube (7) at its upper end by two grip rings (3,8).

The two grip rings are designed to provide the final element of the metal boundary required to prevent helium diffusion. On one side they are bonded to the FRP neck using epoxy, and on the other side they are attached to copper components of the resonator. This provides metal contact to the FRP both inside and out so that differential thermal expansion or contraction will place the FRP/Cu joint in compression. In order to prevent damage to the stainless steel lining of the FRP neck, a plastic insert is placed between the stack and the FRP. This plastic sleeve (5) also serves as a filler between the 1.5" diameter stack and the 1.7" inside diameter of the FRP neck. Below the plastic liner is the cold heat exchanger element (6) which is held in place by soft soldering it to the reducer tube. Both heat exchanger elements (4,6) are composed of multiple layers of thin copper strips as described in Chapter III.

The copper reducer tube (7) is designed to provide a smooth transition from the stack to the lower portion of the resonator-trumpet-sphere acoustical element. The tube is then connected to the stainless steel sphere by a copper sleeve (9), which is then hard soldered to a fitting piece designed to match the curve of the sphere (10). The

stainless steel sphere was chosen based upon its commercial availability and was used to simulate an open-ended tube. The final element of the resonator, the trumpet (11), is located within the sphere. The trumpet is designed to allow the pressure waves to transition into the spherical volume in a way that is smooth and does not cause excessive velocities in the oscillatory fluid.

APPENDIX E. MANUFACTURER SPECIFICATION SHEETS

This appendix contains the manufacturer's specification sheets for the following commercially available items used in the STAR project; (1) the PICOMIN™ Model 22 accelerometer, (2) the Emerson & Cuming STYCAST® 2850FT epoxy, (3) the Dexter HYSOL EA9396 adhesive, (4) the OMEGA® PX80 pressure transducer, and (5) the Servometer Corporations electroformed nickel bellows. The specifications sheet for the Y-cut quartz disk used in the construction of the driver microphone is also included in order to provide clarification of it's dimensions. Finally the manufacturer's specification sheets for the Eltec model 304 impedance converter is included, as are plots of the Eltec's measured performance as a function of current supply and driving voltage and a schematic diagram of the 304 and its constant current source.



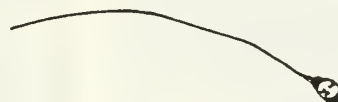
MODEL 22

140 milligram
Microminiature
PICOMIN®
ACCELEROMETER

The Endevco Model 22 Accelerometer is an extremely small, adhesive mounted accelerometer. Its small mass allows it to measure the vibration characteristics of very small test specimens or lightweight, thin structures, effectively eliminating mass loading effects.

The PICOMIN® Accelerometer features a broad frequency and wide temperature response. Base strain sensitivity is low, a characteristic of Endevco shear accelerometers. The unique replaceable cable interface with the Model 22 minimizes the spurious effects of cable strain and permits rapid replacement of damaged cables.

A hard anodized mounting surface provides electrical insulation from the test specimen and eliminates the effect of ground loop voltages. The Model 22 is a self-generating piezoelectric transducer and requires no external electric power for operation.



ACTUAL SIZE

SPECIFICATIONS FOR MODEL 22 ACCELEROMETER (According to ANSI and ISA Standards)

DYNAMIC

CHARGE SENSITIVITY ^{1,2}	0.4 pC/g typical; 0.3 pC/g minimum
VOLTAGE SENSITIVITY ^{1,3}	1.6 mV/g typical
MOUNTED RESONANCE FREQUENCY	54 000 Hz typical
FREQUENCY RESPONSE (charge) ⁴	±5% typical, ±7% maximum, 20 to 10 000 Hz, reference 100 Hz.

TRANSVERSE SENSITIVITY	5% maximum; 3% available on special order
AMPLITUDE LINEARITY, RANGE	Sensitivity increases approximately 1% per 250 g, 0 to 4000 g. ⁵

ELECTRICAL

TRANSDUCER CAPACITANCE	250 pF typical at 72°F (22°C), including 6 in. (150 mm) cable.
TRANSDUCER RESISTANCE	2 000 MΩ minimum at 72°F (22°C); 100 MΩ minimum at 350°F (177°C).
GROUNDING	Signal return connected to case. Anodized mounting surface provides electrical insulation.
INSULATION RESISTANCE ⁶	1 000 MΩ minimum at 100 V dc
INSULATION CAPACITANCE ⁶	50 pF typical

NOTES:

¹This unit has reverse polarity. A negative output is produced for an acceleration directed from the mounting surface into the body of the accelerometer. See ISA-AP37.2, 1964.

²Use Endevco Model 2640, 2680 or 2700 Series Charge Amplifier.

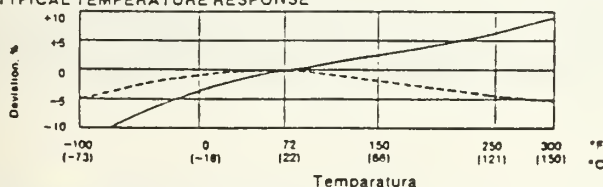
³With 6 in. (150 mm) replaceable Model 3003-B Cable Assembly, 250 pF total typical capacitance.

⁴In shock measurements, minimum pulse duration for half-sine or triangular pulse should exceed 0.10 ms to avoid excessive high frequency ringing. See Endevco Piezoelectric Accelerometer Manual.

⁵Shock induced zero shift, at room temperature, will be less than 3% of reading for shock levels 0 to 1 000 g. In the range of 1 000 to 4 000 g, the zero shift will be ±5% of reading, typical.

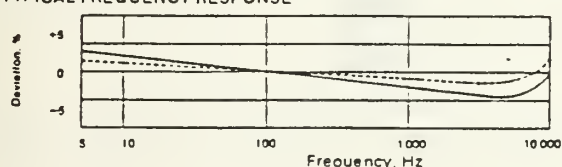
⁶Signal ground to mounting surface.

TYPICAL TEMPERATURE RESPONSE



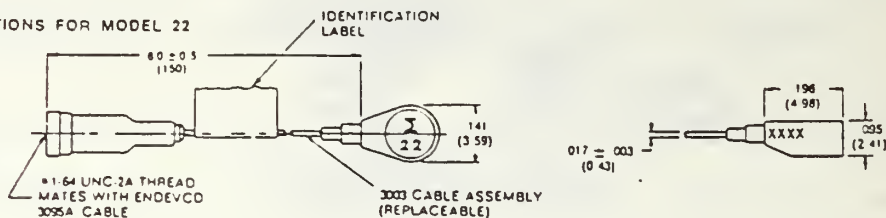
The solid curve shows the typical charge-temperature response. The broken line shows the typical voltage-temperature response with the 6-inch cable and 300 pF external capacitance.

TYPICAL FREQUENCY RESPONSE



The solid curve shows the typical charge-frequency response. The dashed line shows the typical voltage-frequency response with the two cables supplied (220 pF) and 350 MΩ or more of load resistance.

SPECIFICATIONS FOR MODEL 22



DIMENSIONS IN INCHES AND (MILLIMETRES)

PHYSICAL

DESIGN	Shear
CRYSTAL MATERIAL	PIEZITE® Type P-8
CASE MATERIAL	Aluminum Alloy
CASE FINISH	Hard anodize
WEIGHT	0.40 gram (2.0 carats) typical, with 6 inch (150 mm) cable; 0.14 gram (0.7 carat) typical, excluding cable.
CONNECTOR	Special connector mates with Model 3003-6 Cable Assembly
MOUNTING	Adhesive. Use Tool No. 17267 (supplied) to remove accelerometer. See Instruction Manual.
ACCESSORIES SUPPLIED	Model 3003-6 Low Noise Coaxial Cable Assembly, 6 inch (150 mm), stainless steel sheath, Kapton® polyimide jacket, capacitance 50 pF typical. Model 3095A-72 Coaxial Cable Assembly, 6 ft. (1.8m) with mating receptacle for 3003 assembly, 10-32 plug on other end, capacitance 180 pF typical. Model 17267 Tool for removal of accelerometer and 3003 cable
ACCESSORIES AVAILABLE	Model 3090C Low Noise Extension Cable Assembly and EJ34 Adapter Model 3093-12 with 10-32 female connector, 12 in. (0.3m)

ENVIRONMENTAL

ACCELERATION LIMITS*	10 000 g in any direction
TEMPERATURE RANGE	Operating: -100°F to +300°F (-73°C to 150°C) Non-Operating: -150°F to +350°F (-100°C to +177°C)
HUMIDITY†	Sealed with silicone compound. Tests indicate 48 hour protection against 97% R.H. at 140°F.
ALTITUDE	Not affected
BASE STRAIN SENSITIVITY	Typically 2.0 equivalent g at 250 µ strain
MAGNETIC SENSITIVITY	0.0009 equivalent g per gauss (10 ⁻⁷ T), typical at 100 g, 60 Hz
ACOUSTIC SENSITIVITY	0.008 equivalent g typical at 140 dB SPL

NOTES:

*When subjected to high displacement low frequency vibration, the cable must be tied down as close as possible to the accelerometer to prevent cable whip and eventual cable failure.

†Removing cable exposes accelerometer to the environment. See Model 22 Instruction Manual for removal instructions.

Continued product improvement necessitates that Endevco reserve the right to modify these specifications without notice.

RELIABILITY: Endevco maintains a program of constant surveillance over all products to ensure a high level of reliability. This program includes attention to reliability factors during product design, the support of stringent Quality Control requirements, and compulsory corrective action procedures. These measures, together with conservative specifications, have made the name Endevco synonymous with reliability. Endevco's Quality and Reliability System meets the requirements of MIL-Q-9858A and MIL-STD-785A.

CALIBRATION: Each unit is calibrated at room temperature for charge and voltage sensitivity, capacitance, maximum transverse sensitivity and charge frequency response from 20 Hz to 4000 Hz. Other calibrations such as Temperature Response at -100°F (-73°C), room temperature, 250°F (121°C), and 350°F (177°C) are available on special order. See Calibration Service Bulletin No. 301.

ENDEVCO

RANCHO VIEJO ROAD • SAN JUAN CAPISTRANO, CA 92675 • TELEPHONE (714) 493-8181

ANAHEIM, CA • ANNAPOLIS, MD • CHICAGO, IL • DAYTON, OH • HOUSTON, TX • LAMBERTVILLE, NJ • ORLANDO, FL • PALO ALTO, CA • W. MYSTIC, CT
ARGENTINA • AUSTRALIA • BRAZIL • CANADA • CHILE • FINLAND • FRANCE • INDIA • IRELAND • ITALY • JAPAN • KOREA • MALAYSIA • MEXICO
NETHERLANDS • NORWAY • SINGAPORE • SPAIN • SWEDEN • SWITZERLAND • TAIWAN • UNITED KINGDOM • URUGUAY • VENEZUELA • W. GERMANY

PRINTED IN U.S.A. REV 4/84

EMERSON & CUMING

TECHNICAL
BULLETIN

TECHNICAL BULLETIN 7-2-7A

STYCAST® 2850FT

Where there's a way.

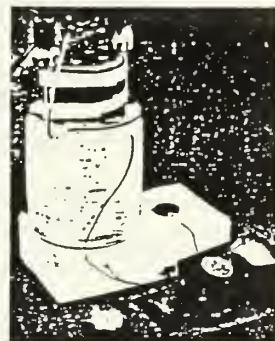
Versatile Epoxy Casting Resin
with High Thermal Conductivity



Giant Castings a Specialty With This Material



New Folder Available on
Other Thermal Conductive Materials



Precise Thermal Conductivity
Measurement of Sample Casting

STYCAST 2850FT is a highly filled epoxy formulation with remarkably good over-all general properties. In addition to having excellent electrical grade insulation properties and excellent resistance to chemicals and solvents, STYCAST 2850FT has unusually high thermal conductivity and low thermal expansion. This combination of properties has shown STYCAST 2850FT to be invaluable in solving problems where electrical insulation and mechanical protection must be maintained while coping with heat transfer considerations.

STYCAST 2850FT is excellent in high voltage applications, e.g. power supplies, transformers, bushings, insulators, etc. In some high voltage applications, the distance between electrodes may be critical and cause surface tracking when STYCAST 2850FT (Black) is used. The use of STYCAST 2850FT (Blue) will solve the problem.

Since STYCAST 2850FT has a slight settling problem, we recommend that the material be remixed before removal from the shipping container.

STYCAST 2850FT is a highly versatile epoxy resin system which may be cured with any one of three curing agents. The choice of catalyst should be made after reviewing your requirements with regard to the following guidelines.

CHOICE OF CURING AGENTS: From the information supplied, select the catalyst which best suits your requirements.

CATALYST 24LV - Room temperature curing - 30 minutes pot life, 1 lb. (0.45 kg) mass - lowest viscosity and best handling properties - generally does not require vacuum deairing - best thermal and mechanical shock - not recommended for applications subjected to temperatures above 250°F (121°C) - will soften slightly above 180°F (82°C) - best adhesion.

TYPICAL PROPERTIES (cured with Catalyst 11):

Cure Shrinkage, cm/cm	.001
Viscosity at 65°C (catalyzed with Cat. 11), cps	3,000
Viscosity at 25°C (catalyzed with Cat. 9), cps	90,000
Viscosity at 25°C (catalyzed with Cat. 24LV), cps	15,000
Thermal Conductivity, (BTU)(in)/(hr)(ft²)(°F)	10
(cal)(cm)/(sec)(cm²)(°C)	0.0014
Specific Gravity	2.3
Tensile Strength, psi (kg/cm²)	8,400 (588)
Compressive Strength, psi (kg/cm²)	16,500 (1,155)
Flexural Strength, psi (kg/cm²)	13,300 (931)
Flexural Modulus, psi (kg/cm²)	2 x 10 ⁸ (1.4 x 10 ⁷)
Elastic Modulus, compressive, psi	1.1 x 10 ⁶
(kg/cm²)	(7.7 x 10 ⁴)
Hardness, Shore D	94
Izod Impact, ft. lb./in. of notch	0.3
(Joules/cm)	(0.16)
Thermal Expansion Coefficient, /°C	29 x 10 ⁻⁶
/°F	16 x 10 ⁻⁶
Max. Service Temperature	400°F (205°C)
Water Absorption, 7 days	less than 0.15%
Volume Resistivity, ohm-cm. 77°F (25°C)	5 x 10 ¹⁶
302°F (121°C)	1 x 10 ¹²
Dielectric Constant, 60 Hz	6.5
1 kHz	6.3
1 MHz	5.9
Dissipation Factor, 60 Hz	0.02
1 kHz	0.008
1 MHz	0.02
Dielectric Strength, volts/mil	550
kv/mm	21.7
Machineability	Poor (must be ground)

continued

CATALYST 9 - Room temperature curing - 45 minutes pot life, 1 lb. (0.45 kg) mass - highest viscosity, but with modestly good handling properties - tough and rigid at all temperatures to 300°F (150°C).

CATALYST 11 - Requires oven cure - 4 hour pot life, 10 lb. (4.5 kg) mass - low viscosity with excellent handling properties - excellent thermal and mechanical shock - best electrical and physical properties at temperatures above 250°F (121°C) - can be used up to 400°F (205°C).

General Instructions: Mix the entire contents of the shipping container to a uniform consistency each time before removing material. Power mixing is preferred. Mold Release 122S will prevent adhesion to molds. Where necessary, entrapped air can be removed by vacuum deairing.

IF USING CATALYST 24LV

1. Add and thoroughly blend 6-1/2 to 7-1/2 parts of Catalyst 24LV by weight for each 100 parts by weight of STYCAST 2850FT. Slight warming, 100°F (38°C), of the resin before catalyst addition will aid pouring and hasten bubble release.
2. Pour into mold. Allow to cure at room temperature, 75°F (25°C), overnight or oven cure for 2 hours at 150°F (66°C).

IF USING CATALYST 9

1. Add and thoroughly blend 3 to 4 parts Catalyst 9 by weight for each 100 parts by weight of STYCAST 2850FT. Slight warming, 100°F (38°C), of the resin prior to adding catalyst will improve pourability. Small amounts (up to 10% by weight) of ECCOBOND® 55 mixed with Catalyst 9 (see Tech. Bull. 3-2-1) may be added to further lower viscosity with some sacrifice in properties.
2. Pour into mold. Allow to cure at room temperature, 75°F (25°C), overnight or oven cure for 2 hours at 150°F (66°C).

IF USING CATALYST 11

1. Add and thoroughly blend 4 to 5 parts by weight of Catalyst 11 for each 100 parts by weight of STYCAST 2850FT. STYCAST 2850FT may be heated at any temperature up to 165°F (74°C) before catalyst addition to lower viscosity and aid pourability.
2. Pour into mold. Cure at any of the following schedules: 16 hours at 180°F (82°C), 2 hours at 212°F (100°C), or 1 hour at 257°F (125°C).

For optimum high temperature performance and minimum coefficient of expansion, post cure for 4 hours at 300°F (150°C).

The shelf life of STYCAST 2850FT, when stored uncatalyzed, in unopened containers at temperatures no higher than 25°C is 6 months.

The handling of this product should present no problems if care is exercised to avoid breathing excessive amounts of the vapors, and if the skin is protected against contamination. The eyes should be protected. Observe precautions in Public Health Service Publication No. 1040, May 1963, Superintendent of Documents, U. S. Government Printing Office, Washington D. C. 20402.

This information, while believed to be completely reliable, is not to be taken as warranty for which we assume legal responsibility nor as permission or recommendation to practice any patented invention without license. It is offered for consideration, investigation, and verification.

DEXTER HYSOL

EA 9396

AEROSPACE ADHESIVE PRODUCTS

DESCRIPTION

EA 9396 is a low viscosity, room temperature curing adhesive system with excellent strength properties at temperatures from -67°F to 350°F. EA 9396 has a shelf life of ten months when stored at 77°F for separate components.

FEATURES

- Low Viscosity
- Long Shelf Life at 77°F
- Cures at Room Temperature
- High Strength at Low and High Temperatures

UNCURED ADHESIVE PROPERTIES

	Part A	Part B	Mixed
Viscosity @ 77°F	800-1200 Poise	1 Poise	30-40 Poise
Shelf Life @ <40°F @ 77°F	1 year 10 months	1 year 1 year	

This material will normally be shipped at ambient conditions, which will not alter our standard warranty, provided that the material is placed into its intended storage upon receipt. Premium shipment is available upon request.

HANDLING

Mixing - This product requires mixing two components together just prior to application to the parts to be bonded. Complete mixing is necessary. The temperature of the separate components prior to mixing is not critical, but should be close to room temperature.

Mix Ratio	Part A	Part B
By Weight	100	30

Note: Volume measurement is not recommended for structural applications unless special precautions are taken to assure proper ratios.

Pot Life (450 gm mass) 75-90 minutes
Method - ASTM D 2471 in water bath

APPLICATION

Mixing - Combine Part A and Part B in the correct ratio and mix thoroughly. THIS IS IMPORTANT! Heat buildup during or after mixing is normal. Do not mix quantities greater than 250 grams as dangerous heat buildup can occur causing uncontrolled decomposition of the mixed adhesive. TOXIC FUMES CAN OCCUR, RESULTING IN PERSONAL INJURY. Mixing smaller quantities will minimize the heat buildup.

Applying - Bonding surfaces should be clean, dry and properly prepared. For optimum surface preparation consult Hysol Bulletin G1-600 "Preparing the Surface for Adhesive Bonding." The bonded parts should be held in contact until the adhesive is set. Handling strength for this adhesive will occur in 24 hours at 77°F after which the support tooling or pressure used during cure may be removed. Since full bond strength has not yet been attained, load application should be small at this time.

Curing - EA 9396 may be cured for 5-7 days at 77°F to achieve normal performance. Accelerated cures of 1 hour at 150°F or at 180°F may be used.

Cleanup - It is important to remove excess adhesive from the work area and application equipment before it hardens. Denatured alcohol and many common industrial solvents are suitable for removing uncured adhesive. Consult with your supplier's information pertaining to the safe and proper use of solvents.

BOND STRENGTH PERFORMANCE

Tensile Lap Shear Strength Tensile lap shear strength tested per ASTM D 1002. Adherends are 2024-T3 clad aluminum treated with phosphoric acid anodize per BAC 5555. (Values are expressed in PSI)

<u>Test Temperature, °F</u>		<u>-67</u>	<u>75</u>	<u>180</u>	<u>300</u>	<u>350</u>
Cure	5 days @ 77°F	3300	4000	3200	1800	1500
	1 hour @ 150°F	3300	4200	3300	1800	1200
	30 min. @ 180°F	3500	4200	3300	1900	1200

Peel Strength

Beil Peel strength tested per ASTM D 3167 after curing for 5 days at 77°F. Adherends are 2024-T3 clad aluminum treated with phosphoric acid anodize per BAC 5555.

<u>Test Temperature, °F</u>	<u>Typical Results (PLI)</u>
77	25
180	20

Service Temperature

Service temperature is defined as that temperature at which this adhesive still retains 1000 PSI using test method ASTM D 1002 and is 300 F.

HAZARD WARNING

For Industrial Use Only!

PART A

CAUTION! The uncured adhesive causes eye irritation and may cause skin irritation as allergic dermatitis. Contains epoxy resins. Use good ventilation. Avoid contact with eyes or skin. Wash thoroughly with soap and water after handling. Do not handle or use until the Safety Data Sheet has been read and understood. Do not cut or weld empty container.

PART B

DANGER! Causes severe skin and eye burns. Do not get in eyes, on skin or on clothing. Wash thoroughly after handling. Vapors may be irritating to the respiratory tract. Avoid breathing vapor. Keep container tightly closed. Use only with adequate ventilation. Do not cut or weld empty container. Do not handle or use until Safety Data Sheet has been read and understood. These warnings are based on *Guides for Classifying and Labeling Epoxy Products According to Their Hazardous Potentialities* prepared by the Epoxy Resin Formulators Division and the Society of the Plastics Industry, Inc., and based on ANSI Z129 standard.

AVAILABILITY

This product is available from Hysol Aerospace and Industrial Products Division, 2850 Willow Pass Road, P.O. Box 312, Pittsburg, CA 94565-3299. Telephone 415 687-4201. TWX 910 387-0363.

Revised 2/88

Properties listed are typical values and are not intended for use in preparing specifications. Actual values may vary. Recommendations and suggestions contained herein are limited to reasonable commercial use. No express warranties are intended by any representation and there are no warranties which extend beyond the description on the face hereof. The user is advised to use either first and cure conditions when evaluating this adhesive that are as representative as possible of those used in the actual manufactured item.

HYSOL

AEROSPACE & INDUSTRIAL PRODUCTS DIVISION

2850 Willow Pass Road, P.O. Box 312, Pittsburg, CA 94565
Phone (415) 687-4201 TWX 910 387-0363

A DIVISION OF THE SPECIALTY CHEMICALS & SERVICES GROUP
THE DEXTER CORPORATION

5 88 14

PX80 & PX90 SERIES SPECIFICATIONS

Supply Current = 1.5 mA & Ambient Temperature = 25°C (Unless otherwise specified)

PARAMETER	PRESSURE RANGE						UNITS	NOTES
	300, 500 psi			1000, 3000 psi				
	MIN	TYP	MAX	MIN	TYP	MAX		
Full-Scale Output Span		100			250		mV	2
Zero Pressure Output			5			5	± mV	2,3,4
Static Accuracy			0.5			0.5	± %Span	5
Input & Output Resistance	4000	5000	6000	4000	5000	6000	Ω	
Temperature Coefficient-Span			1.0			1.0	± % Span	1,2,3
Temperature Coefficient-Zero			1.0			1.0	± % Span	1,2,3
Supply Current		1.5	2.0		1.5	2.0	mA	6
Output Load Resistance	2			2			MΩ	7
Insulation Resistance (50VDC)	50			50			MΩ	
Pressure Overload			3X			3X	Rated	8
Operating Temperature	-40 °C to +125 °C							
Storage Temperature	-65 °C to +150 °C							
Media	Compatible with 316 Stainless Steel							
Weight	8 Grams							

SPECIFICATION NOTES

1. Temperature range: 0° to 50°C in reference to 25°C.
2. With external resistors (R1 or R2), (R3 or R4) and R5 included in circuit shown in Figure 1. If R1 is required then R2 is left open (R2 = ∞) and vice versa. If R3 is required then R4 is a short (R4 = 0) and vice versa.
R3 or R4 is used for OFFSET COMPENSATION
R1 or R2 is used for THERMAL OFFSET COMPENSATION
R5 is used for THERMAL SPAN COMPENSATION
Positive offset is when the voltage at Pin 4 is higher than at Pin 1. Positive offset is compensated by adding R4 and shorting R3. For negative offset compensation the reverse is true.
Positive thermal offset is when thermal effects cause the voltage at Pin 4 to increase faster than at Pin 1. Positive thermal offset is compensated by adding R1 and leaving R2 open. For negative thermal offset compensation the reverse is true.
3. A computer printout is supplied with each sensor detailing the values of the 3 required external resistors along with open and short information for the other two locations.
4. Vacuum for absolute and one standard atmosphere for sealed gage.
5. Includes repeatability, pressure hysteresis and linearity (best fit straight line).
6. Guarantees output/input ratiometricity.
7. Prevents increase of TC-Span due to output loading.
8. 3X or 10,000 psi maximum whichever is less.

WARRANTY

OMEGA warrants this unit to be free of defects in materials and workmanship and to give satisfactory service for a period of 12 months from date of purchase. OMEGA Warranty adds an additional one (1) month grace period to the normal one (1) year product warranty to cover handling and shipping time. This ensures that our customers receive maximum coverage on each product. If the unit should malfunction, it must be returned to the factory for evaluation. Our Customer Service Department will issue an Authorized Return (AR) number immediately upon phone or written request. Upon examination by OMEGA, if the unit is found to be defective it will be repaired or replaced at no charge. However, this WARRANTY is VOID if the unit shows evidence of having been tampered with or shows evidence of being damaged as a result of excessive current, heat, moisture, vibration or misuse. Components which wear or which are damaged by misuse are not warranted. These include contact points, fuses and traces.

THERE ARE NO WARRANTIES EXCEPT AS STATED HEREIN. THERE ARE NO OTHER WARRANTIES, EXPRESSED OR IMPLIED, INCLUDING BUT NOT LIMITED TO THE IMPLIED WARRANTIES OF MERCHANTABILITY AND OF FITNESS FOR A PARTICULAR PURPOSE. IN NO EVENT SHALL OMEGA ENGINEERING, INC. BE LIABLE FOR CONSEQUENTIAL, INCIDENTAL OR SPECIAL DAMAGES. THE BUYER'S SOLE REMEDY FOR ANY BREACH OF THIS AGREEMENT BY OMEGA ENGINEERING, INC. OR ANY BREACH OF ANY WARRANTY BY OMEGA ENGINEERING, INC. SHALL NOT EXCEED THE PURCHASE PRICE PAID BY THE PURCHASER TO OMEGA ENGINEERING, INC. FOR THE UNIT OR UNITS OR EQUIPMENT DIRECTLY AFFECTED BY SUCH BREACH.



One Omega Drive, Box 4047
Stamford, Connecticut 06907-0047
(203) 359-1660 Telex 996404 Cable OMEGA
FAX (203) 359-7700

Printed in U.S.A.

Return Requests/Inquiries

Direct all warranty and repair requests/inquiries to OMEGA Customer Service Department, telephone number (203) 359-1660. Before returning any instrument, please contact the OMEGA Customer Service Department to obtain an authorized return (AR) number. The designated AR number should then be marked on the outside of the return package.

To avoid processing delays, also please be sure to include:
1. Returnee's name, address and phone number.
2. Model and Serial numbers.
3. Repair instructions.

OMEGA® is a registered trademark of OMEGA ENGINEERING, INC.

© Copyright 1988 OMEGA ENGINEERING, INC. All rights reserved, including illustrations. Nothing in this manual may be reproduced in any manner, either wholly or in part for any purpose whatsoever without written permission from OMEGA ENGINEERING, INC.

M566/106

SERVOMETER

Q 82-1352

PROPOSED ELECTROFORMED NICKEL BELLOWS DESIGN

SK - 11397 REV 'A'

Customer LOS ALAMOS NATIONAL LAB

Application Engineer

Address GROUP P-10 MS M754

PETER L. THOMPSON

LOS ALAMOS, NM 87545

Date 12/27/82

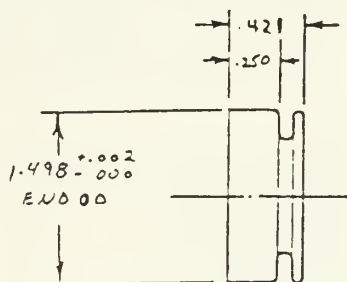
Engineer JOHN WHEATLEY

P/N

Telephone (505) 567-7499 Ext.

Inquiry

TYPE 'A'
OPEN END



REV 'A': 1.498 ± .002 00
WAS 1.495 ± .002 10
P/LT 1/4/82

TOLERANCES		
.XX	=	±.015
.XXX	=	±.005

Bellows O.D. (in.) = 1.500
 Bellows I.D. (in.) = 1.000
 Convolution Pitch (in.) = .171
 Wall Thickness (ref.) = .0025
 Effective Area (in.)² = 1.156
 No. Grooves = 1
 Convolutions Active:
 Before Assembly = 1.5
 After Assembly = 1.5
 Max. Allowable Axial Stroke:
 Compression (in.)* = .050
 Extension (in.)* = .050
 Max. Pressure Ratings (psi):
 Working-@50% Stroke = 30
 Proof-@Free Length = 50
 Burst-@Free Length = 70
 Buckling-@ " (int.) = 700
 Spring Rate (lbs./in.)
 @ .010 comp/rev: 175
 Before Assembly = 21 7 3.8 · 10³ N/mm
 After Assembly = 21
 Spring Rate Tolerance = ±30%

Max. Bend Angle (degrees)* = N/A
 Max. Off-Set Rating (in.)* = N/A
 Min. Life Expectancy (cycles) = ∞
 Regular Nickel For Soldering YES
 Sulfur-Free Nickel For Welding
 Or Corrosion Resistance NO
 Gold Plate: Yes No
 Class Type Grade

Other Finish
 Leak Test: Yes No X

Notes:
 1. Max. Operating Temp. For Continuous Usage 350°F (260°F If Solder Ass'y.).
 2.*-Values Are Mutually Exclusive. If Combinations Of These Are Required, Please Consult Us.
 3. Bellows Normally Have A .0001 Inch Copper Lamina Which Is Centered In Wall.

BRANCH OFFICES:
Chicago, Illinois
Philadelphia, Pennsylvania

International Testing Laboratories, Inc.

Materials Testing and Consulting Engineers

578-582 MARKET STREET
NEWARK, N. J. 07102

Phone 527-1201 527-1773-5-6

Cable Address: INTEL

Telex: 139187

METALLURGICAL REPORT

No. S34729 DATE February 2, 1988

From Servometer Corporation
501 Little Falls Road
Cedar Grove, New Jersey 07009

Sample of : Electro-Deposited Sheet Metal

Marked : SERVOMETER CORPORATION
501 Little Falls Road
Cedar Grove, New Jersey 07009
MATERIAL : REGULAR NICKEL
Purchase Order No. 17120

RESULTS :

PHYSICAL TESTS

Tensile Strength, PSI : 172,500
Yield Strength, PSI : 136,400
Elongation in 2 inches : 2.00%

VICKERS HARDNESS, 500 Gram Load

488

CHEMICAL ANALYSIS

Nickel + Cobalt : 99.92%
Sulphur : 0.018%

To Servometer Corporation
Cedar Grove, New Jersey 07009

INTERNATIONAL TESTING LABORATORIES, INC.

The liability of the International Testing Laboratories, Inc. with respect to the services rendered for herein shall in no event exceed the amount of the invoice. Our reports pertain to the sample tested only. Information obtained herein is not to be reproduced, except with our permission.

David H. Hoffman

INT. LAB. REV. 100-10007



CORPORATION miniature metal bellows
501 LITTLE FALLS ROAD
CEDAR GROVE, NEW JERSEY 07009
AREA CODE 201 785-1630

CUSTOMER: Naval Postgraduate School
CUSTOMER'S PURCHASE ORDER NUMBER: N62271-89-M-0440
SHIPMENT DATE: February 7, 1989
CONTENTS OF SHIPMENT: 20 Pcs. SK-11397 Rev. A Bellows

Drawing: Dimensions and tolerances: X

Materials: Bellows: Servometer Spec. N99100 X

Joints:

End Fittings:

Other:

Physical and chemical test reports enclosed

Finish: _____

Performance: Designed: _____ X _____
Tested: _____

Spring rate: Tested: _____ 100% _____

Load rate: Tested: _____ N/A _____


Servometer Corporation

Glenn A. Weinrich Q.A. Mgr.

S-82

Y-cut quartz disk, fine lapped finish. Thickness is $\frac{0.0041}{0.0035}$ inch.

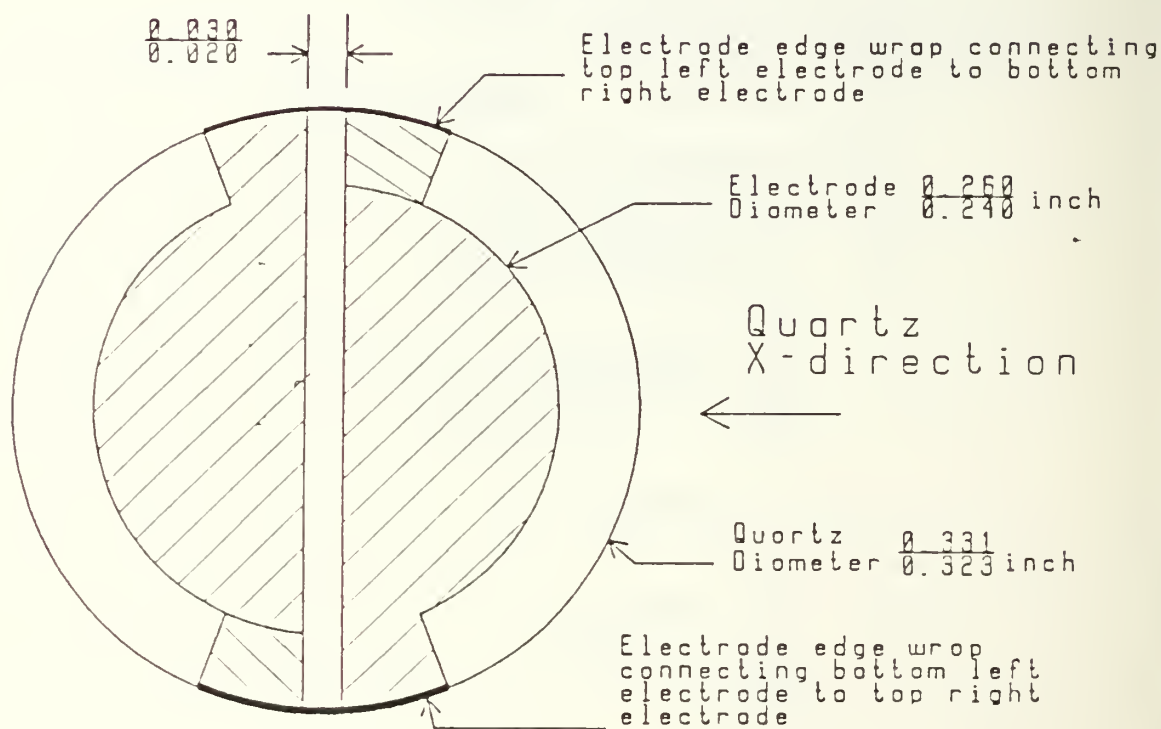


Figure E-1. Dimensions of Valpey-Fisher Quartz Disk Showing Electrode Configuration

IMPEDANCE CONVERTERS

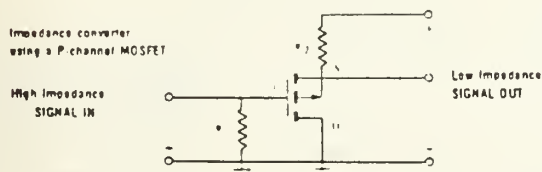
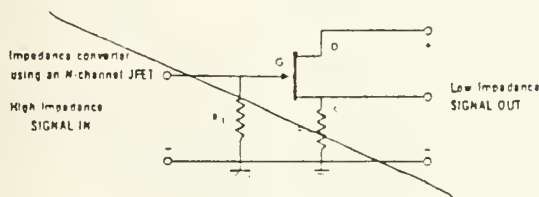
MODEL 304 impedance converter has the complete circuit, bias resistor R_1 , source resistor R_2 and the FET sealed into a standard TO-72 transistor housing.

R_1 , R_2 , and the FET can be specified.

Sockets made from Teflon and polyester are available for applications requiring removal of the circuit for testing, cleaning or exchange.

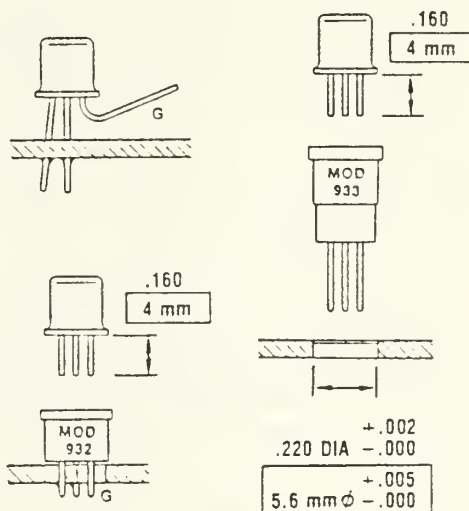


	N ch. JFET	P ch. MOSFET
1	S	D
2	D	G
3	G	S
4	GND	



DESIGN

The connection to the gate terminal is the most critical connection. At the gate, the signal is still a high impedance voltage signal. Care must be taken to assure the connection to the gate terminal is not influenced by noise or a relative low insulation resistance which would lower the input impedance and increase the noise of the impedance converter.



The following plug-in sockets are recommended:

- Eltec model 932, Teflon (shown)
- Eltec model 933, Teflon (shown)
- Eltec model 934, Polyester, (see 932)

IMPEDANCE CONVERTERS

Impedance converters change difficult to measure high impedance voltage signals into easily measured low impedance voltage signals.

They effectively convert the electrical charge or output from a high impedance sensor into useable voltage signals.

Exhibiting near unity gain, impedance converters generally consist of a FET, a high megohm resistor for biasing and a low value resistor in the output circuit.

The FET senses the formed charge or voltage stored in the input capacitance at the gate and this effects a proportional change in source to drain current.

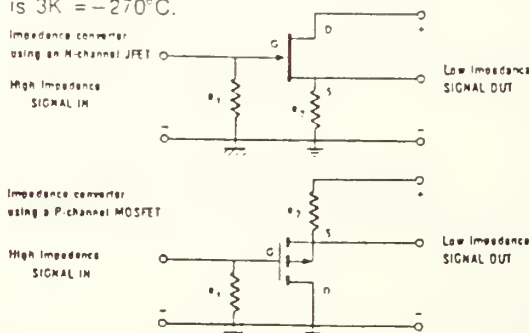
The high megohm resistor R_1 connects the gate of the FET to a fixed or zero bias level and continually discharges the input capacitance at a rate depending upon its resistance value.

The change in source to drain current mentioned above creates an output voltage signal across the low value resistor R_2 in the output circuit. This signal is at a low impedance level.

Two basic types of FET's can be used:

JFETs exhibit very low noise at RT. The gate reverse current I_{gss} changes with operating temperature. It doubles for every 10°C increase in temperature. It decreases the same ratio for decrease in temperature. The lowest operating temperature is about 73K = -200°C.

MOSFET's exhibit relative higher noise at RT. The gate reverse current I_{gss} does not change with temperature. Lowest operating temperature is 3K = -270°C.



SPECIFICATIONS

Using an N-channel JFET

Pinch-off voltage $V_{GS(off)}$	-1V max
Maximum voltage BV_{GSS}	-50 V
Input impedance	$2 \times 10^9 \Omega$
Output impedance	5 k Ω
Noise (DC-100 kHz) @ 1V	6 μ V rms
Gate reverse current $I_{gss@RT}$	0.1 nA
Operating current	80 μ A
Maximum drain current I_{DSS}	0.6 mA
Gain	0.7
Operating temperature	-55°C to +150°C

SPECIFICATIONS

Using a P-channel MOSFET

Threshold voltage $V_{GS(th)}$	-5V max
Maximum voltage BV_{GSS}	± 40 V
Input impedance	$5 \times 10^{11} \Omega$
Output impedance	6.2 k Ω
Noise (DC-1MHz) @ 12V	25 μ V rms
Gate reverse current I_{gss}	-10pA max
Operating current $I_{D(on)}$ $V_{GS} = V_{GS} - 12V$	-2.5 mA
Maximum drain current I_{DSS}	-50 mA
Gain	0.95
Operating temperature	-55°C to +150°C

Prototype and production quantities can be made to meet specific applications.

The customer must specify:

- 1- Bias resistor R_1 : Any Eltec high megohm resistor value, up to $1 \times 10^{12} \Omega$.
- 2- Source resistor R_2 : Any standard resistor value and tolerance.
- 3- Transistor: Specify FET and/or specific requirements.

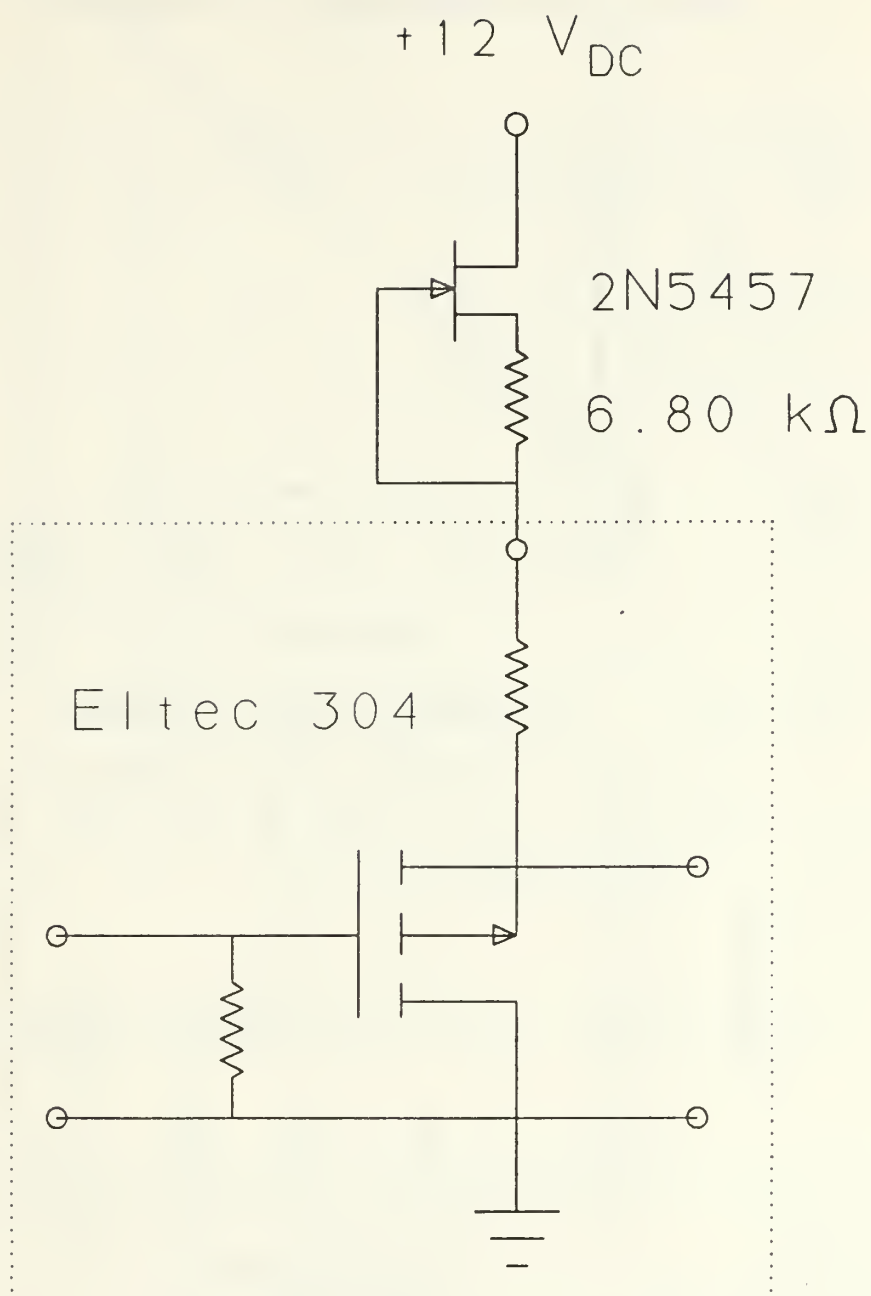
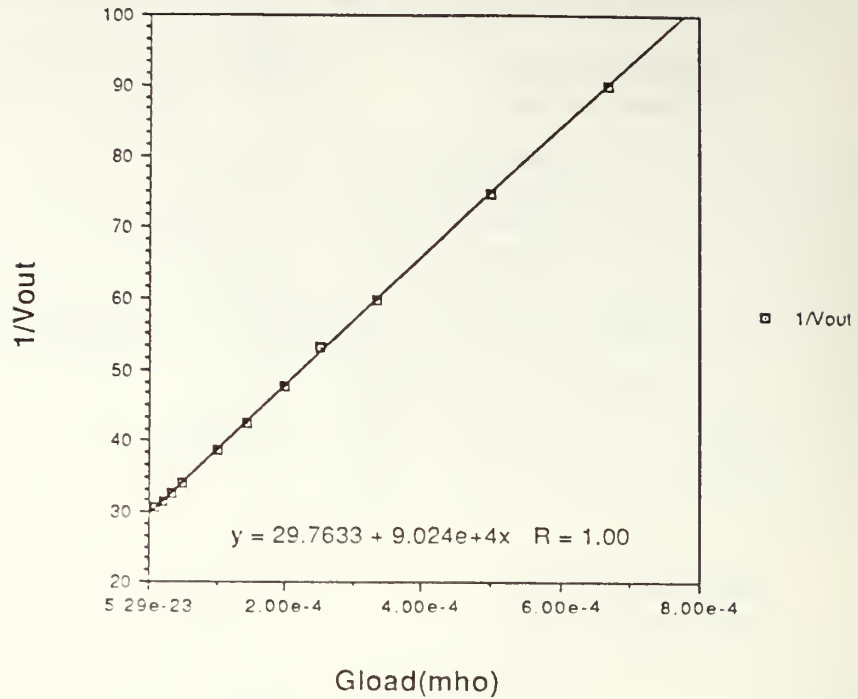


Figure E-2. Schematic of Eltec Impedance Converter with Constant Current Source Circuitry

Eltec Output Impedance



Current Supply Dropout

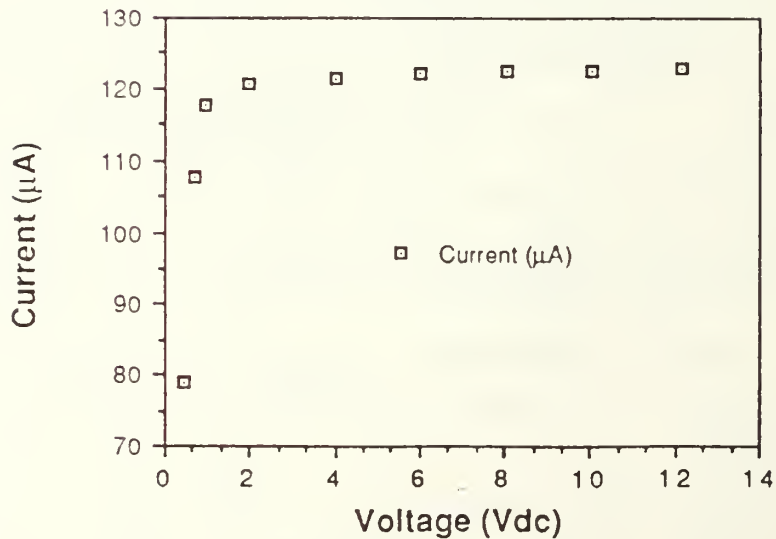


Figure E-3. Eltec 304 Output Impedance and Current Supply Dropout Curves
 a. Based on the slope, the output impedance of the microphone pre-amp is 3.03 k Ω
 b. Supply current is maintained constant to voltages as low as 2 V_{DC}

APPENDIX F. GAS DISTRIBUTION SYSTEM

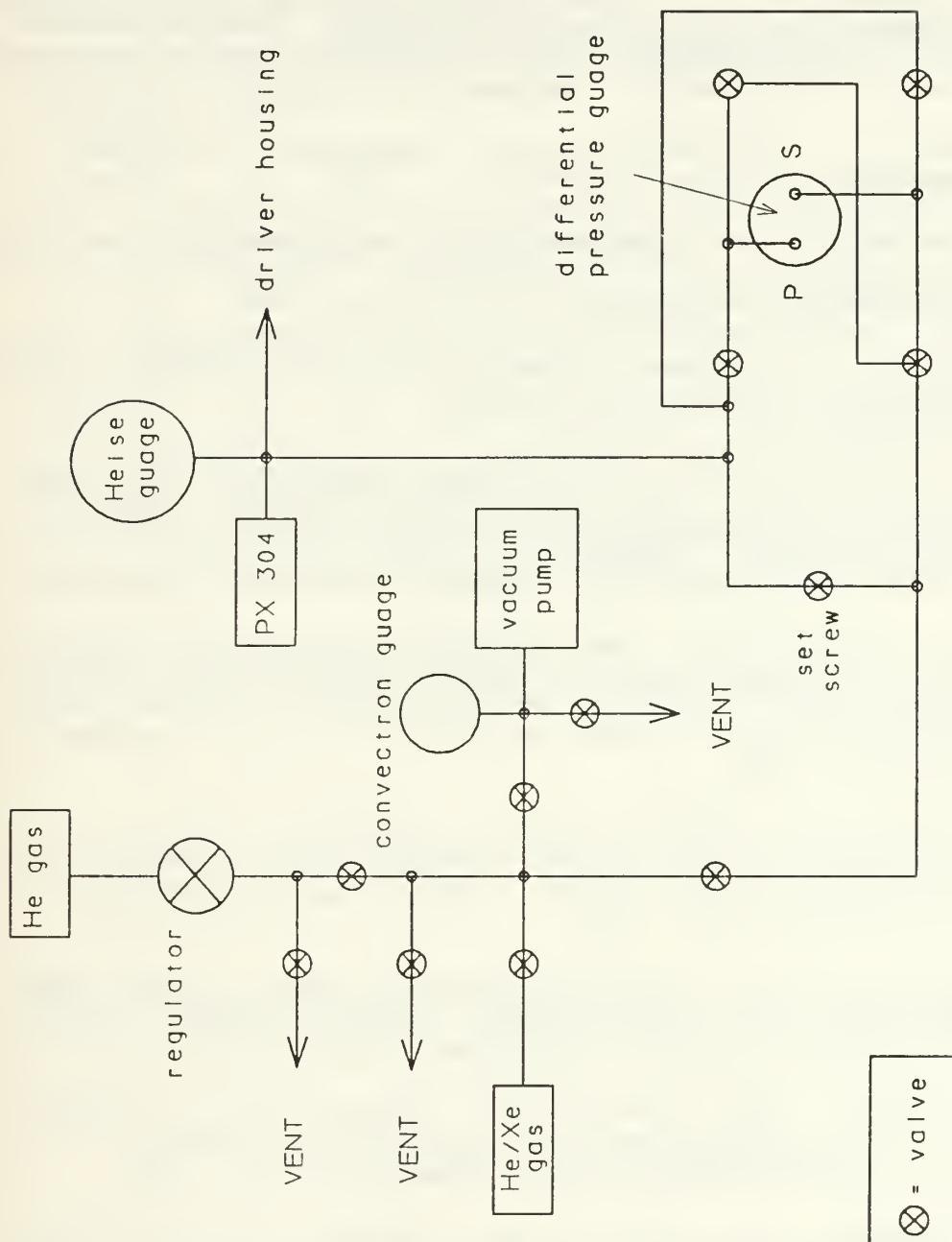


Figure F-1. Gas Distribution System

REFERENCES

1. Fitzpatrick, M., Electrodynamic Driver for the Space Thermoacoustic Refrigerator (STAR), Masters Thesis, Naval Postgraduate School, Monterey, California, March 1988. [DTIC Report No. ADA 192 337]
2. Rott, N., "Thermoacoustics", Advances in Applied Mechanics, Vol. 20, 1980.
3. Hofler, T. J., Thermoacoustic Refrigeration Design and Performance, Ph.D. Dissertation, University of California, San Diego, California, 1986.
4. Swift, G.W., "Thermoacoustic Engines", Journal of the Acoustical Society of America, Vol. 84(4), p.1145, 1988.
5. Susalla, M. P., Thermodynamic Improvements for the Space Thermoacoustic Refrigerator (STAR), Masters Thesis, Naval Postgraduate School, Monterey, California, June 1988. [DTIC Report No. ADA 196 958]
6. Get Away Special Team, Get Away Special (GAS) Small Self-contained Payloads--Experimenter Book, National Aeronautics and Space Administration, Goddard Space Flight Center, Special Payloads Division, Greenbelt, MD, July 1984.
7. Boyd, A.W., Kosinski, B.P., and Weston, R.L., "Autonomous Measurement of Space Shuttle Payload Bay Acoustics During Launch", Naval Research Reviews, Vol. 39(1), p.9, 1987.
8. Byrnes, R. B., Control and Measurement of the Space Thermoacoustic Refrigerator, Masters Thesis, Naval Postgraduate School, Monterey, California, June 1989.
9. Kinsler, L.E., Frey, A.R., Coppens, A.B., Sanders, J.V., Fundamentals of Acoustics, Third Edition, p.2, John Wiley and Sons, Inc., New York, NY, 1982.
10. Kinsler, L.E., Frey, A.R., Coppens, A.B., Sanders, J.V., Fundamentals of Acoustics, Third Edition, pp.231-235, John Wiley and Sons, Inc., New York, NY, 1982.

11. Hofler, T.J., Wheatley, J.C., Swift, G.W., and Migliori, A., "Acoustic Cooling Engine", U.S. Patent 4,722,201, 2 February 1988.
12. Landau, L.D. and Lifshitz, E.M., Fluid Mechanics, Pergamon Press Inc., Elmsford, NY, 1959.
13. Hofler, T. J., "Accurate Acoustic Power Measurements with a High-intensity Driver", Journal of the Acoustical Society of America, Vol. 83(2), p.777, February 1988.
14. Kinsler, L.E., Frey, A.R., Coppens, A.B., Sanders, J.V., Fundamentals of Acoustics, Third Edition, p.16, John Wiley and Sons, Inc., New York, NY, 1982.
15. Kinsler, L.E., Frey, A.R., Coppens, A.B., Sanders, J.V., Fundamentals of Acoustics, Third Edition, pp.351-353, John Wiley and Sons, Inc., New York, NY, 1982.
16. Kinsler, L.E., Frey, A.R., Coppens, A.B., Sanders, J.V., Fundamentals of Acoustics, Third Edition, p.208, John Wiley and Sons, Inc., New York, NY, 1982.
17. McCarty, R.D., Computer code HELIUM, National Institute of Standards and Technology, Boulder, CO, 1986.

INITIAL DISTRIBUTION LIST

	No. Copies
1. Library, Code 0142 Naval Postgraduate School Monterey, CA 93943-5002	2
2. Professor S.L. Garrett, Code 61GX Naval Postgraduate School Monterey, CA 93943-5000	6
3. Dr. T.J. Hofler, Code 61HF Naval Postgraduate School Monterey, CA 93943-5000	3
4. Professor A.A. Atchley, Code 61AY Naval Postgraduate School Monterey, CA 93943-5000	1
5. Commanding Officer Naval Research Laboratory ATTN: E. Senasack (code 8220) P. Hastman (code 8222) T. Kowocki (code 8222) C. Merk (code 8211) 4555 Overlook Avenue Washington, D.C. 20375-5000	4
6. Professor R. Panholtzer, Code 62PZ Naval Postgraduate School Monterey, CA 93943-5000	2
7. D. Rigmaiden, Code 72 Naval Postgraduate School Monterey, CA 93043-5000	1
8. Los Alamos National Laboratories Condensed Matter and Thermal Physics (Group P-10) ATTN: Dr. G.W. Swift P.O. Box 1663/MS 764 Los Alamos, NM 87545	1
9. Lt. Michele Fitzpatrick 1634 W. Norwegian St. Pottsville, PA 17901	1

10. Lt. Michael P. Susalla 1
4148 Mustang St.
San Diego, CA 92111
11. National Center for Physical Acoustics 1
ATTN: Librarian
P.O. Box 847
Fraternity Row
University, MS 38677
12. Lt. R.E. Volkert 3
Naval Postgraduate School
SMC 1984
Monterey, CA 93943
13. Capt. D.A. Harris 3
P.O. Box 1854
Greenwood, Nova Scotia
Canada B0P 1N0
14. Mr. F. M. Murray, P.E. 1
JBL Incorporated
8500 Balboa Blvd.
Northridge, CA 91329
15. Lt. S. Cobb 1
SSD/CLFPD
P.O. Box 92960
LLAFB
Los Angeles, CA 90009-2960
16. Mr. T. C. Moore 1
Develco, Inc.
175 Nortech Parkway
San Jose, CA 95142-2306
17. Mr. J. Adeff 1
Code 61
Naval Postgraduate School
Monterey, CA 93943
18. Mr. D.V. Conte 1
Program Manager - NGAS Magnavox
1313 Production Road
Ft. Wayne, IN 46808
19. Professor D.E. Hall 1
California State University
Department of Physics and Physical Science
Sacramento, CA 95819

20. Defense Technical Information Center
Cameron Station
Alexandria, VA 22304-6145

2

Thesis
H289307 Harris
c.1 Design and calibration of an electrodynamic driver for the Space Thermoacoustic Refrigerator (STAR).

Thesis
H289307 Harris
c.1 Design and calibration of an electrodynamic driver for the Space Thermoacoustic Refrigerator (STAR).

Design and calibration of an electrodyna



3 2768 000 83352 9

DUDLEY KNOX LIBRARY